Doctoral Dissertation
Doctoral Program in Civil and Environmental Engineering ($32^{nd}$ cycle)

# Complex formations with a block-in-matrix fabric

## Maria Lia Napoli

∗ ∗ ∗ ∗ ∗ ∗

### Supervisors
Prof. Monica Barbero, Supervisor
Prof. Claudio Scavia, Co-supervisor
Prof. Andrea Festa, Co-supervisor

**Doctoral Examination Committee**
Prof. Simonetta Cola, Università degli Studi di Padova (IT)
Dr. Aycan Kalender, Referee, Hacettepe University (TR)
Dr. Edmund Medley, Terraphase Engineering, Oakland (US)
Prof. Harun Sonmez, Referee, Hacettepe University (TR)
Prof. Ludger Oswaldo Suarez-Burgoa, Universidad National de Colombia (CO)

Politecnico di Torino
November 6, 2020

I hereby declare that, the contents and organisation of this dissertation constitute my own original work and does not compromise in any way the rights of third parties, including those relating to the security of personal data.

.........................................
Maria Lia Napoli
Turin, November 6, 2020

# Summary

This Ph.D. thesis studies geotechnically complex formations with a block-in-matrix internal arrangement in order to better understand the technical difficulties associated with their identification, characterization and modeling and to provide possible solutions and tools to overcome these challenges. The complexity of these heterogeneous formations originates from the great variability in their structure, lithology and geotechnical properties. A large number of widespread geologic units, such as conglomerates, agglomerates, glacial tills, weathered rocks and, above all, melanges, belong to this category of complex formations.

The definitions, perspectives and classifications of such materials have been the subject of much debate and confusion among experts since the 1950's. In 1994 Edmund Medley coined the term "bimrock", the acronym for "block-in-matrix rocks", to conveniently denote the wide variety of heterogeneous formations composed of strong rock blocks embedded in a bonded matrix of finer texture. The great potential of this term was that it had no geological connotation, since it generically indicated all rock-soil mixtures. Nonetheless, inappropriate geologic definitions are still being used in the literature, engendering great confusion among geopractitioners and readers. Hence, the first objective of this Ph.D. research was to shed light on this nebulous terminology, by developing a clear classification for block-in-matrix complex formations.

Previous research has demonstrated that rock inclusions (their content, position, shape, etc.) strongly influence the overall mechanical behavior of heterogeneous geomaterials. Since the commonly used deterministic approaches cannot capture the inherent spatial and dimensional variability of these complex formations, a novel stochastic approach has been introduced in this research in order to investigate how rock inclusions may influence the stability and failure modes of bimrocks. Specifically, 2D and 3D numerical simulations were carried out on many slope and tunnel models with different block contents, dimensions, positions, shapes and orientations, highlighting the benefits of using such a statistically-based approach. Moreover, from an operative point of view, rock blocks and their characteristics strongly influence the choice of the most appropriate earthwork equipment and underground excavation and support methods. However, reliable estimates of block quantities and characteristics are not straightforward and constitute one of the

greatest challenges for geopractitioners.

Stereological principles are generally applied to infer 3D block contents from 1D or 2D measurements, but they are often fraught with a high magnitude of error. In order to provide information that may help to address the research gaps regarding this topic, two novel statistically-based tools, implemented in different Matlab codes, were developed in this research. The first investigates the degree of error that can be introduced by inferring the 3D block contents from 2D measurements, providing an uncertainty factor to adjust the initial estimates. The second was developed mainly for practical applications. In particular, the new proposed tool allows the probability of encountering blocks when tunneling in heterogeneous ground to be estimated and could help to reduce tunneling risks.

In order to explore and tackle the many difficulties inherent in the characterization of these geomaterials, a typical Italian melange from the Oltrepò Pavese area was thoroughly investigated. In particular, the efforts undertaken to collect and prepare intact specimens, which were mainly caused by its sensitivity to water, are described in detail, as are the laboratory tests, which often required non-conventional procedures. A series of triaxial tests were carried out with the aim of providing all the necessary information to set up and calibrate a 3D numerical model reproducing the laboratory tests. However, remolded specimens had to be used, since the different matrix properties and block characteristics (dimensions, lithologies, etc.) of the natural samples did not allow the tests to be performed under controlled and repeatable conditions. To obtain the real geometry of the specimens tested, X-ray Computed Tomographies were performed on the heterogeneous samples. Although the numerical model is beyond the scope of this research, it could be a valid tool to predict the mechanical behavior of geomaterials like the Oltrepò Pavese melange, but with different block contents, shapes and mechanical characteristics when subjected to various stress histories.

# Acknowledgements

# Contents

# List of Tables

11

12

13

# List of Figures

17

20

21

# Chapter 1

# Complex formations

A "complex formation" is a lithological and/or structurally discontinuous deposit (rock unit or soil) with highly contrasting mechanical properties at a significant scale as far as engineering works are concerned (Cancelli 1986, D'Elia et al. 1986, Barla and Perello 2014). The "complexity" ascribed to these formations can be caused by genetic (sedimentation and metamorphism, mass movements, volcanic activities, etc.) or epigenetic (tectonic deformations, weathering, stress release, chemical alteration, etc.) processes (Anagnostou et al. 2014, Harrison 2014). Examples of the origins of litho-structural heterogeneity are shown in Figure 1.1. It is worth pointing out that, from an engineering point of view, this "complexity" should be intended as "geotechnical" rather than "geological", although the distinguishing features of complex formations (i.e. heterogeneity and chaotic structures) are strongly related to particular geological processes. However, as underlined by many authors, a complex geological history does not always result in geotechnical complexity, and vice versa (D'Elia et al. 1986, Anagnostou et al. 2014, Barla and Perello 2014, Harrison 2014). As an example, the geotechnical behavior of highly sensitive marine clays or turbidites, which are "geologically non-complex" units, is extremely difficult to define. For this reason they are considered (geotechnically) complex formations (D'Elia et al. 1986, Anagnostou et al. 2014, Barla and Perello 2014). On the contrary, many "geologically complex" units cannot be defined as (geotechnically) "complex formations", since the mechanical properties of their different lithologies do not vary in a significant way. Hence, it is fundamental to distinguish between geological and geotechnical complexity, since only the latter makes engineering works extremely challenging.

The mechanical characterization of (geotechnically) complex formations is extremely problematic, since the properties that govern the geotechnical behavior of these deposits vary rapidly and erratically within the study area and are strongly heterogeneous and scale-dependent. This implies that it is generally difficult to obtain a Representative Elementary Volume (REV) to be tested in the laboratory, which means that parameters found at the scale of laboratory samples (mesostructure) are

not always representative of the overall behavior of the deposits at smaller scales (macrostructure).

| Origin | Examples |
|---|---|
| *Genetic processes* | |
| Sedimentation and metamorphism | Rock formations consisting of alternating beds of various lithological types such as flysch, sedimentary melanges ("olistostromes") and turbidites; alluvium or other quaternary soil deposits consisting of alternating fine- and coarse-grained layers and lenses |
| Glacial movements, subglacial erosion | Moraines of central Europe or northwest America, characterized by variable fine- and coarse-grained soil fractions with variable quantities of bigger or smaller boulders |
| Mass movements | Landslide breccias |
| Igneous processes | Sedimentary formations penetrated by magmatic intrusion dikes |
| *Epigenetic processes* | |
| Tectonic processes | Variably fractured rocks; rapidly changing orientation of schistosity and bedding planes due to intensive folding; tectonic melanges consisting of a sheared fine-grained matrix with rock fragments |
| Weathering | Rock mass with open discontinuities due to chemical weathering by meteoric water near the surface (Brekke and Howard 1972) |
| Alteration | Irregular occurrence of soil-like granite even at greater depths due to hydrothermal alteration of micas and feldspars into clay (Barbier 1977) |
| Solution | Carbonatic rocks with variable quantities of smaller or larger karst cavities, possibly filled by breccias following cavity collapses |
| Combinations | Hydrothermally altered rock in fault vicinity; fractured and/or weathered host rock in the vicinity of intrusion dikes |

Figure 1.1: Genetic (original complexities) and epigenetic (acquired complexities) processes leading to present rock mass heterogeneity (Anagnostou et al. 2014).

In order to define and describe in a simple way the type of complexity of such geomaterials, a series of classification systems for structurally complex formations has been proposed since the International Symposium on "The Geotechnics of Structurally Complex Formations" held in Capri (Italy) in 1977 (Esu 1977).

## 1.1 Classification of complex formations

The first classification of "structurally complex formations" was proposed by Esu (1977) (Figure 1.2).

| | A1 | Layered clay shales and shales (with or without fissility) more or less fissured and/or jointed. Geotechnical complexity depending upon mineralogy and stress history (mainly vertical loading). |
| A2 | Sheared clay shales and shales. Geotechnical complexity depending upon mineralogy and stress history (mainly shearing). |
| B1 | Ordered sequences of more or less fissured and jointed layers of competent rock and clay or shales. Geotechnical complexity depending upon mineralogy and stress history (mainly vertical loading). |
| B2 | Disarranged layers of competent rock and clay or clay shale from highly fissured and jointed up to sheared. Geotechnical complexity depending upon heterogeneity, mineralogy and stress history (mainly shearing). |
| B3 | As B2, with a chaotic structure. Geotechnical complexity depending upon heterogeneity, mineralogy and stress history (repeated cycles of shearing with large displacements). |
| C | Blocks or fragments of more or less weathered rocks in a clayey matrix (residual and colluvial soils). Geotechnical complexity depending upon heterogeneity and mineralogy. |

Figure 1.2: Classification of structurally complex formations (after Esu 1977, Barla and Perello 2014).



Figure 1.3: From the left: complex formations belonging to group A (D'Elia et al. 1986), group B and group C (Festa et al. 2010).

Three main groups of rock bodies characterized by calcareous and arenaceous-pelitic or calcareous-pelitic lithologies are considered in the classification of Figure 1.2. The first (group "A") includes homogeneous jointed or sheared clay shales and shales. The second (group "B") includes mainly heterogeneous deposits with both fissured/disarranged layers of competent rock and a matrix of finer texture (mainly clayey). Rock fragments or blocks can also be found within the softer

27

matrix. The last group (group "C") includes very heterogeneous geologic bodies, formed by clayey soils and rock blocks, including submarine slide deposits, colluvial soils, etc.. Some examples are given in Figure 1.3.

Figure 1.4 shows another classification proposed for complex formations such as flysch by Marinos and Hoek (Marinos and Hoek 2001, Marinos et al. 2019). These rock masses were classified in 11 types according to their siltstone-sandstone proportion and tectonic disturbance, and a certain range of GSI (Geological Strength Index) values was assigned to each flysch type. In fact, the chart was developed in order to accommodate these geomaterials in the GSI system, which relates the properties of the intact rock elements to those of the overall rock mass (Hoek 1994).
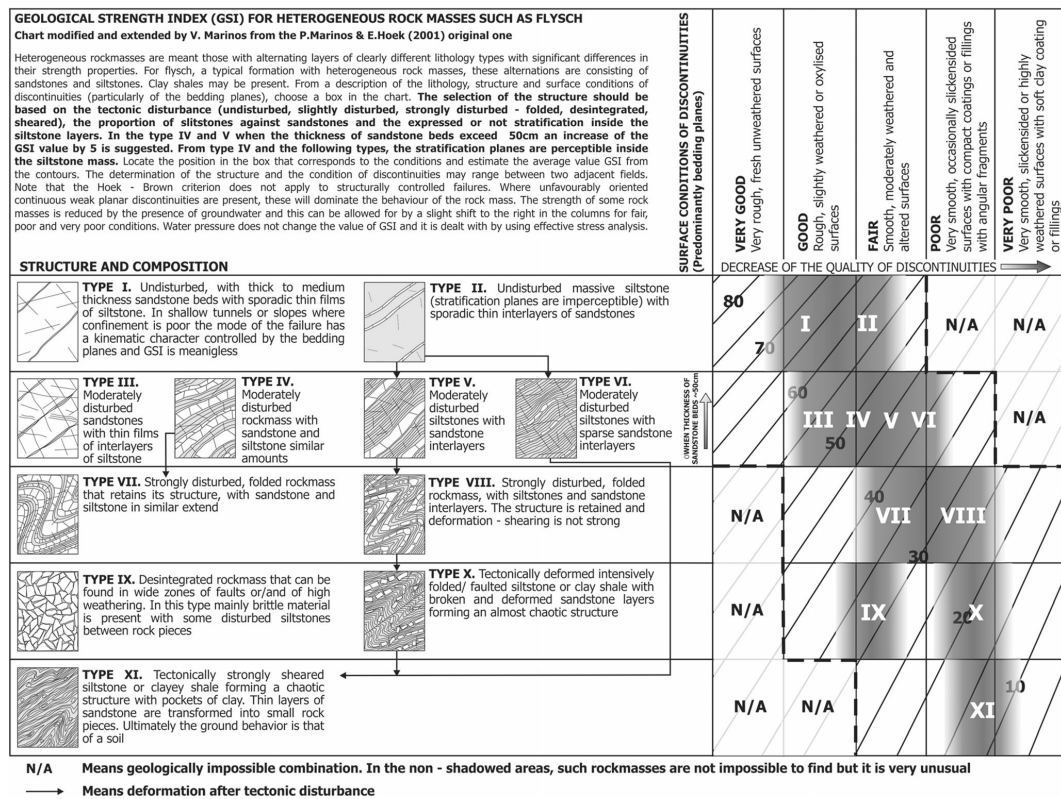


Figure 1.4: Classification for heterogeneous rock masses such as flysch (Marinos et al. 2019).

This Ph.D. reserach concerns the study of chaotic geologic bodies with a block-in-matrix structure, which mainly refer to groups "B3" and "C" in the classification of Figure 1.2. These are the most problematic complex formations to characterize (Barla and Perello 2014) and encompass a wide range of geomaterials with a

block-in-matrix internal arrangement, including conglomerates, agglomerates, olistostromes, breccias, flysch, fault-shear zones, weathered rocks, melanges and other rock-soil mixtures, as illustrated in Figure 1.5 (Medley 2001, Gokceoglu and Zorlu 2004, Sonmez et al. 2004a, Wakabayashi and Medley 2004, Afifipour and Moarefvand 2014c, Kalender et al. 2014).
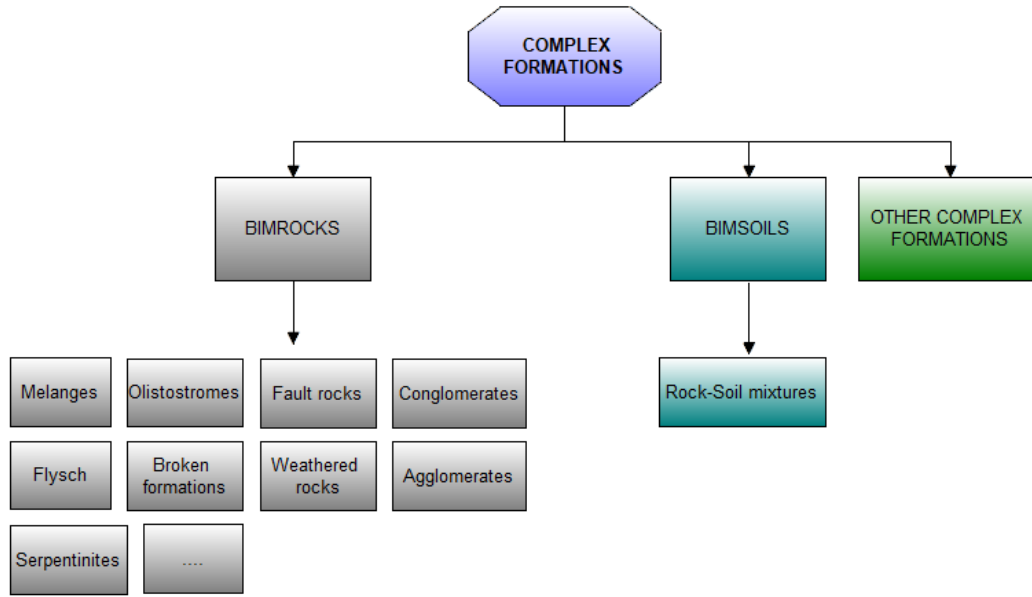


Figure 1.5: Classification of block-in-matrix deposits belonging to complex formations, obtained from the literature.

## 1.2 Complex Formations with a block-in-matrix fabric

Geological materials are generally classified as either *soils* or *rocks*. However, many heterogeneous and often chaotic geological deposits with a block-in-matrix fabric do exist worldwide, which constitute a transition zone between soils and rocks. These heterogeneous geomaterials are characterized by a great variability of mechanical parameters and lithological changes within short distances, which are also often associated with erratic permeability values. When dealing with such block-in-matrix formations, it is not possible to resort to classic soil/rock mechanic procedures in order to evaluate their mechanical behavior. In fact, soil mechanics equipment allows only low nominal loads and pressures to be applied, while with rock mechanics equipment is not possible to control the pore pressures (Dong et al. 2013b). For all these reasons, the determination of the geomechanical properties

of such geomaterials is extraordinary problematic. This is why they belong to the so-called "complex formations" or "structurally complex formations" (D'Elia et al. 1998, Anagnostou et al. 2014).

Technical difficulties, delays, economic repercussions and security risks have been faced in many engineering works in these geomaterials (Medley and Goodman 1994, Goodman and Ahlgren 2000, Medley 2001, Medley 2007a, Anagnostou et al. 2014, Lunardi et al. 2014). Some examples are illustrated in Chapter 2.

The critical conditions associated with complex formations have encouraged many researchers and geopractitioners to focus on this topic over the last decades. Geologists have studied the different processes leading to the formation of such rock units, in order to differentiate them and try to provide some classifications (Esu 1977, Riedmüller et al. 2001, Festa et al. 2010). On the other hand, geotechnical engineers have focused their attention on how to characterise these formations and correctly model, design and construct engineering works in these geomaterials. Dott. E. Medley and Dott. E.S. Lindquist at the University of Berkeley - California have been the first authors to face and fully document, from an engineering point of view, the problem of the structural complexity of such heterogeneous deposits (Medley 1994, Lindquist 1994b). In their Ph.D. Dissertations, a detailed research on "melanges" belonging to the Franciscan Complex (see section 1.2.1) and similar block-in-matrix rocks is presented and their experimental results are still taken into account by practitioners dealing with such complex rock bodies all over the world.

## 1.2.1   The Franciscan Complex

The Franciscan Complex (or simply "Franciscan") is a subduction accretionary complex composed of oceanic and trench rocks formed on the western margin of North America. The Franciscan covers about one third of northern California and is mainly composed of sandstones, conglomerates and mudrocks; however, it also contains mafic oceanic crustal fragments with limestone, chert, blueschist and other rock types (Raymond 2017).
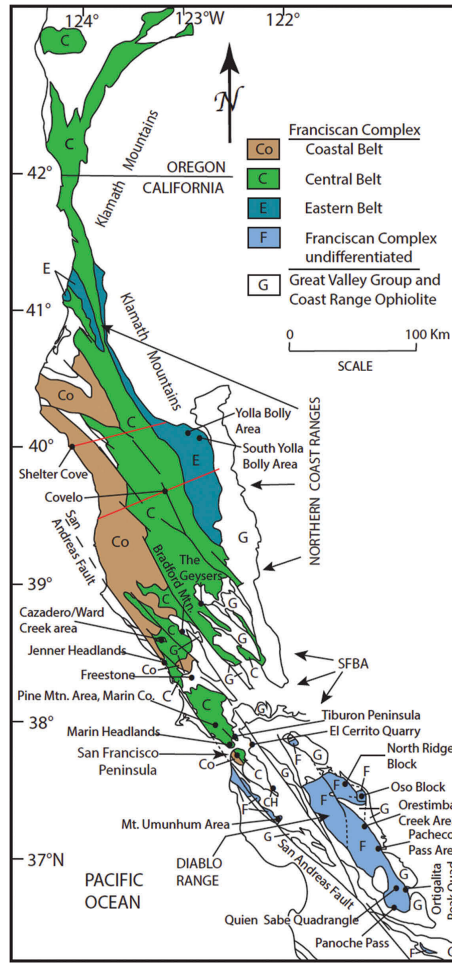
Figure 1.6: Geologic map of the Franciscan Complex (Raymond 2017).

Many different types of melanges (which is a French word that means "mixture", well representing the chaotic structure of these geomaterials) can be found in the Franciscan Complex. Sedimentary, tectonic, diapiric and polygenetic (i.e. melanges formed by the interplay and superimposition of different processes) melanges with different internal block-in-matrix fabric (ranging from sedimentary and igneous to metamorphic), relatively continuous or sheared fabric and variable block shapes, dimensions and compositions have been recognized by many experts in the field (Hsu 1968, Cowan 1974, Medley 1994,Wakabayashi et al. 2002, Festa 2011, Festa et al. 2012, Festa et al. 2020).

Since the 1950's, many geologists and geotechnical engineers have been involved in detailed studies concerning the Franciscan melanges. In fact, due to the chaotic conditions of these rock masses, a great number of engineering projects have suffered technical problems, requiring innovative and specific research ( Lindquist and Goodman 1994, Goodman and Ahlgren 2000, Medley 2007a, Medley and Zekkos

31

2011). Since then, due to the world-wide distribution of melanges and similar block-in-matrix rock bodies (Figure 1.7), further studies concerning such complex formations have been performed in many other countries.
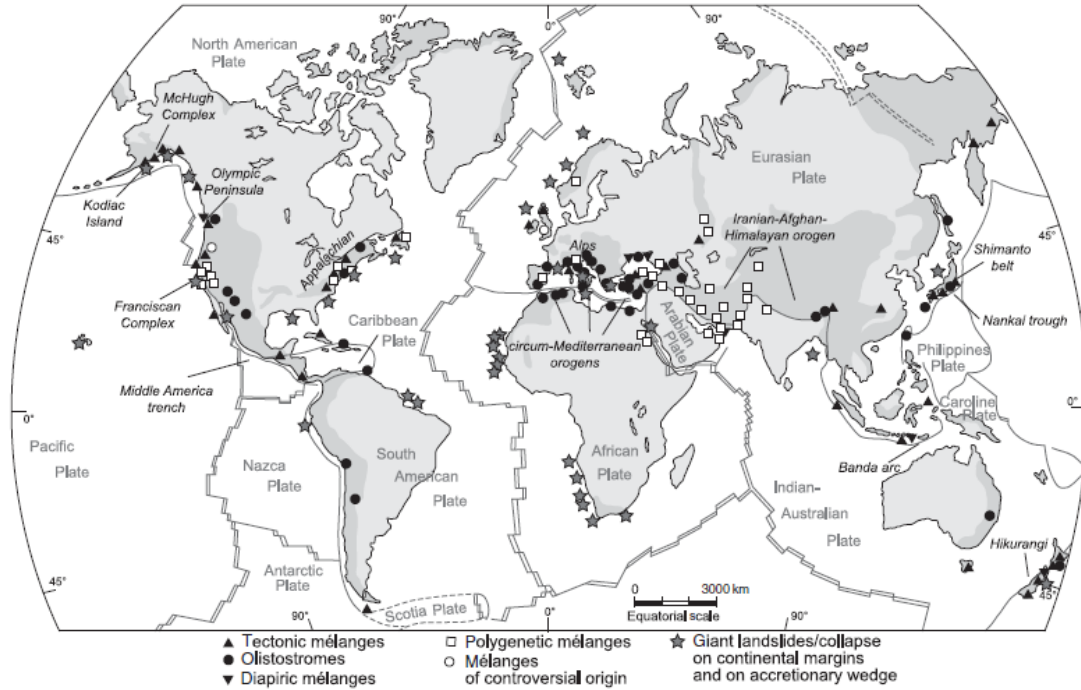


Figure 1.7: World map of melanges (Festa et al. 2010).

However, an enormous number of ambiguous and inappropriate geological synonyms associated with mixed, chaotic and fragmented rocks has been adopted for years by geopracticioners from all over the world. In particular, the term "melange" has often been inappropriately used to describe a wide variety of complex and often chaotic formations with a block-in-matrix fabric (Medley 1994). Moreover, further confusion has also resulted from the many inappropriate aliases found in the literature for the term "melange" (i.e. complex formations, mega breccias, Franciscan Complex, tectonic breccias, varicolored clays, argille scagliose, sedimentary chaos, etc.) (Raymond 1984, Lindquist 1994b, Raymond 2017). This has caused many scientific debates among geologists and has been a source of great confusion and misinterpretations in the literature, especially among engineers (Medley 2001, Wakabayashi et al. 2002, Festa et al. 2019a).

In the next sections, a brief overview of the origin and definitions of melanges is given. This is believed to be necessary to clarify some aspects related to the most abundant and widely distributed complex formations.

### 1.2.2   Melanges

This section intends to explain the reasons why many aliases for the term "melange" exist and a great confusion was caused by the use of such terms. This is done by means of an overview of geologic studies on melanges available in the literature, starting from the origin of the term. This overview not only highlights that a great number of heterogeneous/chaotic rock units belong to melanges, but also underlines the fact that different opinions, definitions, classifications and perspectives have been supported by many geologists in the last 70 years. Hence, it will be evident how difficult it was and can be to identify and correctly classify these heterogeneous geologic bodies.

#### 1.2.2.1   The origin of the term "melange"

In 1919 the British geologist Edward Greenly introduced the term "melange" to indicate tectonic rock bodies of north Wales characterized by lenticular and predominantly hard blocks of sedimentary rocks enclosed in a finer-grained and generally schistose matrix. Greenly coined this term to differentiate these rocks formed by tectonic processes from other "chaotic" rock units originated by sedimentary (gravitative) processes, such as the Wildflysch Auct., largely described in the Alps after Kaufmann (in Studer 1872, Kaufmann 1886).
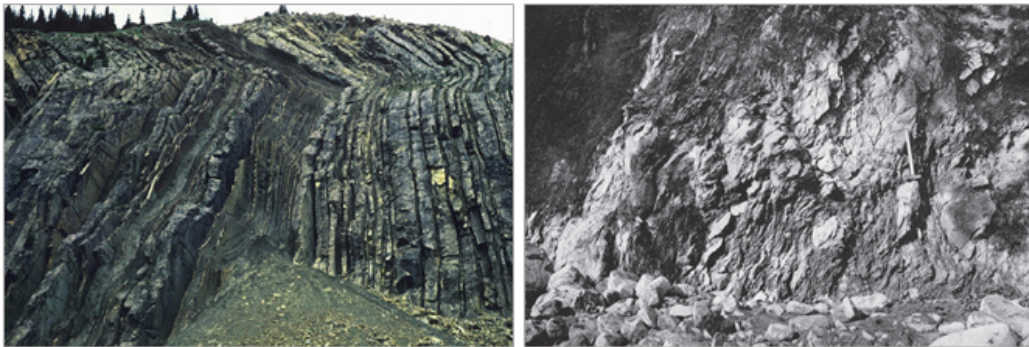


Figure 1.8: Comparison between flysch (on the left) and wildflysch (on the right) (Mutti et al. 2009).

Wildflysch had some features in common with flysch. However, wildflysch presented disruption and exotic blocks (i.e. rock inclusions that have not the same origin of the matrix) within the mainly clayey or shaley intensely deformed matrix (Mutti et al. 2009, Festa et al. 2010, Festa et al. 2020). Hence, Kauffman used the term *wildflysch* because of their "undisciplined nature of bedding" strongly contrasting with the alternating well-bedded strata known as flysch (Figure 1.8).
The interpretation of flysch already provoked considerable controversy among geologists (Mutti et al. 2009). Hence, it is easy to guess that the interpretation of

wildflysch sparked scientific debates within the experts, as well. However, even more extensive debate and disputes have been generated by geologists for the definition and interpretation of melange deposits. The most striking example is the Franciscan Complex, in California, for which some details are provided in chapter 1.2.1.

### 1.2.2.2 Definitions of the term "melange"

In the beginning, since a specific and clear definition of the term was not provided by Greenly, the term "melange" was not adopted for more than twenty years (Raymond 1984, Wakabayashi and Medley 2004, Festa et al. 2010, Raymond 2017). Only in the 1950s, after the works of Bailey and McCallien and Gansser (Bailey and McCallien 1950, Gansser 1955), several authors began to denote a number of disrupted rock bodies with different geological, lithological and structural features, with the term "melange". Such a rough and widespread use of the term melange started spreading confusion and debates among the geologists since the 60's.

In 1968 the melange concept was formalized by Hsu for the first time (Hsu 1968). Hsu, who studied the Franciscan complex, defined melanges to be chaotic units originated from tectonic processes leading to fragmentation, mixing and incorporation of exotic blocks within the matrix (Festa et al. 2010, Festa et al. 2016). The author provided the following definition of melanges: "*.. mappable bodies of deformed rock characterized by the inclusion of tectonically mixed fragments or blocks, which may range up to several miles long, in a pervasively sheared, fine-grained and commonly pelitic matrix. Each melange includes both exotic and native blocks*".

After Hsu (1968), the term "melange" was increasingly used to designate several complex geological formations with rock blocks and fragments of different sizes and shapes embedded in a deformed matrix (Cowan 1985). Moreover, it was used both in a purely genetic and descriptive sense, engendering confusion among researchers, who proposed many different and ambiguous definitions and classifications (Raymond 1984, Cowan 1985, Festa et al. 2010). Some authors (Gansser 1955, Hsu 1968) sustained the genetic definition of the term "melange", i.e. formed by tectonic processes only. Hence, they distinguished melanges from block-in-matrix rock sedimentary deposits, called "*olistostromes*".

Other researchers (Gansser 1955, Cowan 1974, Hsu 1974, Raymond 1975, Raymond 1984, Cowan 1985, Wakabayashi and Medley 2004, Remitti et al. 2007, Festa et al. 2010, Wakabayashi 2015, Festa et al. 2016), on the contrary, used the term "melange" in a descriptive way. They subdivided melanges in several categories considering the geological formation processes: "tectonic melanges", "diapiric melanges", "ophiolitic melanges" or "polygenetic melanges" (melanges formed by both tectonic and sedimentary processes) and "sedimentary melanges" (i.e. olistostromes).

In the 1970s, after further studies, several authors (Hsu 1974, Cowan 1978), who

initially gave the term "melange" a genetic meaning, modified their definitions, avoiding any specification of the origin of the matrix. In fact, since fragmentation and mixing were recognized as essential processes in the formation of melanges, sedimentary events were accepted as one of their possible forming processes (Raymond 1984, Cowan 1985, Festa et al. 2010, Raymond 2017).

In 1974, Cowan defined melanges as "*mappable bodies of deformed rocks characterized by the inclusion of tectonically mixed fragments of blocks ... in a pervasively sheared, fine-grained and commonly pelitic matrix*" (Cowan 1974).

In 1984, Raymond defined a melange as a "*body of rock mappable at a scale of 1:24,000 or smaller and characterized both by the lack of internal continuity of contacts or strata and by the inclusion of fragments and blocks of all sizes, both exotic and native, embedded in a fragmented matrix of finer grained material*" (Raymond 1984). This last definition implied that melanges may be originated by different geological processes (tectonic, sedimentary, diapiric or a combination of these contributions) but, also, that they should contain "*exotic*" blocks (i.e. originated in foreign rock units). This requirement, already introduced by Hsu in 1968, was another controversial issue. In fact, some geologists have distinguished heterogeneous rock bodies containing only "*native*" blocks (i.e. intraformational) from melanges containing both native and exotic blocks (Raymond 1975, Raymond 1984, Festa et al. 2012, Raymond 2017, Festa et al. 2020). In particular, the term "*broken formation*" was introduced by Hsu in order to define a (tectonic) stratally disrupted rock body containing only native blocks (Hsu 1968).

The term "olistostrome" (from the Greek *olistomai*, which means to slide, and *stroma*, which means accumulation) was first introduced by (Flores 1955) to define "*sedimentary deposits occurring within normal geological sequences that are sufficiently continuous to be mappable, and that are characterized by lithologically and (or) petrographically heterogeneous materials, more or less intimately admixed, that were accumulated as a semi-fluid body*". (Flores 1955) and (Flores 1956) further specified that olistostromes do not show true internal bedding, and that they can be differentiated in a matrix ("binder"), which consists of "prevalent pelitic, heterogeneous material", and dispersed "bodies of harder rocks" ("from pebbles to boulders up to several cubic km").

In contrast to the term melange, olistostrome (Flores 1955), which is widely used in chaotic rocks literature, has a genetic connotation, being synonymous with a sedimentary melange in a broad sense. It includes the terms *endolistostrome* and *allolistostrome* (Elter and Raggi 1965), which describe chaotic rock units formed by sedimentary (gravitational) processes (i.e. mass transport deposits and complexes), embedding *native* and *exotic and native* blocks, respectively. Therefore, endolistostrome is synonymous with sedimentary broken formation, whereas allolistostrome is synonymous with sedimentary melange (Raymond 1984, Festa et al. 2019a).

35

Sedimentary melanges and broken formations that formed as a result of sedimentary mass-transport or mass-wasting processes preserved in exhumed convergent margins represent the ancient counterpart of modern mass transport deposits (Lucente and Pini 2008). The latter are commonly characterized by great internal heterogeneity and deformation, representing the product of single or multiple, and superimposed depositional events (Ogata et al. 2014, Della Valle et al. 2015, Festa et al. 2016, Ogata et al. 2020).

At present day, the larger part of "melange workers" agree in using the term *melange* as a descriptive and non-genetic term, defining a mappable body (at 1:25000 or smaller scale) of internally disrupted and mixed rocks, with "exotic" lithologies included as discrete masses (i.e. blocks) in a pervasively deformed finer grained matrix, without restriction to any particular lithological unit (e.g., Raymond 1984, Cowan 1985, Festa et al. 2010, Festa et al. 2019a). As stated above, different processes may lead to the formation of a melange: the adjectives "tectonic", "sedimentary" and "diapiric" can therefore be used to indicate the interpreted origin of melanges. The adjective "polygenetic" on the other hand indicates melange formed by the interplay and superimposition of tectonic, sedimentary and/or diapiric contributions (see Festa et al. 2020 for a complete review).

### 1.2.2.3 Melange classifications

Several classifications have been provided for melanges and similar rock bodies in the last 40 years (Figure 1.9).

Hsu (1968), sustaining the genetic definition of melanges, subdivided fragmented and mixed rock bodies into (tectonic) broken formations, tectonic melanges, having a pervasively sheared, fine-grained and pelitic matrix with both native and exotic rock inclusions, and (sedimentary) olistostromes.

Hsu (1974), once eliminated the requirement of exotic blocks within a melange body, distinguished only chaotic rock bodies (i.e. melanges) from those having no (or very low) lack of continuity between different geologic strata (i.e. formations). Raymond (1984) considered melanges to be tectonic rock bodies without stratal continuity but with exotic blocks, and divided them into four classes: diapiric, tectonic and polygenetic melanges and allolistostromes. Adopting the terminology proposed by Elter and Raggi (1965), sedimentary melanges were called "allolistostromes". If no exotic blocks were contained within rock units, they were assigned the appellation of "tectonic broken formations" or "endolistostromes" (sedimentary broken formations).

| REFERENCE | COHERENT UNITS | DISRUPTED UNITS | EXTENSIVELY DISRUPTED UNITS | NOTES |
|---|---|---|---|---|
| Greenly (1919) | Formation | Melange (T) - Olistostrome (S) | | |
| Hsu (1968) | Formation | Broken formation (T) | Melange (T) - Olistostrome (S) | *Melanges, unlike broken formations, should contain both native and exotic blocks* |
| Hsu (1974) Cowan (1978, 1985) | Formation | Broken formation - Melange (S/T) | | |
| Raymond (1984) | Formation | Tectonically broken formation (T) Endolistostrome (S) | Tectonic melange Allolistostrome (S) | *Melanges, unlike broken formations, should contain exotic blocks* |
| Festa (2012) | Formation | Broken formation (S-T-D-P) - Melange (S-T-D-P) | | *Melanges, unlike broken formations, should contain both native and exotic blocks* |
| *Process of formation: S=Sedimentary, T=Tectonic, D=Diapiric, P=Polygenetic* | | | | |

Figure 1.9: Classification of melanges.

Cowan (1985) proposed a largely descriptive classification of chaotic rock units with a block-in-matrix fabric. In his work, based on field studies along the Pacific margin of North America, the author subdivided melanges in four types (Figure 1.10): stratified sequences of sandstone and mudstone, progressively disrupted by layer-parallel extension (Type I); progressively disrupted sequences of mudstone, tuff, chert and sandstone (Type II); block-in-matrix mudstone chaos (Type III); mudstone dominated brittle fault zones (Type IV). These melange types can be differentiated mainly on the basis of their mesoscopic fabric (pinch and swell, boudinage, foliation, etc.), lithological composition and distinguishing features of rock inclusions (their shape, dimension and lithology). It is worth pointing out that the requirement that melanges contain exotic blocks is not included for all the types of melanges (e.g., Type I melange does not contain exotic blocks).

A more detailed classification of melanges (Figure 1.11), based on several field observations of chaotic rock units around the world, has been proposed in 2010 by Festa and coworkers (Festa et al. 2010). Six types of melanges have been identified (on the basis of their process of formation) and are briefly described in what follows.
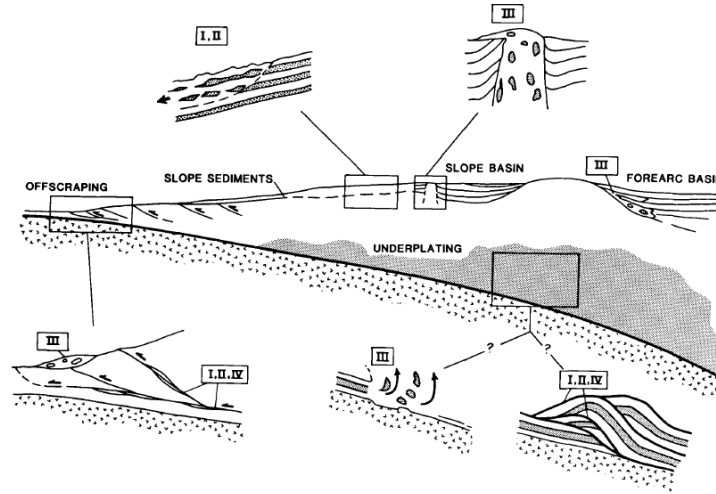
Figure 1.10: An active convergent margin with different settings responsible for the formation of the four types of melanges (Cowan 1985).



| Types of Mélange related to: | Geodynamic environments | Processes | Triggering mechanisms | Products | Mesoscale characteristics | Minor related products |
|---|---|---|---|---|---|---|
| 1. Extensional tectonics | Rifting | MTP (debris avalanches and flows, etc.) | Tectonic | MTD (megabreccias, breccias, olistolith fields, debrites, slide blocks, etc.) | Chaotic angular clasts (cm to >10 m) in fine-grained (pelitic) matrix | Fault zones along normal fault? |
| 2. Passive margin a. *Downslope mass-transport deposits* | Passive margins (after rifting) | SSD and mass-wasting related progressive deformation from slumping to debris flow, to complete stratal disruption | Tectonic, sedimentary | MTD, poorly sorted olistostromes (olistoliths, slide blocks) | Chaotic monomictic brecciated (matrix-supported) masses | *In situ* fluidification: mud diapirs? |
| b. *Mass-transport deposits at the ocean-continent transition (OCT)* | Ocean-continent transition | SSD and MTP with related progressive deformation from slumping to debris flows, to gravitational sliding | Tectonic, sedimentary | MTD, olistostromes with continent rock olistoliths (tens of meters to several km slide blocks) in a matrix of oceanic origin | Chaotic polymictic brecciated (matrix-supported) masses (including native, extra-basinal and/or exotic blocks) | |
| 3. Strike-slip tectonics and transform setting | Different types of collision | TSD: fault-to fold-related, fluidification (overprinting previous mass-wasting-related deformation) | Tectonic | BrFm; méanges (exotic blocks being commonly recycled from other previously formed mélanges) | Structurally ordered BIM fabric (parallel orientation of blocks and matrix features — i.e. pseudo-bedding) | Olistostromes *s.l.*; mud diapirs *s.l.* |
| 4. Convergent margins and oceanic crust subduction a. *Mass-transport deposits at the wedge front* | Subduction (at the front of the wedge) | MTP (debris flows and avalanches, slumps, slides, etc.) | Tectonic, sedimentary | MTD, olistostromes (olistoliths, olistolith fields and swarm, slide blocks) | Chaotic BIM fabric (including native, extra-basinal and/or exotic blocks) | Mud diapirs and mud volcanoes, serpentinite |
| b. *Broken fms and tectonic mélanges* | Subduction (at the base of the wedge) and subduction channel | TSD: fault-to fold-related, fluidification (overprinting previous mass-wasting-related deformation); tectonic mixing | Tectonic | BrFm; mélanges (exotic blocks being recycled from other previously formed mélanges or formed by subduct. channel processes) | Structurally ordered BIM fabric (parallel orientation of BIM features — i.e. pseudo-bedding) | |
| 5. Collision | Different types of collision | TSD: fault-to fold-related, fluidification (overprinting previous mass-wasting-related deformation) | Tectonic | BrFm; méanges? (exotic blocks being commonly recycled from other previously formed mélanges) | Mainly structurally ordered BIM fabric (that in some cases over-printed chaotic BIM fabric) | Olistostromes *s.l.*; mud diapirs *s.l.* |
| 6. Intracontinental deform. a. *Mass-transport deposits at the wedge front* a1. *Precursory olistromes* | At the base or at the front of intra-continental thrust sheets or nappes | MTP (debris flows and avalanches, slumps, slides, etc.) | Tectonic, sedimentary | MTD, olistostromes (olistoliths, olistolith fields and swarm, slide blocks) | Chaotic BIM fabric (from matrix-supported cm-to m in size blocks to clast supported >10 m blocks and olistoliths) | Mud diapirs and mud volcanoes |
| a2. Olistostromal carpet a3. Tectonic mélanges | | TSD: fault-to fold-related, fluidification (overprinting previous mass-wasting-related deformation) | Tectonic, sedimentary Tectonic | Mélanges (exotic blocks being commonly recycled from other previously formed sedimentary mélanges); BrFm | Chaotic BIM fabric overprinted by tectonic deformation and shearing Structurally ordered BIM fabric | |
| b. *Intra-nappe* b1. Sedimentary b2. Tectonic and/or tectono-sedimentary | Within intra-continental thrust sheets or nappes | MTP (debris flows and avalanches, slumps, slides, etc.) TSD: fault-to fold-related, fluidification (overprinting previous mass-wasting-related deformation) | Tectonic, sedimentary Tectonic | MTD, olistostromes (olistoliths, olistolith fields and swarm, slide blocks) BrFm; mélanges (exotic blocks being commonly recycled from other previously formed sedimentary mélanges) | Chaotic BIM fabric (blocks of intra-basinal origin) Structurally ordered BIM fabric (parallel orientation of blocks and matrix features — i.e. pseudo-bedding) | Mud diapirs and mud volcanoes |
| c. *Epi-nappe* c1. Sedimentary | A top of intra-continental thrust sheets or nappes (e.g. piggy back, top thrust basins) | MTP (debris flows and avalanches, slumps, slides, etc.) | Tectonic, sedimentary | MTD, olistostromes (olistoliths, olistolith fields and swarm, slide blocks) | Chaotic BIM fabric (originated from the succession tectonically imbricated in the thrust-sheet) | Mud diapirs and mud volcanoes |
| c2. Tectono-sedimentary | | TSD (overprinting previous mass-wasting-related deformation) | Tectonic, sedimentary | BrFm, mélanges | Structurally ordered BIM fabric | Olistostromes *s.l.*; mud diapirs *s.l.* |
| c3. Diapiric | | Extrusion of non-to poorly consolidated sediments | Tectonic, sedimentary | Mud diapirs and mud volcanoes | Zonation of deformation from core to margins | Olistostromes *s.l.* |
| 7. Sub-aerial deformation a. *Sedimentary* | On the Earth and/or other planets surface | MTP and glacial processes (debris flows, avalanches, slides, etc.) | Sedimentary, glacial, tectonic | MTD (debris flows/avalanches, alluvial fan deposits, talus breccias/megabreccias, block falls, glacial till, etc.) | Chaotic BIM fabric (block of intra-basinal origin) | |
| b. *Impact of bodies* | | Impact of bodies on planet surfaces | Impact processes | Ejected breccias and megabreccias | Chaotic breccias in a fluidal matrix | |
| BIM — Block-in-matrix BrFm — Broken Formation | | MTD — Mass-transport deposits MTP — Mass-transport processes | | SSD — Soft sediment deformation TSD — Tectonic stratal disruption | | |

Figure 1.11: Subdivision and classification of melanges and broken formations on the basis of their geodynamic setting of formation, processes, triggering mechanisms, products and mesoscale characteristics (Festa et al. 2012).

38
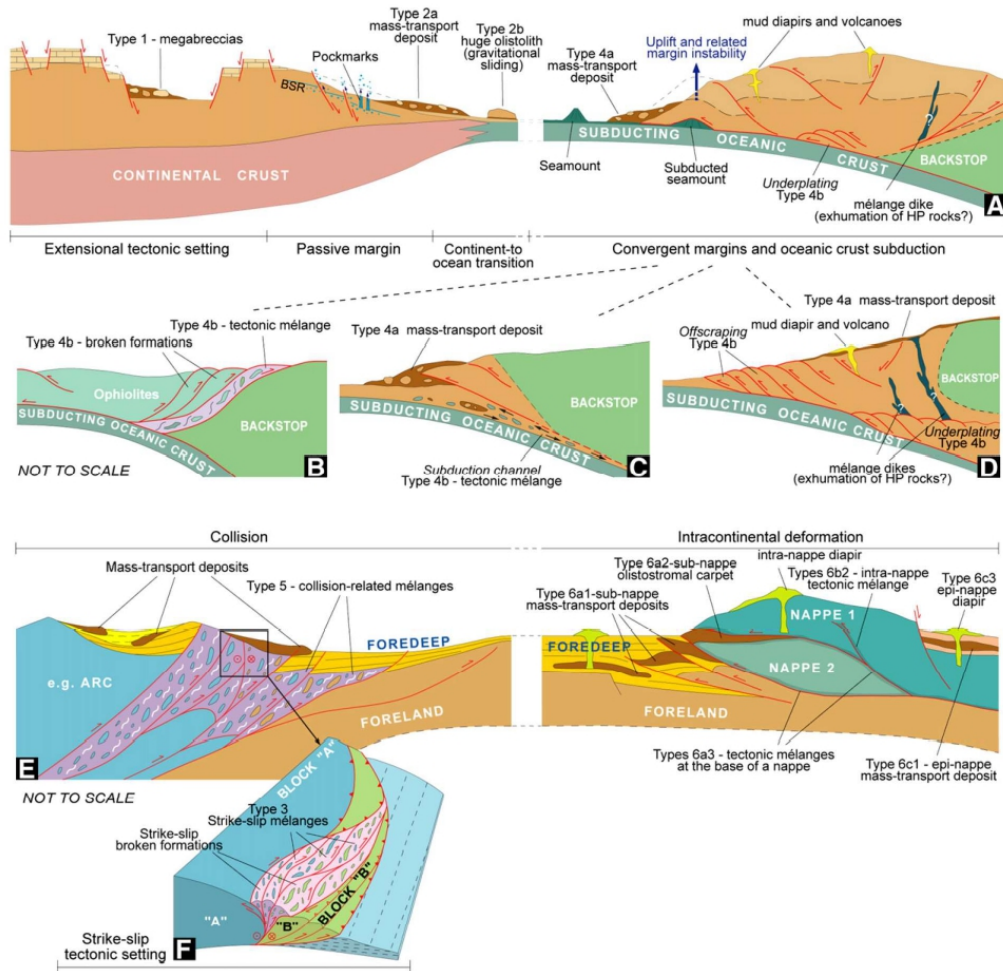
Figure 1.12: Conceptual model for the formation and emplacement of melanges associated with (A) extensional tectonics (type 1 melanges), passive margin (type 2a melanges), ocean-continent transition settings (type 2b melanges) and convergent margins (type 4 melanges). Different models and cases of subduction settings are shown: (A) open-double verging wedge with a low elevation backstop; (B) obduction of ophiolites; (C) close wedge and subduction channel; (D) close and smaller wedge with an high elevation of the backstop; (E) collisional tectonics (type 5 melanges; intra-continental deformation (type 6 melanges), and (F) strike slip tectonics (type 3 melanges) (Festa et al. 2012)

TYPE 1

The formation of this type of melanges is associated with processes related to extensional tectonics (i.e. stretching of the crust with formation of grabens and related crestal gravitational collapses). The matrix is generally formed by pelagic limestones. The blocks are originated by normal faulting producing collapses, and consequent accumulation, of cemented carbonate platform margins (Figure 1.12A).

39

This leads to mainly angular clasts with variable dimensions (from decimeters up to several tens of meters) having an intrabasinal composition. These chaotic (sedimentary) rock bodies, which constitute type 1 melanges, are known as megabreccias and olistoliths.

TYPE 2

The formation of this type of melanges is associated with instability processes, forming slides, slumps, cohesive debris flows, normally related to continental rifting phases (i.e. extensional tectonic which create new ocean basins) occurring in passive margin settings (which mark the transition between oceanic and continental crusts), as shown in Figure 1.12A.

*Olistostromes* are the chaotic rock bodies originated by such gravity-driven geologic processes. Angular blocks are randomly distributed within a fine-grained matrix and can present very large dimensions. For instance, in the case of rock inclusions originated by the failure of seamounts or submarine volcanoes, geologists have found blocks up to several kilometers embedded in the argillaceous-siliceous matrix.

Folding, boudinage, foliation and fluidal structures characterize this type of melanges and are due to plastic deformations that happened when the material was not consolidated yet (Figure 1.13). Seismic activities, gas hydrate dissociations and tectonic reactivations have been considered some of the possible triggering mechanisms.
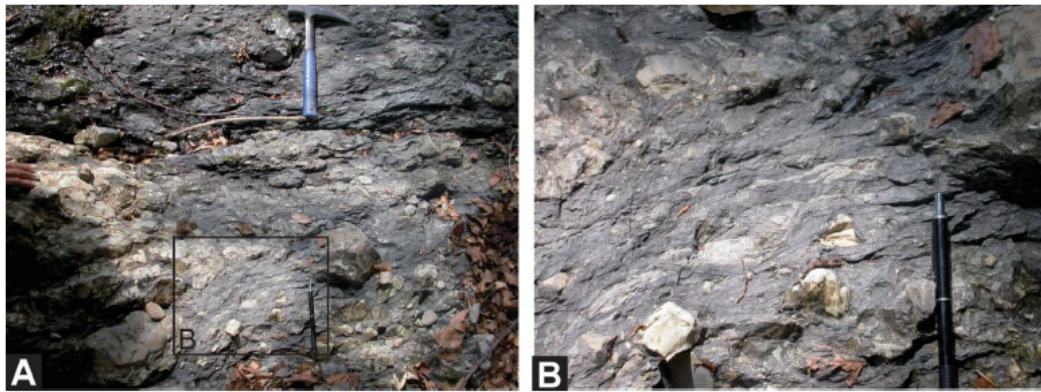


Figure 1.13: Olistostromes, type 2 melange (Festa et al. 2010).

TYPE 3

The formation of this type of melanges is associated with strike-slip deformation, altering coherent stratigraphic successions and producing disrupted units with a block-in-matrix fabric (Figure 1.12F). The blocks have elongated shapes of variable dimensions (up to hundreds of meters) and are arranged according to the shear direction. A progressive decrease of disruption can be observed when moving away from the fault zone.

TYPE 4

The formation of this type of melanges is associated with subduction. Melanges belonging to this class are chaotic and often present pinch and swell, boudinage and folds. Both intrabasinal and/or extrabasinal rock blocks can be recognized in these melange bodies (Figure 1.12A). Subduction erosion, mud diapirism, thrust faulting, folding and subduction of seamounts (causing over steepening and mass transport processes) are the principle triggering mechanisms responsible for the formation of this class of melanges (or broken formations if no exotic blocks can be recognized). Layer-parallel extensions, vein systems, boudinage and scaly fabrics can be recognized in several melanges/broken formations of type 4 (Figure 1.14), due to fluid overpressures, shear stresses and lithostatic loads.
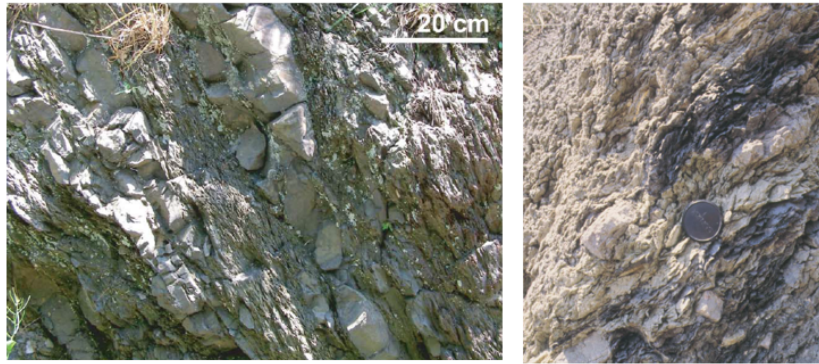


Figure 1.14: On the left: Layer-parallel extension (central Appalachian, USA); on the right: scaly fabric of an Italian melange (Northern Apennines) (Festa et al. 2010).

TYPE 5

The formation of this type of melange is associated with collision (Figure 1.12E).

TYPE 6

This last type of melanges is related to intracontinental deformation (Figure 1.12E). Festa and coworkers (2010) subdivided this type of melanges in three classes: "*sub nappe*", "*intra nappe*" and "*epi nappe*" melanges. Before providing a description of such classes, it seems worth providing a definition of the term "*nappe*". Nappes are elementary geological structures defined as "*large-scale, allochthonous tectonic sheet-like body, which was displaced along a basal, originally nearly horizontal fault (either contractional, or extensional, depending on the emplacement mechanism)*" (Prokešová et al. 2012).

*Sub-nappe melanges*

Sub-nappe melanges, having the same main features of olistostromes, mainly include chaotic rock units with block-in-matrix fabrics. These melanges could be

formed:

- at the front of thrust/nappe systems where debris flows/avalanches occurred (Type 6a-1 in Figure 1.12E);

- in correspondence of advancing/obduction nappes and/or accretionary wedges, later overridden, forming the so-called "olistostromal carpet" (Type 6a-2 in Figure 1.12E). These melanges often present large slabs of disrupted strata and shearing (Figure 1.15);

- at the base of regional-scale thrust sheets or nappe systems (Type 6a-3 in Figure 1.12E), where overpressures and fluid circulation in the shear zones produce tectonic melanges with a fabric that changes from a structurally ordered (near the shear zone) to a more chaotic one, moving away from the shear zone (Figure 1.16).
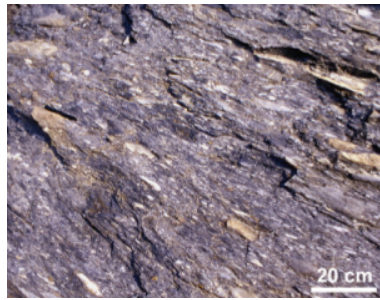


Figure 1.15: Flattened clasts of the olistostromal carpet at the base of the Ligurian nappe (Cinque Terre, Italy) (Festa et al. 2016).



Figure 1.16: Broken formation (red Flysch) at the base of the Molise Unit (central Apennines, Italy)(Festa et al. 2010).

42

*Intra-nappe melanges*

Intra-nappe melanges are related to nappe translations causing deformations. They have been subdivided in two classes, on the basis of the process of their formation: sedimentary and tectonic-tecto-sedimentary melanges. Sedimentary melanges include conglomerates, breccias and megabreccias (Figure 1.17). The formation of this type of melange is mainly associated with tectonic events, causing submarine gravity-driven instabilities (rock falls, grain flows, etc.). Tectonic-tecto-sedimentary melanges formed in a tectonic setting, mainly along weakness horizons (type 6b-2 in Figure 1.12E).



Figure 1.17: Breccias at the front of Matese, central Apennines (Italy) (Festa et al. 2010).

*Epi-nappe melanges*

These melanges occur in piggy-back basins (Figure 1.12E). Festa and coworkers (2010) subdivided this type of melanges in three classes: sedimentary, tectono-sedimentary and diapiric melanges.

The classification proposed by Festa et al. (2010) clearly shows that many different types of melanges do exist and highlights how difficult it could be to correctly identify the typology and the origin of chaotic rock units with block-in-matrix fabrics. However, an accurate identification and interpretation of the geology of the rock mass is essential in order to make correct predictions about its conditions (geometrical, mechanical and hydraulic properties and anisotropic matrix fabric) and its mechanical behavior during the execution of engineering works (Button et al. 2004).

## 1.3 Bimrocks

As shown in the previous Section 1.2, the vast geologic terminology used to indicate the many rock units with a block-in-matrix fabric (as shown in Figure 1.5) has engendered great confusion among geopractitioners and is in the main incomprehensible to most engineers (Lindquist 1994b, Medley 2007a, Medley 2008).

Since many similarities can be observed, from a geotechnical point of view, in all these geological formations, Raymond (Raymond 1984) coined the expression "*block-in-matrix-rocks*", which had no geological connotation. This expression was used to denote blocks of one lithology embedded in a material of another lithology. Although simple and clear, this definition was considered inadequate since it did not include many monolithologic block-in-matrix-rocks (such as sheared serpentinites) that exist in nature (Lindquist 1994b).

Later, in 1994, Medley introduced the word "*bimrock*", an acronym standing for Raymond's "block-in-matrix-rock" (Medley 1994). This term, which had no geological connotation either, was defined by Medley to be "*a mixture of rocks, composed of geotechnically significant blocks within a bonded matrix of finer texture*" (Medley 1994). In this definition, the expression "geotechnically significant blocks" highlights that a sufficient mechanical contrast between competent blocks and weaker matrix exists, and that both the volume and dimension of the blocks influence the rock mass properties at the scales of engineering interest (Medley 2001, Medley 2007b).

Since then, the term "bimrock" has been widely and conveniently used worldwide to indicate these heterogeneous and complex geological formations by many geologists but, mostly, by many engineers. Subsequently, following Medley's line, the acronym "*bimsoil*" (block-in-matrix soil) was used by engineers to designate geologic units with rock blocks embedded in a soil-like matrix (Medley and Goodman 1994, Kalender et al. 2014, Sonmez et al. 2016). Nevertheless, the geologic term "melange" has often been used in scientific works as a synonym of the general term "bimrock", engendering confusion among geopractitioners and researchers. This has been identified by the experts in this field as the most common misattribution made by engineers and other technicians (Lindquist 1994b).

In the next Section an attempt to make a clear classification of bimrocks is made, since this has not yet been proposed in the literature. Such a classification may help authors to publish more coherent and correct works and readers (especially if they are not particularly expert in this field) to better understand the topics and results.

# 1.4 A new classification for geotechnically complex formations

As discussed above, many different types of melanges exist in nature, each one with distinct characteristics. As a consequence, a specific melange could of course be a bimrock (or a bimsoil) and a specific bimrock (or bimsoil) could be a melange. However, not all bimrocks or bimsoils are melanges. Moreover, two melanges, even if belonging to bimrocks or bimsoils, may present very different characteristics and, as a consequence, extremely dissimilar mechanical behaviors. A striking example is given by the comparison between tectonic and sedimentary melanges. While the blocks in the former have an elongated shape, and are aligned with the main shear and/or fault zone, sedimentary melanges are characterized by a random distribution of irregularly shaped blocks within the matrix (Festa et al. 2019b) (Figure 1.18).
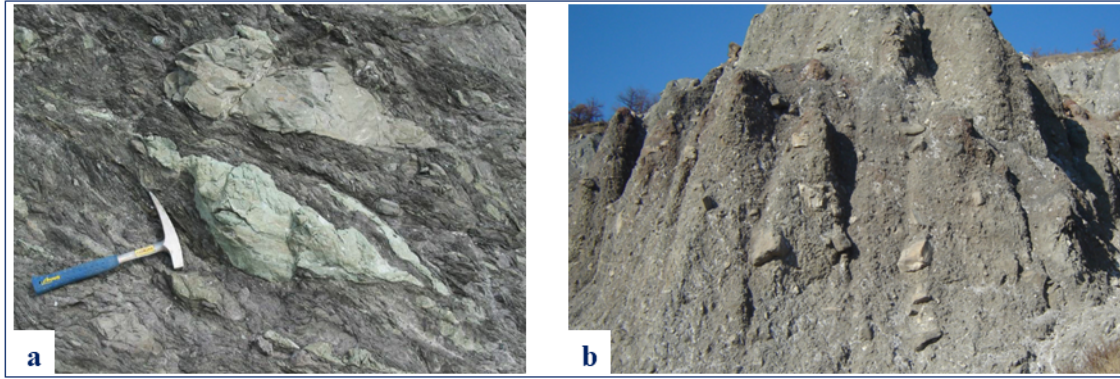


Figure 1.18: An example of tectonic and sedimentary melanges (Festa et al. 2010).

Moreover, the matrix can range from cemented, compacted and/or lithified (i.e. rock) to loose and/or uncemented (i.e. soil), whatever the type of melange.
This variability is not clearly stated in the many published works concerning various heterogeneous rock masses.
Hence, without detailed specification of the internal block-in-matrix arrangement, degree of lithification or consolidation of the matrix and its composition, it is extremely difficult to compare the results provided by different studies.
In order to try to shed light on these concepts, in this Ph.D. a new classification of geotechnically complex formations was developed. As shown in Figure 1.19, the complex formations were subdivided into *block-in-matrix formations* and *other complex formations*, giving particular attention to the first category to which *bimrocks* and *bimsoils* belong.

Figure 1.19: New classification of complex formations. Some examples of block-in-matrix deposits are given in brackets with the color blue.

Among the block-in-matrix rocks (bimrocks) the terms *hard* and *soft* were introduced to differentiate these complex formations on the basis of the properties and nature (composition) of their matrix. Specifically:

- "*hard bimrocks*" consist of hard blocks enclosed in a compacted or lithified

matrix and include both metamorphic and non-metamorphic rock units. The blocks are bonded with the matrix (i.e. welded block-matrix contacts). Moreover, the matrix is not sensitive to water because of its mineralogical composition.

Sedimentary melanges belonging to this first category of geotechnically complex formations are mass transport deposits whose matrix commonly consists of pelagic limestone (i.e. carbonate-rich) or sandstone. They range from megabreccias to olistolith fields, debrites and slide blocks. Some notable examples are the Upper Cretaceous megabreccias of the Maiella Mt. (Festa et al. 2014), the Upper Cretaceous megabreccias of the Calcareous Alps (Ortner 2001), carbonatic breccias, ophicalcites and serpentinite breccias.

Tectonic melanges include fault and shear zones with hard blocks in a compacted or lithified matrix, such as the Franciscan Complex and serpentinite melanges (Cloos 1984, Raymond 2017, Wakabayashi 2019).

Broken formations include hard native blocks in a compacted, lithified or serpentinite matrix. The Taconic melange is an example of this category of hard bimrocks (Festa et al. 2010, Festa et al. 2019b).

- "*Soft bimrocks*" are composed of hard blocks in a softer clayey to marly matrix. Although the blocks are bonded with the matrix, which is water sensitive and, unlike hard bimrocks, can be easily dissolved in water because of its mineralogical composition (clay or marl). Therefore, high changes in volume (e.g., shrinkage and swelling) and loss in strength can occur if the matrix comes into contact with water.

  Sedimentary melanges belonging to soft bimrocks are mainly represented by mass transport deposits with a clayey to marly matrix, and range from debris flows to blocky flows (Festa et al. 2016, Ogata et al. 2020). The Val Tiepido-Canossa argillaceous melange (Festa et al. 2015), studied in detail in this Ph.D. (see Chapters 5 and 6), belongs to this category, as well as broken formations and tectonic melanges, formed along fault rocks and shear zones, and characterized by a clayey to marly matrix (Remitti et al. 2007, Vezzani et al. 2010). Argille scagliose and argille varicolori are some examples of broken formations belonging to soft bimrocks (Pini 1999);

- "*bimsoils*" differ from bimrocks because the blocks are not bonded with the matrix (i.e. block-matrix contacts are unwelded), and the block-in-matrix assemblage results in a loose deposit. The bimsoils are mainly represented by, but not restricted to, recent continental deposits (e.g., colluvium, glacial till, alluvial and fan deposits, etc.), volcanic products (e.g., loose agglomerates) and weathered rocks. They correspond to block-in-matrix formations that have been named "unwelded bimrocks" by several authors (Sonmez et al.

2009, Afifipour and Moarefvand 2014c, Kalender et al. 2014, Mahdevari and Maarefvand 2017);

- finally, the lack of hard blocks isolated within a softer matrix allows "other complex formations" to be distinguished from bimrocks and bimsoils. This category includes complex formations characterized by the alternating of levels or beds with a different competence, which are commonly disrupted.

From Figure 1.19 it can be seen that some geologic bodies can fall within more than one category. For example, *argille scagliose* and *Red Flysch* can belong both to *soft bimrock* or to *other complex formations*, depending on the occurrence or not of blocks within the matrix, according to their primary lithostratigraphic characteristics.

Another striking observation which emerges from this new classification is that geologic units such as melanges and broken formations can be found both in the *hard* and *soft* bimrock categories, depending on the consolidation, lithification degree and composition of the matrix. Likewise, it can be noticed that conglomerates and agglomerates may belong to both the *hard bimrock* and *bimsoil* categories. However, this should not be surprising. In fact, from a geotechnical point of view, the characteristics of the matrix (e.g., consolidation and lithification degree, mineralogical composition, etc.) can significantly vary between different sedimentary melanges, conglomerates, etc.. Properties such as bonding, permeability and strength of the matrix are of utmost importance, since they greatly affect the collection methods (i.e. double barrel core sampler, manual sampling, etc.), preparation of intact specimen processes (i.e. water circular saw, dry saw, etc.), laboratory testing equipment to be used (i.e. for soils or rocks), testing procedures and, of course, test results. This is precisely the reason why this classification has been introduced.

# Chapter 2

# State of the art on bimrocks and bimsoils

A wide range of geologic bodies with a block-in-matrix structure can be found in many regions of the world. Due to their significant spatial, lithological, geo-hydrological and mechanical variability, these complex formations are extremely challenging to recognize, characterize and model (Lindquist 1994b, Medley and Lindquist 1995, Medley 2001, Button et al. 2004, Festa et al. 2010, Dong et al. 2013a). Serious technical problems, unexpected ground failures and delays during many engineering works have occurred and have been documented since the '90s. A few examples are reported in this Chapter (see Section 2.3) to highlight how mischaracterizations and wrong forecasts in the planning phases have led to adverse and costly consequences.

As a result, a lot of scientific research has been conducted on bimrocks and bimsoils in the last few decades. Private and public institutions have also funded several research programs all over the world. The common aim was to investigate the many factors affecting the mechanical behavior of these geomaterials (i.e. block-size distributions, block contents, shape and orientation of rock inclusions, etc.) and to define systematic approaches to properly characterize and model bimrocks and bimsoils, in order to correctly carry out civil engineering works in these complex formations.

The main findings from the literature are presented in this Chapter. Particular reference is made to the very first studies carried out on the Franciscan melange by Medley and Lindquist (Lindquist 1994b, Medley 1994), as already mentioned in Chapter 1. These authors laid the foundations of the current knowledge on these heterogeneous geomaterials. Among the other results, they found that the block-size distribution of the Franciscan melange is scale-independent, or fractal. This was a major scientific discovery, and this is why the literature review of this Ph.D. dissertation presents the characteristics of bimrocks and bimsoils starting from the

definition of fractals and their properties.

# 2.1 Characteristics of bimrocks

## 2.1.1 Scale invariance

*Fractals*, whose name comes from the latin verb *frangere* (i.e. to break), are objects that, although not exactly identical at different scales, preserve their statistical attributes (Mandelbrot 1983, Pilgerstorfer and Schubert 2014). *Self-similarity* and *scale-invariance* are typical properties of fractals.

If an object shows the same geometrical properties at many scales it can be defined scale-invariant. Scale invariance is a form of self-similarity. A self-similar system is one composed of elements that looks exactly the same as a parent whole.

An example of fractal is reported in Figure 2.1, where the self-similarity notion is also presented.

Figure 2.1: The Sierpiński fractal triangle, subdivided into smaller equilateral triangles (Mandelbrot 1983).

Specifically, the midpoints of each side of any triangle can be considered as the vertices of a new triangle to be removed from the original: for instance, if we consider the black triangle on the left in Figure 2.1, then the white triangle in the second figure from the left represents the removed triangle. This removal operation creates three triangles (i.e. the black triangles in the second figure from the left), each of which is exactly 1/2 the size of the parent triangle and has an area exactly 1/4 of the original area. Moreover, each remaining triangle is similar to the original. Turcotte (1986) defined "fractals" all the scale-invariant processes characterized by a mathematical relationship of the form:

$$N(r) \sim r^{-D} \tag{2.1}$$

between the number, N(r), and size, r, of their elements (Turcotte 1986).

A fractal can be defined with its fractal dimension, D. This parameter indicates the complexity of an object with nonuniform density. The formal definition of D is:

$$D = \frac{Log N(r)}{Log(r)} \tag{2.2}$$

Considering the Sierpiński triangle of Figure 2.1, the second triangle from the left consists of 3 small (black) triangles exactly like the original. Each of these triangles is characterized by a magnification factor, r, equal to 2 (i.e. the smaller triangles could be scaled by 2 to obtain the original triangle). The resulting figure consists of 3 separate identical miniature pieces, N(r) = 3. Hence, the fractal dimension of the Sierpiński triangle, D, is equal to logN(r)/log(r) = 1.585.

A wide range of natural phenomena related to different fields (rock engineering, geology, botanic, astronomy, etc.) have been found and demonstrated to be self-similar or fractal. Fragmentation of rocks, granulometric distributions in rock falls, snow avalanches and rock avalanches, plant root systems, size-frequency relations for asteroids and meteorites, etc. (Mandelbrot 1983, Turcotte 1986, Perfect 1997, Crosta et al. 2007, De Biagi et al. 2017) represent some notable examples.

Many studies on bimrocks, and especially on the Franciscan melanges, have recently demonstrated that the distribution of the maximum size of rock inclusions is self-similar or fractal, too (Medley 1994, Medley and Lindquist 1995). This implies that macro and micro views of two sub-areas of the same outcrop are similar with respect to arrangements and proportions of rock blocks (e.g. two photographs of the same bimrock outcrop will show similar proportions and arrangements of the rock inclusions at different scales) (Goodman and Ahlgren 2000).

## 2.1.2   Self-similarity of Franciscan melanges

Starting from the very first studies in this field, the self-similarity of melanges was apparent in outcrops and geologic maps. However, no quantitative measurements were undertaken until the 90's. It was Lindquist in 1991 who first measured block dimensions of a 6 m$^2$ Franciscan melange outcrop, determining its fractal dimension, D (Lindquist 1991).
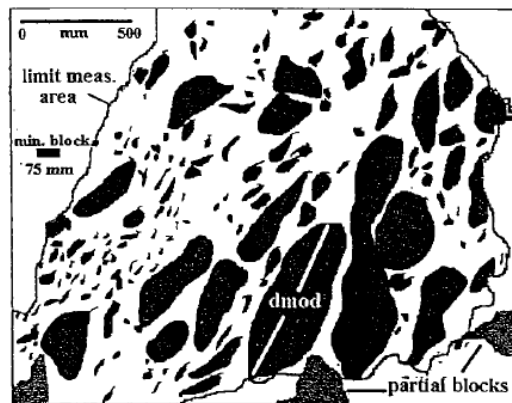


Figure 2.2: Maximum visible dimension of blocks in the melange at Mendocino (California) (Medley and Lindquist 1995).

Three years later, Medley (Medley 1994) extended Lindquist's work, performing a detailed study on several measurement areas, in order to confirm the scale-independence of block size distributions of some Franciscan melanges. His work consisted in the construction of log-histograms (i.e. histograms plotted on logarithmic axes) of block sizes and relative frequencies measured at different outcrop scales. At first, the author investigated 6 areas ranging from 0.04 m$^2$ to 18.91 m$^2$. Computer image analysis was used for analysing the set of photographs taken at the different scales, in order to automatically measure the maximum visible dimension ($d_{mod}$) of all the blocks found within each area (Figure 2.2).

In order to plot the frequency histograms, several block size classes had to be defined. The central endclass (i.e. the "node") was determined by calculating 5% of the square root of the relative analyzed area ($0.05\sqrt{(A)}$). Endclasses smaller than the node diminished by incremental halves, while endclasses larger than the node incrementally doubled (Medley and Lindquist 1995).

Log-histograms were then constructed, counting the number of rock blocks belonging to each endclass. As shown in Figure 2.3a, all the plots presented an evident similarity. Block sizes were then normalized by the square root of each sampling area, in order to compare the results (Figure 2.3b). The normalized histograms presented parabolic shapes. However, they all showed a linear arrangement of data points located to the right of the peak. This linear arrangement implied fractal block size distributions. This finding was encouraging, although not sufficient to assess the scale-independence of Franciscan melanges. Hence, additional analyses were carried out. Further field measurements and several geologic maps were used in order to include larger measurement areas, ranging from a few square centimeters to around 1000 km$^2$ (Figure 2.4).

The results of Medley's work are illustrated in Figure 2.5, where:

- the x-axis is the log of the maximum observable dimension, d, of any rock block in each observation area, A, normalized by $\sqrt{(A)}$;

- the y-axis is the log of frequency.
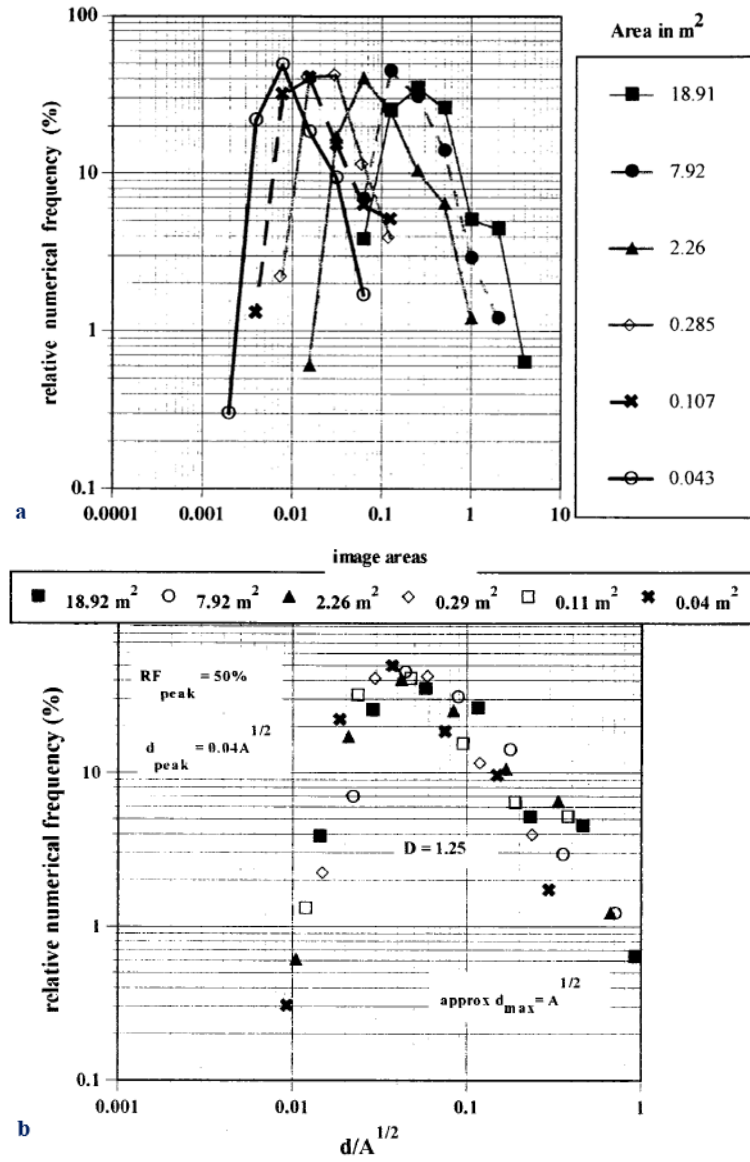
Figure 2.3: a) Log-histograms of block sizes at a melange outcrop in California; b) normalized log histograms showing parabolic shapes (Medley 1994).

| Location | Source | Area (A) | $\sqrt{A}$ | $0.05\sqrt{A}$ | No. blocks | shortest $d_{mod}$ | longest $d_{mod}$ | D Fract. Dim |
|---|---|---|---|---|---|---|---|---|
| Caspar Beach | photo | 454 cm$^2$ | 21.3 cm | 1.07 cm | 286 | 0.19 cm | 5.6 cm | 1.44 |
| Caspar Beach | photo | 0.11 m$^2$ | 0.33 m | 1.65 cm | 79 | 0.36 cm | 9.8 cm | 1.1 |
| Caspar Beach | photo | 0.29 m$^2$ | 0.53 m | 0.027 m | 229 | 0.006 m | 0.12 m | 1.67 |
| Caspar Beach | photo | 2.26 m$^2$ | 1.5 m | 0.075 m | 173 | 0.019 m | 0.95 m | 1.3 |
| Caspar B each | photo | 7.92 m$^2$ | 2.81 m | 0.14 m | 173 | 0.04 m | 1.98 m | 1.65 |
| Caspar Beach | photo | 18.92 m$^2$ | 4.35 m | 0.22 m | 158 | 0.04 m | 2.49 m | 1.46 |
| Lone Tree Slide Marin Co., CA | field meas. (Medley, 1994a) | 32 892 m$^2$ | 181 m | 9.05 m | 117 | 0.3 m | 15.2 m | 1.2 |
| Walker Ck, Marin Co., CA | Reid (1978) | 1.17 km$^2$ | 1.08 km | 54 m | 94 | 4.8 m | 222 m | 1.58 |
| Three Peaks, Marin Co., CA | Peterson (1979) | 1.26 km$^2$ | 1.12 km | 56 m | 124 | 2.4 m | 65.3 m | 1.32 |
| York Mtn, San Luis Obispo Co., CA | Seiders (1982) | 3.43 km$^2$ | 1.85 km | 93 m | 181 | 12 m | 2.04 km (but 1.44 km used) | 1.06 |
| Marin Co., CA | Ellen & Wentworth (in press) | 916 km$^2$ | 30.3 km | 1.52 km | 314 | 125 m | 17.1 km | 1.56 |

Figure 2.4: Summary of data used by Medley for his study (Medley and Lindquist 1995).
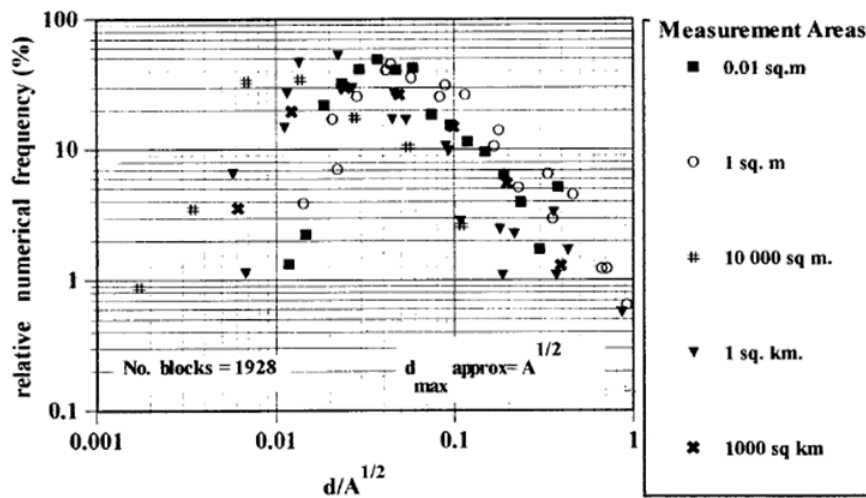


Figure 2.5: Normalized log histograms including data from measurement areas ranging over 7 orders of magnitude (Medley 1994).

From Figure 2.3 and Figure 2.5 it was observed that (Medley 1994, Medley 2001):

- all block size distributions, regardless of the measurement area, had similar parabolic shapes. This feature demonstrated the fractality of the Franciscan

54

melanges analyzed. This means that block size distributions follow a power law relationship with a negative exponent. The absolute value of such an exponent is the fractal dimension, D;

- a fractal dimension, D, of approximately $1.1 \div 1.7$ was found for Franciscan melanges;

- the largest block sizes were approximatively equal to $\sqrt{(A)}$, where $\sqrt{(A)}$ corresponds to the characteristic engineering dimension, $L_c$ (see Section 2.1.3), which represents the dimension of the problem at hand;

- 99% of blocks were smaller than $75\%\sqrt{(A)}$;

- regardless of the size of the measured area, block sizes had peak relative frequencies at about $5\%\sqrt{(A)}$ or, equivalently, $5\%L_c$;

- blocks smaller than $5\%\sqrt{(A)}$ were often undercounted, due to the difficulty of precisely counting them, and constituted more than 95% of the total number of the measured rock blocks. However, since their total volume was less than 1% of the total melange volume, their contribution to the global mechanical behavior of the rock formation was considered negligible.

In light of the above, blocks smaller than $5\%\sqrt{(A)}$ were assumed to have a negligible effect on the overall mechanical behavior of a heterogeneous rock mass. On the other hand, the maximum block size was considered equal to $75\%\sqrt{(A)}$. In fact, a melange with blocks greater than this dimension could be considered as a blocky (fractured) rock mass (Medley 2001, Riedmüller et al. 2001, Kahraman and Alber 2006).

### 2.1.3 Characteristic engineering dimension

As discussed in the previous section, block sizes in melanges can exceed more than 7 orders of magnitude, from millimeters to tens of kilometres (Medley 1994, Medley 2007a, Wakabayashi et al. 2002, Medley and Sanz Rehermann 2004, Tsiambaos 2010).
Since block size distribution of melanges has been found to be scale independent, blocks can be found at all scales of observation (Medley and Lindquist 1995, Medley 2001, Medley and Sanz Rehermann 2004, Kim et al. 2004, Medley 2004). As a consequence, a specific rock inclusion can be identified as "block" at one scale (e.g., laboratory specimen) but could be part of the "matrix" if a different scale is considered (e.g., bimrock slope). Hence, in order to distinguish what "matrix" is from what "block" is, a block-matrix threshold must be identified on the basis of the specific scale of engineering interest.

In this regard, Medley (Medley 1994) introduced the "*characteristic engineering dimension*", $L_c$, indicating the scale of the problem at hand.

As reported in Figure 2.6, $L_c$ may variously indicate the diameter of a specimen or that of a tunnel, the depth of the failure surface in a landslide or can be an indicator of an outcrop size, such as $\sqrt{(A)}$ (where A is the total site area), etc..

As shown in Section 2.1.2, Medley assessed that all rock inclusions below $5\%L_c$ (or $0.05\sqrt{(A)}$) cannot be considered geotechnically significant (i.e. they do not influence the strength of melanges) and can be demoted to the matrix. On the other hand, beyond about 70% VBP, blocks start to touch and the rock mass can be analyzed as a "blocky rock mass with infilled joints" using conventional rock-engineering approaches.

In light of the above, since Medley's work, the block-matrix threshold has been assumed equal to $5\%L_c$ while the maximum block size was assumed equal to 75% $L_c$ (or $0.75\sqrt{(A)}$).
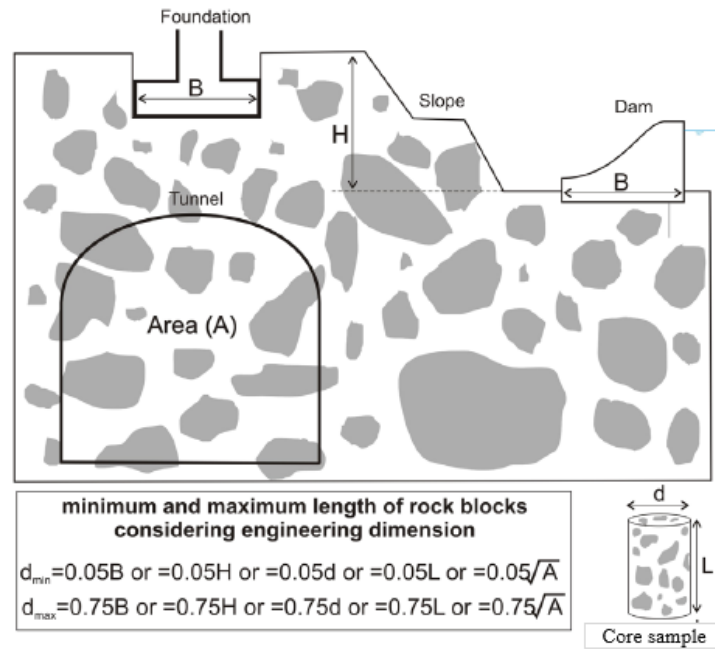


Figure 2.6: Different characteristic engineering dimensions, $L_c$, for several engineering works (Sonmez et al. 2016).

The importance and the effect of taking into account the scale of the problem on the block/matrix threshold is clearly illustrated in Figure 2.7, where a sketch of a Franciscan melange map of 50 m by 50 m is represented. The characteristic dimension of the entire site is represented by the square root of its area (i.e. $L_c = \sqrt{(A)}$),

corresponding to 50 m.
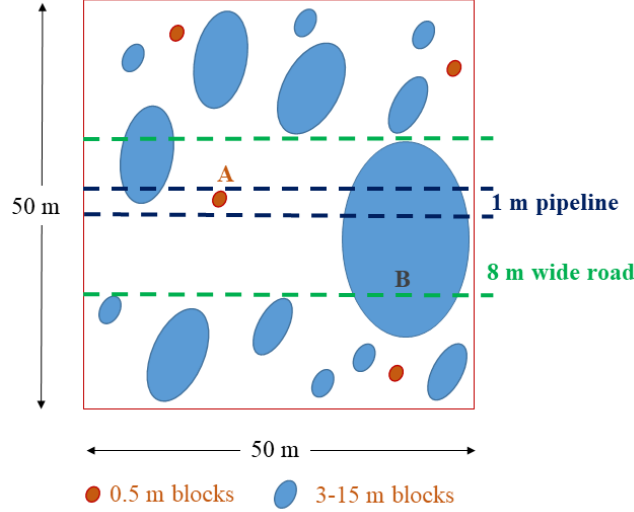


Figure 2.7: Sketch of a melange bimrock map showing different engineering works to be constructed: a 8 m wide road and 1 m wide, 1 m deep pipeline trench (modified from Medley 2001).

Hence, at the scale of interest of the overall site, the block/matrix threshold is $0.05L_c = 0.05\sqrt{(A)} = 2.5$ m and the reasonably largest block is equal to $0.75L_c = 0.75\sqrt{(A)} = 37.5$ m. As a consequence, the brown blocks of Figure 2.7, smaller than 2.5 m, should be considered to be part of the matrix. All the other rock inclusions, on the contrary, can be assumed to be "blocks".

In the case of a 8 m wide road project crossing the same site, the width of the road is assumed as the $L_c$. At this scale of interest the block/matrix threshold is $0.05L_c = 0.4$ m and the maximum block size is equal to $0.75L_c = 6$ m. This implies that the smallest brown block (i.e. the block A in Figure 2.7), which was assigned to the matrix at the site scale, can in this case be considered "block". On the contrary, the large rock inclusion on the right (i.e. the block B in Figure 2.7), which was considered to be a "block" at the site scale, can be treated as a massive and unmixed rock mass. In fact, it is too large to be considered as an individual block within the melange (Medley 2001).

Finally, if a smaller engineering work is analyzed, for example a 1 m deep pipeline trench, $L_c$ can be taken as the depth of the trench. In this case, the block/matrix threshold is $0.05L_c = 0.05$ m. The block A of Figure 2.7 may now cause problems for the trenching contractor during the excavation works, as its dimension is close to $0.75L_c = 0.75$ m.

### 2.1.4 VBP estimation

Several authors have shown that the presence of blocks, with their sizes, volumetric proportions and spatial distributions, strongly influences the mechanical behavior of block-in-matrix formations (Medley 1994, Lindquist 1994a, Medley 1997, Kahraman and Alber 2006, Barbero et al. 2007, Barbero et al. 2012, Coli et al. 2012, Sonmez et al. 2016).

Laboratory and in situ tests, as well as numerical studies, have indeed demonstrated that the strength and failure mode of bimrocks and bimsoils are strongly affected by the quantity, position, shape, orientation and dimension of the blocks (Irfan and Tang 1993, Lindquist 1994b, Li et al. 2004,Medley and Sanz Rehermann 2004, Barbero et al. 2006, Xu et al. 2008, Coli 2010, Minuto and Morandi 2015, Khorasani et al. 2019). In particular, higher VBPs lead to strength increases, lower deformability and more tortuous failure surfaces. Moreover, when tunnelling in these complex geomaterials, the presence of rock blocks can induce, among other problems, damage to cutters, face instabilities, sinkholes, unexpected high stresses on tunnel linings, obstructions and, as a consequence, schedule delays and extra costs (DiPonio et al. 2007, Gwildis et al. 2018, Hunt and Del Nero 2010, Hunt 2014).

Hence, when dealing with a bimrock or bimsoil, it is essential to take the presence of the blocks into account.

Empirical approaches have been proposed to estimate the strength and deformability of bimrocks and bimsoils on the basis of their VBP (Kalender et al. 2014, Lindquist 1994b, Sonmez et al. 2004a,Sonmez et al. 2014). Some details on these methods are given in the following Section 2.2. However, reliable estimations of the 3D block contents still remain a critical issue. In fact, the measure of the VBP can accurately be made by disintegrating bimrock specimens in the laboratory (by means of 3D sieve analyses), provided that the blocks can be easily separated from the matrix (Sonmez et al. 2004a, Tien et al. 2010, Tsiambaos 2010, Mahdevari and Maarefvand 2017). If the density of both matrix and blocks are known and a significant contrast exists, it is also possible to evaluate the VBP from the density of the specimens (Tsiambaos 2010, Sonmez et al. 2016). However, at site scales, these methodologies cannot be used. Hence, it is necessary to resort to approximated approaches that assume 1D or 2D bimrock or bimsoils properties to be stereologically equivalent to 3D properties. These techniques include linear/areal observations and interpretations of boreholes, scanlines (1D model borings), photographs or geologic maps, as well as 2D digital image analyses (Medley 2001, Medley 2007a, Sonmez et al. 2004a, Pan et al. 2008, Coli et al. 2012, Zhang et al. 2015, Cen et al. 2017). These techniques are described in detail in the following Sections 2.1.4.1, 2.1.4.2. However, since rock inclusions in bimrocks and bimsoils have no uniform spatial distributions, shapes and sizes, these methods may lead to serious errors in the estimations of inclusion sizes and proportions. Furthermore, the accuracy of the

estimates strongly depends on the sampling length (Medley and Goodman 1994, Medley and Lindquist 1995, Medley 2001, Haneberg 2004, Tien et al. 2010, Xu et al. 2011). Hence, the introduction of an uncertainty factor is required in order to take potential measurement errors into account. This factor should reduce the calculated VBP when evaluating strength parameters (to err on the side of safety) and should increase the calculated VBP when planning engineering works in bimrocks (to avoid economic repercussions) (Medley 1997,Medley 2001, Medley and Zekkos 2011, Kalender et al. 2014).

As described in the following Section 2.1.4.1, Medley (1997) worked on the estimation of potential errors in the VBP evaluation based on the assumption of equivalence with 1D measurements. The author provided a chart to adjust the estimated VBP by means of an uncertainty factor in relation to the measured block proportion and total length of drilling.

In this Ph.D. research, two statistical approaches to (i) estimate the uncertainty in inferring the VBP from 2D measurements and (ii) predict the probability of encountering blocks in underground excavations have been developed and are illustrated in Chapter 4.

### 2.1.4.1  Linear block proportion (LBP)

The linear block proportion (LBP) is the ratio of the total length of all blocks intersected by drill cores (or scanlines) to the total length of drilling.

Previous findings from the literature seem to indicate that this parameter could be considered equivalent to the real tridimensional block proportion (i.e. VBP) if the length of the exploration core is at least 10 times the expected maximum dimension of blocks ($10d_{max}$) (Medley 1997, Medley 2007b, Tsiambaos 2010, Medley and Zekkos 2011). This requirement is due to the extremely variable positions and dimensions of rock inclusions within heterogeneous rock bodies.

However, since drillings are expensive, time consuming and often troublesome, it is often not feasible or even impossible to perform explorations of such a length. If the abovementioned requirement on the minimum length of drilling cannot be respected, an uncertainty factor should be introduced (Medley 2001).
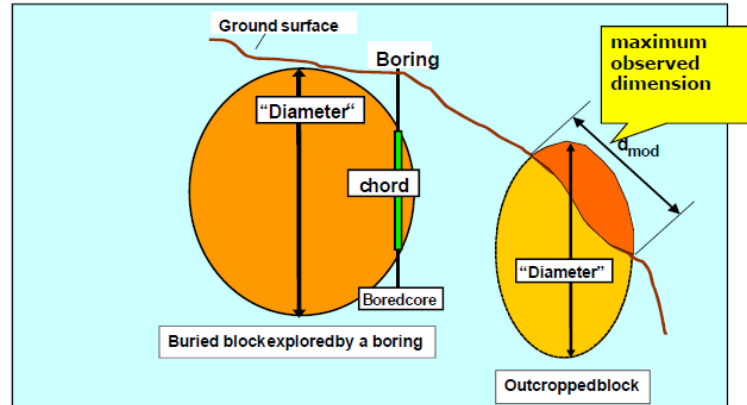
Figure 2.8: Differences between the maximum observed block dimension (dmod), the block-core intersection length and the actual equivalent diameter of the rock block (Medley 2012).

Furthermore, since rock inclusions very rarely have circular (spherical) shapes, block-core intersections (i.e. the lengths of the chord intercepts along the drilling cores) are generally different from the characteristic block dimensions (i.e. the equivalent diameters of the blocks). Specifically, since drilling cores have a higher probability to be close to the edges of the blocks, chord lengths tend to underestimate their actual dimensions (Figure 2.8). Consequently, assuming 1D measurements to be stereologically equivalent to 2D (or 3D) values could lead to severe underestimations of both the predicted dimensions of rock inclusions and VBPs (Medley 1994, Medley 2001, Medley and Goodman 1994, Wakabayashi et al. 2002). A few authors have investigated the potential errors that could be made assuming VBP to be equivalent to LBP as well as 1D block size distributions to match 3D block size distributions (Medley 1997, Medley 2002, Haneberg 2004).

Medley (1997) evaluated the uncertainty associated with the estimation of VBP from cumulative LBP. He fabricated four artificial bimrock models with known block-size distributions and known, but different, VBPs. Each model was sawn in ten slices. Ten scanlines were then drawn on each slice, representing model boreholes, as shown in Figure 2.9.
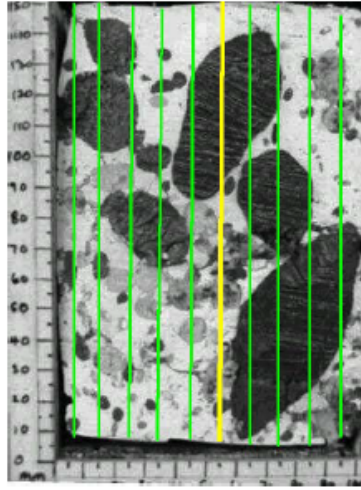
Figure 2.9: 10 model borings (scanlines) created on a typical bimrock sample (Medley 2002).



| 34.7 | 25.9 | 6.3 | 0.0 | 27.0 | 13.3 | 22.5 | 26.8 | 31.1 | 41.7 |
| 40.0 | 33.3 | 44.0 | 29.6 | 18.5 | 39.7 | 42.5 | 25.3 | 19.1 | 40.3 |
| 31.3 | 24.5 | 25.3 | 21.1 | 27.8 | 41.3 | 53.6 | 23.4 | 41.4 | 23.4 |
| 34.0 | 33.8 | 10.1 | 22.9 | 56.6 | 39.0 | 34.0 | 23.2 | 52.6 | 27.0 |
| 27.2 | 34.2 | 21.9 | 17.0 | 57.0 | 51.3 | 42.4 | 54.8 | 51.3 | 42.0 |
| 26.3 | 28.1 | 16.3 | 26.0 | 46.7 | 54.3 | 45.1 | 46.1 | 60.9 | 48.3 |
| 44.2 | 28.0 | 29.9 | 34.2 | 57.0 | 58.8 | 37.5 | 41.2 | 46.9 | 29.6 |
| 31.3 | 36.7 | 41.3 | 39.5 | 32.6 | 30.3 | 21.9 | 30.7 | 33.5 | 32.7 |
| 50.0 | 41.5 | 40.7 | 26.5 | 28.0 | 23.8 | 27.6 | 13.0 | 35.9 | 36.4 |
| 58.9 | 45.5 | 30.5 | 11.1 | 28.1 | 23.3 | 17.6 | 30.3 | 32.4 | 47.6 |

Figure 2.10: Plan view of the 32%VBP model indicating the array of 100 LBP (Medley 1997).

The LBP of each scanline was calculated considering all the intercepts (between scanlines and blocks) greater than the matrix-block threshold.
As shown in the plan view of Figure 2.10, 100 LBP were obtained for each bimrock model and a significant variability in the results was found (i.e. LBP from 0% up to 60.9%). The author randomly combined the data in order to investigate if a good estimation of the VBP could be obtained from the LBP values and if this

corresponded to a minimum sampling length. Specifically, sub-sets of 2, 4, 6, 8, 10, 15 and 20 scanlines were used combining each randomization 40 times.

From the analyses, it was found that as the sampling length increased, data scattering reduced. Furthermore, as the VBP of bimrock models increased, the variability (i.e. standard deviation) of the estimated VBP decreased (Figure 2.11).
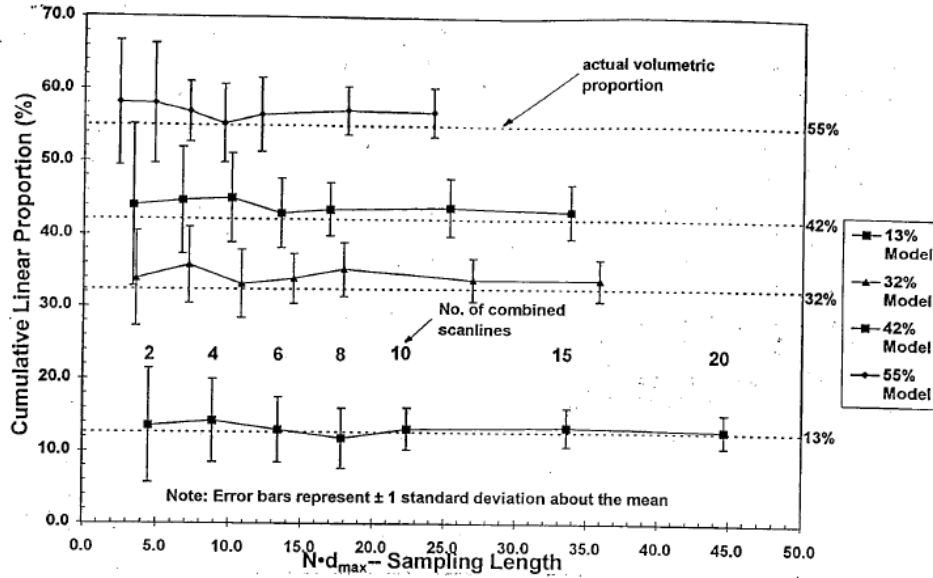


Figure 2.11: Reduction of standard deviations with increasing sampling length and VBP (Medley 1997). The sampling length, $N_{dmax}$, is expressed as a multiple of the length of the largest block, $d_{max}$).

In his work, the author also proposed an uncertainty factor for the determination of a range of VBPs which should contain the real 3D block quantity. This factor can be obtained from Figure 2.12 on the basis of the LBP value measured and the sampling length, expressed as a multiple (N) of the length of the largest block ($d_{max}$). The example illustrated in this Figure with the dotted line indicates that if the total length of drilling performed is about 4 times $d_{max}$ and the LBP measured is about 40%, by interpolating between 42 and 32 diagonal lines, an uncertainty factor equal to 0.23 is found. This means that a VBP range of 31%-49% should be considered.

Using the same dataset, Medley also statistically analyzed the variability in the estimates of block size distributions, finding slight equivalence between 1D and 3D size distributions, regardless of the number of vertical boreholes (Figure 2.13). Block shapes and orientations, boring directions, total length of drilling and VBPs were found to influence the estimates of both LBP and 1D block size distribution.
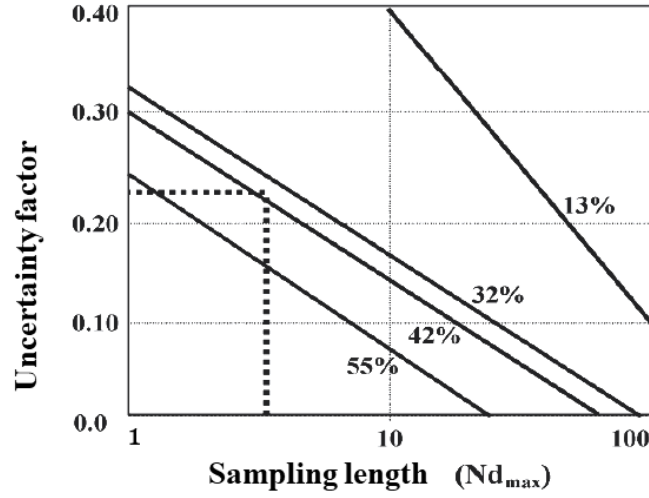
Figure 2.12: Uncertainty in estimates of volumetric block proportion as a function of the length of linear measurement, expressed as a multiple (N) of the length of the largest block ($d_{max}$), and the measured linear block proportion (Medley 2001).
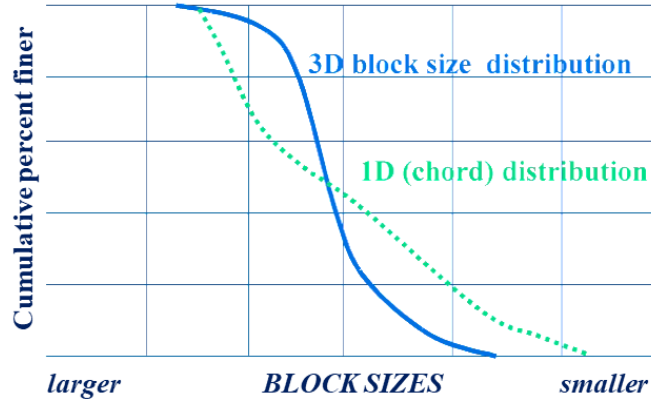


Figure 2.13: Schematic 3D block size distribution and 1D chord length distributions for the 4 physical melange models. A slight match between the original block size distribution and the 1D chord length distributions is shown. (Medley 2001).

Moreover, since scanlines intersected more often larger than smaller blocks, the frequency of smaller rock inclusions was underestimated while that of larger blocks was overestimated. Furthermore, as already highlighted for the exploration core drillings, the scanline lengths were generally smaller than block equivalent diameters. As a consequence, the real block dimensions were underestimated (Medley and Lindquist 1995, Medley 2001, Medley 2002, Medley and Zekkos 2011).

### 2.1.4.2 Areal block proportion (ABP) and 2D image analysis

Digital image analysis is a widely used technique in different scientific frames (medical sciences, civil engineering, etc.) allowing quantitative measures and statistical analyses to be carried out on heterogeneous materials, such as asphalt concrete (Wu et al. 2018), heterogeneous geologic formations (Lebourg et al. 2004, Xu et al. 2008), etc..

2D image analysis has been used as an effective methodology to estimate the areal block proportion (ABP) of a bimrock or bimsoil, which is the ratio between the total area of all blocks measured on an outcrop, specimen or geologic map and the total area of the surface analyzed. In fact, it allows for the evaluation of the size distribution of the maximum observable block dimension ($d_{mod}$), statistical block shape distribution and spatial variability of rock inclusions (Coli et al. 2012, Zhang et al. 2015).

Many authors have performed manual or digital image processing (DIP) in order to investigate specific characteristics of different rock-soil mixtures (Medley and Goodman 1994, Medley 1994, Sonmez et al. 2004a, Fagereng 2011, Xu et al. 2011, Coli et al. 2012, Kahraman et al. 2015, Zhang et al. 2015, Jiméneze Ugalde and Fontoura 2016). Sonmez et al. (Sonmez et al. 2004b, Sonmez et al. 2004a) analyzed several outcrop images of the Ankara agglomerate in order to estimate the 2D BP and evaluate possible deviations from the real VBP. To this aim, the authors calculated the ratio of the longest to the shortest axes of blocks considering different sampling directions. They found that only 25% of blocks had axial ratios greater than 1.2, which indicated that the block shapes were approximately equi-dimensional in 3D. Therefore, the 2D block proportions where considered to be equivalent to 3D values. Xu and coworkers (Xu et al. 2011) used the digital image processing (DIP) to study the granulometric characteristics of the Xiazanri Rock-Soil (RS) mixture slope (China). Several pictures were taken in situ and then analyzed using the DIP code. Among these, seven pictures were selected in order to evaluate rock block contents and block size distributions. The area covered by the seven processed images was about 26 $m^2$. The authors found an extremely high heterogeneity in the measured block proportions (variable from 33% to 75%) and decided to average these results for the preparation of a sample of the R-S mixture to be tested with a large scale direct shear apparatus. Coli and coworkers (Coli et al. 2012) performed a digital image processing (DIP) of photographs taken in the shale-limestone chaotic complex of the Santa Barbara open pit mine (Italy). Binary images were obtained from the original photographs by means of appropriate image segmentation processes. The authors introduced a geostatistical analysis of binary bimrock outcrop pictures through variogram analyses of the rock block indicator variable IB(x,y), denoting the presence (or absence) of blocks in the investigated domain. The aim of the work was to study the morphological and spatial variability of the calcareous fragments (information about average inclusion sizes,

VBP, geometric anisotropy and average distance between the blocks). Kahraman et al. (Kahraman et al. 2015) determined the areal BP (assumed to be equal to the VBP) of 132 specimens of Misis fault breccia (Turkey) using image analyses, in order to investigate possible correlations between VBP and both S-wave and P-wave velocity.

Many authors also resorted to the DIP technique in order to perform numerical simulations on heterogeneous samples using real 2D block positions and shapes, from DIC analyses (Xu et al. 2008, Li et al. 2016, Jiméneze Ugalde and Fontoura 2016). Xu et al. (2008) simulated a large-scale direct shear test on a RS mixture using the Finite Element Method (FEM). Li et al. 2016 used both Computed Tomography (CT) and DIP to reconstruct a typical section of a RS mixture specimen and reproduce its behavior under triaxial test by means of FLAC3D code, using 2D plane strain conditions. Jiméneze Ugalde and Fontoura 2016 carried out direct shear and biaxial compression tests on virtual samples of a conglomeratic rock of Costa Rica using the PLAXIS code in order to study its mechanical behavior.

Some authors have also highlighted that some problems can arise when estimating VBPs with this technique. In fact, roughness of outcrops (causing light reflection differences), similar colours of matrix and blocks (making extremely difficult to distinguish the two components) and often too small geologic outcrops may produce low quality photographs (Zhang et al. 2015, Jiang et al. 2016).

Nevertheless, in-situ 2D measurements and digital image analysis techniques are extremely useful to predict the block content of heterogeneous geologic bodies. In fact, they are easier and less expensive than 1D measurements from drilling explorations to perform. However, data obtained from these analyses should not be used without accounting for the uncertainty. In this regard, as mentioned above, a statistical approach is presented in Chapter 4.1, which was developed to quantitatively estimate the uncertainty that can be introduced by inferring the VBP of a bimrock or bimsoil from 2D outcrop measurements.

## 2.2   Empirical approaches

Much research has been carried out in the last few decades to develop systematic approaches to properly determine the strength and deformation parameters of bimrocks and bimsoils in order to perform reliable numerical simulations and correctly carry out civil engineering works in these complex formations. On the basis of laboratory and in-situ test results, some authors proposed preliminary strength criteria which assume bimrocks to be homogeneous and isotropic geomaterials with equivalent mechanical properties that can be determined according to the matrix strength parameters and VBP (Lindquist 1994b, Sonmez et al. 2009, Kalender et al. 2014). These simple and convenient methods were used by several geopractitioners to predict the mechanical behavior of bimrocks and bimsoils (Kim et al. 2004, Adam et al. 2014, Minuto and Morandi 2015). From these studies the validity of

the empirical approaches was confirmed. In fact, they allow for the contribution of the blocks to the overall strength of the geomaterial avoiding too conservative results that could be obtained if the strength and deformation properties of the weaker matrix only are considered. However, as discussed in the next Chapter 3, a source of weakness of these approaches is that tortuosity cannot be taken into account, since they allow a homogeneous equivalent material to be analyzed.

### 2.2.1 The Lindquist (1994) approach

In his Ph.D. research, Lindquist (1994b) studied how the presence of the blocks and their characteristics (i.e. VBP and orientation) influence the strength and deformability of melanges. To this end, Lindquist analyzed in detail the results of triaxial tests carried out in the '80s on Franciscan melange specimens collected from beneath Scott Dam, California (see Section 2.3.3). Furthermore, 60 artificial melange specimens were fabricated with four different VBPs and orientations of the blocks. Moreover, 7 pure matrix and 10 pure blocks specimens were also created. A schematic drawing of the model specimens tested is given in Figure 2.14.
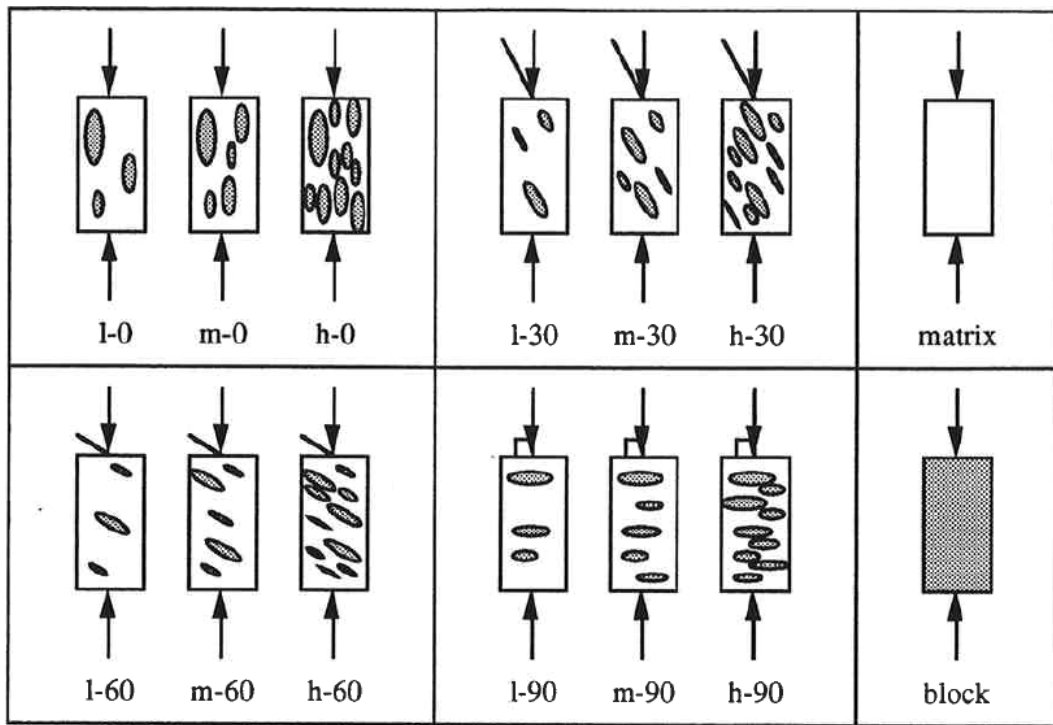


Figure 2.14: Lindquist's artificial specimen types (Lindquist 1994b).

The dimension, shape and block size distribution of the particles incorporated in the models were chosen on the basis of measurements at a number of melange outcrops

66

along the California coast. A sand-cement mixture was used to simulate the blocks, while a bentonite-cement mixture was used for the matrix. Thin layers of wax coated with talcum powder (to reduce the friction between the matrix and wax) were used to simulate planes of weakness within the matrix. Triaxial compression tests were then carried out on these artificial specimens. Lindquist's work showed that higher VBPs generally led to a lower deformability, no change in strain at failure, decrease in the cohesion, increase in the friction angle and more tortuous failure surfaces. More in detail, (i) the lowest and greatest deformability moduli were provided by the specimens with vertically (0°) and horizontally (90°) aligned blocks, respectively; (ii) the lowest cohesion was registerd in the specimens with blocks oriented at 30° to the axial loading direction, whatever the VBP; and (iii) the increase of the internal friction angle depended on the VBP rather than on the block orientation.

From the findings of this research, the author proposed the shear strength model of Eq. 2.3:

$$\tau_p = c_{matrix} \cdot (1 - VBP) + \sigma \cdot tan(\varphi_{matrix} + \Delta\varphi_{matrix}(VBP)) \qquad (2.3)$$

where:

$\tau_p$ is the equivalent mass shear strength;

$c_{matrix}$ is the cohesion of the matrix, which is assumed to decrease with increasing VBP;

$\varphi_{matrix}$ is the internal friction angle of the matrix;

$\Delta\varphi_{matrix}(VBP)$ is the increase of the internal friction angle, assumed to be, above 25% VBP, equal to 3° for every VBP increase of 10%.

This approach, widely used by geopracticioners all over the world (Kim et al. 2004, Adam et al. 2014, Minuto and Morandi 2015), allows the modelling of heterogeneous formations as they were equivalent homogeneous materials with mechanical properties increased according to their block content.

As shown in Figure 2.15, the empirical strength criterion proposed by Lindquist provides the most conservative angle of internal friction increase as a function of the VBP, with respect to other models proposed in the literature.
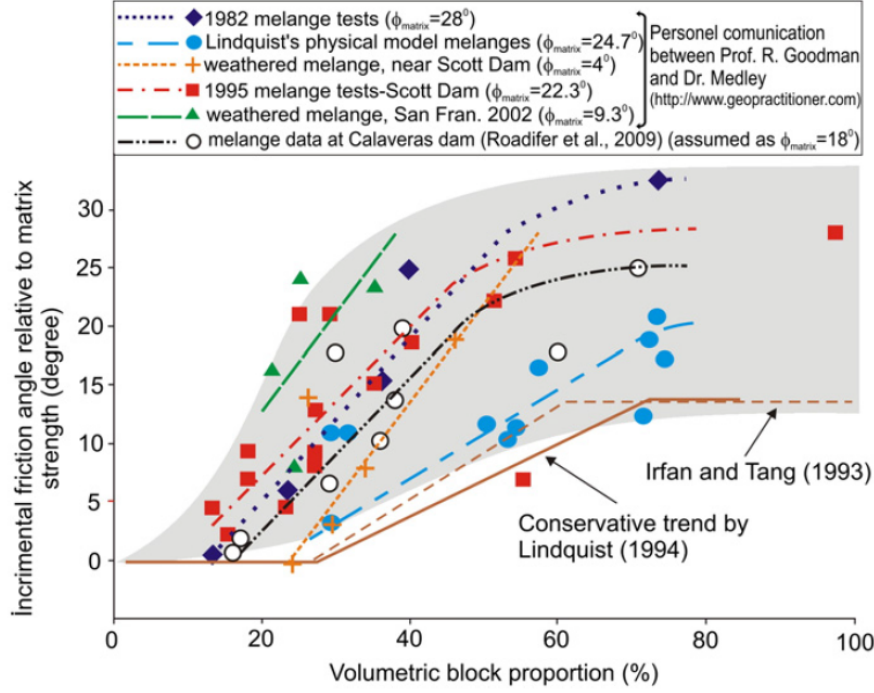
Figure 2.15: Angle of internal friction increase with respect to the matrix strength versus VBP, and possible incremental zone (Kalender et al. 2014).

## 2.2.2 The Kalender et al. (2014) approach

Kalender et al. (2014) developed a preliminary approach to predict the lowest strength parameters of hetrogeneous geomaterials characterized by a strength of block-matrix contacts lower than the matrix one (i.e. unwelded materials). Their approach was developed on the basis of laboratory test results carried out in their research work together with well documented findings from the literature (Lindquist 1994b, Coli et al. 2009, Sonmez et al. 2009).

The application of this criterion requires simple input parameters such as the compressive strength of the matrix (or, equivalently, a qualitative description of the adhesion between the matrix and blocks), the shape and angularity of blocks, the angle of repose of blocks and the VBP. The friction angle, cohesion and uniaxial compressive strength (UCS) of the equivalent homogeneous geomaterial, $\varphi_{bimrock}$, $c_{bimrock}$ and $UCS_{bimrock}$, respectively, can be obtained from Eqs. 2.4, 2.5 and 2.6:

$$\varphi_{bimrock} = \varphi_{matrix} \cdot \left[ 1 + \frac{1000 \cdot \left( \frac{tan(\alpha)}{tan(\phi_{matrix})} - 1 \right)}{1000 + 5 \cdot \left( \frac{100 - VBP}{15} \right)} \cdot \left( \frac{VBP}{VBP + 1} \right) \right] \quad (2.4)$$

$$UCS_{bimrock} = [(A - A^{(VBP/100)})/(A - 1)] \cdot UCS_{matrix} \quad , \quad 0.1 \leq A \leq 500 \quad (2.5)$$

$$c_{bimrock} = UCS_{bimrock} \cdot [1 - sin(\varphi_{bimrock})]/[2 \cdot cos(\varphi_{bimrock})] \quad (2.6)$$

where:

$\alpha$ is the angle of repose of blocks;

UCS is the material uniaxial compressive strength;

A is a parameter that can be defined according to both the compressive strength of the matrix and parameter $\alpha$.

Specifically, the $\alpha$ and A parameters can be selected from the graph of Figure 2.16.
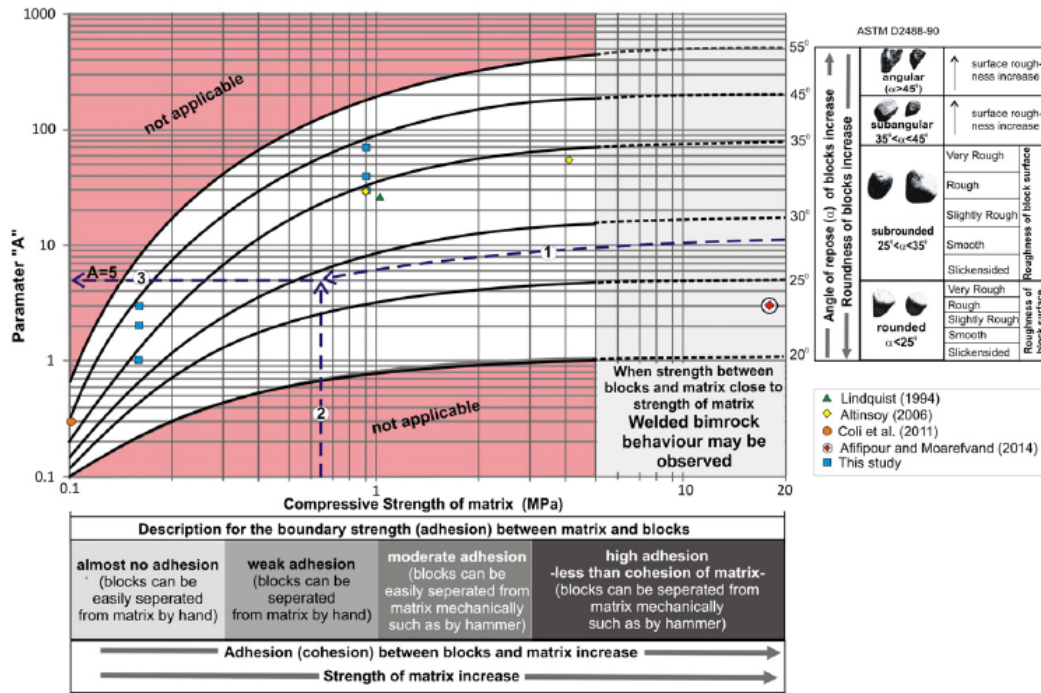


Figure 2.16: Graph developed for the selection of the parameters A and $\alpha$ (Kalender et al. 2014).

The application of this method has provided rather conservative results. Hence, according to Figure 2.17, the authors have suggested to increase the $\alpha$ value for well rounded and rounded blocks, from $\alpha < 25°$ to $\alpha$ equal to 25° and 30°, respectively (Sonmez 2020, personal communication).
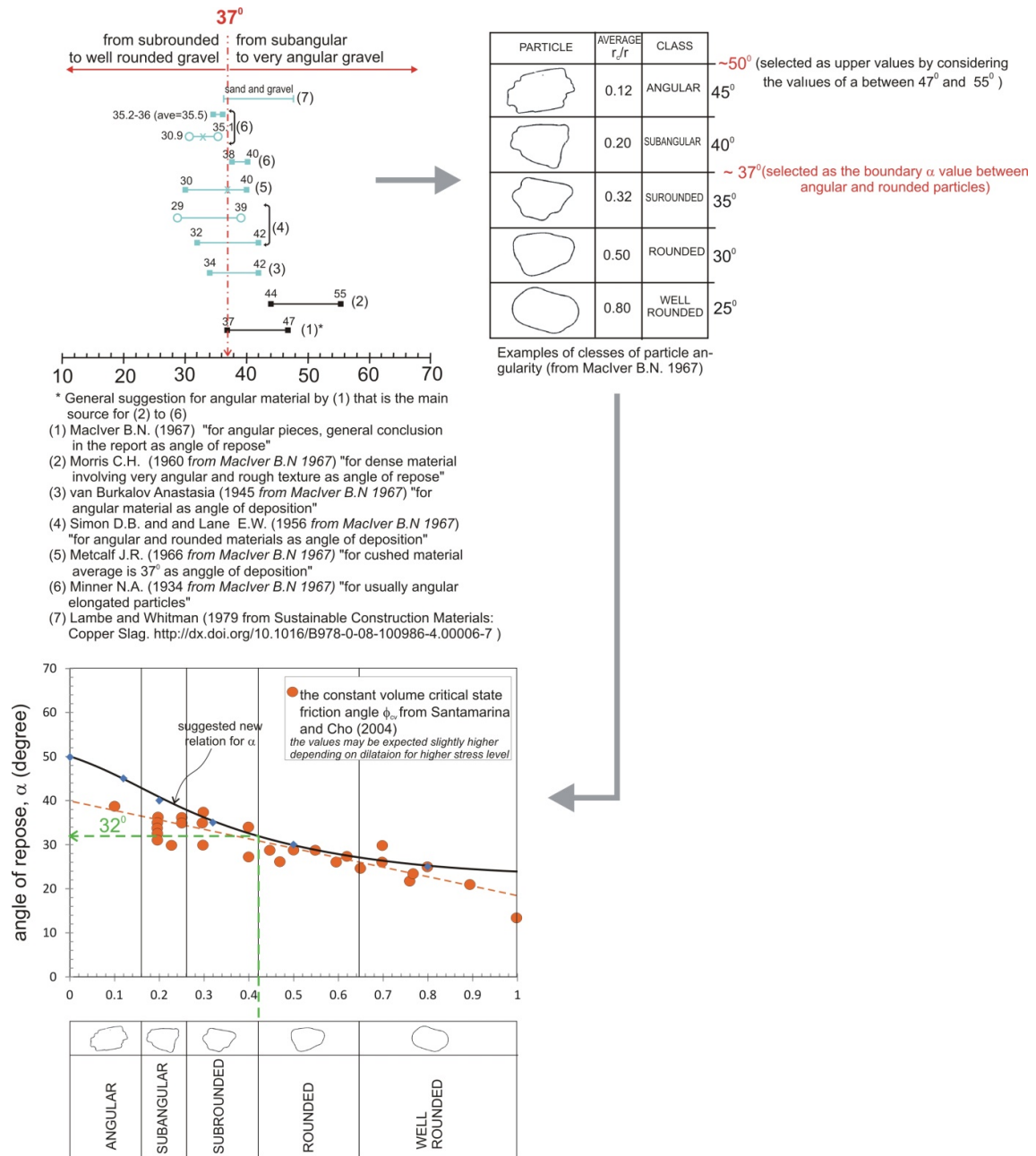
Figure 2.17: Updated guide for the selection of the $\alpha$ parameter.

The novelty of the method proposed by Kalender et al. (2014) is that it takes into account the contact strength between the matrix and blocks and its possible effects on the overall strength of bimrocks.

## 2.3   Technical difficulties encountered in working with bimrocks and bimsoils

Melanges and similar bimrocks are extremely challenging geomaterials to deal with. First, it can be difficult to recognize them from in-situ common investigations (e.g. from borehole data alone), especially if no expert geologists are consulted (Medley 2001, Riedmüller et al. 2001, Button et al. 2004, Wakabayashi and Medley 2004, Medley 2007a). Over the years, geotechnical engineers and engineering geologists have often misinterpreted and mischaracterized bimrocks with costly consequences and technical difficulties during the construction of engineering works (Wakabayashi and Medley 2004, Medley 2008, Pilgerstorfer and Schubert 2014). Furthermore, the designing and constructing activities in these heterogeneous geologic formations are particularly problematic. Many engineering projects have suffered serious problems caused by the extreme difficulties in the characterization and modelling of such geomaterials, even if correctly identified. This is due to their considerable spatial, lithological, dimensional and mechanical variability. As a consequence, simplified approaches, neglecting the presence of the blocks, have been frequently followed by geopractitioners (Medley 2007a, Medley 2008, Coli et al. 2011, Gao et al. 2014).

In order to reduce the technical problems and delays occurring during earthworks, tunnelling excavations and construction of other civil engineering works, an accurate planning activity and a proper modelling is required, as proved by several case histories briefly described in this Section.

The landslide of Coleman Beach in California concerns a misinterpretation of geology made on the basis of a few exploration borings, where blocks were erroneously interpreted as bedrock. This misinterpretation resulted in landslide repair works costing ten times as much as initially predicted (Medley 2001, Medley 2007b, Medley and Zekkos 2011).

The second case history, the Richmond Transport Tunnel excavation, highlights that VBPs are underestimated and block sizes in melanges are very often underestimated if evaluated on the basis of the block intercepts of exploration core drillings only. In fact, since exploration cores hardly intersect blocks at their maximum dimension, chord lengths are rarely equal to the actual block size (Medley 2001, Medley 2007b, Medley 2008, Wakabayashi et al. 2002). Unexpected large blocks filling the face of a tunnel can cause technical problems such as instabilities, obstructions, expensive blasting or jack hammering, etc. (Medley 2001, Wakabayashi et al. 2002, Adam et al. 2014, Gwildis et al. 2018).

Finally, the evaluation of the Scott Dam foundation melange strength, was the first accurate study carried out on melanges. Among other details, it demonstrates how blocks contribute to increase the bimrock strength. This implies that the commonly used simplified approach, which neglects the presence of the blocks assigning the strength and deformability properties of the matrix to the whole system, can be

excessively over conservative and not always representative of the problem at hand (Goodman and Ahlgren 2000, Medley 2007b, Medley and Zekkos 2011).

## 2.3.1 The landslide of Coleman Beach, California

A hillside repair was designed to mitigate the risk for the Coast Highway at Coleman Beach, about 120 km north of San Francisco, continually disrupted by a landslide (Figure 2.18).



Figure 2.18: Several homes and the Coast Highway at Coleman Beach, California, affected by the landslide (Medley 2007b).

A few exploration borings were made. Their interpretation enabled to identify a sandstone bedrock over which a shallow strata of clay and boulder colluvium was supposed to be sliding (Figure 2.19).

Since it was concluded that it was a shallow landslide, it was proposed to remove the failed soil and re-grade the slope. The total cost was estimated in several hundred thousand dollars.

However, during the execution of the work, the contractor did not find the sandstone bedrock neither the failure surface, which was expected at the contact between the upper soil strata and the underlying sandstone bedrock. On the contrary, the contractor encountered many rock blocks, even several meters in size, embedded in a pervasively sheared shale. Many efforts were made to remove the blocks, since blasting was not permitted in that area. These unexpected events caused significant variations in the planned works. The excavations were deepened far below the design depth, up to several tens of meters, with consequent huge extra costs. In fact, more than a million dollars was the final cost of the works (Medley 2007b, Medley and Zekkos 2011).
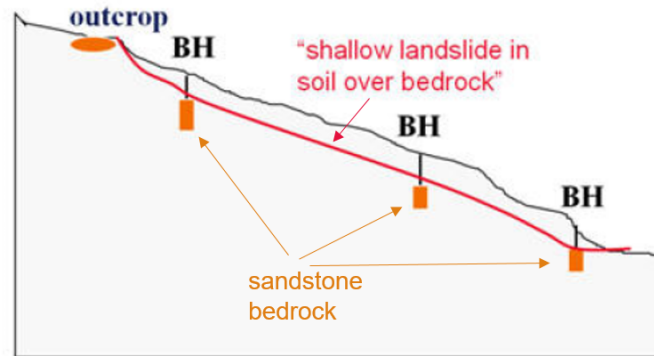
Figure 2.19: Schematic cross section of the slope. The geologic interpretation of boreholes (BH) identified a shallow landslide over an assumed continuous sandstone bedrock (modified after Medley 2007b).

The problem arose because of the wrong interpretation of the exploration drilling data. As shown in Figure 2.20, the rock layers intersected in the lower part of each borehole, and identified as "sandstone bedrock", were actually isolated blocks of great dimensions belonging to a pervasively sheared melange. This misinterpretation was mainly caused by the fact that available geologic maps, showing that the landslide was located in a melange formation, were not examined (Medley 2007b).
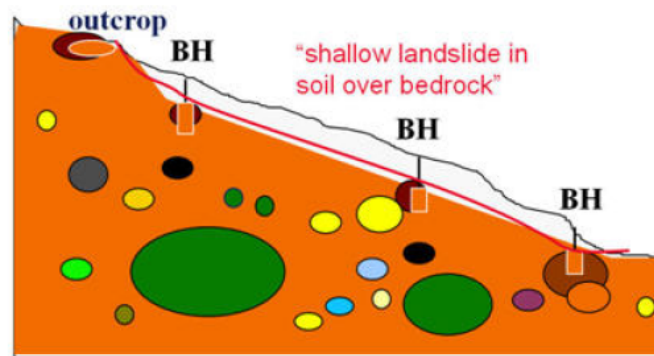


Figure 2.20: Schematic cross section of the real geology of the slope located in a melange. The borings intersected isolated blocks of the bimrock causing a wrong geologic interpretation (Medley 2007b)

## 2.3.2   The Richmond Transport Tunnel, San Francisco

A 4.3 m diameter sewage pipe was constructed in the 90s in San Francisco. It was installed within a 6 m diameter tunnel excavated within the Franciscan melange.

The 740 m of core recovered from the exploration drilling was analyzed in order to estimate the linear block proportion (LBP) of the melange, which was estimated to be equal to 38%.

However, the predictions made by the contractor on the basis of the 1D block distributions were not completely representative of the real 3D conditions. First of all, 3D block size distribution of smaller blocks was overestimated while that of larger blocks was underestimated. The many small intact blocks (even smaller than the block-matrix threshold of $5\%L_c$, equal to 0.3 m) encountered during the tunnelling caused many problems to the muck delivery system (Medley 2007b). However, the higher frequency of very small rock inclusion in the melange should have been expected (Medley 1994, Medley 2001, Medley 2007b, Medley and Lindquist 1995). Moreover, during the excavation the contractor encountered a 200 m greywacke block, which was not expected on the basis of the drilling exploration. However, analysing the available geologic maps of that area, Medley (Medley 1994) estimated that the largest block within the mapped site, A, could have been even 600 m large (equal to $\sqrt{A}$).

### 2.3.3   Scott Dam, California

Scott Dam, located on the Eel River in Northern California 160 km north of San Francisco, is a concrete gravity structure built in the 1920's (Figure 2.21). Although being a very important, strategic and expensive engineering construction, more than 220 m long and about 40 m high, it was built on a weak and extremely complex geologic rock unit, the Franciscan melange. This caused many further site investigations, design changes, geologic and geotechnical studies, laboratory tests on both artificial and real melange specimens and numerical modeling (Goodman and Ahlgren 2000, Medley 2007b, Medley and Zekkos 2011).



Figure 2.21: Scott Dam, California (Medley 2008).

In 1955, springs appeared downstream on the left abutment, where a landslide was already detected in 1920. Since installed monitoring systems confirmed that sliding was occurring, new investigations and technical measures were undertaken. In 1970's the California Department of Water Resource's Division of Safety of Dams (DSOD) required specific studies on the left abutment and foundation stability. The geotechnical analysis performed assumed the strength of the melange under the dam to be the same of that of the weak matrix (a sheared shale). Under this simplified assumption, the calculation indicated that the dam would slide along the base contact with melange. However, the foundation rock was clearly stronger than it was assumed to be, since the structure was still intact after more than 50 years. This behavior was ascribed to the presence of the blocks in the sheared shale of the foundation material (Medley and Zekkos 2011). Hence, some years later, the Scott Dam's foundation material was represented as a two-component stochastic mixture of stronger and weaker components. Such a model, although reasonable, was not easy to implement. This led to a new characterization of the Franciscan melange, by means of innovative laboratory studies commissioned by the Dam owner, who funded two Ph.D. researches: the Medley and the Lindquist research activities (Lindquist 1994b and Medley 1994). Many artificial melange specimens were fabricated with variable block proportions (25%, 50% and 70% VBP). 60 triaxial compression tests were carried out with four different loading directions and five different confining pressures. Moreover, pure matrix and pure block specimens were also tested. The principal findings of the research are the following (Lindquist 1994b, Goodman and Ahlgren 2000):

- friction angle increased for higher VBP values;

- cohesion slightly decreased with increasing VBP;

- VBP was the most important factor affecting the strength of the material;

- the higher the VBP the rougher the failure surfaces, which developed within the matrix generally along the block boundaries;

- the increase in the friction angle for higher VBPs was associated with the augmented roughness of the failure surfaces;

- the decrease of the cohesion for higher VBPs was associated with the increasing proportion of the failure surfaces traversing the matrix and developing along the block-matrix boundaries.

In light of the above, the shear strength of the foundation depended mainly on the VBP of the melange underlying the Dam. With the aim of estimating the amount of geotechnically significant blocks within the foundation material, estimations of the LBP were made on photographs, field observations and analyses of the 150 m of cores recovered from exploration drillings (Figure 2.22).
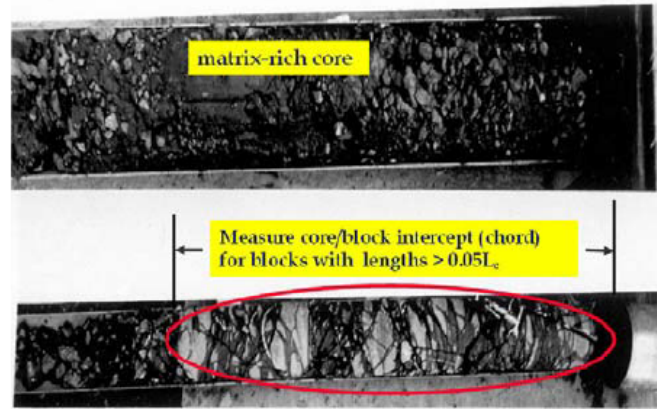
Figure 2.22: Typical core of Franciscan melange recovered at Scott Dam (Medley 2007b).

The block-matrix threshold, necessary to discriminate blocks from matrix, was defined on the basis of the characteristic engineering dimension, $L_c$. This parameter was identified with the thickness of the potential shear zone, equal to 3 m, as shown in Figure 2.23.
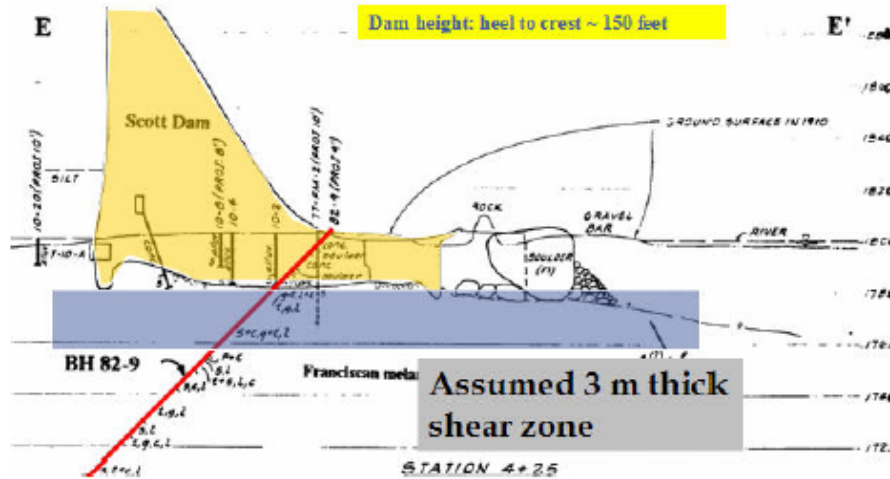


Figure 2.23: Scott Dam cross section, with the indication of the potential 3 m thickness shear zone (Medley 2007b).

Consequently, the smallest geotechnically significant block was assumed to be at least 0.15 m (corresponding to $5\% L_c$). The calculated linear block proportion was about 40%. However, since the largest observed block ($d_{max}$) was in the range 30-43

m, the total length of the cores should have been at least 300-430 m (10 $d_{max}$) in order to allow the LBP to be considered equivalent to the real tridimensional block proportion (Medley 1997). Consequently, an uncertainty factor equal to 0.2 was applied to the LBP estimated(i.e. 40±0.2%), leading to an adjusted VBP in the range 32%-48%.
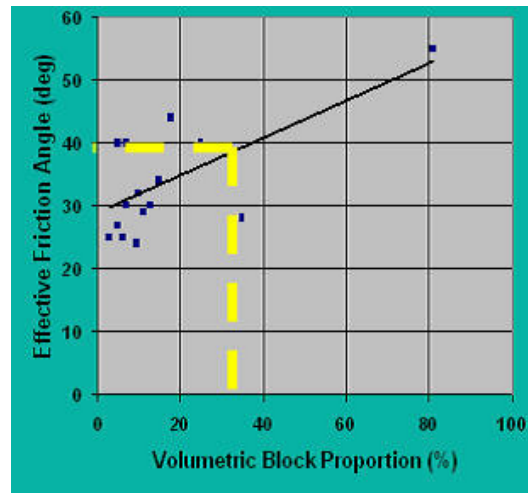


Figure 2.24: Effective friction angle of the melange versus the VBP (Medley 2007b).

Laboratory tests on many melange specimens, obtained from core drilling at Scott Dam, confirmed the findings of the previous research of Lindquist (1994b). In particular, as shown in Figure 2.24, the effective friction angle of the material increased with increasing VBP. To conclude, it was assessed that the Dam was safe and that no reinforcement was necessary. In fact, geotechnical analyses demonstrated that the strength of the foundation rock mass was considerably greater than that of the matrix, due to the presence of the blocks.

# Chapter 3

# Numerical stability analyses of heterogeneous complex formations

Stability problems occurring in heterogeneous formations have been analyzed almost exclusively with deterministic approaches (Irfan and Tang 1993, Püstow 2001, Medley and Sanz Rehermann 2004, Kim et al. 2004, Adam et al. 2014, Minuto and Morandi 2015). The main findings of these studies show that stability increases with increasing VBP and that both the position and shape of failure surfaces are strongly affected by the presence of the blocks. However, the uncertainty in the results that may be caused by different block arrangements and dimensions as well as the occurrence of block-poor (or block-rich) zones within the geomaterial can only be taken into account if a stochastic approach is used.

Recent works (Napoli et al. 2017, Napoli et al. 2018b, Guerra et al. 2016) have also demonstrated that when analyzing a slope stability in a heterogeneous geomaterial, the limit equilibrium method (LEM) cannot be applied using the classic grid search method with circular failure surfaces. In fact, these failure surfaces, which intersect the stronger blocks, are not representative of the real problem and lead to higher and unreliable safety factors. The tortuosity of the failure surface must therefore be taken into account. Hence, if a LEM approach has to be used, a possibility can be to manually draw possible failure surfaces negotiating around the blocks and evaluate the relative SFs, as was the case in Irfan and Tang 1993, Medley and Sanz Rehermann 2004, Minuto and Morandi 2015 and Guerra et al. 2016. Another possibility is to use the recently developed pyBIMstab software (Montoya-Araque and Suarez-Burgoa 2018, Montoya-Araque et al. 2020), which performs 2D stability analyses either for heterogeneous or homogeneous geomaterials with the LEM approach. This open-source application software uses the optimum pathfinding algorithm named A$^*$ (A star) to automatically generate tortuous failure surfaces

when a block-in-matrix material is analyzed (Montoya-Araque and Suarez-Burgoa 2019). The potential of this tool is that it allows the subjectivity of tracing tortuous surfaces by hand to be avoided.

In this dissertation, the influence of the rock inclusions on the stability of block-in-matrix formations is investigated using a novel stochastic approach. 2D Finite Element (FEM) and 3D Finite Difference (FDM) analyses were carried out on heterogeneous models generated by means of different Matlab codes. These codes, performing Monte Carlo simulations, were implemented to take the spatial and dimensional variability of the blocks (inherent in bimrocks and bimsoils) into account. In particular, tunnel and slope stability analyses were performed assuming that the geomaterial has different block shapes, dimensions and VBPs and generating, for each VBP, many configurations. Moreover, the matrix-only approach, which does not take the presence of blocks into account, and the empirical approaches of Lindquist (1994) and Kalender et al. (2014), presented in Section 2.2, were also applied, by way of comparison. These methods assume bimrocks/bimsoils to be homogeneous and isotropic masses and are often used by geopractitioners when planning engineerign works in these complex formations.

## 3.1   The MATLAB©codes

Different Matlab codes were created and used to obtain the heterogeneous slope and tunnel models analysed. The codes generate circular, elliptical or spherical blocks with random axes lengths (radii, in the case of circular blocks) and positions within the domain geometry, according to specific statistical rules and given VBPs, eccentricities and orientations (Napoli et al. 2018b).

Given the geometry of the model, the desired VBP, the eccentricity and orientation of the blocks, each Matlab script randomly generates n axes, d, (diameters, in the case of circular blocks) extracted from a population distributed according to the cumulative distribution function, F(d), of Eq. 3.1:

$$F(d) = (a^{1+D} - d^{1+D})/(a^{1+D} - b^{1+D}) \tag{3.1}$$

whose probability density function is the truncated negative power law of Eq. 3.2:

$$f(d) = -(1 + D)/(a^{1+D} - b^{1+D}) \cdot d^{D} \tag{3.2}$$

where D is the fractal dimension, a and b are the extreme block dimensions (corresponding to 5% $L_c$ and to 75%Lc, respectively, being $L_c$ the height of the slope or the tunnel diameter) and F(d) is the bin increment between the extreme values a and b, which is set equal to 0.0001.

An example is given in Figure 3.1, where 10% of the extracted blocks has a diameter greater than 1.25 m.
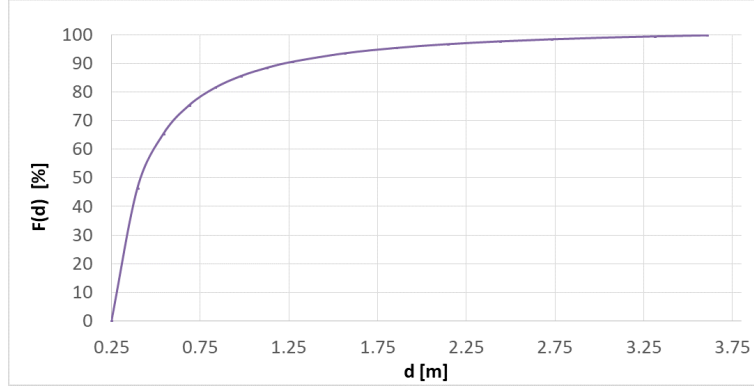
Figure 3.1: Cumulative distribution function of block dimensions.

A "while" loop is used to stop the extractions when the VBP of all inclusions (calculated as the sum of the volume of all blocks divided by the volume of the bimrock model) corresponds to the value required.

To maximize the code performance, blocks placing is made from the largest to the smallest one. Moreover, to correctly place the blocks within the bimrock models, the Matlab code checks that: (i) blocks do not interpenetrate each other; (ii) blocks do not intersect the external boundaries of the model within which they are located. This would lead to a partial loss of the rock block volume, with a consequent underestimation of the effective VBP, which would no longer reflect the desired percentage of inclusions. To these aims, the Matlab code guarantees that a minimum distance (equal to 10 cm) between two blocks and between blocks and external slope boundaries exists.

The main Matlab code output consists of a .txt file containing the coordinates of both the center and the vertex of the semi-major axis and the length of the semi-minor axis of each elliptical block. In order to import the bimrock configurations in the analysis software (e.g., RS2), all Matlab output files were converted in .scr files, so as to be visualized in the AutoCAD software and then saved in a DXF format.

## 3.2    2D stability analyses

### 3.2.1    Stability analyses of slopes in bimrocks

In order to determine how rock blocks may influence the overall behaviour of bimrock slopes (i.e. factor of safety and failure surfaces), 2D Finite Element (FEM) analyses were performed using the RS2 code.

RS2 is a Finite Element code from Rocscience commonly used to model and analyze geotechnical structures for civil and mining applications.

As well konwn, the finite element method is a numerical technique for solving partial

differential equations in engineering and applied science. The domain of interest is split into small finite portions of simple shape, named finite elements. These elements, connected by shared nodes, discretize the continuum and constitute the mesh. Interpolation functions (e.g., polynomial functions) are then used to interpolate the field variables (i.e. stresses and displacements) over the element.

When a slope stability analysis has to be carried out, the advantage of the FEM approach with respect to the limit equilibrium method (LEM) is that no assumption needs to be made in advance concerning the shape and position of the failure surface. Moreover, the analysis can be performed in both elastic and plastic conditions and it is possible to follow the strain process (i.e. to model progressive failure).

In order to obtain a single factor of safety representative of the global stability of the slope, the Shear Strength Reduction (SSR) technique can conveniently be used. This technique progressively reduces the shear strength of the geomaterials which constitute an initially stable slope (i.e. cohesion and friction angle) until a failure state is found, according to the following Eqs. 3.3 and 3.4.

$$c^{trial} = \frac{c}{F^{trial}} \tag{3.3}$$

$$\varphi^{trial} = arctan\left(\frac{tan\varphi}{F^{trial}}\right) \tag{3.4}$$

where $c^{trial}$ and $\varphi^{trial}$ are the reduced shear strength parameters.

If the slope is initially unstable, an increase of the cohesion and friction angle parameters is made until the limiting condition is achieved.

A great number of heterogeneous slope models was generated by means of a stochastic approach (i.e. by means of the Matlab codes described in section 3.1) and then imported into RS2. The 2D slope models analyzed have all the same geometric characteristics, such as height and slope ratio, and are composed of stronger rock inclusions embedded in a weaker matrix. An example of a bimrock model slope is given in Figure 3.2.
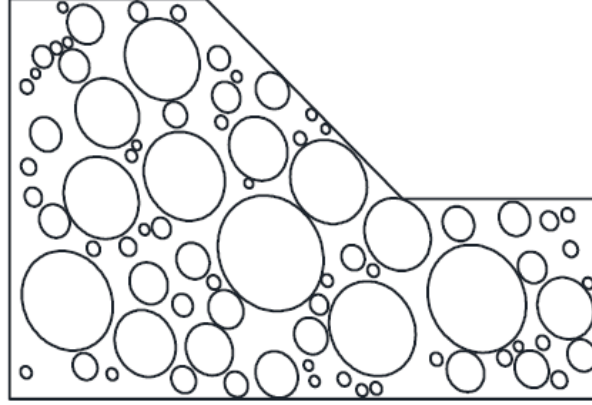
Figure 3.2: A bimrock slope model with elliptical blocks, eccentricity equal to 0.5, orientation equal to 60° and VBP equal to 55%.

The models analyzed have variable block shape, eccentricity, orientation and VBP content, as shown in the scheme in Table 3.1. For each set of geometric input parameters assumed, 15 configurations were generated with the Matlab code and, hence, 15 simulations were carried out for each VBP. This procedure provides for a sufficient statistical validity of the results (Napoli et al. 2018b). Moreover, in order to highlight potential inaccuracies caused by designing neglecting the presence of the blocks, three simplified approaches commonly used by technicians were also applied by way of comparison. These approaches (i.e. the matrix-only, the Lindquist and the Kalender et al. methods) assume bimrocks to be homogeneous equivalent geomaterials.

| | | | Number of simulations performed | | | | |
|---|---|---|---|---|---|---|---|
| **Shape** | **Eccentricity** | **Orientation** | **0% VBP** | **25% VBP** | **40% VBP** | **55% VBP** | **70% VBP** |
| Circular | 0 | - | | 15 | 15 | 15 | 15 |
| Elliptical | 0.5 | 0° | | 15 | 15 | 15 | 15 |
| Elliptical | 0.5 | 30° | | 15 | 15 | 15 | 15 |
| Elliptical | 0.5 | 60° | | 15 | 15 | 15 | 15 |
| Elliptical | 0.5 | 90° | | 15 | 15 | 15 | 15 |
| Elliptical | 0.5 | random | 1 | 15 | 15 | 15 | 15 |
| Elliptical | 0.866 | 0° | | 15 | 15 | 15 | 15 |
| Elliptical | 0.866 | 30° | | 15 | 15 | 15 | 15 |
| Elliptical | 0.866 | 60° | | 15 | 15 | 15 | 15 |
| Elliptical | 0.866 | 90° | | 15 | 15 | 15 | 15 |
| LINDQUIST APPROACH | | | | - | 1 | 1 | 1 |
| KALENDER APPROACH | | | | 1 | 1 | 1 | 1 |

Table 3.1: Number of simulations performed for each configuration analyzed.

The Shear Strength Reduction technique was applied to determine the critical factor at which failure occurs (SRF), i.e. the safety factor (SF) of the slope.

As shown in Figure 3.3, in order to avoid disturbance due to the boundary conditions, the model was expanded by adding a homogeneous outer layer in all the slope models. The same characteristics of the matrix and an elastic behavior were assigned to this layer. Moreover, a ten stages excavation process was simulated to reproduce the face geometry of the slopes.

Both vertical and horizontal translations were restrained at the bottom boundary, while the vertical boundary was restrained laterally, but was free to move vertically. Six-node triangular elements, with higher density around the rock inclusions, were used to mesh the models.
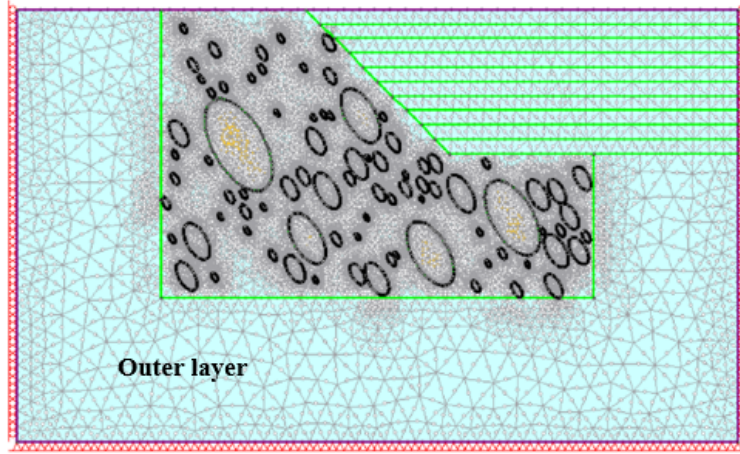


Figure 3.3: A bimrock slope model with elliptical blocks, eccentricity equal to 0.866, orientation equal to 60° and VBP equal to 25%.

### 3.2.1.1   The input parameters

The input parameters that were used in all the analyses for the heterogeneous and the simplified matrix-only models are given in Table 3.2. Both the matrix and blocks were assumed to have an elastic-perfectly plastic behavior and to obey the Mohr-Coulomb failure criterion.

| | $E$ $[GPa]$ | $\nu$ $[-]$ | $\gamma$ $[kN/m^3]$ | $c$ $[kPa]$ | $\varphi$ $[°]$ |
|---|---|---|---|---|---|
| Matrix | 0.04 | 0.25 | 22 | 30 | 24 |
| Blocks | 5.1 | 0.22 | 27 | 600 | 40 |

Table 3.2: Input parameters for the matrix and blocks of heterogeneous and matrix-only models (from Li et al. 2004).

84

The input parameters used for analyzing the equivalent homogeneous models according to the simplified approaches proposed by Lindquist (1994) and Kalender et al. (2014), described in Sections 2.2.1 and 2.2.2, are listed in Table 3.3 and Table 3.4. The $\alpha$ value of the Kalender et al. (2014) approach was selected from Figure 2.17.

Since for VBPs lower than 25% the Lindquist approach provides the same bimrock strength parameters of the matrix, only 40%, 55% and 70% VBP models were modelled.

| $VBP$ | $(1-VBP)$ | $c_{bimrock}$ | $\Delta\varphi_{matrix}$ | $\varphi_{bimrock}$ |
|:---:|:---:|:---:|:---:|:---:|
| $[\%]$ | $[-]$ | $[kPa]$ | $[°]$ | $[°]$ |
| 40 | 0.6 | 18 | 4.5 | 28.5 |
| 55 | 0.45 | 13.5 | 9 | 33 |
| 70 | 0.3 | 9 | 13.5 | 37.5 |

Table 3.3: Input parameters for the equivalent homogeneous slope models, according to the Lindquist criterion (Lindquist 1994b).

| $VBP$ | $UCS$ | $c$ | $\varphi$ |
|:---:|:---:|:---:|:---:|
| $[\%]$ | $[kPa]$ | $[kPa]$ | $[°]$ |
| 25 | 86.63 | 27.4 | 25.4 |
| 40 | 80.56 | 24.4 | 27.6 |
| 55 | 71.18 | 20.9 | 29.2 |
| 70 | 56.72 | 16.5 | 29.8 |

Table 3.4: Input parameters for the equivalent homogeneous approach of Kalender et al. (2014). The parameters $\alpha$ and A were set as equal to 30° and 18, respectively.

### 3.2.1.2   Results

The results obtained are listed in Table 3.5 in terms of normalized safety factors (SFs) and standard deviations. The SFs were normalized by dividing them by the SF of the matrix-only model to generalize the findings.

For the sake of clarity, the SFs are partially presented in Figure 3.4 (SFs of Table 3.5A and B, related to the homogeneous approaches, circular blocks and elliptical blocks with e=0.5) and Figure 3.5 (SFs of Table 3.5A and C, related to the homogeneous approaches, circular blocks and elliptical blocks with e=0.87), while 3.6 contains the average normalized SFs of all the analyses. These results indicate that the presence of the blocks provides little geomechanical advantage for low VBP values (i.e. 25% VBP), while for higher rock contents the SFs increase significantly. In particular, the average normalized SF increases up to around 6% for 25% VBP,

85

7% for 40% VBP, 21% for 55% VBP and 55% for 70% VBP, with respect to that of the matrix.

**A**

| MATRIX ONLY | HOMOGENEOUS EQUIVALENT | LINDQUIST (1994) | KALENDER ET AL. (2014) |
|---|---|---|---|
| Norm_SF = 1 | VBP [%] | Norm_SF | Norm_SF |
| | 25 | - | 1.03 |
| | 40 | 1.00 | 1.02 |
| | 55 | 1.03 | 1.02 |
| | 70 | 1.09 | 1.05 |

| e = 0 | Circular blocks | |
|---|---|---|
| VBP [%] | Standard deviation | Norm_SF |
| 25 | 0.053 | 1.03 |
| 40 | 0.058 | 1.01 |
| 55 | 0.083 | 1.11 |
| 70 | 0.171 | 1.37 |

**B**

| Elliptical blocks | | | | | | | | | | |
|---|---|---|---|---|---|---|---|---|---|---|
| e=0.5 | i = 0° | | i = 30° | | i = 60° | | i = 90° | | i = random | |
| VBP [%] | Standard deviation | Norm_SF | Standard deviation | Norm_SF | Standard deviation | Norm_SF | Standard deviation | Norm_SF | Standard deviation | Norm_SF |
| 25 | 0.064 | 1.00 | 0.030 | 1.01 | 0.108 | 1.05 | 0.075 | 1.03 | 0.051 | 1.01 |
| 40 | 0.067 | 1.05 | 0.050 | 1.03 | 0.096 | 1.02 | 0.050 | 1.05 | 0.060 | 1.02 |
| 55 | 0.143 | 1.21 | 0.044 | 1.09 | 0.074 | 1.07 | 0.080 | 1.07 | 0.075 | 1.09 |
| 70 | 0.188 | 1.55 | 0.133 | 1.28 | 0.143 | 1.18 | 0.187 | 1.25 | 0.163 | 1.39 |

**C**

| Elliptical blocks | | | | | | | | |
|---|---|---|---|---|---|---|---|---|
| e=0.877 | i = 0° | | i = 30° | | i = 60° | | i = 90° | |
| VBP [%] | Standard deviation | Norm_SF | Standard deviation | Norm_SF | Standard deviation | Norm_SF | Standard deviation | Norm_SF |
| 25 | 0.044 | 1.01 | 0.079 | 1.06 | 0.099 | 1.05 | 0.060 | 1.04 |
| 40 | 0.039 | 1.05 | 0.108 | 1.07 | 0.041 | 1.04 | 0.049 | 1.03 |
| 55 | 0.062 | 1.10 | 0.104 | 1.12 | 0.053 | 1.07 | 0.076 | 1.08 |
| 70 | 0.153 | 1.38 | 0.079 | 1.17 | 0.095 | 1.30 | 0.104 | 1.29 |

Table 3.5: Results of the 2D slope stability analyses.

Moreover, it seems that if a preferred orientation of the clasts exists, this may affect the stability of slopes in bimrocks. In particular, from Figures 3.4 and 3.5 it can be seen that the highest SFs are provided when the major axes of the rock blocks are inclined 0° to the horizontal, whatever the eccentricity. It is important to note that this inclination deviates greatly from that of the slopes, which is 45°, and may produce more tortuous failure surfaces.

Moreover, if VBPs $\geq$ 55% are considered, rounded blocks and blocks with a random orientation (i.e. configurations with e=0.5 and i=random) also provide high SFs.

As shown in Figure 3.6, all the other heterogeneous configurations analyzed present a positive correlation between the normalized SFs and VBPs, although the strength increase cannot be easily attributed to the block characteristics (eccentricity and orientation).

On the other hand, a less marked increased in the SFs for increasing block contents is provided by the equivalent homogeneous approaches of Lindquist (1994) and, especially, of Kalender et al. (2014). In particular, $\Delta SF_{70\%}$ equal to only 9% and 5% is provided by the Lindquist and Kalender approaches, respectively, compared

to the SF of the matrix-only model. This increase is remarkably lower than the minimum $\Delta SF_{70\%}$ provided by the heterogeneous configurations, which is 17% for the configurations with elliptical blocks with e=0.87 and i = 30°.

Hence, both these approaches are significantly conservative and should be used for predesign stages only (Napoli et al. 2018b).
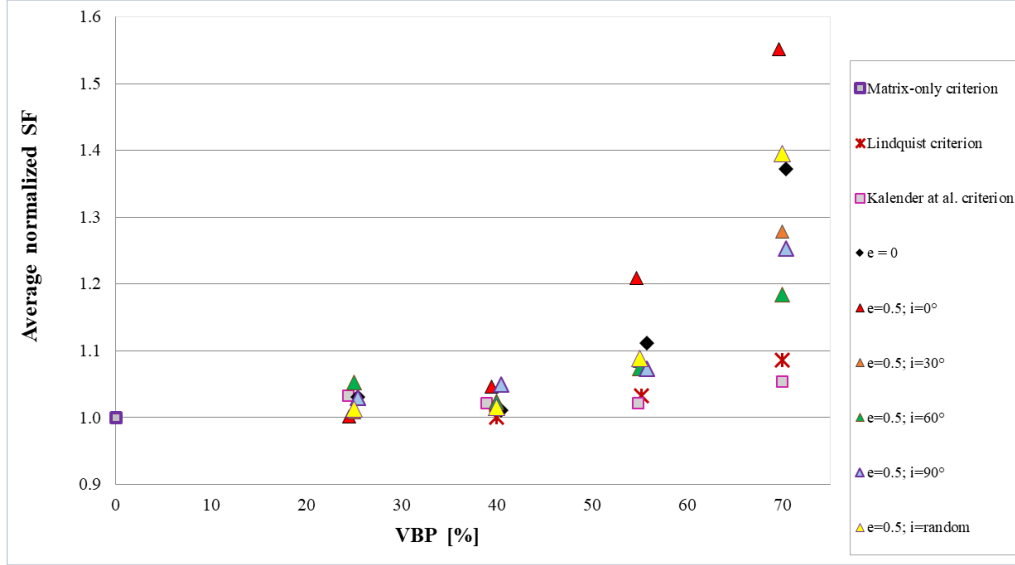


Figure 3.4: Average normalized SFs obtained for the homogeneous equivalent slope models and heterogeneous slopes with block eccentricity, e, equal to 0 and 0.5. Some SFs are slightly shifted on the left/right to avoid graphical overlapping.
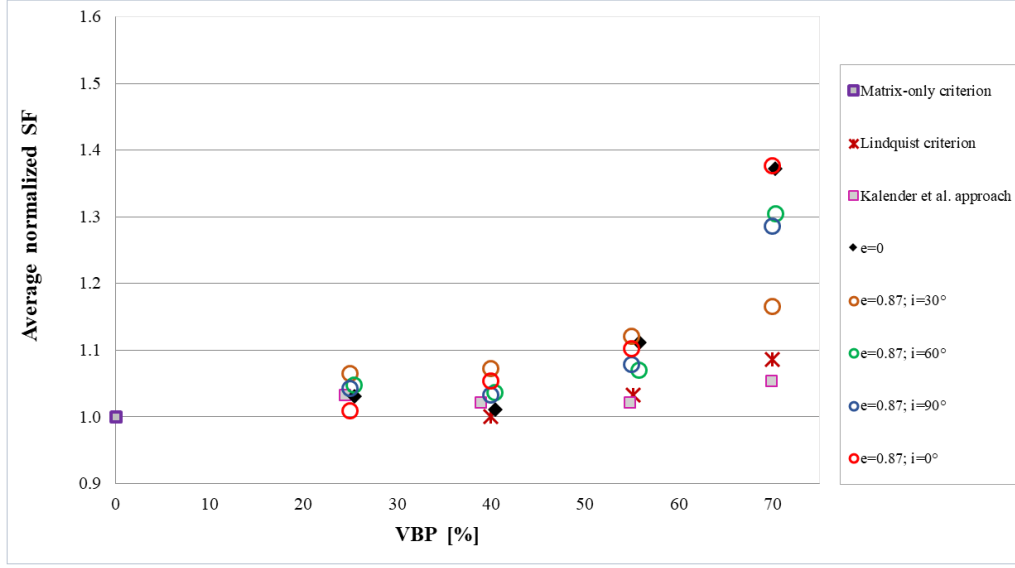
Figure 3.5: Average normalized SFs obtained for the homogeneous equivalent slope models and heterogeneous slopes with block eccentricity, e, equal to 0 and 0.87. Some SFs are slightly shifted on the left/right to avoid graphical overlapping.
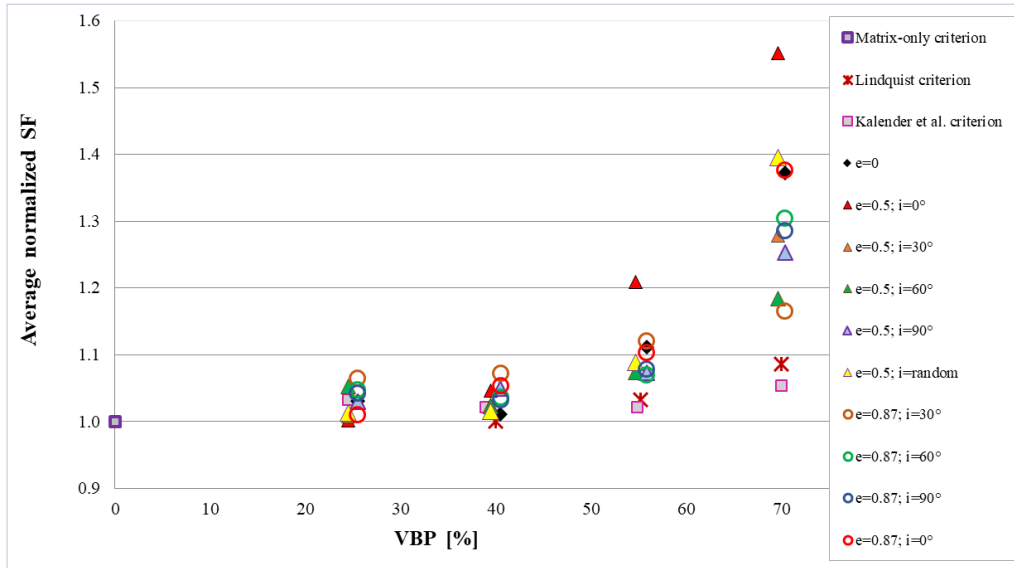


Figure 3.6: Average normalized SFs obtained for all the slope models analyzed. Some SFs are slightly shifted on the left/right to avoid graphical overlapping.

The higher strength can be ascribed to the increase of failure surface tortuosity with increasing VBP. In fact, as indicated in Figure 3.7, shear strains and failure

surfaces visibly develop within the matrix in a tortuous fashion, the more evident the higher the VBP values. As a consequence, the instable volumes can be both more superfcial or deeper than the matrix one, as the VBP increases (i.e. higher VBPs produce more variable instable volumes).
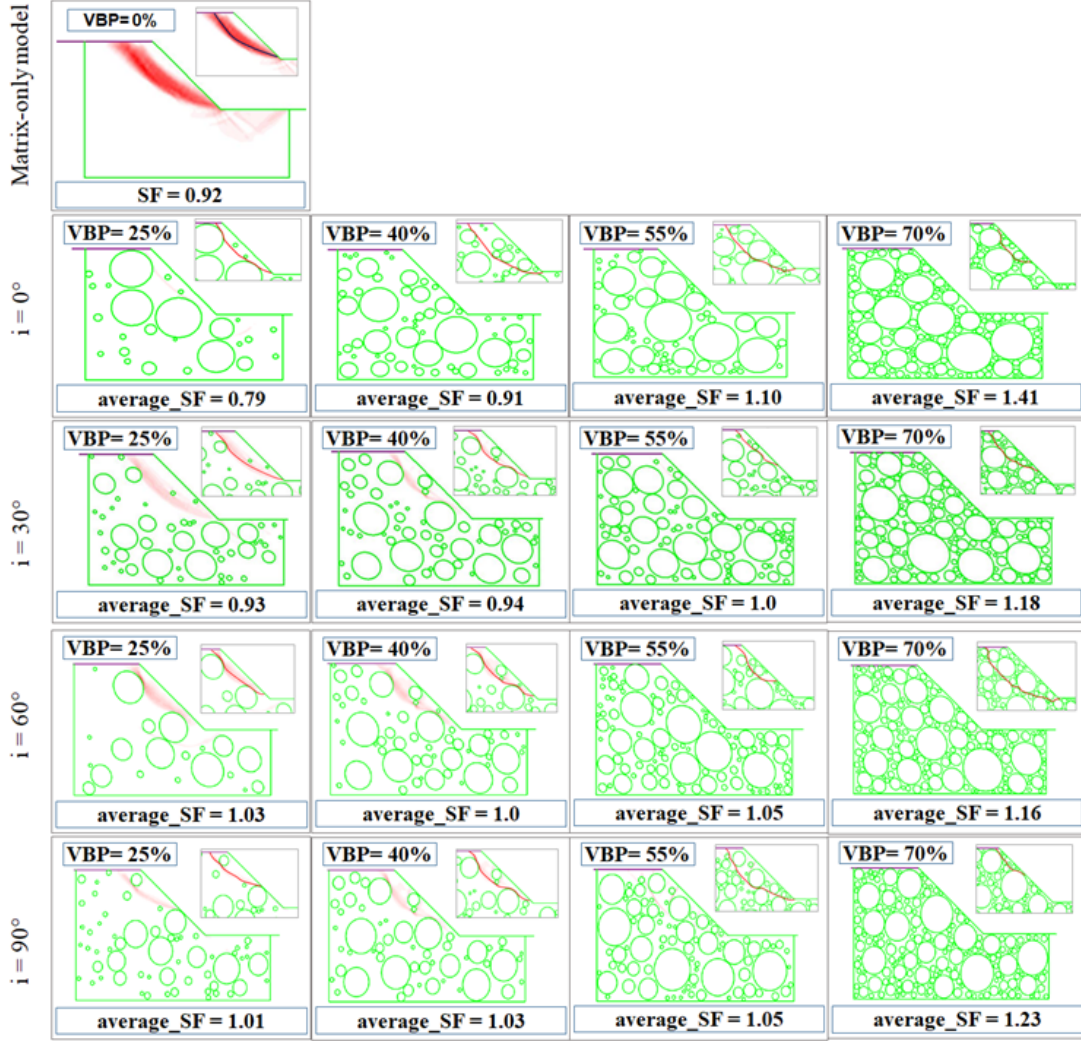


Figure 3.7: Failure surfaces and SFs obtained for one of the 15 bimrock configurations generated for each VBP and orientation, i, considered. The matrix-only model result is also shown (Napoli et al. 2019a).

Hence the use of a matrix-only model, which does not take the presence of blocks into account, leads (i) to unrealistic positions of the failure surfaces and (ii) to significant underestimations of the SFs, especially for VBPs equal to 55% and 70%, for

89

blocks with orientations equal to 0° with respect to the horizontal or for circular-shaped rock inclusions. These findings are consistent with previous results (obtained performing deterministic LEM stability analyses) reported in Medley and Sanz Rehermann (Medley and Sanz Rehermann 2004) and Irfan and Tang (Irfan and Tang 1993) and with those (obtained performing numerical analyses) found by Barbero et al. (Barbero et al. 2006).

Another important aspect highlighted by the results obtained is that a great variability can be observed in the SFs of the 15 analyses carried out for each VBP assumed. In particular, as shown in Figure 3.8, for the case e=0.5 and i=30°, and in Table 3.5, for all the configurations analyzed, the SFs dispersion considerably augments for higher VBPs (Napoli et al. 2017, Napoli et al. 2018b, Napoli et al. 2018a, Napoli et al. 2019a). For a given VBP, the difference ($\Delta$SF) between the maximum and the minimum SF obtained ranges from around 0.1 ($\Delta SF_{25\%}$ VBP, e=0.5, i=30°) up to 0.62 ($\Delta SF_{70\%}$ VBP, e=0.5, i=90°).
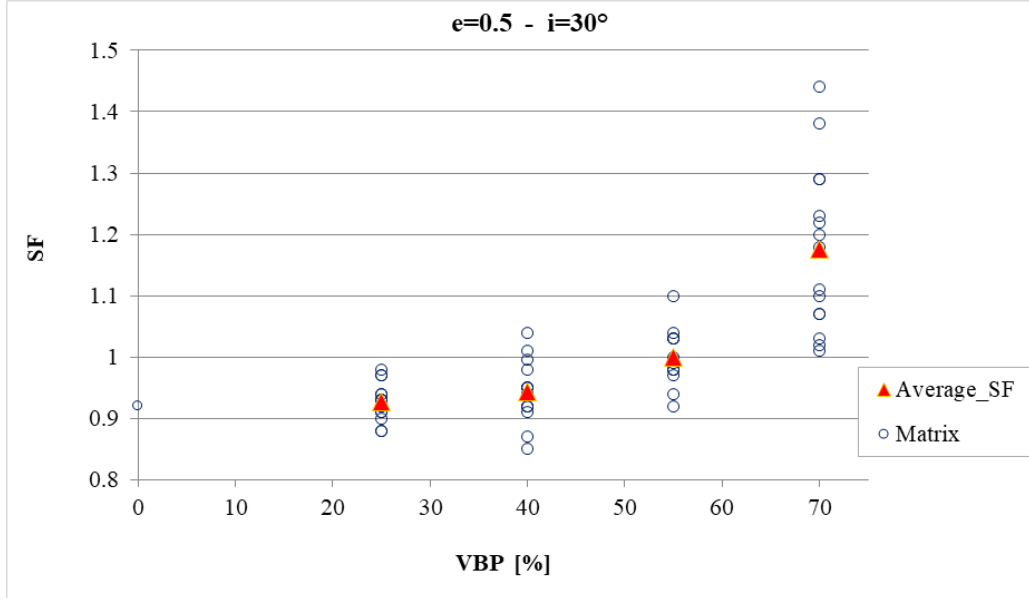


Figure 3.8: Results obtained for the analyses of heterogeneous slopes with block eccentricity, e, of 0.5 and inclination, i, of 30°.

This great variability of the results (SFs, position of failure surfaces and dimension of volumes involved) provided by the configurations with the same VBP highlights the necessity of performing stability analyses in these heterogeneous materials according to a stochastic approach, in an attempt to avoid mistakes that can be made performing deterministic analyses.

### 3.2.2   2D simulations of a tunnel excavation in bimrocks

In order to investigate how the presence of boulders and cobbles may influence the overall behaviour of a heterogeneous formation during the excavation of a deep unsupported circular tunnel, a great number of block-in-matrix models was generated using the Matlab code illustrated in section 3.1 and analyzed using the RS2 FEM code. Elliptical blocks with eccentricity set as equal to 0.5, random orientations and variable VBPs were considered (e.g. simulating a chaotic melange). An example is given in Figure 3.9.
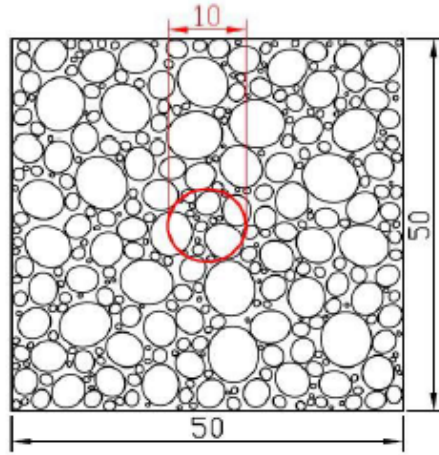


Figure 3.9: Example of a 70% VBP block-in-matrix formation generated with the Matlab code, where the excavation of a tunnel (circular cross section of 10 m diameter) is simulated.

With the purpose of avoiding boundary effects, the models were modified to include on each side a homogeneous outer layer $5L_c$ long (i.e. 50 m), being $L_c$ the tunnel diameter (Figure 3.10). The matrix properties and an elastic behavior were assigned to this layer.
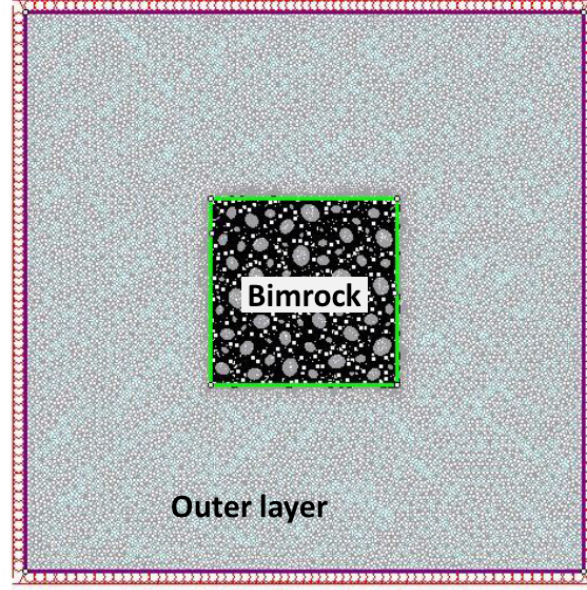
Figure 3.10: Example of a modified model: the bimrock is located in the center of the homogeneous outer layer, which is assumed to have the same properties of the matrix (Napoli et al. 2019b).

All the boundaries were restrained both vertically and horizontally. Six-node triangular elements were used to mesh the models. To guarantee a high mesh quality, a non-uniform mesh size, denser near the blocks, was created and local mesh refinements were adopted where necessary (Figure 3.11).

Displacements and characteristic curves, stresses and yielded zones were compared and analyzed in detail with particular reference to the right sidewall (point R.S.), crown (point C.) and left sidewall (point L.S.), respectively (Figure 3.11). No support pressure either at the wall or at the face was assumed.
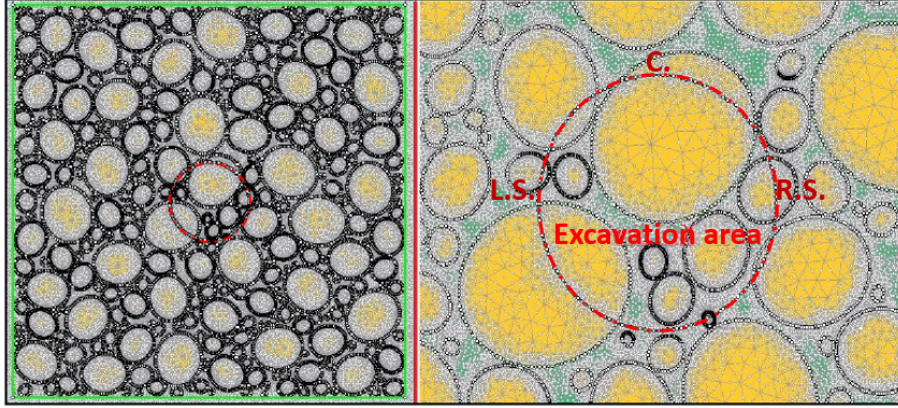
Figure 3.11: On the left: a 70% VBP configuration with the location of the tunnel identified with the red circle. On the right: a detail of the mesh created for the same bimrock model (Napoli et al. 2019b).

### 3.2.2.1   The input parameters

The input parameters assigned to the matrix and blocks are listed in Table 3.6. A constant and isotropic field stress was assigned to the different configurations, assuming an in situ state of stress (p0) dependent on the VBP assumed. In particular, an increasing equivalent unit weight was assigned to the geomaterial for higher VBPs, obtaining p0 values ranging from 1.65 MPa to 1.74 MPa. Moreover, 12 excavation stages (the first in elastic conditions and without the presence of the tunnel) were simulated to reproduce the progressive tunnel excavation. The convergence-confinement approach was applied. This method simulates the advancements of the excavation reducing progressively the stresses acting on each node located on the tunnel boundary. A stress reduction of 10%p0 was set for each stage (Napoli et al. 2019b).

| Parameter | Matrix | Blocks |
|---|---|---|
| $E\,[GPa]$ | 0.04 | 40.7 |
| $\nu\,[-]$ | 0.3 | 0.3 |
| $\gamma\,[kN/m^3]$ | 22 | 27 |
| $c\,[kPa]$ | 65 | 11000 |
| $\varphi\,[°]$ | 28 | 50 |

Table 3.6: Input parameters for the matrix and blocks (modified from Adam et al. 2014).

#### 3.2.2.2 Results

The results obtained are reported in the following Figures 3.12 - 3.16. Inspection of Figures 3.12, 3.13, 3.14 and 3.15 indicates that for increasing VBPs a marked reduction in radial displacements is registered with respect to those of the matrix. Moreover, it evidences a relevant data scattering. In particular, lower VBPs lead to a greater variability in the results. This outcome is the opposite of the results found in the slope stability analyses of Section 3.2.
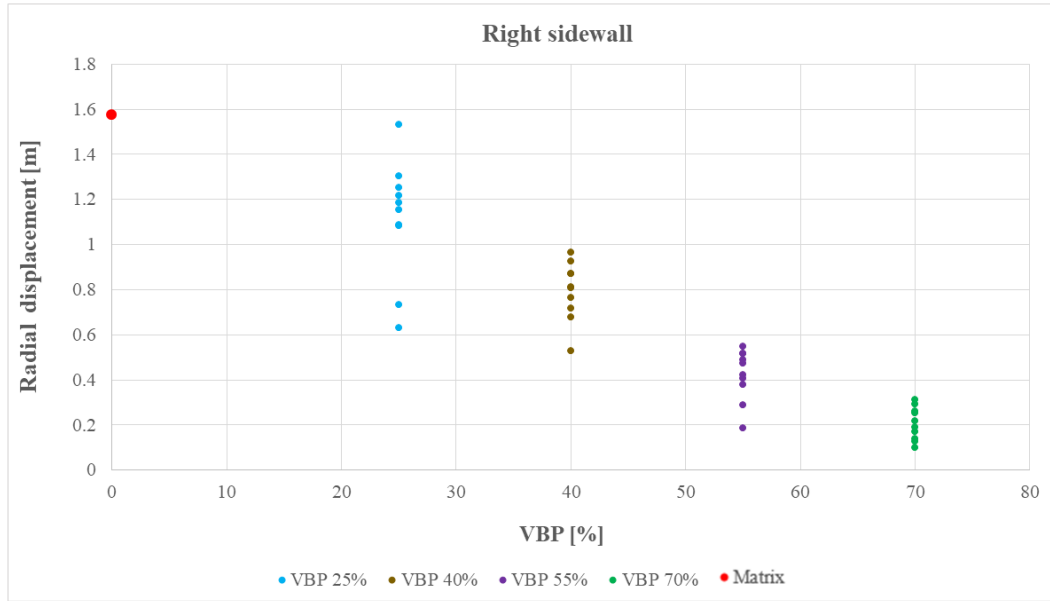


Figure 3.12: Radial displacements at points R.S. versus the VBP under no support pressure, for each configuration analyzed (Napoli et al. 2019b).
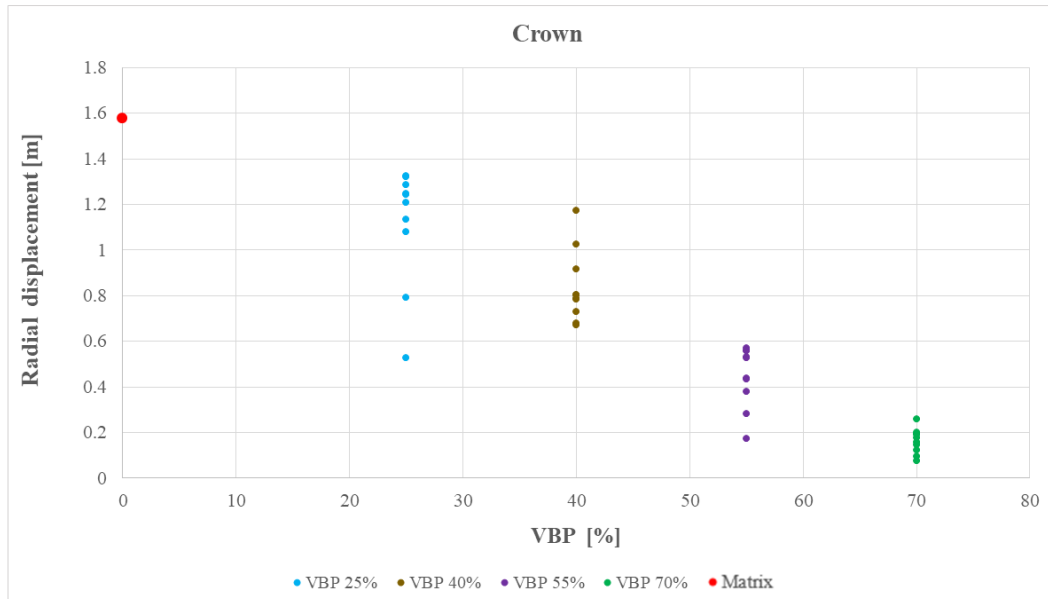
Figure 3.13: Radial displacements at points C. versus the VBP under no support pressure, for each configuration analyzed (Napoli et al. 2019b).
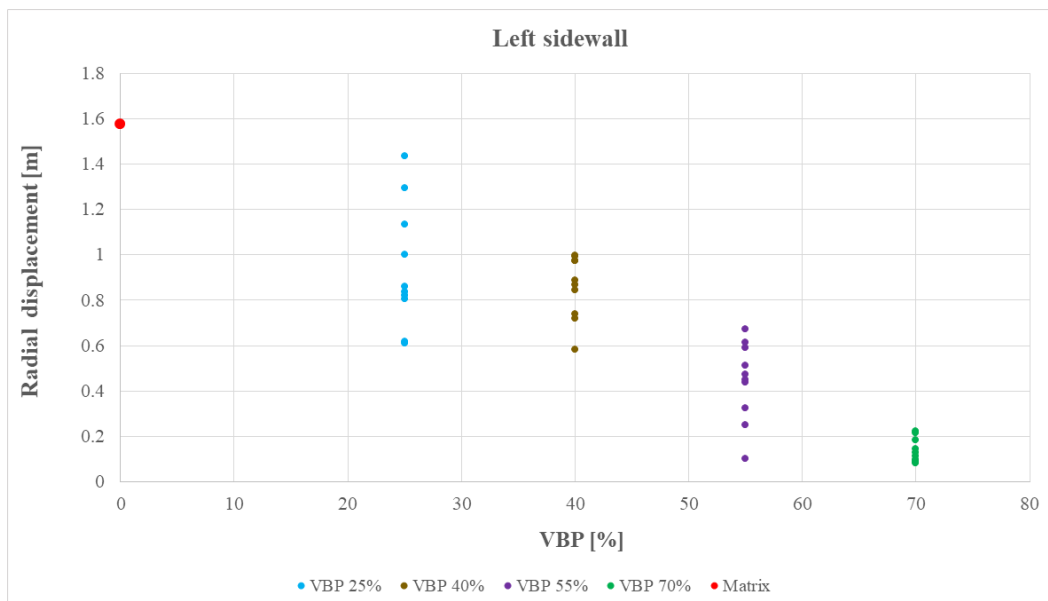


Figure 3.14: Radial displacements at points L.S. versus the VBP under no support pressure, for each configuration analyzed (Napoli et al. 2019b).
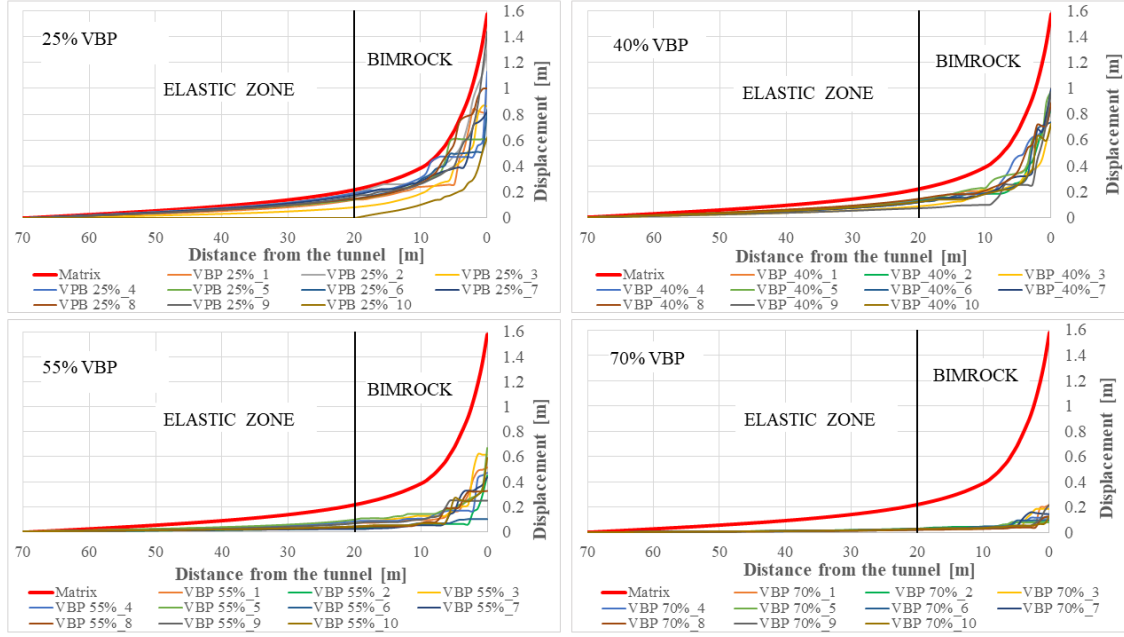
Figure 3.15: Point L.S. (left sidewall): radial displacements versus distance from the tunnel for all the configurations analyzed for each VBP and comparison with the matrix-only model result (red line). The elastic zone corresponds to the outer homogeneous layer (Napoli et al. 2019b).

The average maximum radial displacements (of the 10 configurations analyzed for each VBP considered) at point L.S. (i.e. the left sidewall), for example, are 0.94 m, 0.87 m, 0.44 m and 0.14 m for the 25%, 40%, 55% and 70% VBP models, respectively. These values are definitely smaller than the maximum radial displacement of 1.57 m obtained with the matrix-only configuration (i.e. the 0% VBP model), as indicated in Table 3.7.

| Displacement [m] | 0% VBP | 25% VBP | 40% VBP | 55% VBP | 70% VBP |
|---|---|---|---|---|---|
| Minimum value | 1.57 | 0.33 | 0.34 | 0.09 | 0.06 |
| Maximum value | 1.57 | 1.70 | 1.33 | 0.90 | 0.46 |
| Left sidewall (L.S.) Maximum average value | - | 0.94 | 0.87 | 0.44 | 0.14 |
| L.S. Standard deviation | - | 0.27 | 0.11 | 0.17 | 0.05 |
| Right sidewall (R.S.) Maximum average value | - | 1.12 | 0.79 | 0.42 | 0.21 |
| R.S. Standard deviation | - | 0.26 | 0.13 | 0.11 | 0.07 |
| Crown (C.) Maximum average value | - | 1.12 | 0.84 | 0.45 | 0.16 |

Table 3.7: Minimum and maximum displacement on the tunnel contour and average maximum displacement obtained, under no support pressure, at points R.S., C. and L.S., for the different VBPs analyzed (Napoli et al. 2019b).

Although a low VBP provides relatively little geomechanical advantage compared to the matrix-only model, the position, dimension, orientation, and number of the blocks located near the tunnel strongly influence the rock mass behavior. As mentioned above and illustrated in Figures 3.12 - 3.15, the radial displacements (at the crown and sidewalls) provided by the 25% VBP models show the greatest variability. On the other hand, for higher rock contents a significant less data dispersion is shown (Figure 3.12, 3.13, 3.14 and 3.16). In fact, the standard deviations of the radial displacements at the crown (point C.) and sidewalls (points R.S. and L.S.) are significantly reduced passing from 25% to 70% VBP tunnel configurations, e.g. the right sidewall standard deviations are reduced from 0.26 (for 25% VBP models) to 0.07 (for 70% VBP models). The variability and the non-uniformity of the radial displacements around the tunnel for the ten configurations analyzed for each VBP is illustrated in Figure 3.16.

This result can be ascribed to block-poor zones variably extended and located within the tunnel models with the same rock content as well as to the different block dimensions, positions and orientations which influence the rock mass behavior, especially for lower VBPs.
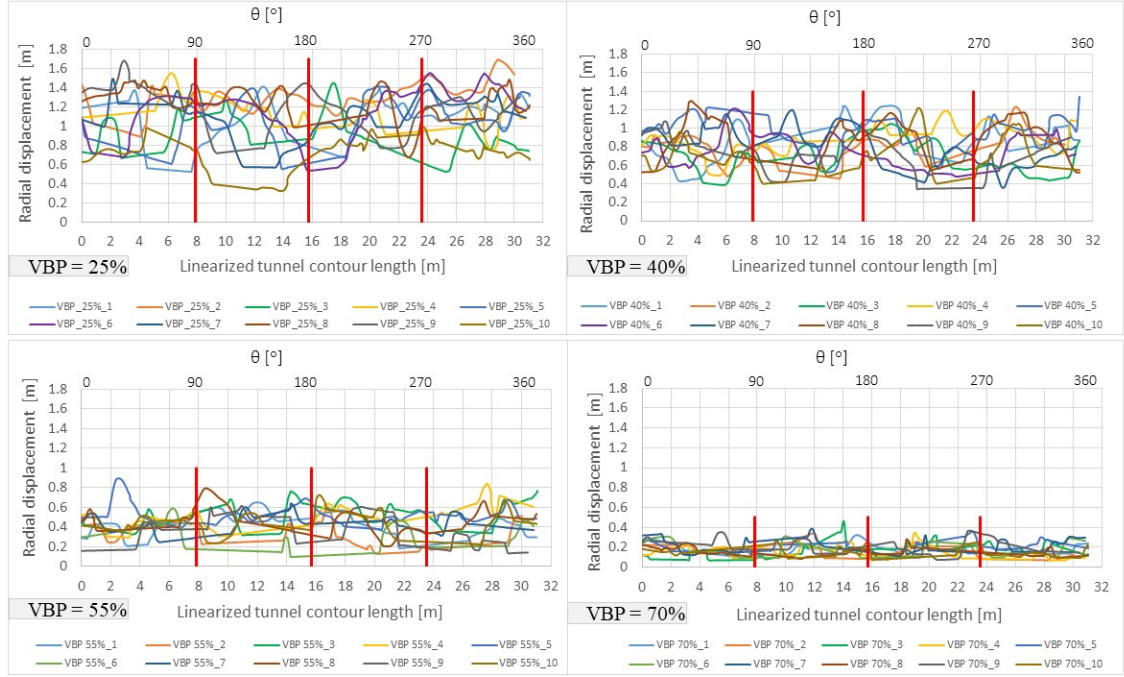
Figure 3.16: Radial displacements vs. linearized tunnel contour length for the ten tunnel configurations analyzed for the different VBP assumed (Napoli et al. 2019b).

Stresses and yielded zones are also affected by the presence of the blocks and are significantly different from the uniform matrix-only results (Figures 3.17, 3.18 and 3.19). As illustrated in Figure 3.17 the extension of the yielded zone considerably reduces for higher VBPs. Moreover, Figures 3.18 and 3.19 indicate that higher stresses are observed in the blocks of greater dimensions located close to the tunnel contour, as well as at the block-matrix contacts. This non-uniformity in the stresses should to be taken into account when designing the tunnel lining.
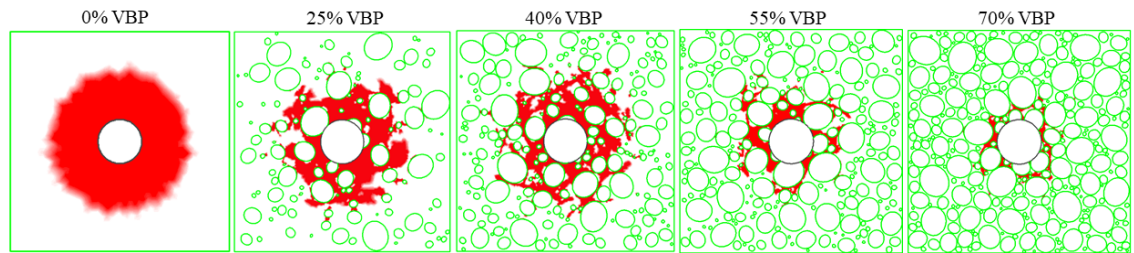


Figure 3.17: Yielded zones for the matrix-only model and for one of the ten tunnel configurations analyzed for each VBP considered.

98
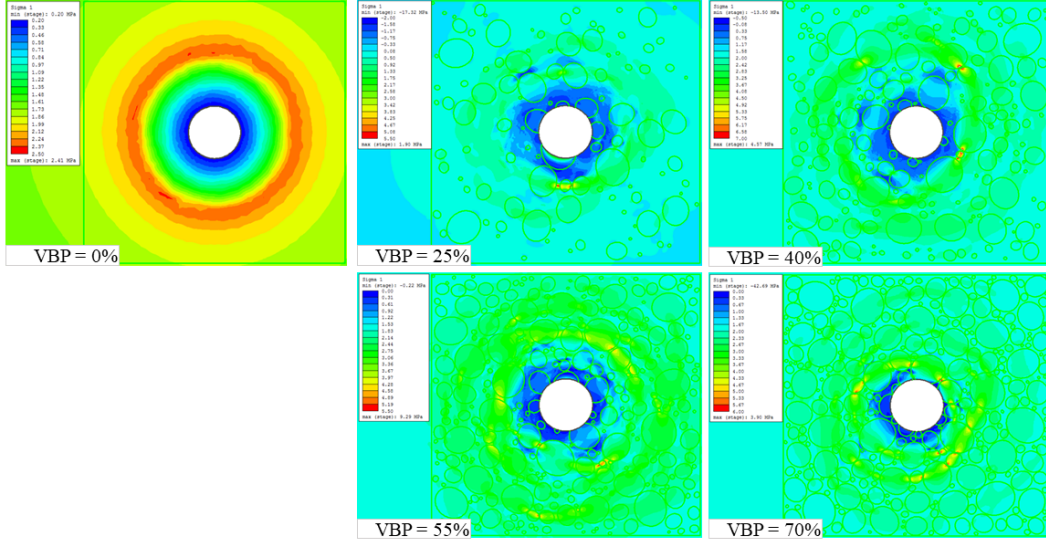
Figure 3.18: Maximum principal stress for the matrix-only model and for one of the ten simulations carried out for each VBP considered (Napoli et al. 2019b).
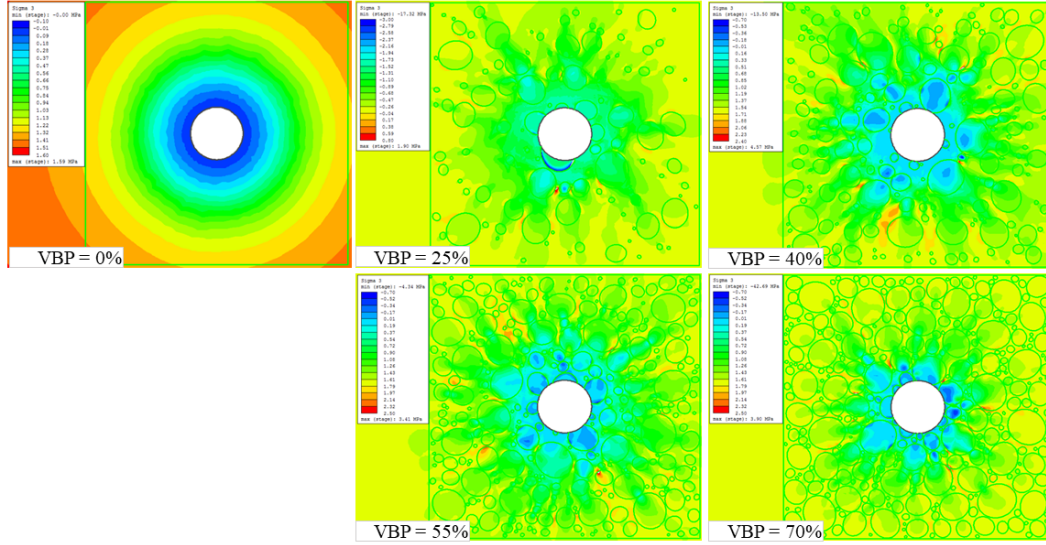


Figure 3.19: Minimum principal stress for the matrix-only model and for one of the ten simulations carried out for each VBP considered (Napoli et al. 2019b).

# 3.3  3D stability analyses

## 3.3.1  Stability analyses of slopes in bimrocks

The aim of this numerical modeling was mainly to investigate the differences, advantages and disadvantages of performing 2D rather than 3D stability analyses. The Finite Difference Method, implemented in FLAC3D, was used to perform slope stability analyses on the same complex formation considered by the author in a recent work (Napoli et al. 2018b).

FLAC3D (Fast Lagrangian Analysis of Continua in 3 Dimensions) is an explicit finite difference code to study the mechanical behavior of a continuous 3D medium as it reaches equilibrium or steady plastic flow (Itasca Consulting Group 2017).

Polyhedral elements are used to create a 3D grid representing the materials to be modeled. Each element of the grid behaves according to a prescribed constitutive model (stress/strain law) and boundary conditions in response to applied forces. The materials can yield and flow, and the grid can deform (in large-strain mode) and move with the material that is represented.

In FLAC 3D, the strength reduction method is used to calculate the safety factor of a slope, according to the Eqs. 3.3 and 3.4. In the analyses carried out in this Ph.D. thesis, a bracketing approach was used (i.e. using the "model factor-of-safety" command of FLAC 3D). This approach requires two starting bracket values corresponding to a stable (the highest value) and unstable (the smallest value) condition. The bracket between the stable and unstable solution is then automatically reduced until the difference between them falls below a given tolerance. Finally, the SF is obtained.

### 3.3.1.1  The input parameters

As in the 2D analyses of section 3.2, 3D slope models with different VBPs were created using the stochastic approach illustrated above, modifying the Matlab code so as to generate spherical rock inclusions. However, 3D models with the highest rock content considered in the 2D analyses (i.e. 70% VBP) could not be obtained due to geometrical limitations, as illustrated in (Song et al. 2008). Hence, 3D slope models with 15%, 25%, 40% and 53% (i.e. the maximum VPB achievable) VBPs were analyzed. A matrix-only slope model (i.e. 0% VBP) was also analyzed by way of comparison. Hence, a total of 41 analyses were carried out.

In order to compare the results, the 3D slopes were created and assigned the same height and slope ratio, mechanical properties (Table 3.8) and constitutive law used by Napoli et al. (2018b).

100

| Parameter | Matrix | Blocks |
|:---:|:---:|:---:|
| $E\,[GPa]$ | 2.5 | 7.2 |
| $\nu\,[-]$ | 0.3 | 0.3 |
| $\gamma\,[kN/m^3]$ | 23 | 23 |
| $c\,[kPa]$ | 10 | 1000 |
| $\varphi\,[°]$ | 28 | 50 |

Table 3.8: Input parameters for 3D slope stability analyses (Napoli et al. 2018b).

### 3.3.1.2   Mesh generation

The generation of the mesh was assisted by the Griddle mesh generation plug-in for Rhinoceros 3D CAD software. This grid generation tool allows the automatic meshing of complex geometries such as block-in-matrix geomaterials. Griddle consists of three main functions: the Griddle GInt command which can be used to clean up the surface meshes, obtained with the Rhino command *"_Mesh"* from the imported DXF file (Figure 3.20). Then, the Griddle *"G_Surf"* command re-meshes the selected surface meshes with triangle or quad-dominant surface elements, as requested by the user. Finally, a high-quality hex-dominant mesh can be produced by the Griddle volume mesher (*"G_Vol"* command), which fills the interior regions bounded by the surface meshes. This 3D mesh can be imported into the FLAC3D code, from Itasca.
The time required to complete all the steps of this mesh-generation procedure varied between a few minutes (for the 0% VBP configuration) up to about 90 minutes (for high VBPs).
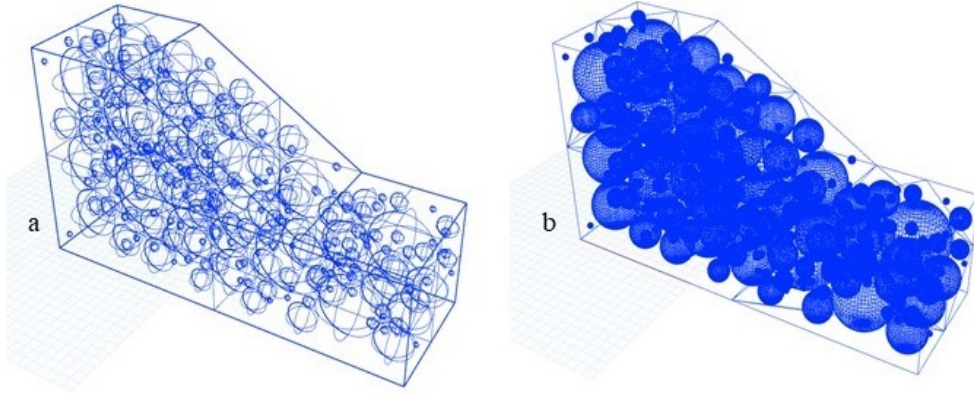


Figure 3.20: a) 3D slope model imported into Rhino as a DXF file; b) 3D slope model after the generation of the Rhino mesh.

### 3.3.1.3   Slope models in FLAC3D

The slope models meshed with the Griddle plug-in were saved as *.f3grid* files and imported into FLAC3D. For the definition of the mechanical properties of the matrix and blocks, they both had to be collected into identifiable regions. Hence, a group name was assigned to the slope and another group name was assigned to the spheres (i.e. rock inclusions) using the "assign a group to the selection" command (Figure 3.21).
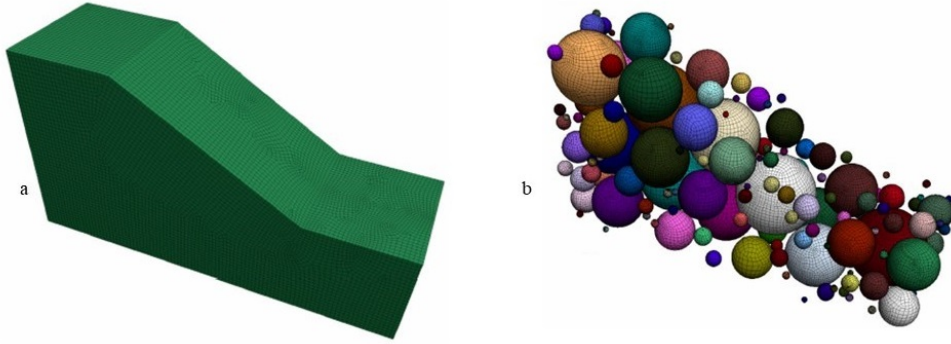


Figure 3.21: Group assignments in FLAC3D: a) slope; b) spheres.

In order to apply the boundary conditions, the "assign group names" command was used to automatically assign a name to the 8 faces of the model (Figure 3.22). The following boundary conditions were applied:

- null velocity for the lateral and bottom surfaces (i.e. "Bottom", "West", "North", "South" and "East" faces);

- no restriction is given to the upper surface (i.e. the "Top" face).
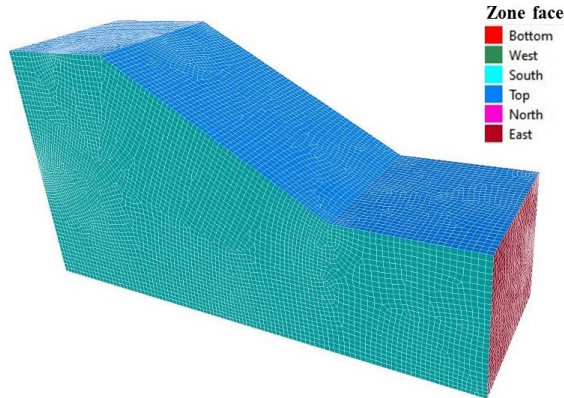


Figure 3.22: Zone face names.

### 3.3.1.4   Results

The results obtained are in agreement with previous findings from the literature (Irfan and Tang 1993, Medley and Sanz Rehermann 2004, Napoli et al. 2017, Napoli et al. 2018b, Napoli et al. 2018a) and with the 2D FEM results illustrated above.

| VBP [%] | SF [-] | Standard deviation [-] |
|---------|--------|------------------------|
| 0       | 1.12   | -                      |
| 15      | 1.22   | 0.032                  |
| 25      | 1.25   | 0.047                  |
| 40      | 1.32   | 0.041                  |
| 53      | 1.52   | 0.080                  |

Table 3.9: Average SFs and standard deviations yielded by the 3D analyses (modified from Napoli 2020).

As shown in Table 3.9 and Figure 3.23, the results clearly show that rock inclusions strongly affect the behavior of the rock mass, increasing its overall strength even for low VBPs. Moreover, it is confirmed that the simplified approach (i.e. the 0% VBP model), ignoring the presence of the blocks, is over conservative and leads to an unrealistic shape and position of the failure surface. Figure 3.24 indicates that more superficial and irregular unstable volumes are indeed obtained from bimrock models with higher VBPs.
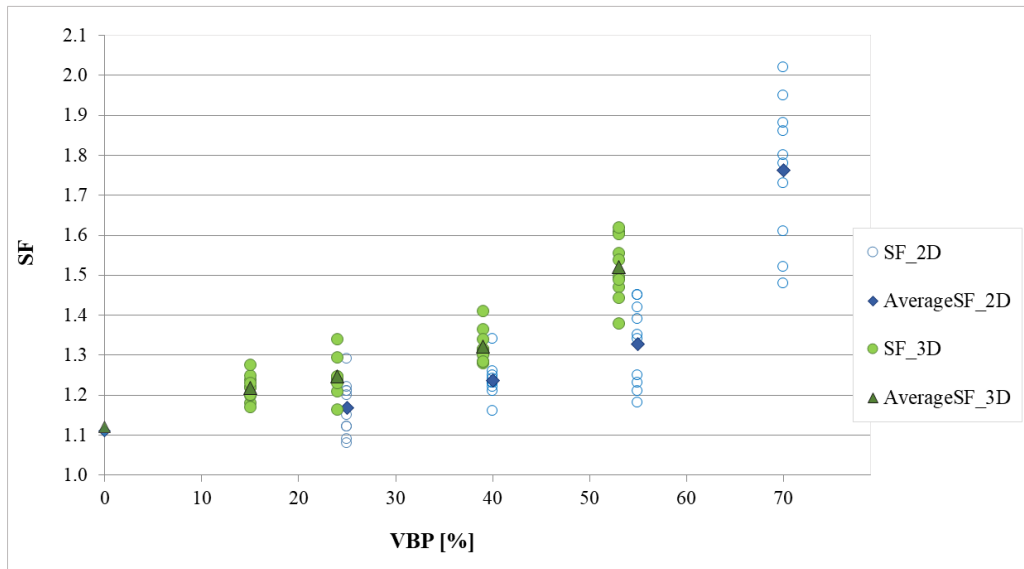


Figure 3.23: Comparison of the SFs obtained from the 2D and 3D numerical simulations. The 3D SFs of the heterogeneous configurations with 25% and 40% VBPs were slightly shifted on the left to avoid graphical overlapping with the 2D results.

103
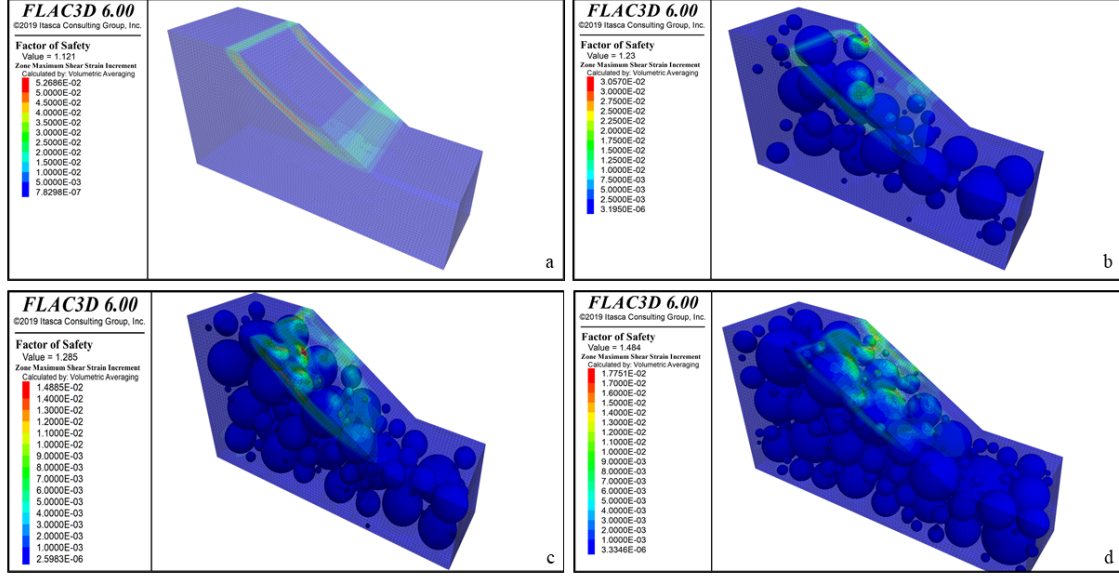
Figure 3.24: Maximum shear strains for: a) the matrix-only model; one of the ten heterogeneous configurations analyzed with: b) 25% VBP; c) 40% VBP; d) 53% VBP.

The comparison with the results of the 2D FEM analyses indicates that, for a given VBP, higher SFs and a lower data dispersion are provided by the 3D simulations. This could be due to the different confinement of the 2D models (i.e. plain strain conditions) with respect to the 3D models, which should lead to more reliable results (Napoli 2020).

However, to considerably reduce the computational time required by the analyses, which ranged from less than 7 hours (0% model) up to about 4 days per simulation, a stochastic 2D modelling seems appropriate. In fact, the simulations performed with the RS2 code required no more than about 8 hours, even for VBPs equal to 70%. Moreover, potential mistakes resulting from 2D rather than 3D analyses should be found to lie on the side of safety.

# Chapter 4

# Approaches to estimate the block content of block-in-matrix geomaterials

As widely discussed in the previous Chapters 2 and 3, the mechanical behavior of bimrocks and bimsoils is strongly influenced by the presence of blocks. Previous findings from the literature have indeed shown that the strength, deformability and failure mode of these geomaterials mainly depend on the VBP and have underlined the importance of taking blocks into account in the planning, designing and construction phases of any engineering work. In fact, as illustrated in Section 2.3, expensive geological and geotechnical mischaracterizations, neglecting the presence of the rock inclusions, have caused technical problems and risks during a number of construction works.

Many authors have also highlighted that block quantities and dimensions play a key role in the choice of appropriate earthwork equipment and underground excavation and support methods. In fact, when excavating in these complex formations, the presence of rock blocks can induce, among other problems, face instabilities, sinkholes and settlements. Moreover, if large blocks cannot be comminuted to small cobble or gravel size by the cutting tools, potential risks can occur, such as obstructions and damage to cutters, with consequent delays and cost increments (DiPonio et al. 2007, Hunt and Del Nero 2010, Hunt 2014, Roberts et al. 2014, Gwildis et al. 2018). Such inconveniences may be avoided by choosing adequate tunnelling techniques and support measures and by designing an appropriate cutterhead. However, a successful tunneling project requires the frequency, quantity and size of the rock blocks to be predicted as accurately as possible.

In light of the above, the evaluation of the VBP and block-size distribution of a bimrock or bimsoil is of utmost importance. However, the estimation of these quantities is not a simple matter and continues to represent a critical issue.

The real block content of a heterogeneous formation cannot be accurately determined apart from the laboratory (i.e. by disintegrating a sample) and the result cannot be extended to smaller (site) scales. As a consequence, the VBP is usually estimated via 1D or 2D measurements (i.e. by LBP or ABP), using stereological techniques. Nevertheless, as reported in the literature, using stereological methods to estimate the actual 3D block content produces results that are fraught with uncertainty. In fact, block shapes and orientations as well as the amount of sampling strongly affect the reliability of 1D and 2D measurements (Medley 1997, Medley 2001, Medley 2002, Haneberg 2004).

Although the VBP estimation constitutes one of the greatest challenges in the research field of block-in-matrix formations, there are only very few studies that have focused on this issue. One of the most relevant works concerning the quantification of the error in VBP estimates inferred from 1D measurements was carried out more than 20 years ago by Medley (Medley 1997), as discussed in Section 2.1.4.1.

Given the central importance of the VBP estimation, one of the purposes of this Ph.D. research was to contribute to a deeper understanding of this issue by developing new approaches and providing results that may help to address the research gaps regarding this topic.

Quantitative evaluations were carried out and new tools were developed through the use of statistical and probabilistic methods to explore (i) the uncertainty present in the estimation of the VBP and (ii) the probability of encountering blocks when tunneling in heterogeneous ground.

More in detail, a statistical approach implemented in a Matlab code was developed to determine the amount of bias introduced when VBPs are inferred from 2D measurements (i.e. ABPs). A graph is provided to obtain an uncertainty factor, UF, to adjust the initial 2D estimate. The evaluation of the UF depends on the block content measured and on the size of the outcrop area investigated.

Another Matlab code was written for estimating the probability of encountering rock blocks that can cause technical problems when tunneling in heterogeneous ground. The Matlab script was then converted into an executable free application, the PBE code, so that it can easily be used for future research or technical applications. The PBE code allows blocks fully or partially located within the entire tunnel Section or in a part of it (at the lateral distance furthest from the centre of the cutterhead) to be taken into account in the analysis. The results provided by this new tool can be extremely useful for making a more rational choice regarding the tunneling technique and the design of an adequate cutterhead. Both these approaches are the subject of recent publications by the author (Napoli et al. 2020a, Napoli et al. 2020b).

## 4.1 An approach to determine the uncertainties in estimates of the VBP from 2D measurements

The approach described in this Section builds on Medley's work (1997), described in Section 2.1.4.1. The novelty of this study is that it statistically investigates the degree of error that can be introduced by inferring the VBP of a heterogeneous geomaterial using 2D outcrop measurements (i.e. ABP) rather than 1D data (i.e. LBP).

Specifically, a Matlab routine (see Section 4.1.1) was implemented to generate several 3D bimrock models enclosing spherical blocks of given VBPs.

The bimrock models were sectioned many times, obtaining a great number of section planes on which the ABP was computed. Statistical analyses were then performed to simulate an increasing size of the outcrop investigated, by selecting different subsets of planes and combining the results. Finally, a chart is provided to adjust the initial 2D estimates by means of an uncertainty factor, selected on the basis of the outcrop size and ABP measured.

The potential of this new approach lies in the fact that working with 2D, rather than the widely used 1D measurements, can often be more convenient. In fact, it is generally more accurate and easier to estimate the 3D block content of a heterogeneous formation from outcrops, photographs or image analyses rather than from borehole drillings. For example, if a tunnel project or a landslide repair is carried out, an outcrop at least equal to the excavation face or instable area can generally be inspected. Moreover, 2D surveys are usually cheaper than 1D measurements.

### 4.1.1 The statistical approach

Five square-shaped parallelepiped domains, enclosing spherical blocks with VBPs from 10% to 50% were generated using a Matlab code. An example is given in Figure 4.1. The sides of the parallelepiped are $L_c$ x $L_c$ x $10L_c$. Its cross-section, corresponding to the area of engineering interest, is $A_c = L_c^2$.

The rock inclusions were assigned a fractal block-size distribution, typical of Franciscan melanges (Medley 1994, Riedmüller et al. 2001, Medley and Zekkos 2011, Khorasani et al. 2019), and were located randomly within the 3D domains, avoiding interpenetrations between spheres and intersections with the edges of the parallelepipeds.

The diameters of the spheres were extracted randomly from a population distributed according to the cumulative distribution function of Eq. 3.1, setting the minimum and largest block dimensions, a and b, to 5% $L_c$ and 75% $L_c$, respectively, and the fractal dimension, D, to 2.5 (Medley 1994, Haneberg 2004, Napoli et al. 2020b). This value was considered representative of a typical bimrock and Napoli

et al. 2020b also demonstrated that no significant differences would be obtained if a different value (e.g., D equal to 2.3 or 2.7) was used.

For each bimrock model, the ratio between the cumulative volume of all the spheres generated up to the i-th extraction and that of the parallelepiped was computed, by continuing to extract the spheres up to the VBP required in input.
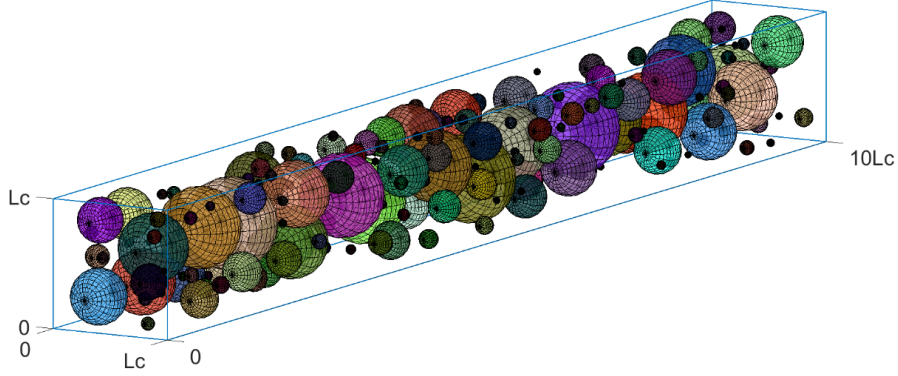


Figure 4.1: A bimrock model with 30% VBP (modified from Napoli et al. 2020b).

The parallelepiped was then sectioned along its longest dimension, with equidistant and parallel planes representing potential outcrop faces. The number of section planes was chosen in order to:

- ensure the statistical validity of the results (i.e. a great number of planes had to be analyzed);

- avoid section planes located too close to each other, which would have provided duplicate results, compromising the reliability of the results. Hence, a minimum distance between two consecutive section planes was guaranteed. An appropriate minimum distance was assumed to be at least equal to the smallest block dimension (i.e. parameter a).

Therefore, 150 planes were generated to section each bimrock model. The ABP of each plane was computed as the ratio between the total area of the intersected blocks (i.e. circles) and $A_c$ (i.e. the domain cross-section, equal to $L_c^2$).

An example of four different planes sectioning a 30% VBP bimrock model is shown in Figure 4.2. Each plane contains the intersected blocks and corresponds to a theoretical planar outcrop face equal to the area of engineering interest, $A_c$. As expected, considerably different ABPs are provided by the four planes.

Then, if an outcrop area four times greater than $A_c$ has to be simulated, these planes can be simultaneously considered, providing an ABP value equal to 16.25% (i.e. the average ABP of the four planes).

From this example, the great discrepancy between the ABP measured and the real

VBP is evident. As expected, this outcome indicates that inferring the VBP from 2D measurements on outcrops that are not large enough with respect to the $A_c$ yields significantly incorrect results.
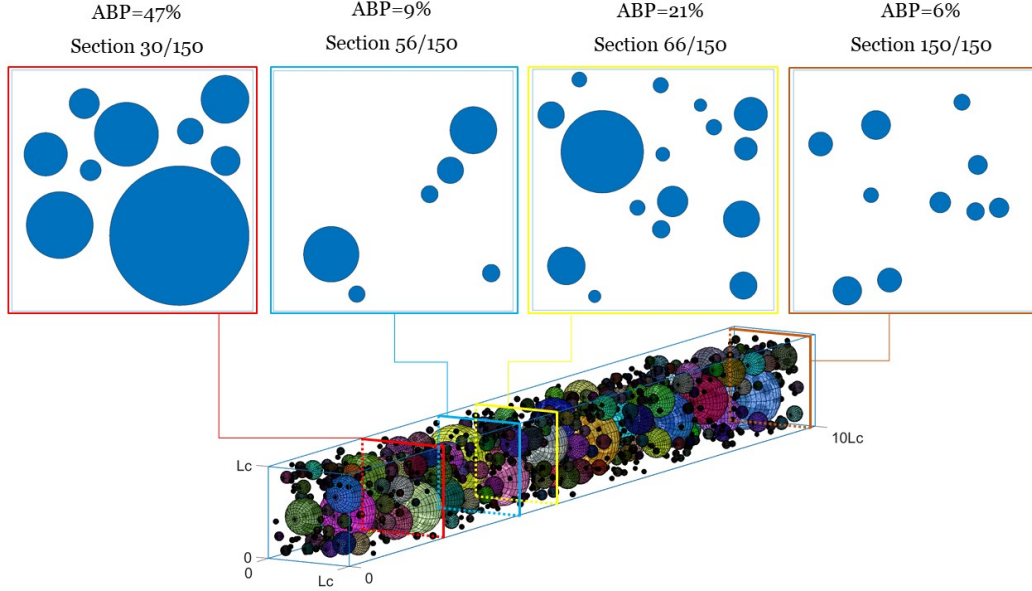


Figure 4.2: Intersected blocks and ABPs identified on four different planes, representing outcrop surfaces. The planes section the 30%VBP parallelepiped of Figure 4.1 (Napoli et al. 2020b).

The aim of this approach was to explore if outcrop surfaces of increasingly larger sizes can provide more reliable VBP estimates.

To this end, statistical processing was carried out by combining a variable number, $\beta$, of section planes, from 1 up to 150. In this way, outcrops with surfaces between a minimum of $A_c$ (i.e. $\beta = 1$) and a maximum of $150 \cdot A_c$ (i.e. $\beta = 150$) were analyzed.

For each $\beta$ combined section planes, a great number of subsets were generated randomly from the total number of 150 planes, avoiding duplicates. Then, the results (i.e. ABP values) were statistically analyzed.

It is worth noticing that the number of combinations (i.e. subsets), N, of $\beta$ elements from a set of 150 elements (i.e. section planes), without duplicates, is $N = \binom{150}{\beta} = \frac{150!}{\beta! \cdot (150-\beta)!}$. N is equal to 150 if $\beta = 1$, but for some other $\beta$ values it is an extremely high number. For example: for $\beta = 10$, $N = \binom{150}{10} \approx 1.17 \cdot 10^{15}$ combinations, for $\beta = 20$, $N = \binom{150}{20} \approx 3.63 \cdot 10^{24}$, and so on. Therefore, in order to contain the computational time of the analyses and avoid overloading the

storage capacity of the computer, the maximum number of subsets was limited to 5000, for each $\beta$ considered.

Similarly to Medley (1997), an uncertainty factor, UF, was obtained from Eq. 4.1 to adjust the initial ABP measured.

$$UF_{\beta=i} = \frac{\sigma\left(ABP_j\right)|_{\beta=i}}{VBP}; \ j = 1, 2, ..., j_{max} \tag{4.1}$$

where:

- $i = 1, 2, ..., 150$ values of $\beta$. It represents the number of section planes analyzed simultaneously;

- $j =$ number of subsets considered for each $\beta = min\left(\binom{150}{\beta}, 5000\right)$;

- $j_{max} = 5000$;

- $\sigma\left(ABP_j\right)|_{\beta=i} =$ standard deviation of the ABP values provided by all the subsets considered for $\beta = i$;

- $VBP =$ real volumetric block proportion of the complex formation simulated.

The results of this approach are given in the next Section 4.1.2.

## 4.1.2 Results

The average ABPs and overall standard deviations obtained for each bimrock model and size of area under investigation (i.e. $\beta$) are illustrated in Figure 4.3. These graphs highlight that the ABPs estimated deviate from the real VBPs especially if small survey areas are analysed (i.e. low $\beta$ values), but also if a great number of $\beta$ section planes are taken into account. However, for greater investigation surfaces the standard deviations decrease and the average ABP values tend to the real VBP.
These findings are consistent with those found by Medley (1997).
Hence, the uncertainty in assuming the equivalence between the ABP and VBP decreases as the size of the investigation area increases and, for a sufficiently large outcrop, it can be considered negligible. However, this error can obviously not be fully eliminated.
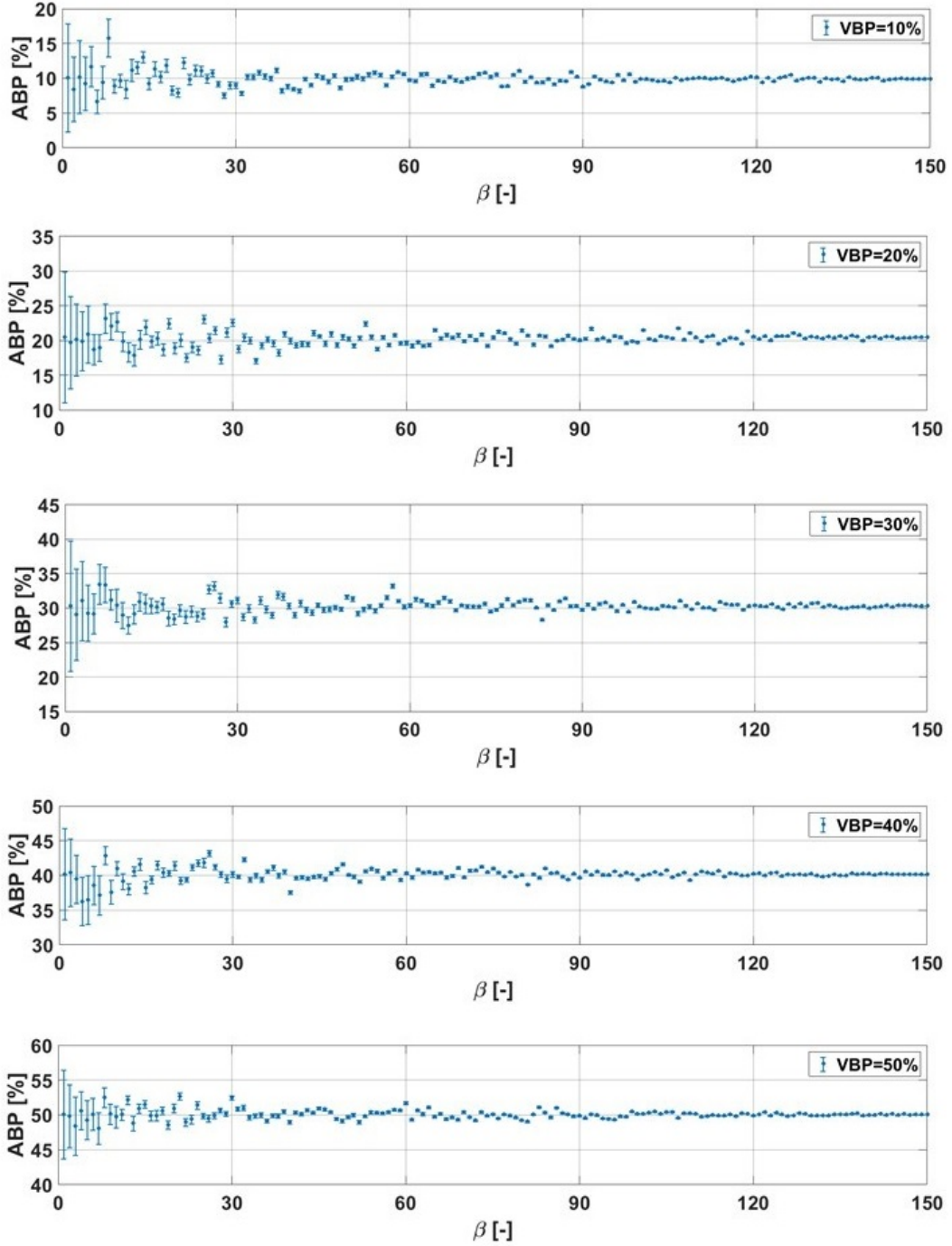
Figure 4.3: Plot of cumulative ABPs vs the multiplicative coefficient of the area of engineering interest, $A_c$ (total investigation surface). Error bars represent $\pm 1$ standard deviation with respect to the mean of the data derived from randomly combined section planes (Napoli et al. 2020b).

111

From the results illustrated in Figure 4.3 and by means of Eq. 4.1, an uncertainty factor, UF, was defined to adjust the ABP estimated and obtain the 3D block content. The correlation between the UF and the size of the outcrop simulated (i.e. $\beta$) is shown in Figure 4.4, for the five bimrock models analyzed.

For all the VBPs considered, a significant decreasing trend of the UF as a function of $\beta$ is obtained. Moreover, in agreement with Medley (1997), lower biased results were obtained from bimrock models with higher VBPs.
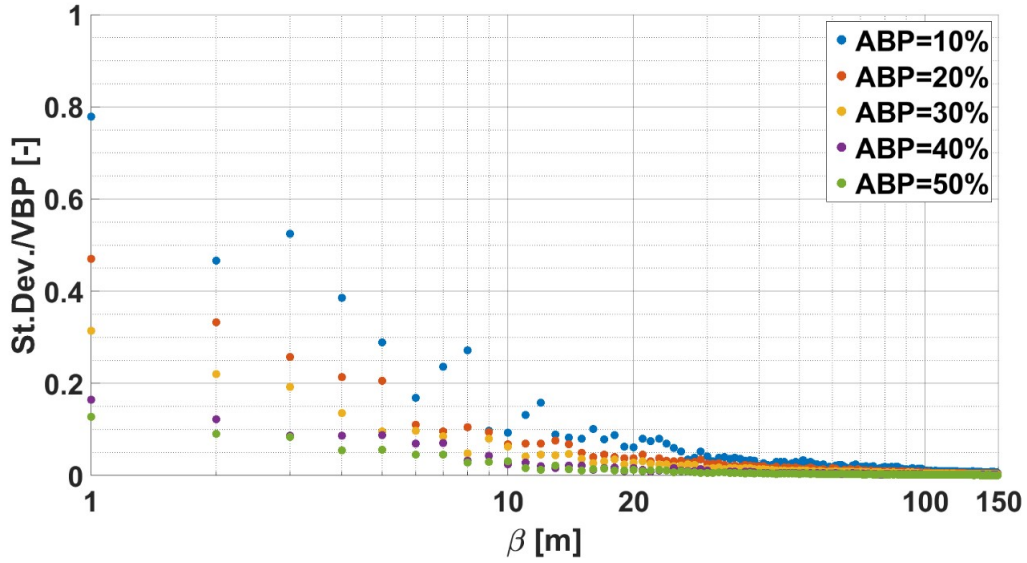


Figure 4.4: Uncertainty in the VBP estimate from 2D measurements, as a function of the total investigation surface (expressed as multiples, $\beta$, of the $A_c$) and block contents measured (ABP) (Napoli et al. 2020b).

From the results of Figure 4.4 it is apparent that the UF stabilises and tends asymptotically to zero for $\beta$ greater than about 10 for VBPs from 30% to 50%, and for $\beta$ greater than about 20 for lower VBPs (10% and 20%). Consequently, particular attention was focused on the uncertainty related to $\beta$ values from 1 up to 20. This choice was also based on the potential difficulty of having a clear outcrop corresponding to $\beta > 20$ since, as shown in Table 4.1, this condition may require very large survey areas.

| Outcrop surfaces, $\beta \mathbf{A}_c$ [m²] | | | | | |
|---|---|---|---|---|---|
| **Typical engineering works and functions** | **Characteristic engineering dimension, $\mathbf{L}_c$ [m]** | $\beta{=}1$ | $\beta{=}20$ | $\beta{=}50$ | $\beta{=}150$ |
| Microtunnel (e.g., water) | 3 (diameter) | 7 | 141 | 353 | 1060 |
| Tunnel (e.g., light rail) | 6.5 (diameter) | 33 | 663 | 1658 | 4975 |
| Tunnel (e.g., highway) | 15 (diameter) | 176 | 3533 | 8831 | 26494 |
| Landslide | 30 (slope high) | 900 | 18000 | 45000 | 135000 |

Table 4.1: Examples of typical engineering works and related characteristic engineering dimensions, $L_c$. Outcrop surfaces corresponding to $\beta A_c$, with $\beta$ equal to 1 (i.e. engineering characteristic area), 20, 50 and 150 are given by way of example (Napoli et al. 2020b).

Similarly to Medley's findings, a logarithmic law approximated the results obtained in Figure 4.4 well, and assumed a linear formulation on the semi-logarithmic plot of Figure 4.5 (see Table 4.2).
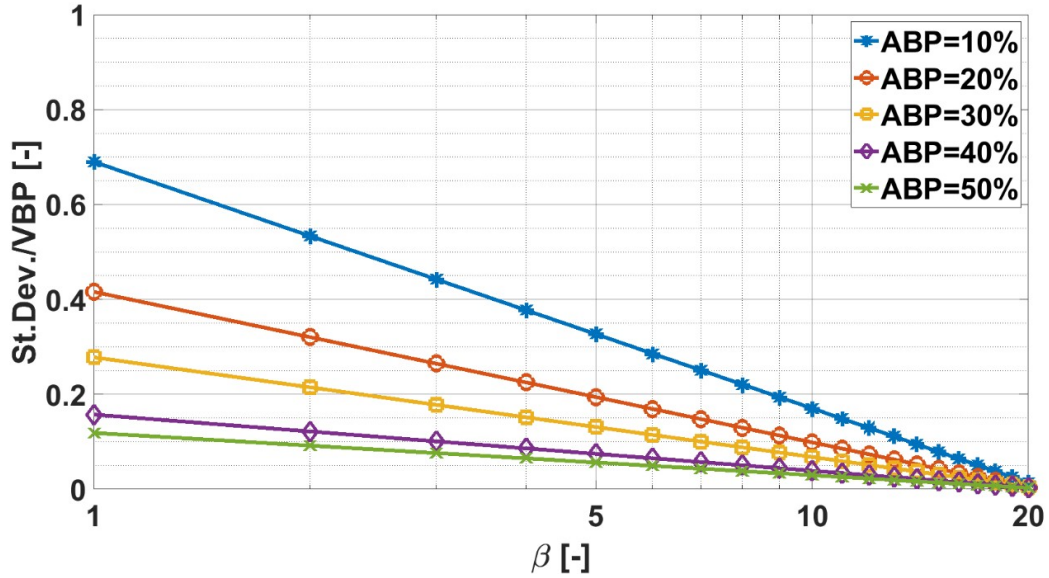


Figure 4.5: Linear fitting of uncertainty factors, for $\beta$ values in the range [0; 20], on the semi-logarithmic plot (Napoli et al. 2020b).

| VBP [%] | Fitting equation [β=1;20] | R² [-] | UF$_{min}$ [-] | UF$_{max}$ [-] |
|---------|---------------------------|--------|----------------|----------------|
| 10 | UF=-0.226·ln(β)+0.690 | 0.911 | 0.014 | 0.690 |
| 20 | UF=-0.137·ln(β)+0.416 | 0.940 | 0.003 | 0.416 |
| 30 | UF=-0.091·ln(β)+0.278 | 0.937 | 0.005 | 0.278 |
| 40 | UF=-0.051·ln(β)+0.157 | 0.951 | 0.003 | 0.157 |
| 50 | UF=-0.039·ln(β)+0.119 | 0.960 | 0.003 | 0.119 |

Table 4.2: Linear fitting parameters (Napoli et al. 2020b).

The chart shown in Figure 4.5 can be used as a design guide to adjust the 2D measurements and obtain a range of VBPs which should represent the actual 3D block content.

For example, if an ABP=30% (i.e. the yellow line in Figure 4.5) is obtained from an outcrop four times larger than the $A_c$ (i.e. $\beta = 4$), the UF is equal to 0.15 and the VBP can be computed as:

$$VBP = ABP \pm UF \cdot ABP = 30 \pm 0.15 \cdot 30 = (25.5 \div 34.5) \qquad (4.2)$$

If an ABP value different from those in Figure 4.5 is obtained (e.g., 35%ABP), an interpolation between the lines available (e.g., 30% and 40%) can be made, as was the case in (Medley 2001). However, if the ABP measured is greater than 50% or lower than 10% the interpolation cannot be made. In fact, it is not possible to accurately predict the UF if the ABP is not within the range analyzed.

Finally, as suggested by (Medley 1997, Medley and Zekkos 2011), the UF should be applied to make prudent and conservative estimates of the corrected block content, depending on the problem at hand. For example, the smallest VBP value of the range obtained should be used if the strength parameters of a bimrock are to be determined. On the other hand, if the VBP is estimated to choose the excavation equipment or to design the cutterhead for a tunnelling project, the highest VBP should be considered. In this way, the engineer will err on the side of safety (Napoli et al. 2020b).

### 4.1.3 Comparison between uncertainties obtained from 1D and 2D measurements

The uncertainty in the estimation of the VBP obtained through this novel approach was compared with that proposed by Medley (Medley 1997, Medley 2001), related to the use of 1D measurements (i.e. borehole drillings) and illustrated in Section 2.1.4.1.

The statistical analysis described in the previous Section 4.1.2 was performed again to determine the UF as a function of $\beta$ for a new 32% VBP model. This block content was chosen since it is one of the VBPs included in the chart provided by Medley

(2001). The result obtained is shown in Figure 4.6.
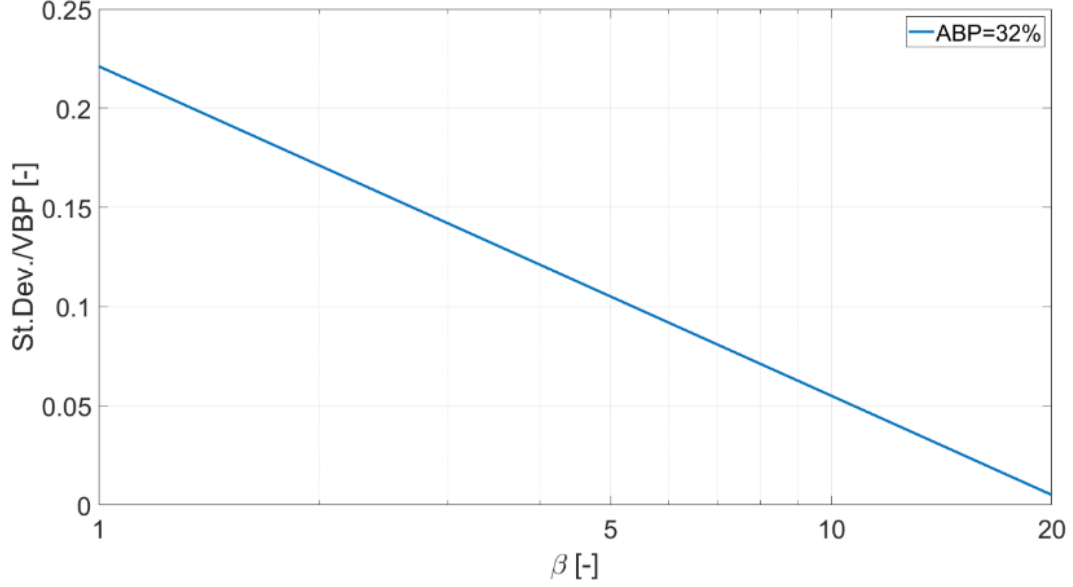


Figure 4.6: UF from 2D measurements of a bimrock model with VBP=32%, as a function of the total investigation area, expressed as a multiple $\beta$ of $A_c$ (Napoli et al. 2020b).

To perform the comparison, first an acceptable UF, from an engineering point of view, was chosen. Then, the relative amount of sampling length, $L_{req}$ (i.e. $d_{max} \cdot N d_{max}$), from Medley's approach, and the outcrop investigation area, $A_{req}$ (i.e. $\beta \cdot A_c$) from this new statistical approach were determined. Specifically, an UF equal to 0.1 was selected. Using this value and intersecting the 32%ABP lines shown in Medley's chart (Figure 2.12) and in Figure 4.6, the multiplicative coefficients N$d_{max}$ = 25.2 (i.e. a total length of drilling $L_{req} = 25.2 \cdot d_{max}$) and $\beta = 5.3$ (i.e. an outcrop area $A_{req} = 5.3 \cdot A_c$) were obtained, respectively.

The total perforation length, $L_{req}$, and the outcrop area, $A_{req}$, corresponding to this result are listed in Table 4.3 for different characteristic engineering dimensions, $L_c$. In fact, both the $A_c$ and $d_{max}$ values depend on the $L_c$, since the area of engineering interest and the maximum block size can be computed as $A_c = L_c^2$ and $d_{max} = 0.75 \cdot L_c$, respectively.

To better compare the results, the outcrop considered in the 2D approach was assumed to be square shaped. In this way, its side, named $L^*$, could be easily calculated as the square root of $A_{req}$ and compared to $L_{req}$.

| Typical engineering works and functions | $L_c$ [m] | Medley's 1D approach results $Nd_{max} = 25.2$ for UF = 0.1 | | New 2D approach results $\beta = 5.3$ for UF = 0.1 | | |
|---|---|---|---|---|---|---|
| | | $d_{max} = 0.75 \cdot L_c$ [m] | $L_{req} = d_{max} \cdot Nd_{max}$ [m] | $A_c = L_c^2$ [m²] | $A_{req} = \beta \cdot A_c$ [m²] | $L^* = \sqrt{A_{req}}$ [m] |
| Microtunnel (e.g., water) | 3 | 2.3 | 56.7 | 9 | 48 | 6.9 |
| Tunnel (e.g., light rail) | 6.5 | 4.9 | 122.9 | 42 | 224 | 15.0 |
| Tunnel (e.g., highway) | 15 | 11.3 | 283.5 | 225 | 1193 | 34.5 |
| Small landslide | 20 | 15.0 | 378.0 | 400 | 2120 | 46.0 |
| Landslide | 30 | 22.5 | 567.0 | 900 | 4770 | 69.1 |

Table 4.3: Outcrop areas and total perforation lengths, $L_{req}$, required to obtain an UF=0.1, when a 32%VBP bimrock and different $L_c$ values are considered (L* is the side length of an equivalent square shaped outcrop with area equal to $A_{req}$).

From Table 4.3 it can be observed that L* is significantly lower than $L_{req}$, which means that 2D measurements are far less onerous than 1D measurements. This outcome highlights the potential of the procedure developed in this research and confirms that the graph in Figure 4.5 represents a valuable tool to get reliable estimates of the VBP from on-site ABP measurements.

## 4.2 An approach to predict the probability of encountering rock blocks when tunneling in heterogeneous ground

Unexpected and expensive difficulties can arise when tunneling in heterogeneous ground due to the mixed-face conditions. The content, lithology, location, strength and abrasivity of strong cobbles and boulders can induce severe technical problems at the heading, mucking system and/or excavation chamber of a TBM, as well as safety risks, schedule delays and extra costs (Medley 2007b, Tarkoy 2008, Hunt and Del Nero 2010). These tunneling risks typically increase if rock blocks are (i) larger than given critical values (Figure 4.7), (ii) located near the tunnel perimeter or (iii) only partially embedded within the tunnel face (Frank and Chapman 2005, DiPonio et al. 2007, Hunt and Del Nero 2010, Hunt and Del Nero 2010, Gwildis et al. 2018).
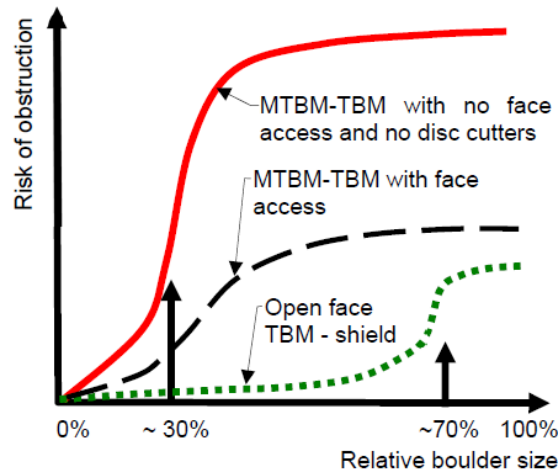
Figure 4.7: Risk of tunnel advance being obstructed increases with relative boulder size (Hunt 2017).
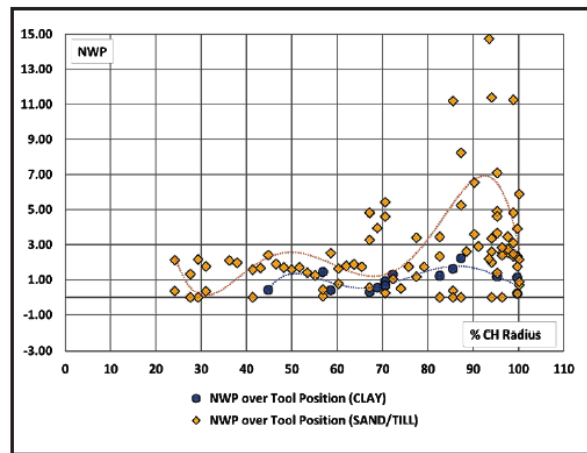


Figure 4.8: Normalized tool wear (NWP, on the y-axis) over cutterhead radius (% CH radius, on the x-axis) (Gwildis et al. 2018). The maximum tool wear is registered at distal tool positions, where the travel speed and impact forces are high in comparison with other tool positions.

Large blocks that extend past the perimeter of the tunnel (i.e. protruding rock blocks) are difficult to cut and more likely to be plucked or pushed aside. Consequently, they may cause significant settlements, mucking system damage, obstructions, boring machine stuck or lining damage due to high contact stresses at the cutterhead-ground interface. Protruding blocks can also produce excessive torque and thrust demand and significant wear (or even breakage) of the cutterhead tools (Figure 4.8), with consequent lower cutting efficiency, more frequent cutter change

117

intervention intervals, safety risks and higher costs (Frank and Chapman 2005, DiPonio et al. 2007, Hunt and Del Nero 2010, Gwildis et al. 2018).

In order to limit and manage the risks associated with the presence of rock inclusions when tunneling in block-in-matrix formations, the block content, frequency and size of the rock inclusions must be properly predicted.

To this aim, a Matlab code implementing a statistical approach was developed. The code, named PBE, allows the probability of encountering blocks of variable sizes to be estimated when the area of intersection with the tunnel face is greater than given critical values. The blocks considered in the analysis can be partially or totally contained within both the whole excavation area and the lateral extremities of the tunnel.

The results obtained by the application of the PBE code could contribute to identifying and reducing the risks of tunneling in heterogeneous ground and to choosing the most appropriate TBM type, including face access, cutterhead design (i.e. shape, opening size, etc.), cutter types and machine power (i.e. torque, thrust and speed).

### 4.2.1 The PBE code

In order to take into account the spatial and dimensional variability inherent in heterogeneous formations, a specific Matlab routine, performing Monte Carlo simulations, was implemented and the executable free code was given in Napoli et al. 2020a. The code, named PBE, creates a great number of heterogeneous ground configurations. An example is given in Figure 4.9.
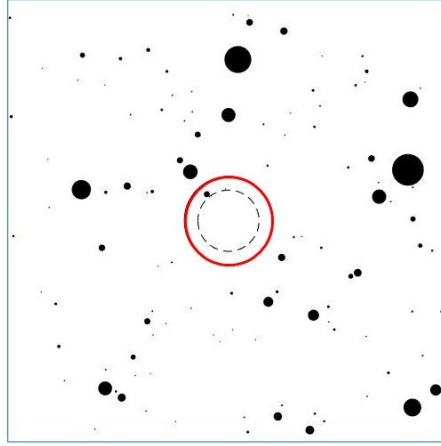


Figure 4.9: An example of a tunnel configuration in a block-in-matrix formation with a VBP equal to 2%. The length of the control area was set at 5 times greater than the tunnel diameter, indicated with the red circle. The dotted line indicates the inner boundary of the tunnel sub-area, where blocks are more difficult to cut and may cause severe impacts, such as higher tool wear (Napoli et al. 2020a).

As shown in Figure 4.9, each configuration is composed of circular blocks with variable sizes. The blocks are located according to a (statistical) uniform distribution within a rectangular control area containing the tunnel geometry. The dimensions of the control area, as well as the radius of the tunnel, can be set each time by the user. To guarantee that the control area is representative of the in-situ geologic conditions, a ratio of at least 5 between the side of the control area and the tunnel diameter is suggested.

The tunnel has a circular cross section and can be located anywhere within the control area by defining the coordinates of its center. In this way, if only a part of the tunnel section is constituted by heterogeneous ground, the tunnel can be moved outwards with respect to the control area so as to locate the homogeneous part outside the control area. For example, as shown in Figure 4.10, if a bimsoil is expected to be present only in half of the tunnel section, the center of the tunnel can be positioned on one control area boundary.
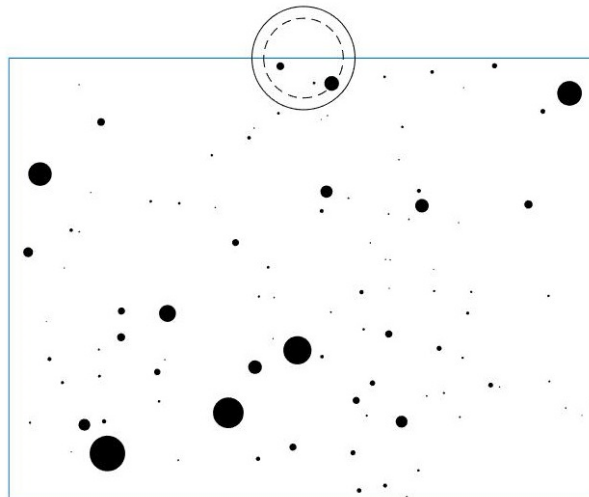


Figure 4.10: An example of a tunnel partially located outside the rectangular control area, to simulate different geologic units being present in a tunnel section.

For the estimation of the probability of encountering rock blocks at the lateral distance furthest from the center of the tunnel, the thickness of an internal circular crown must be defined. This parameter represents the distance of the inner boundary of the circular crown from the tunnel perimeter, and corresponds to the dotted line in Figures 4.9 and 4.10.

As illustrated in Section 3.1, the PBE randomly extracts n block diameters (d) from a population distributed according to a truncated negative power law, whose cumulative distribution function is shown in Eq. (3.1), until the block content requested as input is achieved. To assess the characteristics of the ground (i.e. block content, minimum and maximum block size, etc.) different approaches can be used:

- careful geologic and subsurface investigations (e.g., geologic maps, geophysical methods, large diameter borings and/or boulder volume surveys);

- semi-empirical correlations of geologic and volumetric data from test pits or previous excavation works in nearby areas (if they have the same geologic characteristics);

- the application of the uncertainty factors proposed in the previous Section 4.1.1 or by Medley (Medley 1997) for 2D or 1D measurements, respectively.

For each configuration generated, the code identifies all the blocks that are either entirely or partially contained within the tunnel section, and computes their number and area of intersection. Then, the PBE checks that the intersection area of each block is greater than a threshold user-defined value. This value, $A_{thr1}$, corresponds to the minimum block size deemed a possible cause of technical problems (i.e. obstruction, tools damage, etc.). Hence, the code discards from the subsequent analyses all the blocks with an intersection area smaller than $A_{thr1}$ (Figure 4.11).
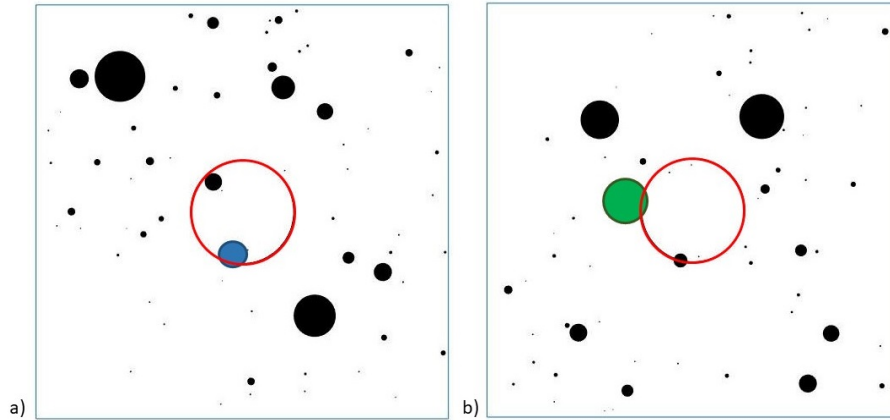


Figure 4.11: Two tunnel configurations with a protruding block: a) the protruding blue block has an intersection area greater than the threshold value, $A_{thr1}$. The code classifies it as a possible cause of obstruction; b) the large protruding green block has an intersection area smaller than the threshold value, $A_{thr1}$. Since it does not represent a possible cause of obstruction or other technical problems, the code discards it from the subsequent analyses. (Napoli et al. 2020a).

In order to estimate the probability of encountering blocks of different dimensions, six size classes of intersecting rock blocks (i.e. six equivalent clast areas) can be set by the user. The lowest limit of the smallest class corresponds to $A_{thr1}$.
Finally, among the other results, the PBE returns the probability that a certain number, n, of rock blocks (with $n = 0, 1, 2, ..., 10, > 10$) belonging to each size class can be encountered during the underground excavation. This probability is

computed as the ratio between the number of configurations in which n blocks of each size class were found and the total number of simulations performed.
The potential of this tool is discussed in the next Section 4.2.2, where an application example is presented.

## 4.2.2 The PBE code: an application example

In order to show the validity of the PBE code, the excavation of a circular tunnel in a block-in-matrix formation was simulated. The input variables required by the PBE code are listed and described in detail in Table 4.4.

| Input parameters | | | |
|---|---|---|---|
| **Parameter** | | **Variable** | **Assigned value** |
| Length of the control area | [m] | B | 65 |
| Height of the control area | [m] | H | 65 |
| Tunnel radius | [m] | R_t | 3.25 |
| Tunnel x-y coordinates | [m] | coord_t | 32.5; 32.5 |
| Threshold area class 1 (Equivalent diameter 0.15 m) | [m²] | A_thr1 | 0.0177 |
| Threshold area class 2 (Equivalent diameter 0.3 m) | [m²] | A_thr2 | 0.0707 |
| Threshold area class 3 (Equivalent diameter 0.5 m) | [m²] | A_thr3 | 0.1963 |
| Threshold area class 4 (Equivalent diameter 0.75 m) | [m²] | A_thr4 | 0.4418 |
| Threshold area class 5 (Equivalent diameter 1 m) | [m²] | A_thr5 | 0.7854 |
| Threshold area class 6 (Equivalent diameter 1.5 cm) | [m²] | A_thr6 | 1.7663 |
| Block content | [-] | BC | 0.02 |
| Minimum expected clast dimension | [m] | a | 0.075 |
| Maximum expected clast dimension | [m] | b | 3 |
| Fractal dimension | [-] | D | -1.75 |
| Number of configurations to generate | [-] | z | 100 |

Table 4.4: Input parameters of the PBE code (Napoli et al. 2020a).

The values assigned in this example to the 16 input parameters are set as default values in the executable code but can be easily modified by the user. As mentioned above, the $A_{thr1}$ parameter corresponds to the minimum block dimension deemed a possible cause of technical problems (i.e. the minimum requested intersection area). To define its default value, according to suggestions from the literature (Frank and

Chapman 2005), an equivalent circular block fully enclosed in the tunnel with a diameter of 15 cm was considered. Hence, $A_{thr1}$ was set as equal to 177 $cm^2$. The other threshold areas listed in Table 4.4 ($A_{thr2}$, $A_{thr3}$, ..., $A_{thr6}$) define 6 size classes, which include circular blocks fully enclosed in the tunnel with an equivalent diameter of:

- class 1: 15-30 cm (i.e. an area in the range 177-707 $cm^2$);

- class 2: 30-50 cm (i.e. an area in the range 707-1963 $cm^2$);

- class 3: 50-75 cm (i.e. an area in the range 1963-4418 $cm^2$);

- class 4: 75-100 cm (i.e. an area in the range 4418-7854 $cm^2$);

- class 5: 100-150 cm (i.e. an area in the range 7854-17663 $cm^2$);

- class 6: >150 cm (i.e. an area > 17663 $cm^2$).

As mentioned above, all the blocks with an intersecting area smaller than $A_{thr1}$ (i.e. 177 $cm^2$, corresponding to an equivalent circular block with a diameter of 15 cm) are discarded from the subsequent analyses.

In this example, 500 simulations were requested. However, since the computation only takes a few minutes, many more configurations can easily be set and obtained. 5 of the 500 configurations generated in the example are illustrated in Figure 4.12, while the probability of encountering n intersecting blocks greater than $A_{thr1}$ both within the tunnel and at the lateral distance furthest from the center of the tunnel section (i.e. inside the circular crown) is given in Table 4.5.
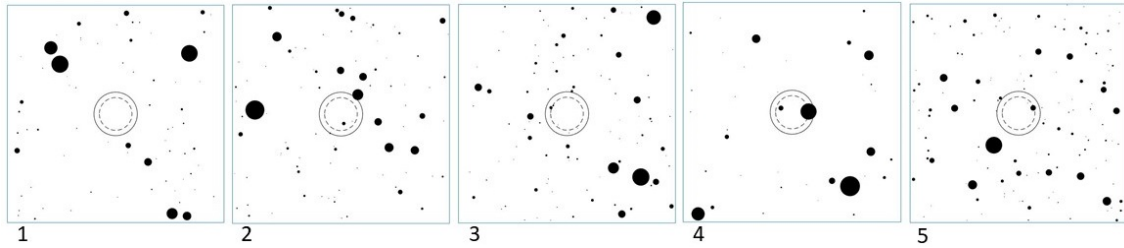


Figure 4.12: Five of the 500 configurations with 2% BC generated with the Matlab code. The tunnel (6.5 m diameter) is represented by the external circle, while the dotted line represents the limit of the tunnel sub-area (i.e. circular crown), whose thickness is chosen equal to about 0.25 times the tunnel radius.

TUNNEL

| Equivalent clast diameter [m] | P 0blocks [%] | P 1blocks [%] | P 2blocks [%] | P 3blocks [%] | P 4blocks [%] | P 5blocks [%] | P 6blocks [%] | P ≥7blocks [%] | Average number of blocks |
|---|---|---|---|---|---|---|---|---|---|
| 0.15-0.30 | 49.4 | 31.4 | 13.8 | 4.4 | 0.8 | 0 | 0.2 | 0 | 0.77 |
| 0.30-0.50 | 67.4 | 27.8 | 4.0 | 0.6 | 0.2 | 0 | 0 | 0 | 0.38 |
| 0.50-0.75 | 79.0 | 19.4 | 1.4 | 0.2 | 0 | 0 | 0 | 0 | 0.23 |
| 0.75-1.0 | 86.6 | 13.0 | 0.2 | 0.2 | 0 | 0 | 0 | 0 | 0.14 |
| 1.0-1.5 | 84.4 | 15.4 | 0.2 | 0 | 0 | 0 | 0 | 0 | 0.16 |
| >1.5 | 90.8 | 8.2 | 1 | 0 | 0 | 0 | 0 | 0 | 0.10 |

CIRCULAR CROWN

| Equivalent clast diameter [m] | P 0blocks [%] | P 1blocks [%] | P 2blocks [%] | P 3blocks [%] | P 4blocks [%] | P 5blocks [%] | P 6blocks [%] | P ≥7blocks [%] | Average number of blocks |
|---|---|---|---|---|---|---|---|---|---|
| 0.15-0.30 | 65.4 | 27.8 | 5.8 | 0.8 | 0.2 | 0 | 0 | 0 | 0.43 |
| 0.30-0.50 | 77.6 | 20.4 | 2.0 | 0 | 0 | 0 | 0 | 0 | 0.24 |
| 0.50-0.75 | 87.4 | 12.0 | 0.6 | 0 | 0 | 0 | 0 | 0 | 0.13 |
| 0.75-1.0 | 93.6 | 6.4 | 0 | 0 | 0 | 0 | 0 | 0 | 0.06 |
| 1.0-1.5 | 86.6 | 13.0 | 0.4 | 0 | 0 | 0 | 0 | 0 | 0.14 |
| >1.5 | 97.6 | 2.4 | 0 | 0 | 0 | 0 | 0 | 0 | 0.02 |

Table 4.5: Probability, P, of encountering n blocks (with n from zero to more than 7) with an intersection area greater than the threshold value $A_{thr1}$, equal to 0.0177 $m^2$. The average number of blocks corresponding to each equivalent clast size is also indicated. The results are related to the entire tunnel section (table above) and to the circular crown (table below). These results are contained in the output text files "*Probability*" and "*Average_N*" of Table 4.6 (Napoli et al. 2020a).

What stands out from this output is the high probability, $P_{0blocks}$, of encountering 0 rock blocks, particularly for smaller clast sizes. In fact, $P_{0blocks}$ is almost always greater than 65%. This result is due to the low BC setting (i.e. 2%). This particularly low block quantity was used to simulate a glacial deposit, where a BC < 2% was found in the majority of tunneling projects documented (Hunt 2017). This low BC produced a great number of configurations without blocks inside the tunnel (e.g., configuration 1 of Figure 4.12). Moreover, there is a very low probability of encountering more than 4 blocks during the tunnel excavation, while no configuration has more than 6 intersecting blocks (i.e. $P_{TUNNEL\_n \geq 7blocks} = 0$).

From Table 4.5 it is also evident that, for a given clast size, the probability of encountering a lower number of blocks is higher than (or at least equal to) the

probability of encountering more blocks (e.g., $P_{1block} \geq P_{2blocks}$), whether the entire tunnel face or a part of it (i.e. the circular crown) is examined.

Moreover, for a given number n of blocks, with $n \geq 1$, the highest probability is obtained for the smallest clast dimension.

Finally, as expected, the probabilities of encountering blocks in the circular crown are much lower than those related to the entire tunnel section, and no configuration has more than 4 blocks (i.e. $P_{CIRCULARCROWN\_n \geq 5blocks} = 0$).

All the outputs generated by the code are listed and described in Table 4.6.

| Output parameters | | |
|---|---|---|
| **Parameter** | | **Output file name** |
| Total number of intersecting blocks | [-] | Total_IB.txt * |
| Total intersection area | [m²] | A_int.txt * |
| Total number of intersecting blocks greater than the threshold value, A_thr1 | [-] | N_crit_IB.txt * |
| Intersection area of all the blocks greater than the threshold value | [m²] | A_int_cr.txt * |
| Probability of finding n intersecting blocks greater than the threshold value during the excavation | | Probability.txt * |
| Average number of intersecting blocks greater than the threshold value during the excavation | [-] | Average_N.txt * |
| Graphical representation of the cumulative distribution function F(d)-d | [-] | CDF.JPG |
| Graphical representation of the configurations generated | [-] | Configuration 1 up to z.JPG |
| List of input variables and values assigned | [-] | Info_viewer.txt |

Table 4.6: Outputs of the PBE code. The output files with the "*" contain the results related to both the entire tunnel section and the circular crown (modified from Napoli et al. 2020a).

It is important to underline that uncertainties will always exist in the determination of some of the input parameters of the PBE code, such as a, b and D but above all the block content, BC. Hence, more than a single value may be considered for each parameter and a number of analyses can anyway be performed in a very short time. In this way, by averaging the results, more reliable statistically-based estimates can be obtained.

However, since a limitation of the current study is that only circular blocks are taken into account, further research could usefully be conducted to modify the code so as to allow different block shapes (e.g., elliptical blocks) to be generated.

# Chapter 5

# The Oltrepò Pavese complex formation

The major goal of this research is to explore and address the challenges of working with complex geomaterials with a block-in-matrix fabric, and to gain a better understanding of the problems associated with their characterization and modelling in order to provide possible solutions to overcome these challenges.

To this end, a complex formation with a block-in-matrix fabric located in the north of Italy, near Pavia, in the hilly area of the Oltrepò Pavese (Figure 5.1 and Figure 5.2) was chosen to analyze the mechanical behaviour of a typical Italian block-in-matrix material with an experimental approach. This geomaterial was selected out of the many Italian complex formations (e.g. Ligurian accretionary complex, Argille scagliose, Argille varicolori, Sicilide and Liguride units, Flysch Rosso at the base of the Molise unit, etc.) because it is one of the most widespread in the Northern and Southern Apennines of Italy.



Figure 5.1: The Oltrepò Pavese hilly area (Pavia, Italy).
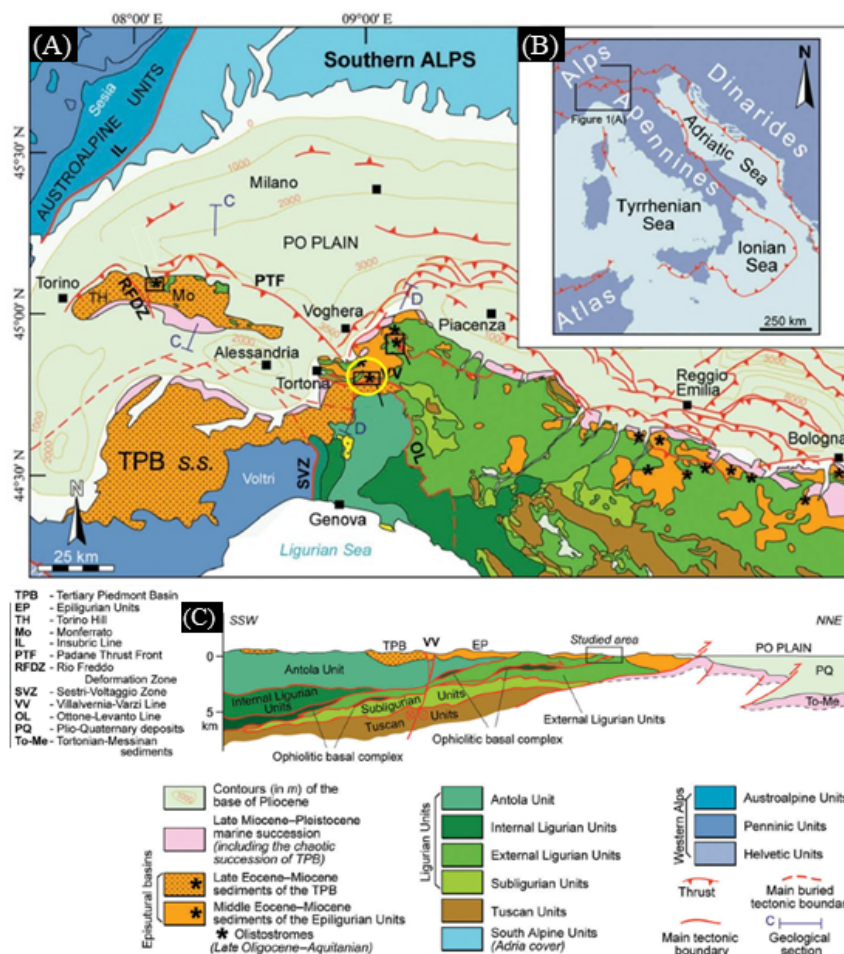
Figure 5.2: A) Structural sketch map of the Northern Appennines showing the location of the area under study, highlighted with the yellow circle. B) Location of Figure A. C) Geologic cross-section of the area under study (modified from Festa et al. 2015).

More in detail, the complex formation under study is a sedimentary melange, known as Val Tiepido Canossa melange, up to 180-200 m in thickness, presenting a chaotic block-in-matrix fabric (Figure 5.3a), which results from the stacking of different Late Oligocene - Early Miocene cohesive submarine debris flow. Each debris flow ranges from meters to tens of meters in thickness and is internally characterized by an inverse grading of the larger blocks. As shown in Figure 5.3b, each stratigraphic layer is composed of rock inclusions characterized by an inverse grading of the largest blocks above a basal shear zone 5-10 cm thick (Festa et al. 2015). Specifically, the rock blocks are mainly limestone, marly limestone and calcarenite

and have variable dimensions, varying from centimeters to a few meters, and irregular to subangular shapes. They are randomly located within a clayey-marly matrix, which is characterized by a brecciated (i.e. clastic) fabric (Festa et al. 2015).

In dry conditions the melange can be assimilated to a weak rock and it looks like a *bimrock*. However, it is very sensitive to water so as it transforms into a *bimsoil* as it gets in contact with water because the matrix is actually an overconsolidated soil. Hence, according to the new classification proposed in this research (see 1.4 and 1.19), this geomaterial can be classified as a *soft bimrock*. The characteristic of water sensitivity made the collection and preparation of intact specimens for laboratory testing an extremely complex task, as illustrated in detail in Section 5.1.
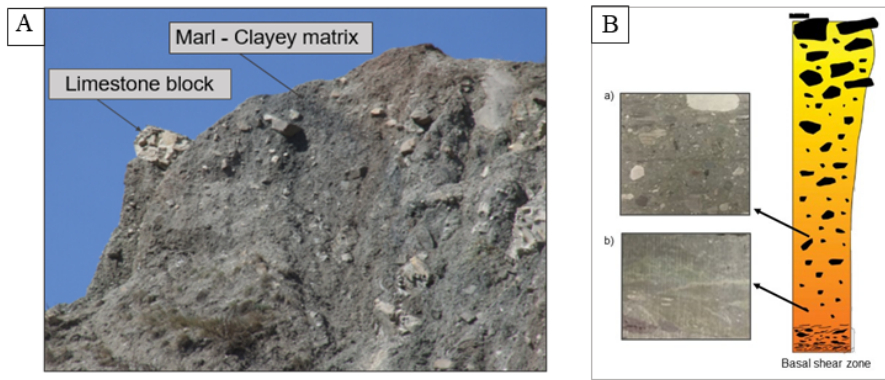


Figure 5.3: A) an outcrop of the sedimentary melange of the Oltrepò Pavese; B) conceptual stratigraphic column of a single melange layer, modified after (Festa et al. 2015): a) heterogeneous melange with blocks of mainly tabular shape, with dimensions gradually decreasing downwards; b) matrix-only melange located near the basal shear zone.

## 5.1 Collection of melange specimens

The weak nature of the marly matrix of the melange and its sensitivity to water, as well as the presence of the stronger blocks, made the collection and preparation of regular and intact specimens to be tested in lab extremely difficult and a time consuming operation. In fact, standard coring was not possible without damaging the material. Moreover, there were no construction sites in that area, so no digger was available to collect the samples. As a consequence, a diamond core drill was initially used in an attempt to extract intact cores of melange (Figure 5.4a). However, although a good and stable drilling hole was obtained (Figure 5.4b), the material jammed into the sampler and it was impossible to remove the core from

127

the drill bit without destroying it (a hammer had to be used to break it).
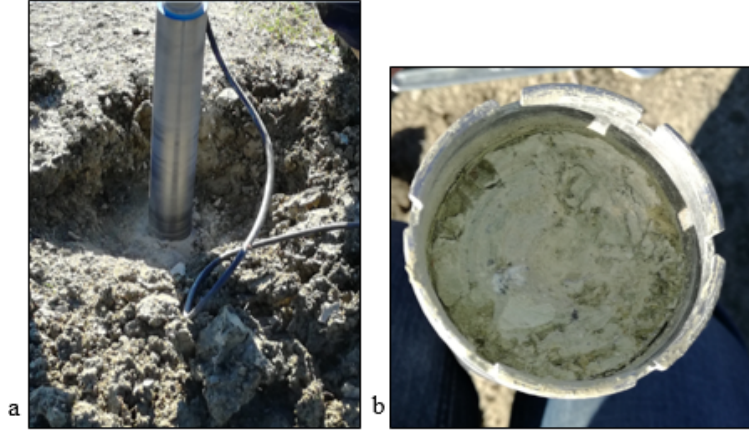


Figure 5.4: a) the diamond core drill used to extract intact core specimens; b) the core get stuck in the drill bit.

Hence, a manual coring was necessary. This required good weather situations, which resulted in a first inspection on November 2017 while the second was possible only on April 2018, due to the intense rainfalls. The samples were extracted with hammers, picks and chisels from about 0.4 m beneath the surface of the outcrops. This trick was adopted in order to remove the superficial weathered strata and obtain intact melange blocks.

The weak nature of the marl as well as the many micro fractures present within the material caused the split of a great number of blocks during the sampling. However, a sufficient number of irregular samples was collected, wrapped and transported to the geotechnical laboratory operating in the Department of Structural, Geotechnical and Building Engineering of Politecnico di Torino.

Figure 5.5 shows a homogeneous melange outcrop where the position of a sample extracted manually is highlighted with the red line, while Figure 5.6 shows three irregular lumps collected: a matrix-only (homogeneous) sample (Figure 5.6a) and two block-in-matrix (heterogeneous) samples (Figures 5.6b and c). The samples were taken on purpose at different depths of the outcrop in order to investigate the characteristics of both the heterogeneous and matrix-only material. In fact, as already discussed above, the melange under study has a repetitive stratigraphy characterized by an inverse grading of largest blocks within each single debris flow.

Figure 5.5: A melange outcrop with the indication (the red line) of the location of an irregular sample extracted manually.
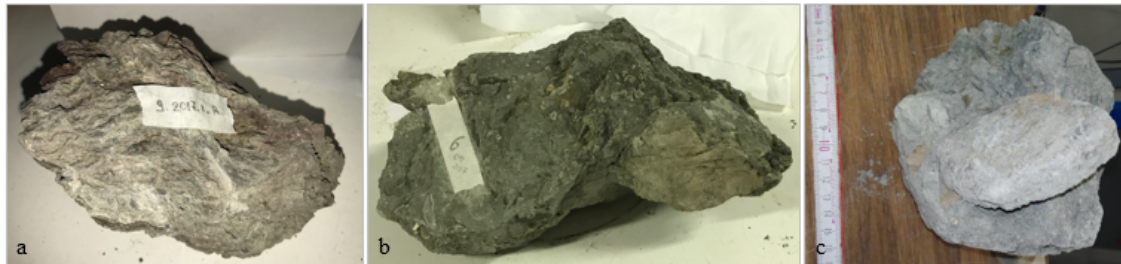


Figure 5.6: Irregular samples: a) matrix-only melange specimen (about 25x15x14 cm); b) heterogeneous melange specimen (about 32x20x15 cm); c) heterogeneous melange specimen (about 22x14x14 cm) with a big rock inclusion.

The heterogeneous lumps were collected at depths at which the samples contained sufficiently small rock blocks to perform laboratory tests with standard equipments. In this way, (i) the strength of the matrix could be evaluated and compared to that of the heterogeneous material and (ii) possible differences in the mechanical behavior of the homogeneous and heterogeneous geomaterials, e.g. failure surfaces, could be investigated.

## 5.2 Preparation of regular samples for laboratory tests

The presence of the clay in the matrix made it extremely problematic to obtain regular specimens to be tested in the laboratory since no standard techniques (like core drillings, oil circular saw or water circular saw) could be used without irreversibly damaging the material. Hence, the following alternative techniques were evaluated:

- the use of a dry circular saw (Figure 5.7a), which could have only produced prismatic (and not cylindrical) specimens, with the limit that some laboratory tests, such as oedometric and triaxial tests, could have not been performed. This technique was applied but it failed, since the trial sample was heavily damaged. Many fractures and block detachments were produced during the cutting phases, due to the vibrations of the machine, as shown in Figure 5.7b;
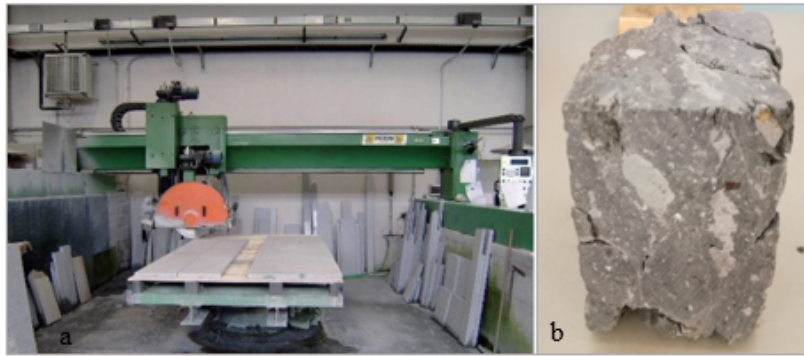


Figure 5.7: The dry circular saw used to cut some melange blocks (Tomaino S.r.l., Torino).

- the laser techniques. This was just evaluated but not even tested, since the minimum dimensions of the specimens were bigger than 2-3 cm, which was the maximum thickness that the laser could have cut;

- the waterjet techniques, which consists of cutting materials, even steel, with a jet of water of thousands of bars of pressure issueing from a few micron orifice. This technique was applied. However, even this method failed since the block cut was strongly damaged by the jet of water, as shown in Figure 5.8.

Figure 5.8: a) Waterjet cutting machine and irregular melange lump with side dimensions of about 23x18x13 cm; b) the melange after the cut (OMT S.r.l., Leinì, Torino).

Since all these techniques could not be applied, a further attempt was made with a DIY dry cutting machine (DISEG, Politecnico di Torino), which was a diamond band saw with a cutting height of 8 cm (Figure 5.9a). A small trial melange sample was cut, obtaining a very good result since the faces became very smooth and no fractures were produced. In order to check if vibrations could have damaged bigger samples, another irregular melange lump about 30 cm long, 14 cm wide and 10 cm high was cut. The result obtained is shown in Figure 5.9b. Although the cut was again very good, it was not possible to cut even the smaller side of the block because of the too small cutting height.
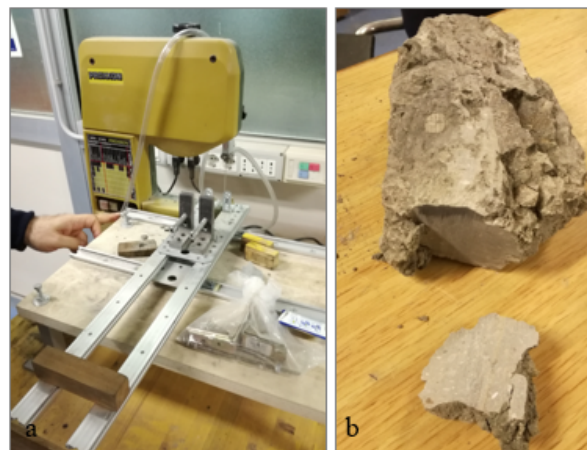


Figure 5.9: a) DIY dry cutting machine; b) an irregular trial melange sample after the cut.

131

Hence, a specific market research was made to find an appropriate diamond band saw, with a sufficient cutting height, weight (to avoid vibrations during the cutting operations) and price. As a result of the research, it was decided to construct the desired diamond band saw buying separately a wood saw and the diamond blade. The saw is the Fervi 0764/455, with a cutting height of 33 cm and a weight of 216 kg. These characteristics were deemed sufficient for the aforementioned cutting operations. The supplied (wood) blade was replaced with a diamond blade (Figure 5.10b) customized by the Italian Turri Technologies S.r.l.. This blade was specifically built for cutting the stronger rock blocks without deforming the softer matrix. The blade rotates at a constant speed while the irregular lump is pushed manually towards the rotating band saw by means of two specially made boards, in order to work in safe conditions (Figure 5.10c).

To contain the dust produced during the cutting, it was also necessary to design and print a plastic element to be connected to a vacuum cleaner (Figure 5.10d).
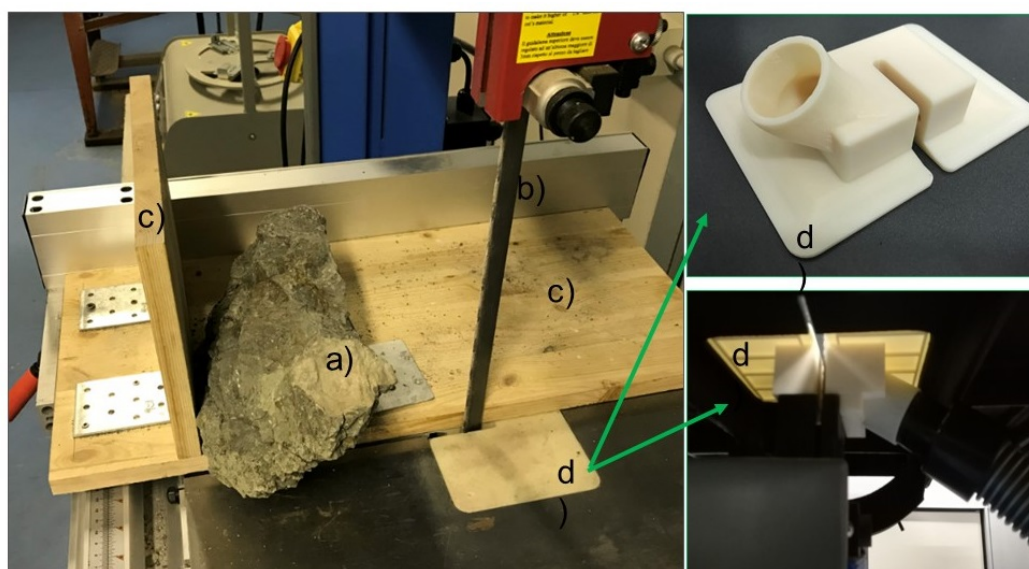


Figure 5.10: Diamond band saw - a)irregular melange lump; b) diamond blade; c) boards; d) plastic element for dust containment assembled on the work table of the Fervi saw and connection between the vacuum cleaner hose.

The first samples cut were not regular enough for laboratory tests. An irregular geometry of the samples was inevitable since it was not possible to hold the shapeless melange lumps still during the cutting operations (Figure 5.11).
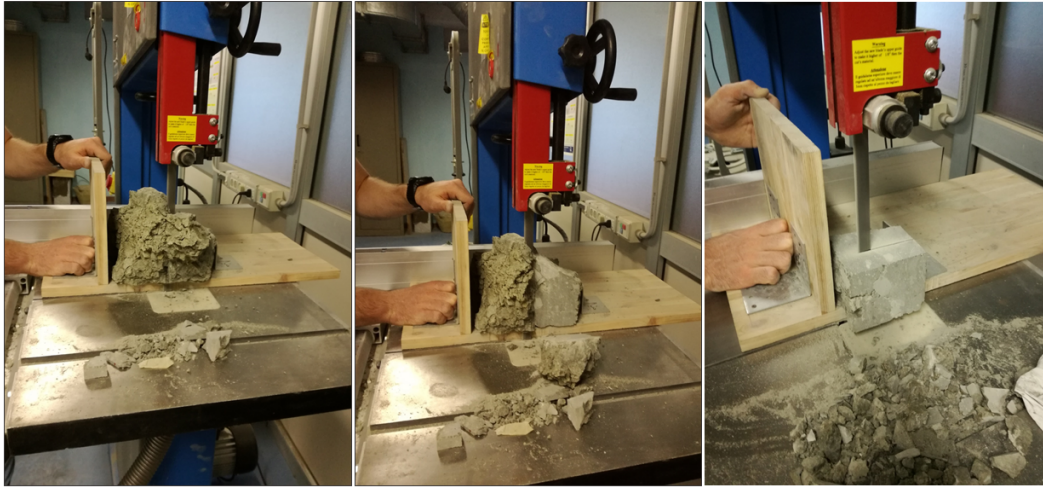
Figure 5.11: The cutting phase of a heterogeneous melange lump.

Hence, to make the blocks more stable, they were incorporated in the paraffin (Figure 5.12a, b). This initial choice was made in order to be able to see the entire irregular blocks and to cut them more efficiently. However, this solution failed because, due to the friction, the paraffin melted and covered the blade (Figure 5.12c), making it impossible to go on cutting. Hence, a mortar was used to incorporate the blocks (Figure 5.12d, e). Plastic bags were also adopted to protect the melange from the grout (i.e. from the water contained in the grout which would have compromised the clayey matrix strength).

With these devices, the sample cuts were easier although far from being simple and flawless. In fact, the presence of innate micro and macro fractures required a great number of cuts before a regular specimen could be obtained. This occurred particularly, but not exclusively, when working with the matrix-only melange samples. In many cases, no regular specimen could be extracted from the original shapeless sample because after several cuts, lasting up to more than two hours, the material was too small or broken.

Figure 5.12: a) An irregular melange specimen in the formwork before the paraffin injection; b) the specimen in the paraffin; c) the melted diamond blade after the first cut; d) irregular melange specimens in the formwork before the mortar injection; e) a melange specimen in the mortar.

Moreover, the calcareous blocks (contained in the heterogeneous specimens) which were found at or very close to the edges of a specimen sometimes detached producing a hole. Consequently, irregular and useless specimens were often obtained. Some examples are given in Figure 5.13. Due to such difficulties, some defects were in any case accepted in the specimens used for laboratory tests (i.e. uniaxial compressive tests). Figure 5.14 shows a matrix-only and a heterogeneous melange specimen, after the cut, which were tested in uniaxial compression (see Section 6.7).
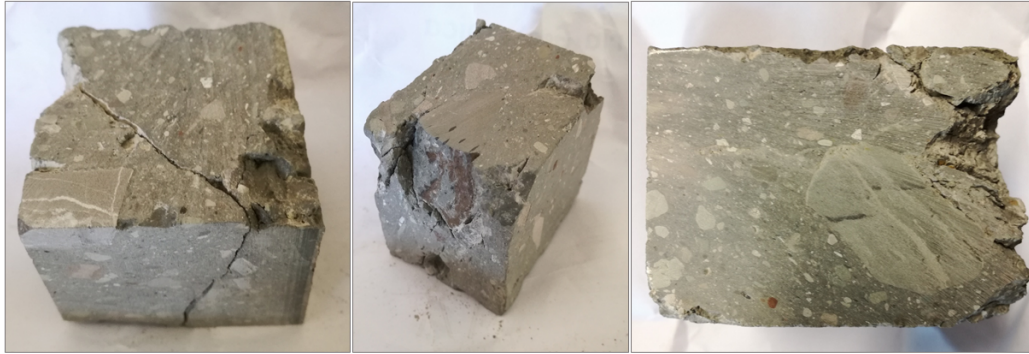
Figure 5.13: Some heterogeneous melange samples damaged during the cutting phase.
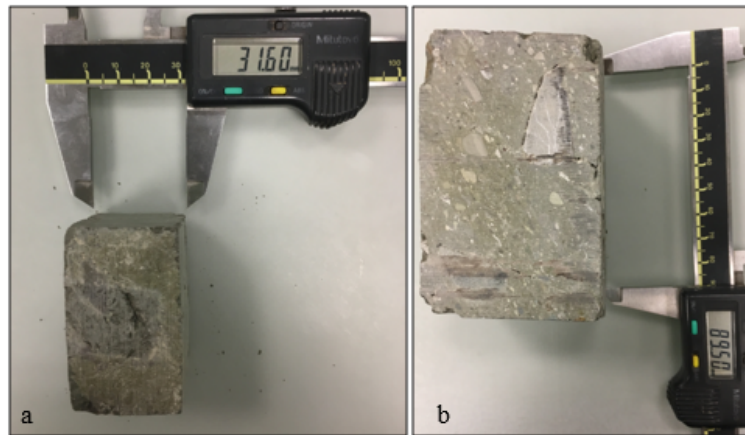


Figure 5.14: a) a matrix-only melange specimen; b) a heterogeneous melange specimen.

# Chapter 6

# Characterization of the Oltrepò Pavese melange

The way rock inclusions affect the overall behavior of bimrocks and bimsoils has long been a question of great interest. In this regard, many laboratory tests have been carried out on different block-in-matrix geomaterials since the 90s. However, research has been conducted almost exclusively on artificial specimens due to both the difficulty of collecting intact samples and the necessity of working under controlled and repeatable conditions (Lindquist 1994b, Sonmez et al. 2006, Akram 2010, Afifipour and Moarefvand 2014c, Afifipour and Moarefvand 2014a, Afifipour and Moarefvand 2014b, Mahdevari and Maarefvand 2016, Li et al. 2016).

In almost all these experimental studies, the matrix was created using Portland cement, which can only simulate the mechanical characteristics of a *hard bimrock*. On the other hand, only a few authors have carried out laboratory tests on real bimrock/bimsoil specimens. Sonmez et al. 2006 performed UC tests on the agglomerate of Ankara and proposed an empirical approach for the determination of the UCS. Kahraman and Alber 2006 performed triaxial and UC tests on fault breccia specimens with rock inclusions weaker than the matrix (i.e. non-conventional bimrock). The specimens tested had different VBPs and dimensions, which were both found to affect the overall strength of the material. Dong et al. 2013b investigated the mechanical properties of the Gibraltar Strait Breccias, consisting of a relatively soft matrix enclosing stronger rock blocks, by using special triaxial tests. The specimens were obtained from offshore drilling during exploratory campaigns for the design of the Gibraltar Strait tunnel.

This Ph.D. research seeks to explore how the presence of blocks may influence the strength and deformability of a *soft bimrock*.

After having presented the efforts made for the collection and preparation of regular samples (ref. Chapter 5), in this chapter all the laboratory tests carried out to investigate the mechanical behavior of the Italian chaotic melange are described in

detail. As previously reported, the Oltrepò Pavese melange is constituted by blocks of different lithologies embedded in a clayey matrix. Specifically, Schmidt hammer tests were carried out on the rock blocks to determine their uniaxial compressive strength. The Atterberg limits and mineralogical analyses were carried out on the loose material to investigate the basic behavior of the clay, composing the matrix, and the mineralogy of its grains. To determine the melange particle sizes, several grading curves were also obtained. Direct shear tests, point load tests and uniaxial compression tests were carried out on the intact heterogeneous material to estimate the strength and deformability of the melange. Finally, ring shear tests were performed on remolded matrix samples to determine its residual strength.

The devices, procedures and results of these tests, as well as their limitations, are described in the following sections.

## 6.1    Schmidt hammer tests

The characterization of the rock blocks composing the melange under study was made using the non-destructive Schmidt hammer test. The Schmidt hammer is a simple and portable device that can be used to classify the hardness (i.e., estimate the uniaxial compressive strength, UCS) of rocks both in situ and in the laboratory. The instrument consists of a spring-loaded piston which is released when the impact plunger, applying a concentrated load, is entirely pressed against the surface of a rock block or outcrop. The rebound height of a mass located inside the piston is measured. It is called the rebound value (R) and represents an index of surface hardness, which can be related to the compressive strength of the material being tested. The harder the rock surface, the shorter the penetration depth and, consequently, the greater the rebound value (Aydin and Basu 2005). In order to ensure reliable test results, the hammer should be pressed orthogonally against the rock specimen surfaces. Adjustments must be provided for different loading directions, as indicated in Figure 6.1b. The rock surfaces should be smooth and free from cracks. Particular attention must be paid to moisture contents and weathering states, since they may produce microstructural changes that can affect the test results. Moreover, if the test is carried out on a rock specimen, the impact points should be sufficiently distant from the boundaries of the block. A minimum edge length of 6 cm and 15 cm are recommended by the International Society for Rock Mechanics (ISRM 2007) and the American Society for Testing and Materials (ASTM D5731 1995), respectively (Aydin and Basu 2005, Basu et al. 2007, Aydin 2009).

Different recommended Schmidt test procedures exist in the literature (Karaman and Kesimal 2015). For example, the ISRM suggests to record 20 rebound values from single impacts (separated by at least the diameter of the plunger), discard the lower ten values and average the remaining ten results (ISRM 2007). The ASTM suggests to record at least 10 rebound values from single impacts (separated by at

least the diameter of the piston), discarding all values differing more than seven units from the average of the ten rebound readings and average the remaining values (ASTM D5731 1995).

Two standard hammers (L and N types) can be used to perform a Schmidt hammer test. Their difference lies in the impact energy, which is 0.735 and 2.207 Nm, respectively (Aydin and Basu 2005, Aydin 2009).
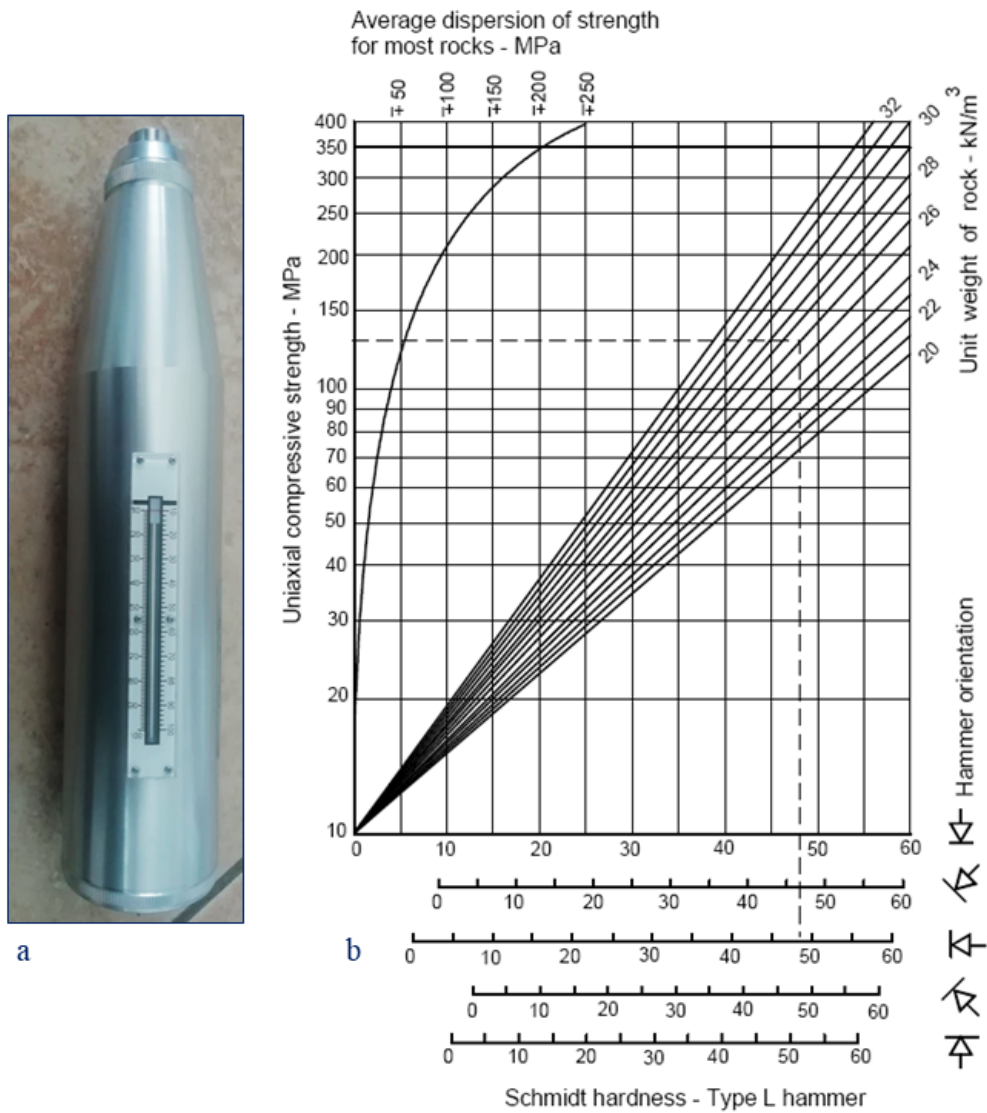


Figure 6.1: a) The Schmidt hammer used for the characterization of the rock blocks of the Oltrepò Pavese; b) UCS estimation chart.

### 6.1.1 Procedure and results

In this study, hardness tests were performed using a standard L-type Schmidt hammer on three different rock block types of the Oltrepò Pavese melange: a limestone, a marly limestone and a calcarenite (Figure 6.2). These blocks were taken in situ, in Montalto Pavese (PV). Their minimum volume was around 2000 $cm^3$ and was determined by means of an X-ray Computed Tomography (CT) carried out at Microservice S.r.l., Alpignano (TO).



Figure 6.2: Rock blocks of the Oltrepò Pavese melange.

All the rock blocks were inspected in order to detect fractures or other macroscopic defects that could have jeopardized the tests. The impact points were kept free of dust and manually smoothed when asperities or altered parts were detected. Although many quarzitic inclusions were detected inside all the rock blocks, no reading was discarded. In fact, according to Aydin (2009), all the values were considered useful to represent the heterogeneity of the surfaces tested.

Each test was performed perpendicularly to the rock face. The results shown in Table 6.3 were obtained following the ASTM Standards (ASTM D5731 1995). The ASTM Standards were used because the blocks were not sufficiently large and regular enough to record at least 20 valid rebound values, as suggested by the ISRM Standards.

The unit weights of the three rock blocks are also listed in table 6.3. They were obtained by means of a precision balance (measuring the weight of the rocks) and an X-ray CT carried out at Microservice S.r.l., Alpignano (TO) (providing the volume of the rock samples).

| Rock type | Average R value | ASTM min and max R values | | ASTM Average R value | $\gamma$ [kN/m³] | $\sigma_c$ [MPa] |
|---|---|---|---|---|---|---|
| Limestone | 24.3 | 31.3 | 17.3 | 23.9 | 25.0 | 33.0 |
| Calcarenite | 28.4 | 35.4 | 21.4 | 27.9 | 26.0 | 44.0 |
| Marly limestone | 38.4 | 45.4 | 31.4 | 37.4 | 24.5 | 62.0 |

Figure 6.3: Schmidt hammer test results and unit weights of the three rock types.

## 6.2 Mineralogical analyses

In order to identify and quantify the mineralogy of crystalline compounds contained in the matrix of the sedimentary melange analyzed, the non-destructive X-ray diffraction (XRD) technique was used. The XRD analysis is based on projection of monochromatic X-rays, generated in a cathode ray tube, onto a crystalline material, contained in a sample holder (Figure 6.4).
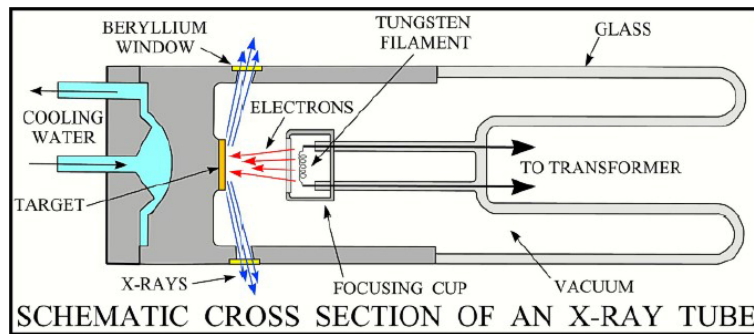


Figure 6.4: A Schematic cross section of a cathode X-ray tube (Poppe et al. 2002).

It consists of a glass ampoule in which a cathode and an anode are contained. By applying a potential difference between the cathode and the anode, an electric accelerator field is generated and X-rays radiate in all directions. The X-rays produced in this way are directed onto the ground sample thanks to a system of divergence slits (Figure 6.5). The slits are necessary to limit scattered (non-diffracted) radiation, reduce background noise, and collimate the radiation.
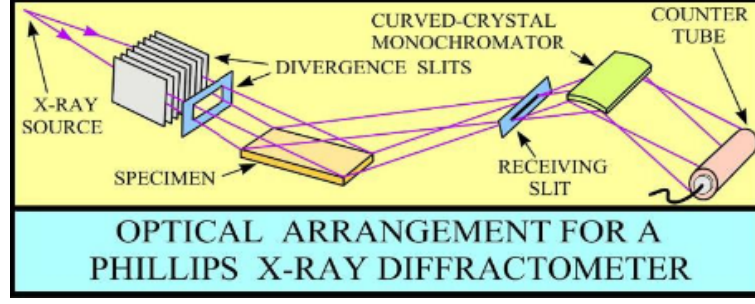
Figure 6.5: Optical arrangement for a Phillips X-ray diffractometer (Poppe et al. 2002).

When the geometry of the incident X-rays satisfies Bragg's equation 6.1:

$$n\lambda = 2d\sin\theta \qquad (6.1)$$

where:
- n is an integer
- $\lambda$ is the wavelength of the x-ray
- d is the spacing of the crystal layers (path difference)
- $\vartheta$ is the incident angle(the angle between incident ray and the scatter plane),
constructive interference is produced (i.e., scattering in a certain direction is in phase with scattered rays from other atomic planes) and diffraction occurs (Poppe et al. 2002, Clark and Dutrow B 2012, INGV 2014). A graphical representation of Bragg's law is given in Figure 6.6.
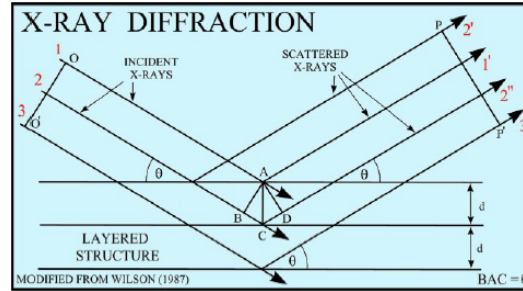


Figure 6.6: Graphical representation of Bragg's law. Three X-rays go through distances significantly different. This difference in the distance crossed is equal to the distance between two adjacent crystalline planes in the crossed material (Poppe et al. 2002).

An X-ray detector records and processes the X-ray signal and, finally, a diffracto-metric spectrum is produced.

142

Since each crystalline phase has a specific X-ray diffraction pattern, which represents its characteristic *fingerprint*, it is possible to identify the mineralogical species univocally.

### 6.2.1 Procedure and results

Mineralogical analyses of the Oltrepò Pavese melange were performed on two samples at the Department of Environment, Land and Infrastructure Engineering (DIATI) of Politecnico di Torino. The melange samples were accurately treated and washed with distilled water. Then, they were finely ground and smeared on the surface of a glass slide, as shown in Figure 6.7a,b,c. The diffractograms obtained for the two melange samples, with the X-ray diffractometer shown in Figure 6.7d, are illustrated in Figures 6.8 and 6.9.

From the analysis of the diffractograms, it was obtained the composition shown in Tables 6.1 and 6.2, which indicates that the melange matrix is dominated by quartz and calcite.
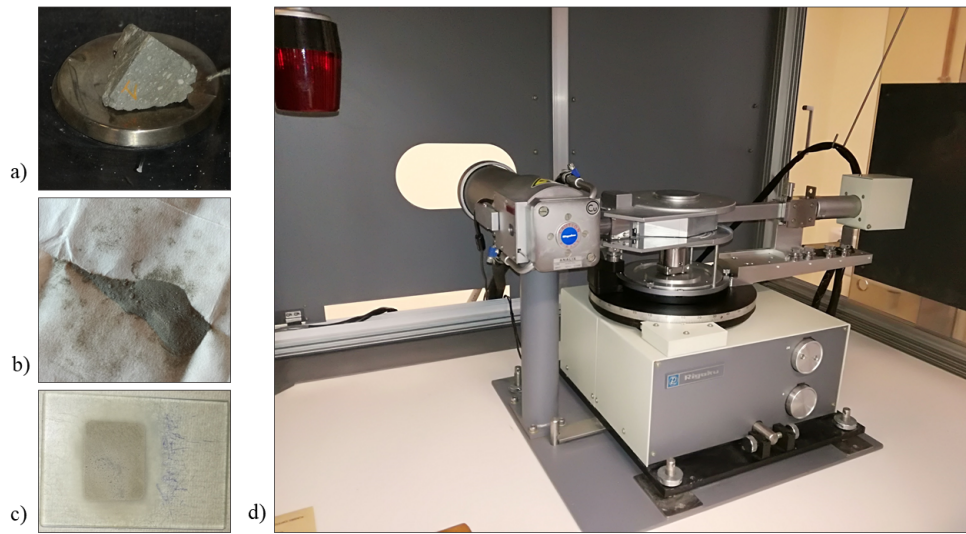


Figure 6.7: a) A melange sample; b) Finer of the melange sample, $\leq 0.09$ mm; c) sample ground and smeared on the surface of a glass slide; d) DIATI X-ray diffractometer.
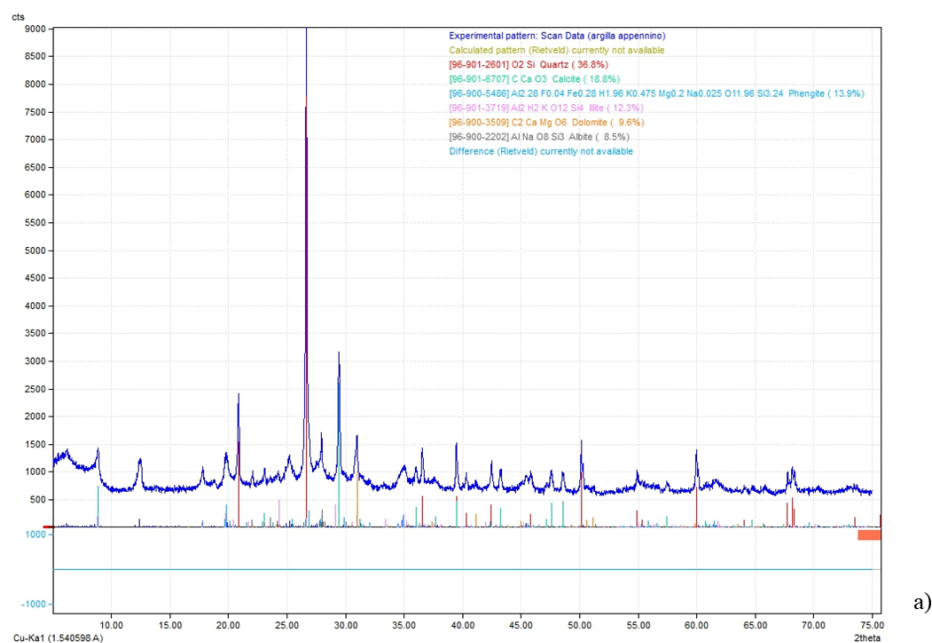
Figure 6.8: Diffractogram a, obtained from the first melange specimen.

| Scan Data results - Diffractogram a | | | |
|---|---|---|---|
| Quartz | about | 37 | % |
| Calcite | about | 19 | % |
| Phengite | about | 14 | % |
| Illite | about | 12 | % |
| Dolomite | about | 10 | % |
| Albite | about | 8 | % |

Table 6.1: Scan data result of diffractogram a.
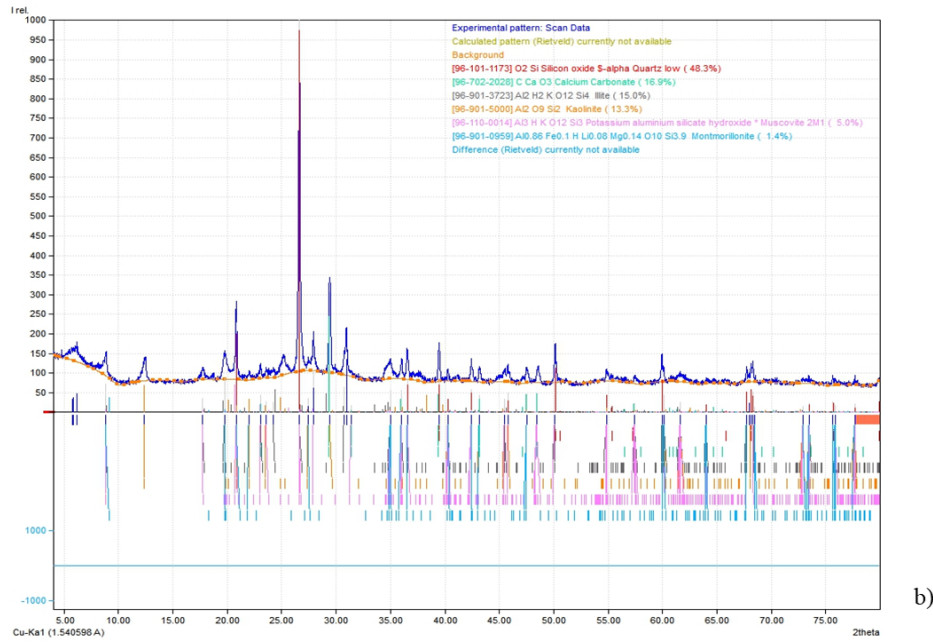
Figure 6.9: Diffractogram b, obtained from the second melange specimen.

| Scan Data results - Diffractogram b | | | |
|---|---|---|---|
| Quartz | about | 44 | % |
| Calcium carbonate | about | 18 | % |
| Illite | about | 14 | % |
| Kaolinite | about | 13 | % |
| Montmorillonite | about | 2 | % |
| Other components | about | 9 | % |

Table 6.2: Scan data result of diffractogram b.

## 6.3  Atterberg limits

The Atterberg limits tests are performed on fine-grained soils (i.e., on the fraction of a soil sample smaller than 425 $\mu$m) in order to determine the amount of water at distinct transitions between different states of soil consistency. In fact, the soil behavior changes from solid to plastic (*plastic limit*) and from plastic to liquid (*liquid limit*) on the basis of its water content, w ($w_P$ and $w_L$, respectively). The liquid and plastic limits are the most commonly used. The values for these limits depend on various soil parameters (e.g., particle size, shape and mineralogy, specific surface area of the particles that are able to attract water molecules, etc.). To determine the liquid limit ($w_L$), the soil is placed in a standard liquid limit

apparatus (the Casagrande cup) and a groove is made in the center with a tool of standardized dimension. The cup is repeatedly dropped and the number of blows is recorded until the two halves flow together. The $w_L$ is the moisture content at which the groove closes over a distance of 13 mm along the bottom of the groove when the Casagrande cup is dropped 25 times.

The plastic limit ($w_P$) of a soil is the moisture content corresponding to the transition from a plastic to a semi solid states of consistency. At this state, the soil just begins to crumble when rolled into a thread of approximately 3 mm in diameter, using an appropriate surface (for example a ground glass plate).

The index of plasticity (PI) represents the sensitivity of a soil (in the mechanical behavior) towards changes in moisture content. The PI is evaluated as the difference between the liquid and the plastic limits.

The relationship between the Atterberg limits and the consistency of fine-grained soils is illustrated in Figure 6.10.
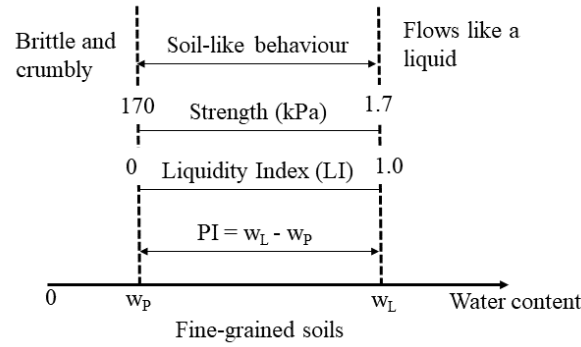


Figure 6.10: Limits of consistency of soils (modified from Atkinson 2007).

## 6.3.1 Procedure

The Atterberg limits were determined for several samples of melange, after the removal of sand and larger particles (the sieve ASTM 40 was used). The choice of working with more than a single sample, as usually done, is dictated by the fact that the geomaterial under study is extremely heterogeneous. Hence, in order to obtain reliable results, more than a single test was considered necessary. Three melange lumps were devoted to these tests. Moreover, in order to examine if relevant variations can be found within the same melange lump, two of the three melange samples (i.e., samples n. 2 and n. 3) were divided in 4 parts and the water content, w, and Atterberg limits were obtained for all of them.

The overall water content of the samples, listed in Table 6.3, was obtained from

Eq. 6.2:

$$w = \frac{W_w}{W_s} \cdot 100 \tag{6.2}$$

where:
- $W_w$ is the weight of water evaporeted by heating the sample to 105°C;
- $W_s$ is the weight of the dry soil.

It is worth pointing out that, since no water is contained in the rock particles of the heterogeneous samples, $W_s$ was obtained by separating the coarse fraction (using the sieve ASTM 60) and considering only the weight of fines.
The melange samples used are shown in Table 6.3, where their description is also provided.

| Sample | 1  | 2  | 3  |
|---|---|---|---|
| *Characteristic of samples* | | | |
| **Year of collection** | 2017 | 2018 | 2018 |
| **Compactness** | Dense | Dense | Dense |
| **Discontinuities** | Yes, slightly visible | Yes, visible | Yes, visible |
| **Weathered state** | Weathered | Slightly weathered | Weathered |
| **Colour** | Gray | Gray | Gray |
| **Water content** | 3% | 5.3% | 4.4% |
| *Characteristic of rock inclusions* | | | |
| **Colour** | Mainly gray and white | Mainly gray, some white and brown | Mainly gray and white |
| **Shape** | Angular / Subangular | Subangular | Angular / Subangular |
| **Roughness** | Moderate | Moderate/High | Moderate/High |
| **% soil greater than 0.2 mm** | 6% | 7% | 17% |

Table 6.3: Characteristics of melange samples.

To obtain the Atterberg limits, distilled water was added and thoroughly mixed to each sample to obtain soil-mixtures, like that shown in Figure 6.11, using a spatula to repeatedly stir, cut and knead them.

Figure 6.11: Soil-mixture.

## 6.3.2  Liquid limits

For the Liquid limit, a sufficient quantity of the soil mixture was put in the Casagrande cup, taking care to prevent the entrapment of air bubbles within the mixture. The soil in the cup was divided into two equal parts by a firm stroke of the grooving tool.
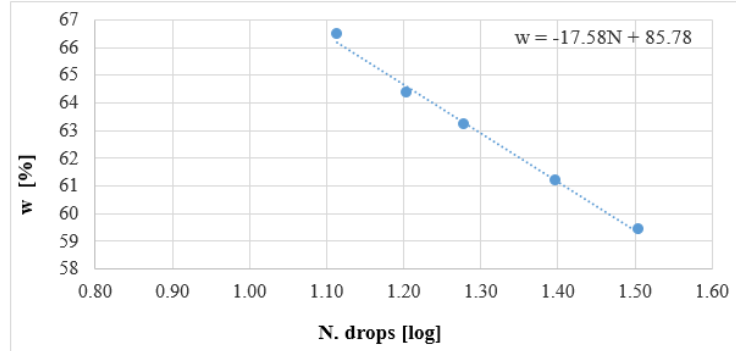


Figure 6.12: Flow curve for the melange sample 1.

The cup was lifted and dropped by turning the crank. The number of drops required for the two halves of the sample to flow together were noted, as well as the tare, the tare with the wet soil and the tare with the dry soil. In this way, it was possible to calculate, for each test, the dry and the wet weight as well as the moisture content, w, using Eq. 6.2.
The relationship between the moisture content and the corresponding number of drops of the cup is represented by means of "flow curves" (on a semi-logarithmic scale), like that of Figure 6.12 obtained for one of the samples analyzed. The straight interpolation line was used to determine the $w_L$, which corresponds to the log(25) drop ordinate. For the sample n.1, as shown in Figure 6.12, it was found:

$$w_L = -17.58 log(25) + 85.78 = 61.20\% \tag{6.3}$$

The $w_L$ values found for all the melange samples tested are listed in Table 6.4.

| Sample | Liquid Limit $w_L$ [%] |
|:------:|:----------------------:|
| 1      | 61.2                   |
| 2.1    | 61.7                   |
| 2.2    | 62.2                   |
| 2.3    | 63.8                   |
| 2.4    | 62.1                   |
| 3.1    | 68.5                   |
| 3.2    | 64.7                   |
| 3.3    | 67.4                   |
| 3.4    | 67.7                   |

Table 6.4: $w_L$ of all the melange samples tested.

As mentioned above, four subsamples were obtained from samples n. 2 and n. 3 and were tested in order to investigate whether differences could have been found within the same block. The results indicated that no significant variations exist within a given specimen.

### 6.3.3 Plastic limits

For the determination of the plastic limits, the leftover soil from the mixture prepared for the Liquid Limit test was used. Since it had a moisture content higher than the plastic limit, it was necessary to thoroughly remix and knead it prior to doing the test. A uniform mass of soil (roughly ellipsoidal in shape) was then rolled between the palm of the hand and the ground glass plate, in order to obtain a 3 mm diameter thread (Figure 6.13). Once the plastic limit was reached, a sample of the soil was taken to determine its moisture content. The soil was then placed in a tared container, which was previously weighted, and the total weight (tare + wet soil) recorded. The soil sample was further oven-dried, so as to determine its dry weight and, as a consequence, the $w_P$ using Eq. 6.2.



Figure 6.13: 3 mm diameter thread for the determination of the $w_P$ of sample n.1

The $w_P$ values found for all the melange samples tested are listed in Table 6.5.

| Sample | Plastic Limit $w_P$ [%] |
|--------|-------------------------|
| 1      | 24.5                    |
| 2.1    | 23.9                    |
| 2.2    | 25.1                    |
| 2.3    | 25.3                    |
| 2.4    | 24.6                    |
| 3.1    | 24.1                    |
| 3.2    | 24.0                    |
| 3.3    | 22.9                    |
| 3.4    | 23.0                    |

Table 6.5: $w_P$ of all the melange samples tested.

### 6.3.4 Plasticity index

The plasticity index (PI) of a soil, which is a dimensionless number, is the numerical difference between its $w_L$ and its $w_P$. The PI found for all the melange samples tested are given in Table 6.6.

| Sample | Plasticity index PI [%] |
|--------|-------------------------|
| 1      | 36.7                    |
| 2.1    | 37.8                    |
| 2.2    | 37.1                    |
| 2.3    | 38.5                    |
| 2.4    | 37.5                    |
| 3.1    | 44.4                    |
| 3.2    | 40.1                    |
| 3.3    | 44.5                    |
| 3.4    | 44.8                    |

Table 6.6: *PI* for all the melange samples tested.

### 6.3.5 Results

The average values of the water content, liquid limit, plastic limit and plasticity index are listed in Table 6.7. From these results, the average $w$, $w_L$, $w_P$ and $PI$

are equal to around 4.2%, 64.4%, 24.2% and 40.2%, respectively.

| Sample | 1 | 2 | 3 |
|---|---|---|---|
| **Characteristic of samples** | | | |
| **Year of collection** | 2017 | 2018 | 2018 |
| **Water content** [%] | 3 | 5.3 | 4.4 |
| **Average** $w_L$ [%] | 61.2 | 62.5 | 67.1 |
| **Average** $w_P$ [%] | 24.5 | 24.7 | 23.5 |
| **Average** $PI$ [%] | 36.7 | 37.7 | 43.5 |

Table 6.7: Results of the Atterberg limits.

The results indicate that the matrix is an inorganic clay of high plasticity (Figure 6.14).
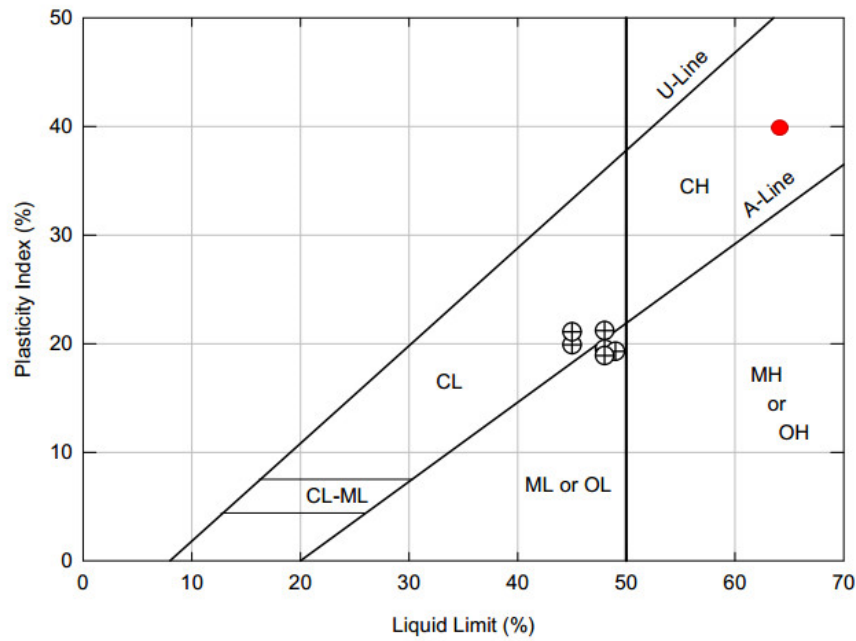


Figure 6.14: Casagrande plasticity chart. The red point refers to the Oltrepò Pavese melange and belongs to High plasticity Clays (CH).

The current state of the melange was then determined from the consistency index ($CI$) or, similarly, the liquidity index ($LI$), which are defined as:

$$CI = \frac{w_L - w}{PI} = 1.50 \tag{6.4}$$

151

$$LI = \frac{w - w_P}{w_L - w_P} = -0.50 \tag{6.5}$$

Since the CI was greater than 1 and the LI lower than 0, the state of the geomaterial under study corresponded to a solid state (Atkinson 2007, Lancellotta 2012).

## 6.4   Grading curves

In order to determine the grading of the melange matrix material, several specimens were analyzed. In fact, given the heterogeneity of the complex formation under study, it was not possible to assume one grading curve to be representative. Hence, two grading curves for the matrix-only melange and three grading curves for the heterogeneous block-in-matrix material were determined.
The homogeneous melange is a silty clay, while the heterogeneous geomaterial is mainly a clay with variable percentages of silt, sand and gravel, as shown in Figures 6.15, 6.16, 6.17, 6.18, 6.19.
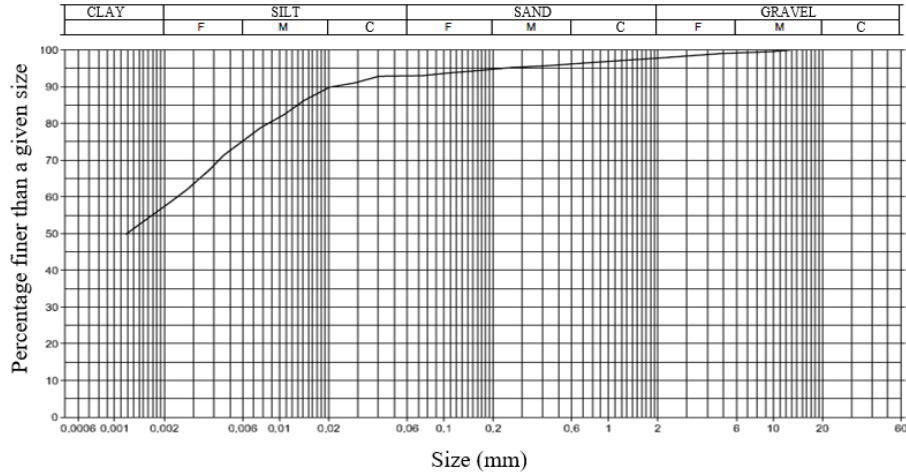


Figure 6.15: Grading curve for the matrix-only melange specimen n. 1: silty clay with 57.3% clay.
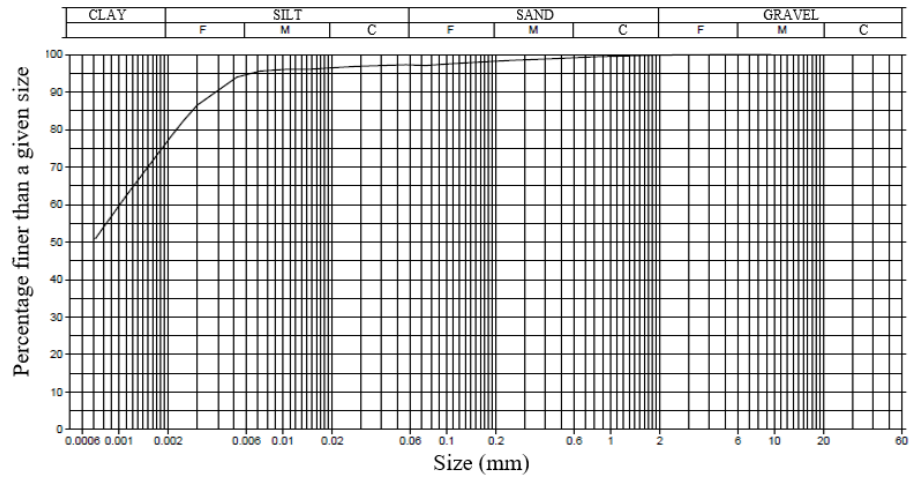
Figure 6.16: Grading curve for the matrix-only melange specimen n. 2: silty clay with 77.3% clay.
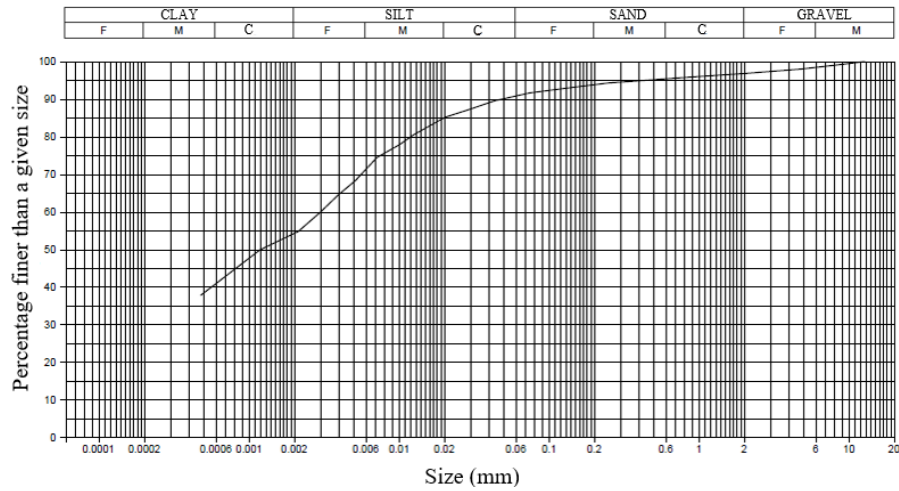


Figure 6.17: Grading curve for the heterogeneous specimen n. 1: clay plus silt (54.3% clay and 36.5% silt) with 6% sand.

153
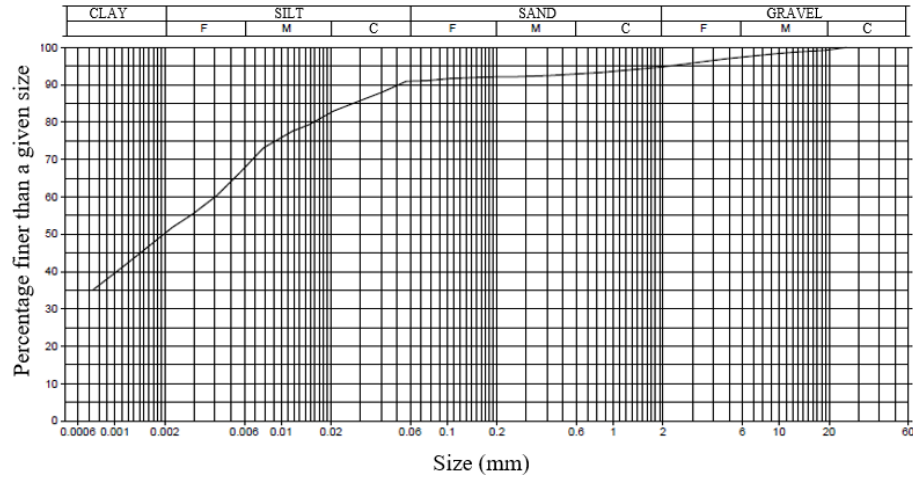
Figure 6.18: Grading curve for the heterogeneous specimen n. 2: clay plus silt (50.3% clay and 40.7% silt) with 5.2% gravel.
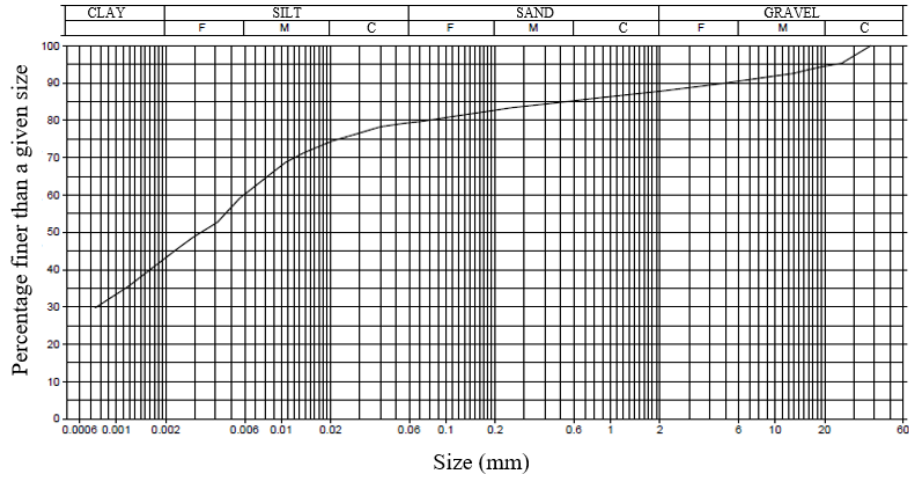


Figure 6.19: Grading curve for the heterogeneous specimen n. 3: clay plus silt (43.2% clay and 36.1% silt) with 12.3% gravel.

The different gravel contents contained in the heterogeneous melange specimens is due to the different location and depth at which they were collected. As discussed previously, the blocks are not distributed uniformly within the melange deposit, since they are characterized by an inverse grading of the largest blocks above a basal shear zone (see Chapter 5). For this reason, the collection of the specimens were made so as to obtain heterogeneous specimens with low VBPs (less than 10-15%), in order to test representative specimens with sufficiently small rock blocks.

## 6.5 Direct shear tests

Direct shear tests are used to determine the peak and residual shear strength of a soil or rock specimen which is laterally restrained and sheared along a mechanically involved horizontal plane under a constant normal stress (Figure 6.20a).
If a rock specimen is tested, the plane of shearing should coincide with a plane of weakness (e.g., a joint, schistosity, cleavage or bedding plane).
The test, performed with the Casagrande shear box, involves a specimen being placed inside a square or circular steel box. Porous plates are placed on the top and bottom surface of the specimen, as shown in Figure 6.20b. This allows free drainage during the consolidation and shearing phases.
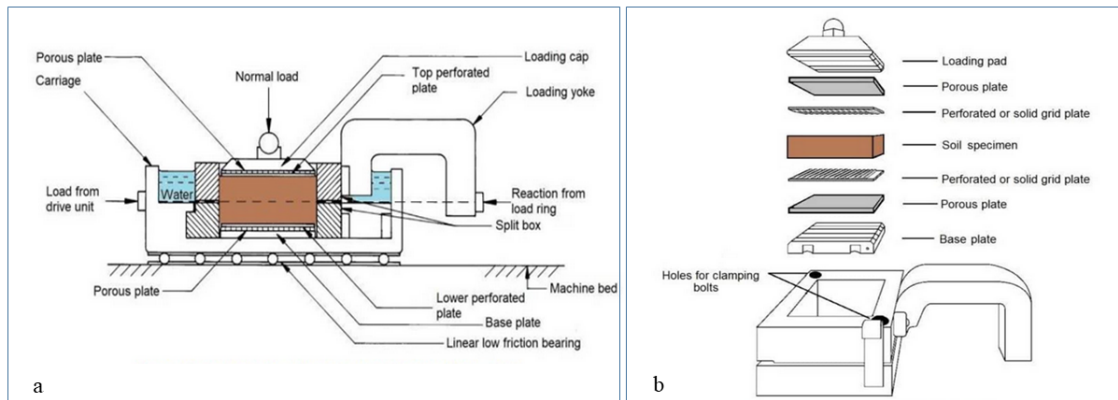


Figure 6.20: a) scheme of the direct shear test apparatus; b) typical shear box assembly (Head and Epps 2011).

The consolidation consists in applying a vertical load to the specimen until the rate of normal displacements recorded is less than 0.05 mm in 10 minutes (ISRM 2007). Subsequently, the shearing stress is applied through a gearing system which moves the split steel box at a constant speed. The lower half of the box is displaced, while the upper compartment (where the normal load is applied) remains stationary. This condition causes shearing along a known plane. The resistance of the specimen to this displacement is measured by the horizontal load cell and represents the strength of the material under shearing. Different normal stresses can be applied to the specimens tested, in order to obtain the Mohr-Coulomb strength envelope and calculate the cohesion and friction angle of the geomaterial.

## 6.5.1 Determination of the normal and shear stresses

The vertical load application system consists of a vertical loading assembly whose lower part is a weight holder attached to the lever arm. Knowing the lever ratio of the equipment, the stress acting in the vertical direction can be obtained from Eq. 6.6:

$$\sigma'_v = \left(W \cdot g \cdot 1000\right)/A \qquad [kPa] \qquad (6.6)$$

being:

- $W$, the weight of the steel plates multiplied by the lever ratio, equal to 10 for the equipment used in this research $[kg]$;
- $g$, the gravity acceleration, equal to 9.81 $m/s^2$;
- $A$, the area of shear surface overlap $[mm^2]$.

The shear stress, $\tau$, can be computed from the ratio between the total shear force, $T$, and the area of shear surface overlap, $A$, from Eq. 6.7:

$$\tau = T/A \qquad [kPa] \qquad (6.7)$$

The maximum $\sigma'_v$ and $\tau$ values obtained correspond to the peak normal and shear stresses, respectively.

## 6.5.2 Procedure

Direct shear tests were performed on 15 matrix-only melange specimens at the Geotechnical Laboratory operating in the Department of Structural, Geotechnical and Building Engineering of Politecnico di Torino. The direct shear test apparatus used in this research mainly consists of a circular Casagrande shear box, a vertical load application system, a horizontal force application device and a controlling stepper drive motor (Figure 6.21).
Due to the peculiarity of the melange under study (see Chapter 5), it was not possible to produce cylindrical specimens to be placed in the circular shear box. In fact, only prismatic specimens could be obtained with the diamond band saw from the irregular samples collected in situ. The samples were cut so as to obtain specimens with as horizontal as possible bedding planes (i.e., parallel to the shearing direction). An example is given in Figure 6.23a.
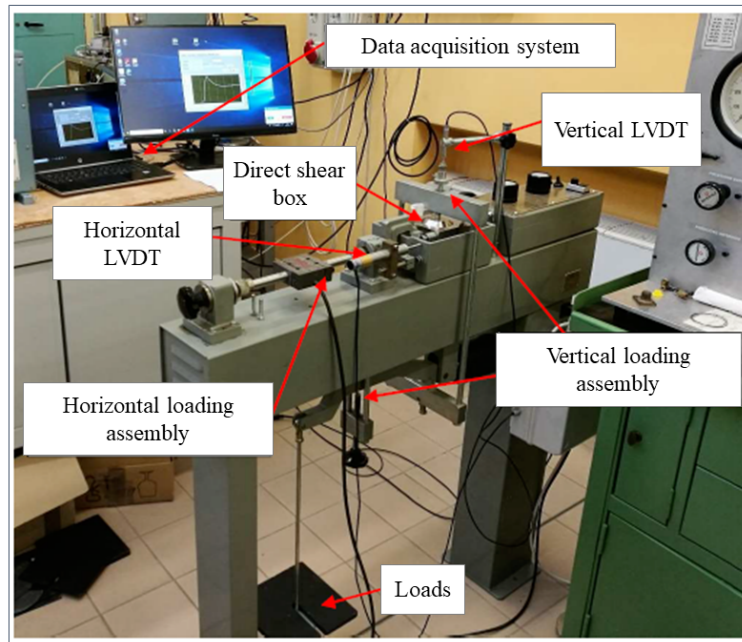
Figure 6.21: The shear test apparatus of the Geotechnical Laboratory (DISEG) of Politecnico di Torino.

In order to perform the direct shear tests, a non-standard preparation procedure was followed. Specifically, the special formwork shown in Figure 6.22 was designed in AutoCad and printed in the Geotechnical Laboratory to incorporate the melange specimens within two cylindrical layers of mortar. These layers had a diameter equal to the hole of the Casagrande shear box. In this way, the irregular melange specimens could be placed and held firmly within the shear box, as illustrated in Figures 6.23f and 6.23g.
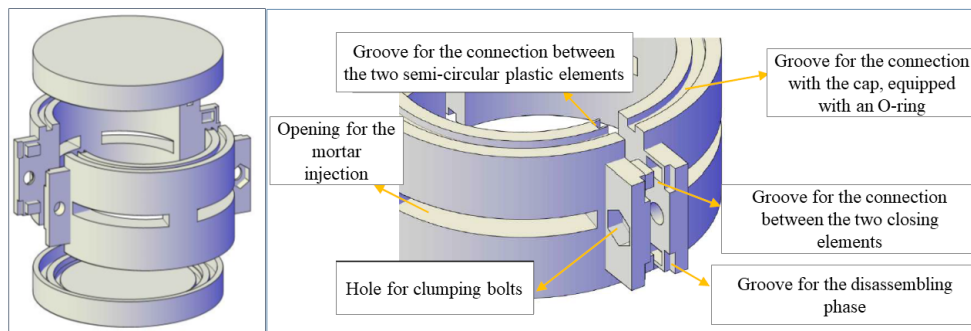


Figure 6.22: Plastic formwork designed in AutoCad.

The procedure for the preparation of each melange+mortar specimen is illustrated

below (Figure 6.23):

1. a thin nail varnish layer was applied to the specimen to protect it from the liquid mortar, which could have damaged its external part. In order to verify that all the surfaces of the specimen were waterproofed, a colored nail varnish was used (Figure 6.23b);

2. a mortar was prepared by mixing 70% cement and 30% water;

3. the melange block was placed in the plastic formwork, made up of 2 semi-circular parts and 2 caps (Figure 6.23c);

4. the mortar was then injected through a specific horizontal opening (Figure 6.22b and Figures 6.23d and 6.23e), and all the way up to it, with a plastic syringe equipped with a nozzle, to obtain the first mortar layer;

5. after at least 24 hours, steps 2 to 4 were repeated to create the second mortar layer. A zone of about 5 mm high was kept free from the mortar (Figure 6.23f), according to the ISRM Standards (ISRM 2007);

6. the specimen was removed from the formwork and tested 7 days after the second layer casting (Figure 6.23g).
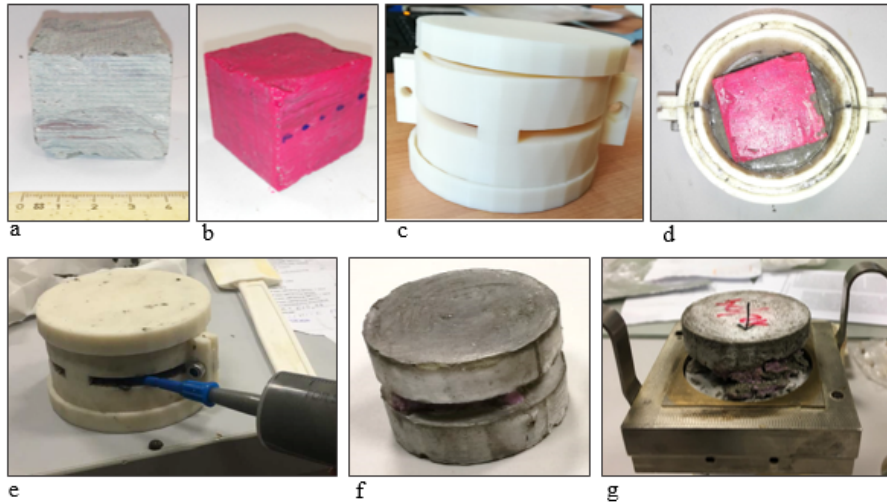


Figure 6.23: a) a melange specimen cut with the diamond band saw; b) thin nail varnish layer applied to the specimen; c) plastic formwork; d) first layer of mortar injected; e) injection of the second layer of mortar; f) the melange specimen held firmly within the mortar. A zone of about 5 mm high was kept free from the mortar; g) the melange specimen inside the Casagrande shear box.

The tests were carried out at shearing rates of approximately 0.16 mm/minute, which was considered adequate since the specimens were assumed to be in dry conditions and the eventual effects of water pressure could be neglected. Different normal stresses were applied to the specimens, in the range $20 - 422$ kPa.

## 6.5.3 Results

The results obtained are illustrated in Figures 6.24 and 6.25 in terms of shear displacements vs. shear stress curves. These data were then processed and, using Eqs. 6.6 and 6.7, Figure 6.26 and Table 6.8 were obtained. The blue points in Figure 6.26 and the graphs shown in Figure 6.24 refer to specimens obtained by cutting a series of irregular samples named "Samples A", which were considered a little more weathered than the other samples, named "Samples B", whose specimens gave the results indicated by the orange points in Figure 6.26 and the graphs shown in Figure 6.25.
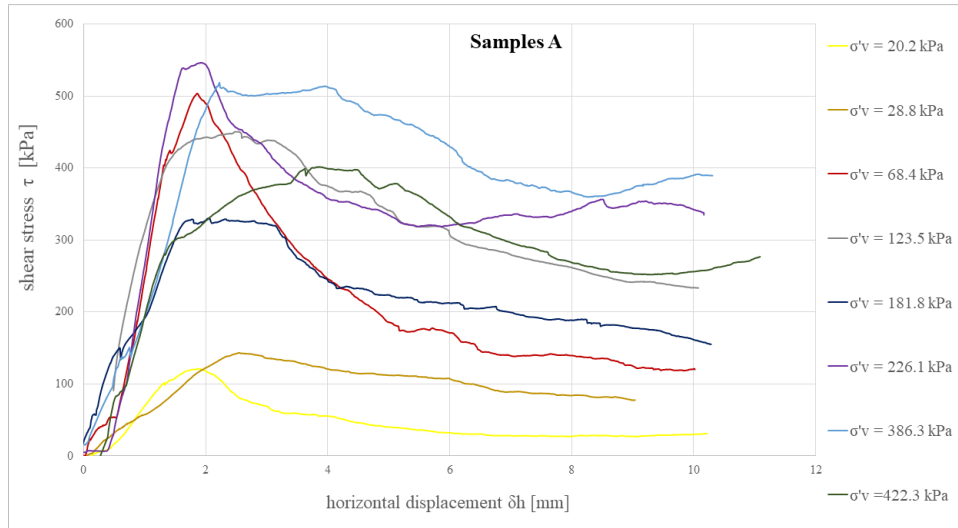


Figure 6.24: Shear stress vs. horizontal displacement of specimens from samples A.
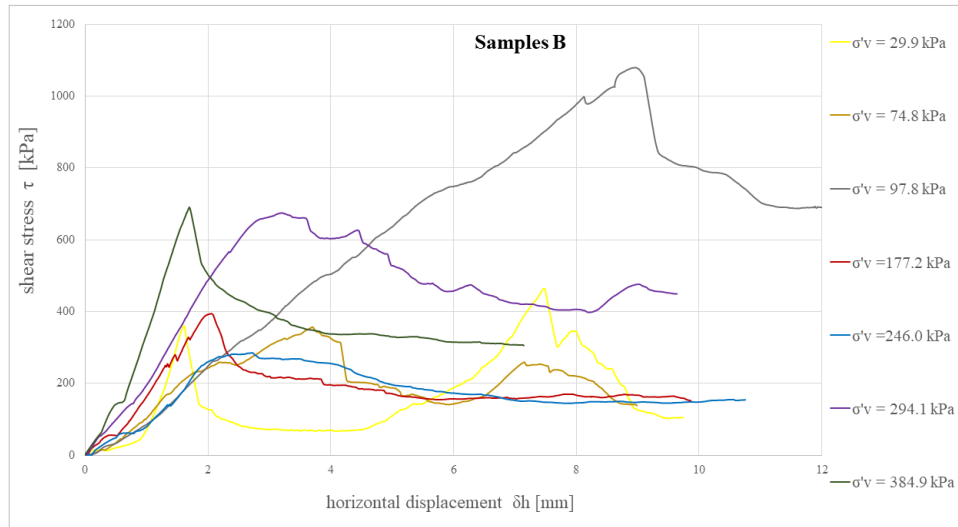
Figure 6.25: Shear stress vs. horizontal displacement of specimens from samples B.
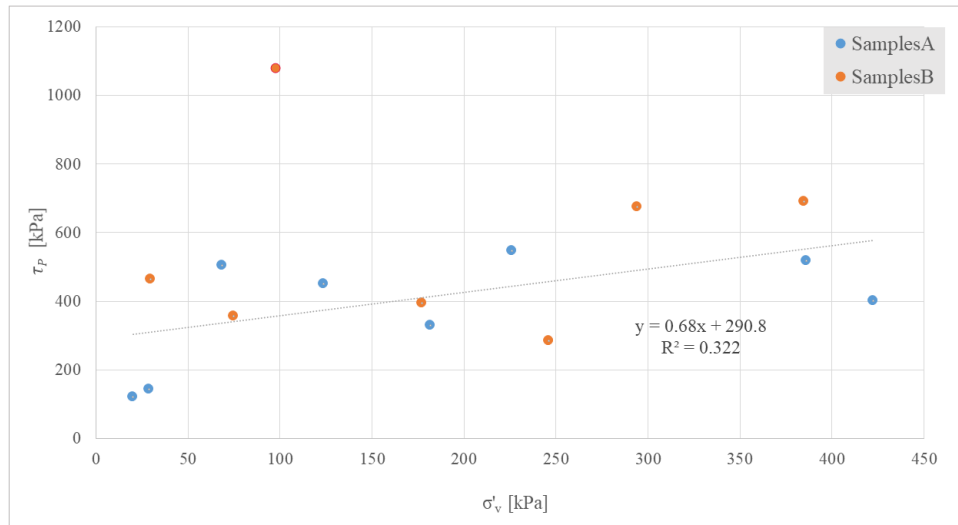


Figure 6.26: Normal vs. peak shear strength for samples A and B. Due to the extremely low water content of the specimens, total stresses were assumed to be equal to effective stresses.

160

| Specimens A | 1 | 2 | 3 | 4 | 5 | 6 | 7 | 8 |
|---|---|---|---|---|---|---|---|---|
| $\tau[kPa]$ | 121.0 | 143.3 | 503.5 | 450.6 | 330.1 | 546.2 | 518.7 | 401.6 |
| $\sigma'_v[kPa]$ | 20.2 | 28.8 | 68.4 | 123.5 | 181.8 | 226.1 | 386.3 | 422.3 |
| Specimens B | 9 | 10 | 11 | 12 | 13 | 14 | 15 | |
| $\tau[kPa]$ | 464.3 | 356.8 | 1079.5 | 394.0 | 284.9 | 674.5 | 690.3 | |
| $\sigma'_v[kPa]$ | 29.9 | 74.8 | 97.8 | 177.2 | 246.0 | 294.1 | 384.9 | |

Table 6.8: Direct shear test results.

As clearly visible from Figure 6.26 and Table 6.8, the results are dispersed and no substantial differences in the behavior of specimens A and B were observed (i.e., samples B, although less weathered, do not show greater strengths than samples A).

Hence, a linear regression was carried out considering all the results of the samples A and B, excluding only the outlier value of specimen 6, characterized by the highest peak shear strength (i.e., $\tau_p = 1079.5$ kPa for $\sigma'_v = 97.8$ kPa). However, an $R^2$ of only 0.322 could be obtained.

The data dispersion was almost certainly caused by the presence of non-horizontal bedding planes in the specimens, which affected their strength.

As mentioned above, the irregular samples were cut in the attempt to obtain specimens with bedding planes parallel to the plane of shearing. However, this was rather difficult and in some cases impossible to achieve. In fact, the bedding planes were not always parallel (i.e., sometimes they were ondulated or had different orientations) nor clearly visible (e.g. due to the weathering of the external part of the samples). For these reasons, the plane of shearing did not always coincide with a plane of weakness. This was clearly visible, after the tests, from the inspection of the failure surfaces, as shown in Figure 6.27.
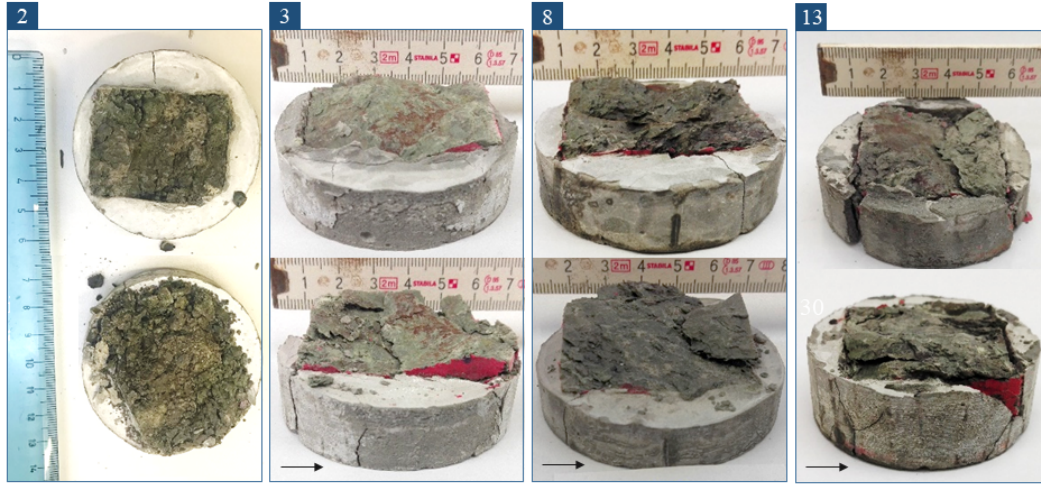
Figure 6.27: Failure surfaces of the specimens n. 2, 3, 8 and 13. The arrow indicates the shearing direction. Different orientations and inclinations of the bedding planes with respect to the shearing direction are clearly visible.

A possible interpretation of the shear tests can be made by subdividing the results into two datasets to obtain a minimum and a maximum shear strength envelope. Specifically, 5 normal stress ranges (i.e., $\sigma'_v = 0 - 50$ kPa, $50 - 100$ kPa, $100 - 200$ kPa, $200 - 300$ kPa and $300 - 425$ kPa) were taken into account providing, for each range, three shear test results (Table 6.9). From these values the minimum and maximum shear strengths were identified and highlighted with the colors blue and green, respectively, in Table 6.9. Finally, the shear strength envelopes illustrated in Figure 6.28 were obtained, which provided a minimum cohesion and friction angle of 211 kPa and 25° and a maximum cohesion and friction angle of 428 kPa and 36°.

| Normal stress range | 0-50 kPa | | |
|---|---|---|---|
| **Specimen** | 1 | 2 | 3 |
| $\sigma'_v[kPa]$ | 20.2 | 28.8 | 29.9 |
| $\tau[kPa]$ | 121.0 | 143.3 | 464.3 |
| **Normal stress range** | **50-100 kPa** | | |
| **Specimen** | 4 | 5 | 6 |
| $\sigma'_v[kPa]$ | 68.4 | 74.8 | 98 * |
| $\tau[kPa]$ | 503.5 | 356.8 | 1079.5 * |
| **Normal stress range** | **100-200 kPa** | | |
| **Specimen** | 7 | 8 | 9 |
| $\sigma'_v[kPa]$ | 123.5 | 181.8 | 177.2 |
| $\tau[kPa]$ | 450.6 | 330.1 | 394.0 |
| **Normal stress range** | **200-300 kPa** | | |
| **Specimen** | 10 | 11 | 12 |
| $\sigma'_v[kPa]$ | 226.1 | 246.0 | 294.1 |
| $\tau[kPa]$ | 546.2 | 284.9 | 674.5 |
| **Normal stress range** | **300-425 kPa** | | |
| **Specimen** | 13 | 14 | 15 |
| $\sigma'_v[kPa]$ | 384.9 | 386.3 | 422.3 |
| $\tau[kPa]$ | 690.3 | 518.7 | 401.6 |
| $c_{min} = 211$ kPa | $c_{max} = 428$ kPa | | |
| $\varphi_{min} = 25°$ | $\varphi_{max} = 36°$ | | |

Table 6.9: Normal stress ranges considered and corresponding test results. The blue and green values correspond to the minimum and maximum strength ($\tau$) of each normal stress range, respectively. The symbol "*" indicates the outlier result discarded. The minimum and maximum cohesion and friction angle obtained are also listed.
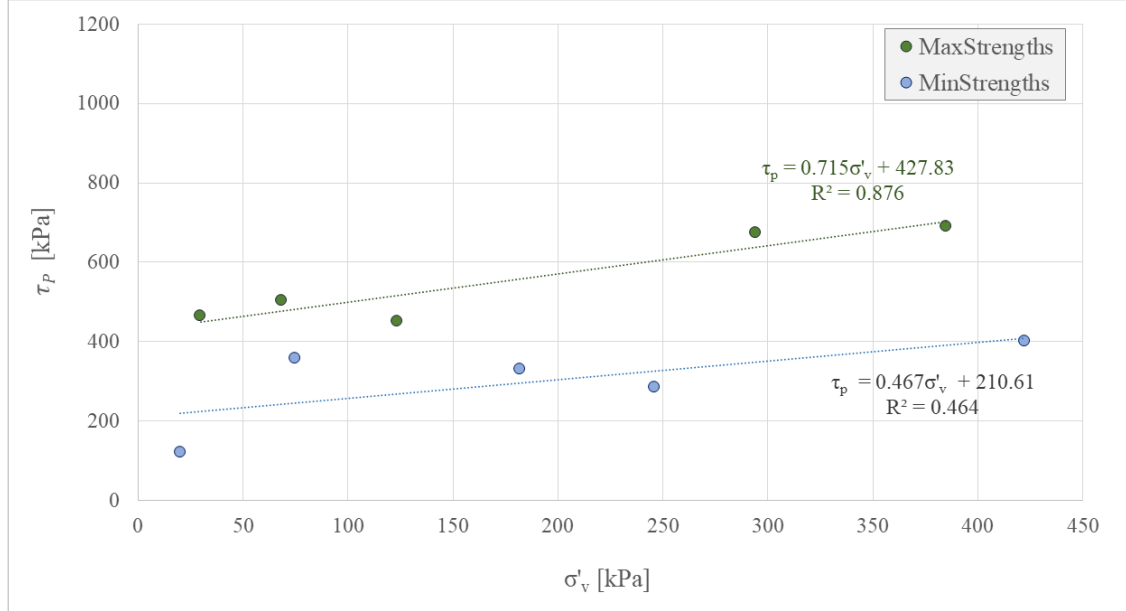


Figure 6.28: Shear strength envelopes: $c_{min} = 211$ kPa, $\varphi_{min} = 25°$; $c_{max} = 428$ kPa and $\varphi_{max} = 36°$.

Although a great deal of effort was put into obtaining these results, they should be considered only as an indication of possible strength values that may characterize the melange. In fact, in order to more precisely determine its strength, a much greater number of direct shear tests should be carried out, taking into account only the results of the specimens with bedding planes parallel to the shearing plane.
An interesting future work will also be to try to study how anisotropy influences the strength of the geomaterial, by carefully examining the different shapes, inclinations and orientations of the bedding planes of each specimen tested.

## 6.6   Point load tests

When dealing with soft rocks, the point load test (PLT) is often the only possibility for evaluating the uniaxial compressive strength (UCS). In fact, many technical problems arise when preparing regular prismatic or cylindrical specimens to be tested in uniaxial compression (Agustawijaya 2007). On the contrary, PLT can be easily conducted even on shapeless lumps and cut blocks (RIG 1994, ASTM D5731 1995, ISRM 2007, Frankovská and Durmekova 2011, Alitalesh et al. 2016).
A typical point load apparatus is shown in Figure 6.29.



Figure 6.29: Point load apparatus of the Geotechnical Laboratory - Politecnico di Torino.

The test is performed with the aim of determining the point load strength index (PLI), $I_{S(50)}$, of rock specimens. The relationship between $Is_{(50)}$ and the UCS is expressed by a conversion factor, C.
The rock samples should present external dimensions preferably not less than 30 mm and not more than 85 mm. Each sample is placed between two truncated

conical platens, which apply a concentrated (compressive) load on the rock until failure occurs. As shown in Figure 6.30, the platens must have spherical tips of radius 5 mm and an opening angle of 60°. A load measuring system indicates the failure load, P, required to break the rock sample. A graduated bar measures the initial distance, D, between the two specimen-platen contact points.
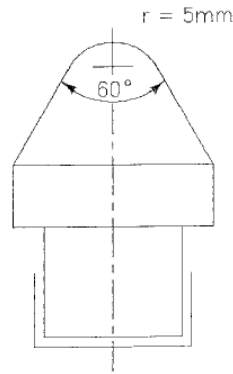


Figure 6.30: Platen geometrical characteristics (ASTM D5731 1995).

The distance, L, between the contact points and the nearest free end of the sample should be greater than 0.5D (Figure 6.31). Furthermore, the specimen should have a width, W, measured perpendicularly to the loading direction, preferably close to the diameter D. In any case, the ratio D/W should vary between 0.3 and 1. When dealing with irregular lumps with non parallel sides, the minimum width W should be evaluated as $(W_1 + W_2)/2$, as shown in Figure 6.31.
The test should be rejected if the fracture surface passes through only one platen loading point.
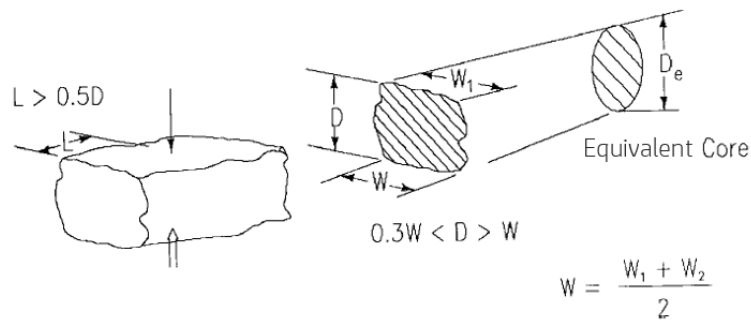


Figure 6.31: Irregular lump test: specimen shape requirement (ASTM D5731 1995).

The ratio between the applied failure load, P, and the equivalent diameter of the rock sample, $D_e$, provides the uncorrected PLI, $I_S$:

$$I_S = \frac{P}{D_e^2} \qquad [MPa] \tag{6.8}$$

where:

$$D_e = \sqrt{4WD/\pi} \qquad [m] \tag{6.9}$$

In Eq. 6.9 the final value of the distance between the two platen contact points, D', can also be used instead of D.

If rock sample dimensions are different from 50 mm, the point load strength index determined by the PLT must be corrected to the standard equivalent diameter ($D_e$) of 50 mm. Hence a shape correction factor, F, should be introduced in order to evaluate the corrected PLI, $I_{S(50)}$.

$$I_{S(50)} = F \cdot I_s \tag{6.10}$$

where F may be evaluated using the following Eq. 6.11 (ASTM D5731 1995):

$$F = \left(\frac{D_e}{50}\right)^{0.45} \tag{6.11}$$

As suggested by ASTM Standards (ASTM D5731 1995), $I_{S(50)}$ is calculated by not considering the two highest and two lowest values from the ten (or more) valid tests, and calculating the mean of the remaining values. If significantly fewer specimens are tested, only the highest and lowest values are to be deleted and the mean calculated from the remaining ones.

Finally, to obtain the UCS of the rock, the strength index $I_{S(50)}$ should be corrected again, by multiplying it for a conversion factor C. The value of this coefficient is generally set as equal to 24 for hard rocks. However, for soft rocks (i.e., argillaceous rocks, siltstones, flysches, ect.), it could be much lower than this value (Marinos and Hoek 2001, Agustawijaya 2007, Tsiambaos 2010, Frankovská and Durmekova 2011, Kanjii 2014, Alitalesh et al. 2016). Previous findings from the literature have shown that C varied from 5 up to 24 for chalks, from about 7 to 18 for sandstone and from 13 to 15 for argillaceous rocks. Hence, a conversion factor equal to 14 was considered reliable for the melange under study.

## 6.6.1   Preparation of the specimens

In order to obtain a preliminary value of the compressive strength of the Oltrepò Pavese melange, a great number of point load tests were carried out on non-cylindrical samples (Figure 6.32), at their natural water content and in dry conditions. The dry specimens were obtained by putting the samples in an oven at a temperature of 105°C for 24 hours. This procedure was undertaken in order to investigate the effect of the water content on the strength of the melange under study. Previous findings from the literature suggest that with decreasing the water

content higher strengths can be obtained (Erguler and Ulusay 2009).
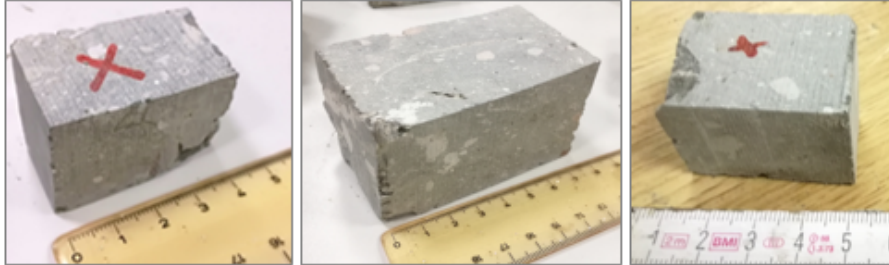


Figure 6.32: Typical melange samples tested with the Point Load apparatus.

The samples, as can be seen from Figure 6.32, were cut with the diamond band saw in order to regularize their geometry (see Section 5.2). The specimens produced for the PLT tests were cut so as to apply the load (as much as possible) perpendicularly to the bedding planes, in order to achieve the greatest strength values.

After the test, the failure surface of each specimen was inspected to verify the validity of the test. A few pictures of the broken melanges are illustrated in Figure 6.33.



Figure 6.33: Typical samples successfully tested with the PL apparatus: the failure surfaces pass through both the platen loading points.

167

## 6.6.2 PLT on melange samples at natural water content

37 samples were tested at their natural water content, w (from 3.5% to 7%). However, only 23 were successfully tested. 2 invalid tests were obtained from samples 6 and 10 and their results were discarded. The other 12 blocks provided no significant results (i.e., P = 0 N).

Deleting the two highest and lowest values, and assuming the conversion factor C=14 (Agustawijaya 2007), the average UCS was found to be 2.10 MPa, with a standard deviation as equal to 1.12.

The minimum and maximum strengths were 0.77 MPa and 5.24 MPa, respectively. The results obtained are listed in Table 6.10.

| Sample | 2L [mm] | W [mm] | D' [mm] | $D_e^2$ [$m^2$] | P [kN] | $I_S$ [kN/$m^2$] | De [mm] | F [-] | $I_{S(50)}$ [kPa] | f [-] | UCS [MPa] | UCS$_{ASTM}$ [MPa] |
|---|---|---|---|---|---|---|---|---|---|---|---|---|
| 1 | 50 | 31 | 29 | 0.0011 | 0.00 | 0.00 | 33.84 | 0.84 | 0.0 | 14 | 0.00 | - |
| 2 | 72 | 35 | 16 | 0.0007 | 0.28 | 392.50 | 26.71 | 0.75 | 296.0 | 14 | 4.14 | 4.14 |
| 3 | 82 | 25 | 22 | 0.0007 | 0.00 | 0.00 | 26.47 | 0.75 | 0.0 | 14 | 0.00 | - |
| 4 | 70 | 30 | 15 | 0.0006 | 0.00 | 0.00 | 23.94 | 0.72 | 0.0 | 14 | 0.00 | - |
| 5 | 72 | 38 | 23 | 0.0011 | 0.50 | 449.08 | 33.37 | 0.83 | 374.4 | 14 | 5.24 | **5.24** |
| 6 | 105 | 80 | 52 | 0.0053 | 0.10 | 18.87 | 72.80 | 1.18 | 22.3 | 14 | 0.31 | *Inv.* |
| 7 | 105 | 60 | 60 | 0.0046 | 0.10 | 21.81 | 67.72 | 1.15 | 25.0 | 14 | 0.35 | $m_2$ |
| 8 | 70 | 55 | 51 | 0.0036 | 0.00 | 0.00 | 59.78 | 1.08 | 0.0 | 14 | 0.00 | - |
| 9 | 110 | 40 | 34 | 0.0017 | 0.00 | 0.00 | 41.62 | 0.92 | 0.0 | 14 | 0.00 | - |
| 10 | 65 | 65 | 44 | 0.0036 | 0.10 | 27.45 | 60.36 | 1.09 | 29.9 | 14 | 0.42 | *Inv.* |
| 11 | 60 | 50 | 50 | 0.0032 | 0.48 | 150.72 | 56.43 | 1.06 | 159.2 | 14 | 2.23 | 2.23 |
| 12 | 44 | 42 | 41 | 0.0022 | 0.30 | 136.76 | 46.84 | 0.97 | 132.8 | 14 | 1.86 | 1.86 |
| 13 | 50 | 36 | 38 | 0.0017 | 0.15 | 86.07 | 41.75 | 0.92 | 79.4 | 14 | 1.11 | 1.11 |
| 14 | 90 | 51 | 49 | 0.0032 | 0.23 | 72.25 | 56.42 | 1.06 | 76.3 | 14 | 1.07 | 1.07 |
| 15 | 58 | 40 | 37 | 0.0019 | 0.00 | 0.00 | 43.42 | 0.94 | 0.0 | 14 | 0.00 | - |
| 16 | 110 | 60 | 48 | 0.0037 | 0.05 | 13.63 | 60.57 | 1.09 | 14.9 | 14 | 0.21 | $m_1$ |
| 17 | 75 | 36 | 40 | 0.0018 | 0.15 | 81.77 | 42.83 | 0.93 | 76.3 | 14 | 1.07 | 1.07 |
| 18 | 80 | 46 | 53 | 0.0031 | 0.00 | 0.00 | 55.73 | 1.05 | 0.0 | 14 | 0.00 | - |
| 19 | 50 | 38 | 46 | 0.0022 | 0.00 | 0.00 | 47.19 | 0.97 | 0.0 | 14 | 0.00 | - |
| 20 | 42 | 26 | 25 | 0.0008 | 0.18 | 217.38 | 28.78 | 0.78 | 169.5 | 14 | 2.37 | 2.37 |
| 21 | 65 | 40 | 34 | 0.0017 | 0.30 | 173.16 | 41.62 | 0.92 | 159.4 | 14 | 2.23 | 2.23 |
| 22 | 39 | 34 | 37 | 0.0016 | 0.10 | 62.40 | 40.03 | 0.90 | 56.5 | 14 | 0.79 | 0.79 |
| 23 | 52 | 44 | 40 | 0.0022 | 0.30 | 133.81 | 47.35 | 0.98 | 130.6 | 14 | 1.83 | 1.83 |
| 24 | 59 | 50 | 24 | 0.0015 | 0.32 | 209.33 | 39.10 | 0.90 | 187.4 | 14 | 2.62 | 2.62 |
| 25 | 80 | 49 | 33 | 0.0021 | 0.30 | 145.64 | 45.39 | 0.96 | 139.4 | 14 | 1.95 | 1.95 |
| 26 | 40 | 31 | 31 | 0.0012 | 0.20 | 163.37 | 34.99 | 0.85 | 139.1 | 14 | 1.95 | 1.95 |
| 27 | 35 | 33 | 19 | 0.0008 | 0.48 | 600.96 | 28.26 | 0.77 | 464.9 | 14 | 6.51 | $M_1$ |
| 28 | 42 | 35 | 20 | 0.0009 | 0.00 | 0.00 | 29.86 | 0.79 | 0.0 | 14 | 0.00 | - |
| 29 | 45 | 33 | 31 | 0.0013 | 0.32 | 245.55 | 36.10 | 0.86 | 212.1 | 14 | 2.97 | 2.97 |
| 30 | 28 | 28 | 26 | 0.0009 | 0.00 | 0.00 | 30.45 | 0.80 | 0.0 | 14 | 0.00 | - |
| 31 | 50 | 27 | 26 | 0.0009 | 0.00 | 0.00 | 29.90 | 0.79 | 0.0 | 14 | 0.00 | - |
| 32 | 32 | 34 | 19 | 0.0008 | 0.40 | 486.07 | 28.69 | 0.78 | 378.5 | 14 | 5.30 | $M_2$ |
| 33 | 75 | 35 | 37 | 0.0016 | 0.10 | 60.62 | 40.62 | 0.91 | 55.2 | 14 | 0.77 | **0.77** |
| 34 | 38 | 35 | 37 | 0.0016 | 0.30 | 181.85 | 40.62 | 0.91 | 165.6 | 14 | 2.32 | 2.32 |
| 35 | 36 | 34 | 36 | 0.0016 | 0.27 | 173.16 | 39.49 | 0.90 | 155.7 | 14 | 2.18 | 2.18 |
| 36 | 65 | 30 | 4 | 0.0002 | 0.00 | 0.00 | 12.36 | 0.53 | 0.0 | 14 | 0.00 | - |
| 37 | 55 | 40 | 41 | 0.0021 | 0.20 | 95.73 | 45.71 | 0.96 | 91.9 | 14 | 1.29 | 1.29 |

| | | |
|---|---|---|
| Average UCS [MPa] | | 2.10 |
| Standard deviation [-] | | 1.12 |

Table 6.10: Results of the point load tests on the sedimentary melange of Pavia with natural water content. "Inv." stands for *invalid test* while letters "m" and "M" refer to the minimum and maximum obtained UCS, respectively, which were discarded according to the ASTM Standards.

### 6.6.3 PLT on melange samples in dry conditions

18 samples were tested in dry conditions. Only 1 invalid test was obtained from sample $4_d$ and the result was discarded. Deleting the two highest and lowest values from the 17 remaining results and assuming C=14 (Agustawijaya 2007), the average UCS was found to be 4.91 MPa, with a standard deviation as equal to 1.19. The minimum and maximum valid UCS found are of 3.59 MPa and 7.63 MPa, respectively. The results obtained are listed in detail in Table 6.11.

| Sample | 2L [mm] | W [mm] | D' [mm] | $D_e^2$ [$m^2$] | P [kN] | $I_S$ [$kN/m^2$] | De [mm] | F [-] | $I_{S(50)}$ [kPa] | f [-] | UCS [MPa] | $UCS_{ASTM}$ [MPa] |
|---|---|---|---|---|---|---|---|---|---|---|---|---|
| 1_d | 56 | 35 | 29 | 0.0013 | 1.20 | 928.08 | 35.96 | 0.86 | 800.1 | 14 | 11.20 | $M_1$ |
| 2_d | 46 | 36 | 28 | 0.0013 | 0.45 | 350.45 | 35.83 | 0.86 | 301.7 | 14 | 4.22 | 4.22 |
| 3_d | 69 | 57 | 25 | 0.0018 | 0.80 | 440.70 | 42.61 | 0.93 | 410.1 | 14 | 5.74 | 5.74 |
| 4_d | 90 | 40 | 27 | 0.0014 | 0.00 | 0.00 | 37.09 | 0.87 | 0.0 | 14 | 0.00 | - |
| 5_d | 72 | 54 | 37 | 0.0025 | 0.80 | 314.31 | 50.45 | 1.00 | 315.6 | 14 | 4.42 | 4.42 |
| 6_d | 60 | 28 | 26 | 0.0009 | 0.48 | 517.58 | 30.45 | 0.80 | 414.1 | 14 | 5.80 | 5.80 |
| 7_d | 60 | 43 | 14 | 0.0008 | 0.30 | 391.20 | 27.69 | 0.77 | 299.9 | 14 | 4.20 | 4.20 |
| 8_d | 62 | 49 | 13 | 0.0008 | 0.15 | 184.85 | 28.49 | 0.78 | 143.5 | 14 | 2.01 | $m_1$ |
| 9_d | 46 | 39 | 35 | 0.0017 | 0.40 | 230.04 | 41.70 | 0.92 | 212.0 | 14 | 2.97 | $m_2$ |
| 10_d | 75 | 45 | 37 | 0.0021 | 1.20 | 565.77 | 46.05 | 0.96 | 545.2 | 14 | **7.63** | **7.63** |
| 11_d | 66 | 45 | 39 | 0.0022 | 1.75 | 782.76 | 47.28 | 0.98 | 763.3 | 14 | 10.69 | $M_2$ |
| 12_d | 77 | 49 | 42 | 0.0026 | 0.70 | 267.01 | 51.20 | 1.01 | 269.9 | 14 | 3.78 | 3.78 |
| 13_d | 55 | 32 | 23 | 0.0009 | 0.30 | 319.97 | 30.62 | 0.80 | 256.6 | 14 | **3.59** | **3.59** |
| 14_d | 70 | 53 | 49 | 0.0033 | 1.10 | 332.50 | 57.52 | 1.07 | 354.1 | 14 | 4.96 | 4.96 |
| 15_d | 41 | 36 | 34 | 0.0016 | 0.70 | 448.94 | 39.49 | 0.90 | 403.7 | 14 | 5.65 | 5.65 |
| 16_d | 40 | 34 | 39 | 0.0017 | 0.70 | 414.40 | 41.10 | 0.92 | 379.4 | 14 | 5.31 | 5.31 |
| 17_d | 45 | 29 | 25 | 0.0009 | 0.30 | 324.83 | 30.39 | 0.80 | 259.6 | 14 | 3.63 | 3.63 |
| 18_d | 80 | 46 | 53 | 0.0031 | 0.00 | 0.00 | 55.73 | 1.05 | 0.0 | 14 | 0.00 | - |
| | | | | | | | | | | Average $UCS$ [MPa] | | 4.91 |
| | | | | | | | | | | Standard deviation [-] | | 1.19 |

Table 6.11: Results of the point load tests on the sedimentary melange of Pavia in dry conditions. Letters "m" and "M" refer to the minimum and maximum obtained UCS, respectively, which were discarded according to the ASTM Standards.

### 6.6.4 Comparison of the results

The final results obtained from the PL tests are listed in Table 6.12. They clearly indicate that dry specimens have a higher strength (almost equal to $2UCS_{Natural-w}$). This outcome confirms previous results from the literature (Erguler and Ulusay 2009), highlighting that laboratory tests must be carried out carefully, considering the actual ground conditions of the specific project.

|  | Average UCS [MPa] | Standard deviation [-] | Min UCS [MPa] | Max UCS [MPa] |
|---|---|---|---|---|
| Natural w | 2.1 | 1.12 | 0.77 | 5.24 |
| Dry condition | 4.9 | 1.19 | 3.59 | 7.63 |

Table 6.12: Comparison of the results obtained with PLT for samples at natural water content and dry condition.

## 6.7 Uniaxial compression tests

The uniaxial compression test is intended to measure the uniaxial compressive strength (UCS) and deformability (i.e Young's modulus and Poisson's ratio) of a rock specimen of regular geometry.

It is well known that the absolute size and shape (i.e., diameter and slenderness, respectively) of the rock specimen can affect its strength. Hence, in order to obtain reliable UC test results, the ASTM and ISRM Standards (ISRM 2007, ASTM D5731 1995) have suggested a slenderness ratio (i.e., height-to-diameter ratio of a cylindrical specimen), H/D, equal to 2.0-2.5 and 2.5-3.0, and a diameter of the sample related to the maximum grain dimension by a ratio of at least 6:1 and 10:1, respectively. In the following sections, reference is made to the more conservative ISRM Standards.

The test can be performed by continuously applying a load at a constant stress or deformation rate. The maximum load, P, carried by the specimen divided by its cross-sectional area, A, is the UCS of the material (Eq. 6.12).

$$UCS = P/A \tag{6.12}$$

Electrical resistance strain gauges, extensometers or other devices can be used to determine circumferential and axial strains for each load increment and, consequently, Poisson's ratio, $\nu$. Finally, the ratio of the axial stress increase to the relative induced axial strain due to the stress increase allows the determination of Young's modulus, E.

### 6.7.1 Procedure

The uniaxial compression tests on the Oltrepò Pavese melange were performed at the Geotechnical Laboratory operating in the Department of Structural, Geotechnical and Building Engineering (DISEG) of Politecnico di Torino, using the computer-controlled compression test machine shown in Figure 6.34, which has a maximum load capacity of 5000 kg. During the tests, a data acquisition system recorded the values of time in seconds, displacement of the piston in millimeters (acquired from an LVDT) and load in kN (acquired from a load cell) with a sampling rate of 100 Hz.
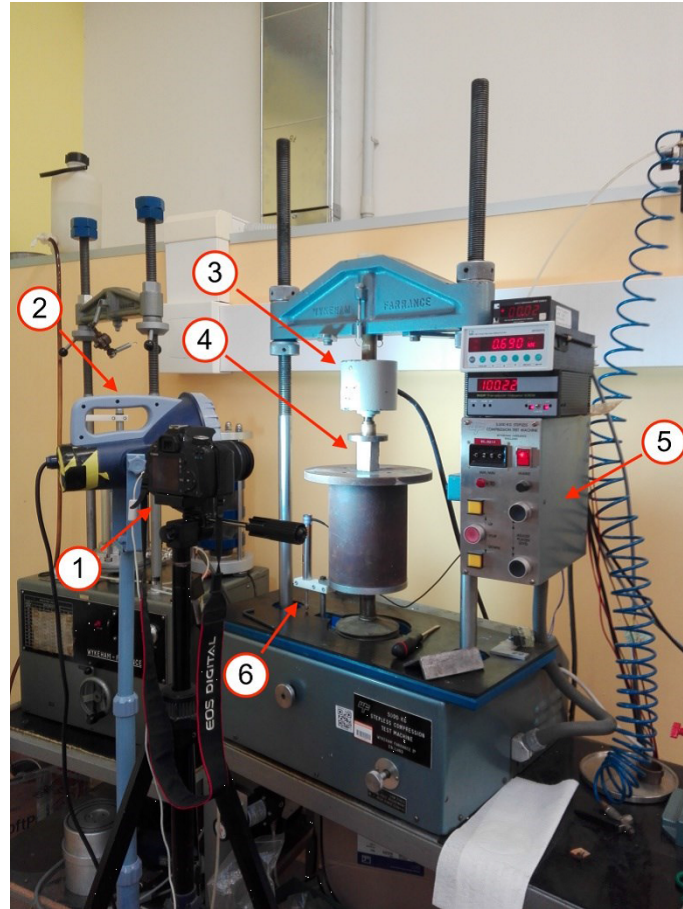
Figure 6.34: The uniaxial compression device of the Geotechnical Laboratory of DISEG − Politecnico di Torino. 1) digital camera on a tripod; 2) halogen lamp; 3) load cell connected to the data acquisition system; 4) specimen; 5) control panel; 6) LVDT connected to the data acquisition system.

Due to the difficulties encountered during the cutting phase of the melange, as described in Section 5.2, only 8 uniaxial compression tests were carried out. Specifically, 3 matrix-only and 5 block-in-matrix specimens with a sufficiently regular geometry could be obtained from more than 16 shapeless samples. It was assumed that the heterogeneity of the 5 block-in-matrix specimens would not have affected the UC test results. In fact, from the observation of the grading curves of the melange (shown in Section 6.4), these samples were expected to have very low VBPs and previous findings from the literature have indeed demonstrated (experimentally and numerically) that no strength increase is registered in heterogeneous materials with rock contents up to 20%-25% (Lindquist 1994b, Medley 1994). The assumption of very low VBPs was later confirmed from the sieve analyses carried out after each test. In fact, the rock block content of all the specimens was less

than 7% (Table 6.13).

Similarly to the PLT, the specimens produced for the UC tests were cut so as to apply the load (as much as possible) perpendicularly to the matrix bedding planes, in order to achieve the greatest strength values. However, since the samples were cut with the diamond band saw (see Section 5.2) a few indications of the ISRM Standards (ISRM 2007) were not met. First of all, it was not possible to obtain specimens with a cylindrical shape. Moreover, the final geometry of the prismatic specimens was never completely free of irregularities. In fact, the specimen ends were often far from being smooth and perpendicular to their axes. In addition, another problem was that the height to the diameter (i.e., width) ratio of 2.5 suggested by the ISRM Standards (2007) could never be obtained. Specifically, the specimens tested had a variable H/D ratio, ranging from 1.38 to 2.10, as indicated in Table 6.13.

Three of the (non-standard) specimens tested are illustrated in Figure 6.35, where some irregularities and defects are clearly visible. These images were obtained by means of the ReCap Photo software, from Autodesk.



Figure 6.35: Heterogeneous specimens n. 6, 7 and 8 of Table 6.13.

Due to the peculiarity of the melange, neither strain gauges nor direct contact extensometers could be used to measure local strains. The strain gauges could not be held in place using common adhesives (e.g. cyanoacrylate) because of the dusty, irregular and heterogeneous surfaces of the specimens. Similarly, due to the high fragility of the material under study, direct contact extensometers could not be mounted on the specimens without damaging them. In fact, they are held in place by the contact force provided from springs, which would have hollowed out the edges of the specimens.

As a consequence, the non-contact Digital Image Correlation (DIC) technique was used for estimating the material displacements and strains (Section 6.7.3). The DIC technique compares a series of digital images, for example of the surface of a loaded specimen, and measures the displacements by matching the same pixels in consecutive photographs, before and after deformation. This technique, among other research fields, has been widely and successfully used in rock mechanics (Lenoir

et al. 2007, Lin and Labuz 2013, Caselle et al. 2019).

## 6.7.2 UCS results

The compressive strength of the melange under study was estimated by means of uniaxial compression tests performed on 8 prismatic specimens under axial deformation control at a constant rate of 0.005 mm/min. A data acquisition system recorded the measurements made during the tests by the load cell and LVDT transducer. All the data (i.e., time, axial displacement, axial load) were recorded and saved in an Excel file. These data were subsequently processed (considering the average heights and cross sections of the specimens) to obtain the stress-strain curves in terms of global deformations (Figure 6.36).

After each test, the specimens were submerged in water and then sieved to determine their VBP. The results of the UC tests are shown in Figure 6.36 and Table 6.13.
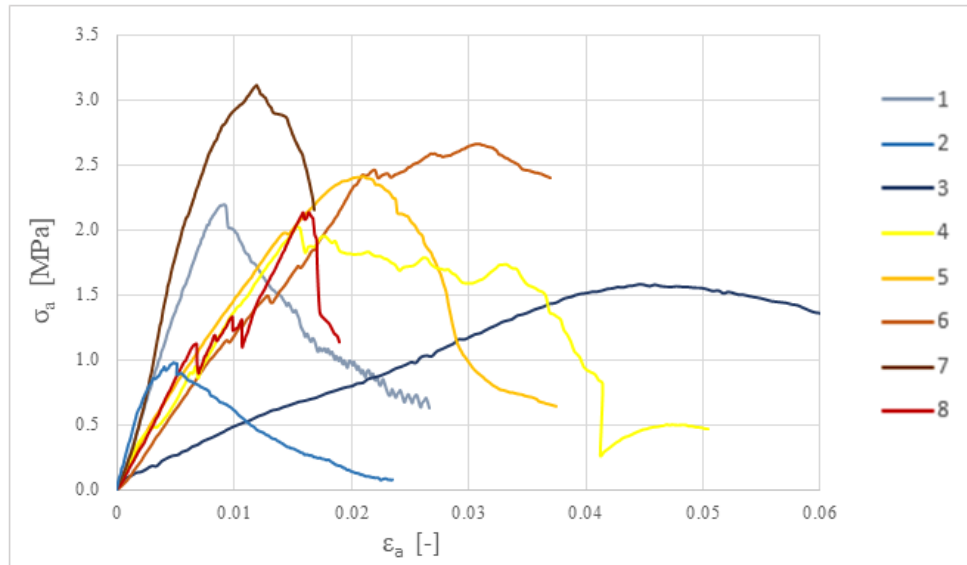


Figure 6.36: UCS vs. axial strain for the 8 specimens tested. The blue curves represent the homogeneous specimens. The yellow/brown curves represent the heterogeneous specimens.

A significant variability in the mechanical behavior of the specimens tested can be observed from Figure 6.36. Different stiffnesses, peak stresses, deformations at failure and post-peak behaviors were shown by the 8 specimens. Specimens 1, 2 and 7 presented the most regular stress-strain curves as well as the lowest deformability and deformations at failure, although their UCS was very different: specimen 2 showed the minimum strength while specimen 7 the maximum UCS of all the specimens tested. Conversely, abrupt changes in stress values are visible for almost all

174

the heterogeneous specimens (especially 4, 6 and 8) both before and after reaching the peak. This characteristic was ascribed to observed local failures of block-matrix contacts which occurred during the tests. Finally, a completely different behavior was exhibited by specimen 3, which showed a much higher deformability and an almost elastic perfectly plastic behavior.

This variability in the results could be due to the anisotropy (i.e., presence of bedding planes, which were also occasionally found to be non iso-oriented) and heterogeneity of the samples.

| Sample | Description | VBP [%] | H/D [-] | UCS [MPa] |
|--------|-------------|---------|---------|-----------|
| 1 | Matrix-only | 0 | 1.38 | 2.20 |
| 2 | Matrix-only | 0 | 1.74 | 0.98 |
| 3 | Matrix-only | 0 | 1.52 | 1.59 |
| 4 | Heterogeneous | 5.1 | 1.67 | 2.03 |
| 5 | Heterogeneous | 6.9 | 1.75 | 2.40 |
| 6 | Heterogeneous | 5.2 | 1.40 | 2.66 |
| 7 | Heterogeneous | 4.9 | 2.10 | 3.12 |
| 8 | Heterogeneous | 2.6 | 1.90 | 2.15 |

Table 6.13: Results of the uniaxial compression tests and sieve analyses.

The results obtained indicate that the average UCS for the matrix-only and heterogeneous melange specimens is 1.59 MPa and 2.47 MPa, respectively, while the average UCS considering all the samples is 2.14 MPa. Hence, the matrix of the melange can be considered as a weak (or soft) rock belonging to the grade R1 of the ISRM classification shown in Table 6.14. According to the ISRM (1981), in fact, rocks with UCS between 0.5 MPa and 25 MPa belong to weak rocks.

| Grade* | Term | Uniaxial comp. strength [MPa] | Point Load Index [MPa] | Field estimate of strength | Examples |
|---|---|---|---|---|---|
| R6 | Extremely strong | >250 | >10 | Specimen can only be chipped with a geological hammer | Fresh basalt, chert, diabase, gneiss, granite, quartzite |
| R5 | Very strong | 100 - 250 | 4 - 10 | Specimen requires many blows of a geological hammer to fracture it | Amphibolite, sandstone, basalt, gabbro, gneiss, granodiorite, peridotite, rhyolite, tuff |
| R4 | Strong | 50 - 100 | 2 - 4 | Specimen requires more than one blow of a geological hammer to fracture it | Limestone, marble, sandstone, schist |
| R3 | Medium strong | 25 - 50 | 1 - 2 | Cannot be scraped or peeled with a pocket knife, specimen can be fractured with a single blow from a geological hammer | Concete, phyllite, schist, siltstone |
| R2 | Weak | 5 - 25 | ** | Can be peeled with a pocket knife with difficulty, shallow indentation made by firm blow with point of a geological hammer | Chalk, marl, claystone, potash, siltstone, shale, rocksalt |
| R1 | Very weak | 1 - 5 | ** | Crumbles under firm blows with point of a geological hammer, can be peeled by a pocket knife | Highly weathered or altered rock, shale |
| R0 | Extremely weak | 0.25 - 1 | ** | Indented by thumbnail | Stiff fault gouge |

* Grade according to Brown 1981
** Point load tests on rocks with a uniaxial compressive strength below 25 MPa are likely to yield highly ambiguous results

Table 6.14: Field estimates of uniaxial compressive strength of intact rock (Marinos and Hoek 2001).

Due to the difficulties already highlighted in Section 5.2 and related to the preparation of the specimens, the results of these non-standard UC tests should be considered only as an indication of the strength of the melange.

Nevertheless, in order to at least qualitatively determine how the non-standard geometry of the specimens could have affected the UC tests, a review of the literature concerning this topic was carried out. Specifically, to investigate the influence of the prismatic shape of the specimens tested on the UCS, reference was made to a recent study conducted by Xu and Cai (Xu and Cai 2017). The authors numerically

176

investigated the influence of different cross-sectional shapes on the strength and deformation behavior of rocks tested in uniaxial compression. Circular, square and rectangular cross-sectional shaped specimens were analyzed, providing very small differences in the peak strengths.

Moreover, the influence of the non-standard slenderness ratios of the specimens tested (i.e., H/D ratios lower than 2.5) on the UCS was also examined through a literature review. Some authors performed laboratory tests on specimens with different slenderness ratios, usually on good quality intact rocks such as marble, sandstone, limestone and basalt (Pellegrino et al. 1997, Tuncay and Hasancebi 2009). In fact, good quality rocks allow a great number of regular specimens to be easily obtained. Numerical analyses have also been undertaken by several authors (Xu and Cai 2017, Peng et al. 2018), who simulated a series of uniaxial compression tests on specimens with different slenderness ratios. All these studies have revealed that the friction of the end plates induces a non-homogeneous strain field in the samples and an overestimation of the uniaxial stresses for H/D ratios generally lower than 2.5. However, the variation of the UCS with decreasing H/D ratios from 2.5 to 1.5 was found to be moderate in most cases, as illustrated in Figure 6.37 and Figure 6.38 from John 1972 and Peng et al. 2018.
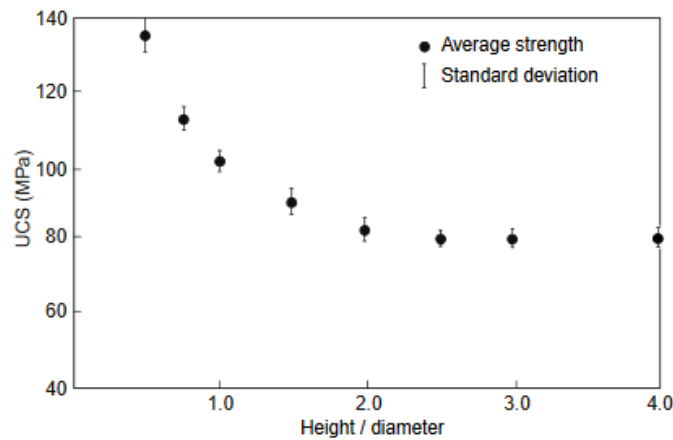


Figure 6.37: Relationship between H/D ratio and UCS value for dry sandstone (after John 1972, from Hawkins 1998).
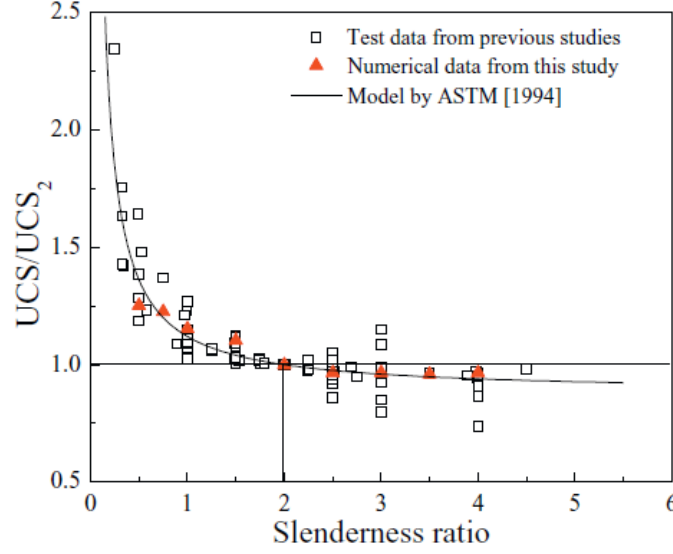
Figure 6.38: Relationship between the normalized UCS and the slenderness ratio. The model by ASTM (1994) and data from previous experimental tests are also plotted (Peng et al. 2018). A moderate increase of the UCS was found for slenderness ratios between 1.5 an 2.5.

Based on all these findings from the literature, it can be assessed that the prismatic shape and the low slenderness ratios (average H/D = 1.7) of the melange specimens tested in this study led to modest effects on the UCS values obtained. They can be considered only slightly overestimated and in any case quite representative of the real strength of the geomaterial.

Moreover, it is interesting to note that the average strength obtained with the UC tests (i.e., 2.14 MPa) is comparable to the average UCS obtained with the PLT on the heterogeneous specimens (i.e., 2.1 MPa). This outcome seems to confirm that a conversion factor C equal to 14 can be applied to point load strength index to reliably predict the UCS of soft rocks, like the Oltrepò Pavese melange.

Another interesting result, concerning the development of the failure surfaces of the melange specimens, was also observed. As shown in Figure 6.39b, the heterogeneous specimens showed failure surfaces which developed tortuously around the blocks (i.e., within the matrix). On the contrary, the homogeneous specimens showed multiple fractures developing mainly horizontally (i.e., along foliation) and diagonally, as can be seen in Figure 6.39a. This result, which indicates that a different mechanical behavior should be expected between homogeneous and heterogeneous geomaterials, confirms previous findings from the literature (Medley 2001, Lindquist 1994b,Napoli et al. 2018a, Napoli et al. 2018b).
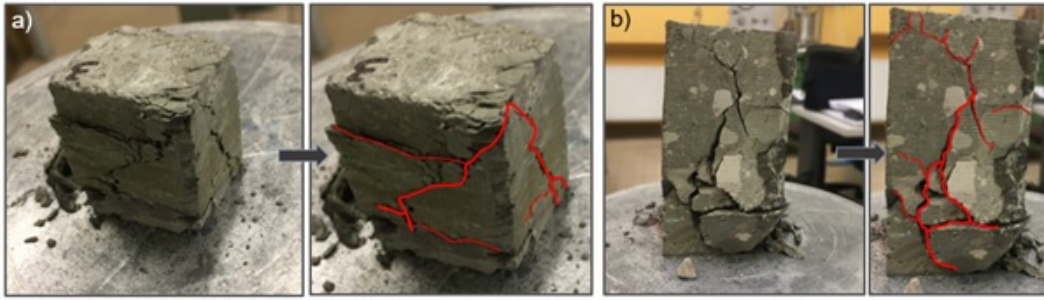
Figure 6.39: Failure surface of specimens under uniaxial compression: a) matrix-only melange specimen (sample 3); b) heterogeneous melange specimen (sample 4).

However, VBPs less than 7% would not have justified this outcome.

The explanation of this behavior is probably related to the presence of unexpected non-calcareous blocks within the heterogeneous melange samples. Specifically, when the specimens were disaggregated after each test, an often relevant number of non-rocky inclusions was found, composed of highly overconsolidated clay. A striking example is given in Figure 6.40.

As shown in Figure 6.41, sometimes these inclusions showed fractures and cracks during the tests, which made it possible to easily identify them. Their damaging also indicates that their strength is probably greater than that of matrix but lower than that of the limestone inclusions.



Figure 6.40: A 2 cm overconsolidated clay inclusion within a heterogeneous melange specimen failed in uniaxial compression. The result of this test was discarded because it was considered not to be representative.
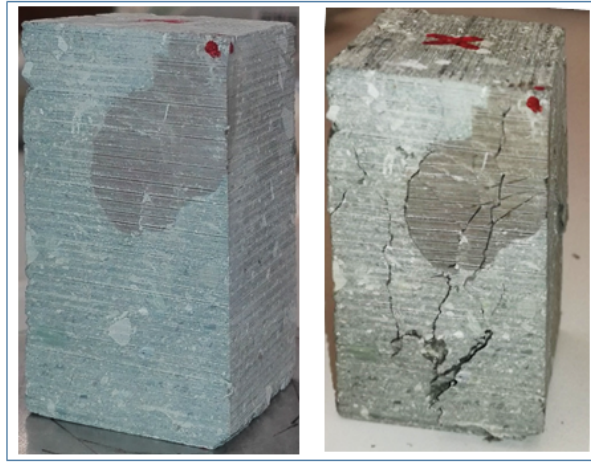
Figure 6.41: A heterogeneous specimen with an overconsolidated clay inclusion (upper brown inclusion), before and after the failure in uniaxial compression. Fractures developed also within the overconsolidated clay inclusion.

The presence of these inclusions enhanced the development of tortuous failure surfaces and probably affected the strength of the material to some degree, as well. However, it was not possible to quantify the volume fraction and size of these overconsolidated clay inclusions. In fact, they could not be separated from the matrix when the specimens were in dry conditions and they degraded in water before the sieve analyses (for the VBP estimation) could start.

Hence, the VBPs listed in Table 6.13, which refer to the rocky components only, do not fully reflect the amount of inclusions stronger than the matrix, which could have also affected the final UC test results.

### 6.7.3 Deformability results

The global strains inferred from the LVDT mounted on the edge of the samples were used to obtain the graphs shown in Figure 6.36. However, these values could not be considered reliable to determine the elastic modulus of the melange for several reasons. First of all, the presence of friction between the specimen ends and the steel platens, as well as the different elastic properties of the two materials (i.e., steel and melange), cause shear stresses at the specimen ends as a result of end restraint. As illustrated by Figure 6.42, this condition leads to a triaxial stress state (close to the ends of the specimen) that tends to transform into a uniaxial state of stress towards the center of the specimen. Moreover, the heterogeneity of the geomaterial and the settling/rotation of the top loading plate due to both the non-planarity and non-parallelism of the bases of the specimens can produce higher global than local (i.e., actual) strains.
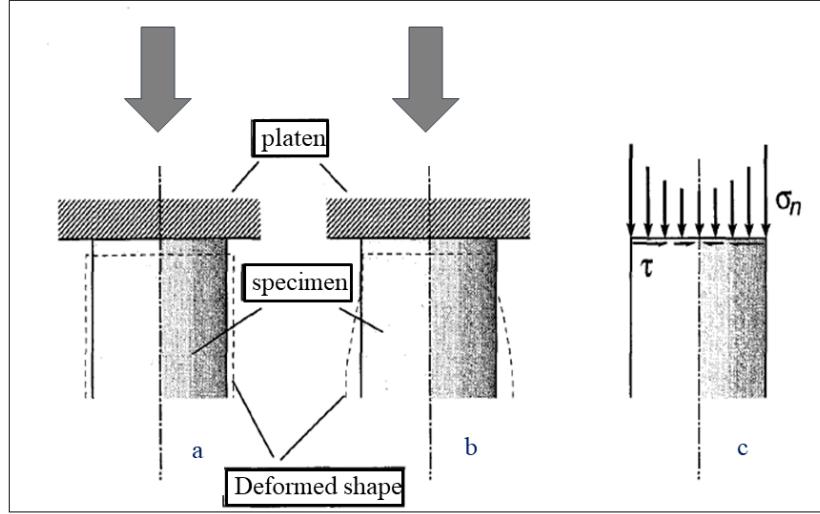
Figure 6.42: Influence of the end-effects caused by the specimen-steel platen contacts on the distribution of stress and displacement inside a cylindrical specimen under uniaxial compression. (a) Theoretical uniform deformation of the specimen; (b) real deformation due to radial restraint at the specimen-platens contact; (c) non-uniform normal stress, $\sigma$, and shear stress, $\tau$, induced at the specimen-platen contacts (Pellegrino et al. 1997).

Therefore, the DIC analysis was used to calculate the deformability modulus of 2 matrix-only and 4 heterogeneous specimens tested.

The DIC technique was applied using the 2D open source Ncorr software package implemented in Matlab (Blaber et al. 2015). The photographs necessary for the analyses were acquired continuously throughout the uniaxial compression tests, using a Canon EOS 550D digital camera. As shown in Figure 6.34, the camera was placed on a tripod in front of one specimen surface, taking photos every 5 seconds. This time interval was considered sufficiently large to allow the photos to be stored, but at the same time small enough to capture the displacements during each test. To guarantee good image quality, the ISO of the camera was set at 200. Since this is quite a low ISO value, a halogen lamp was used to work in sufficiently bright conditions (Figure 6.34). A higher ISO setting would have made the camera sensor more sensitive to light (i.e., photos could have been taken in darker conditions without the need to use a flash), but would have also created more noise, producing a lower image quality. The aperture of the diaphragm, which regulates the amount of light that passes through the lens to the camera sensor, was set to intermediate values, f/7-f/11.

The surface of the homogeneous (i.e., matrix-only) specimens was speckled before the tests, as shown in Figure 6.43, in order to determine the displacements of

the same pixels correctly. This operation was not necessary for the heterogeneous specimens, since the presence of two contrasting components (i.e., blocks and matrix) was sufficient for the software to produce good results.



Figure 6.43: Homogeneous specimen n.1 speckled for the DIC analysis.

The Ncorr program requires the definition of a region of interest (ROI) on the reference image. On this region, the user must identify the subsets (i.e., smaller regions) on which to perform the analysis (Figure 6.44). In this research, the edges of the specimen were excluded from the ROI in order to avoid numerical errors during the computation.

The similarity between the reference subset and the current subset is defined by comparing the gray scale values within the reference subset with the gray scale values within the current subset. To do this, a cross correlation algorithm based on the nonlinear least squares criterion is used, in which the optimization is performed by applying the Gauss-Newton iterative method starting from a first attempt solution (Blaber et al. 2015).
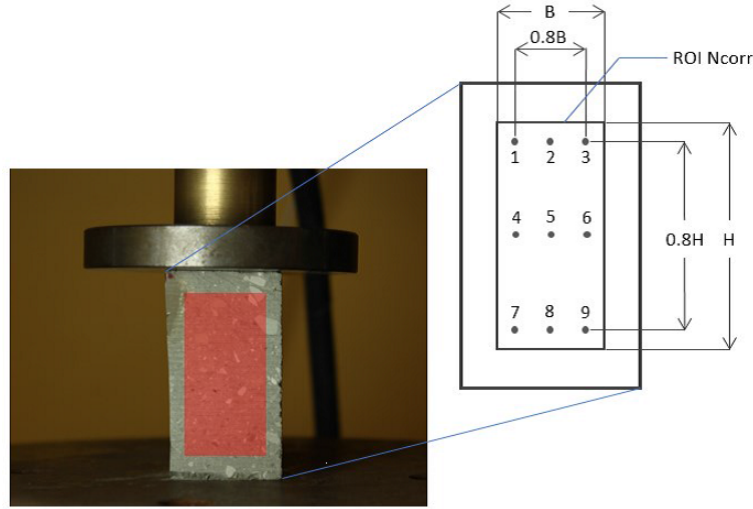
Figure 6.44: An example of the ROI and subsets for a heterogeneous specimen tested.

At first, the 9 points of Figure 6.44 were defined inside the ROI region to calculate their displacement and the corresponding deformation. The points were located far enough from the edges of the specimen for the reasons highlighted above. The deformability values obtained with the Ncorr program were then associated with the corresponding axial stresses, using the timestamps included in the output file of the data acquisition system. However, the results in terms of stress-strain relationship showed a high dispersion. An example is given in Figure 6.45 for the specimen n. 8.
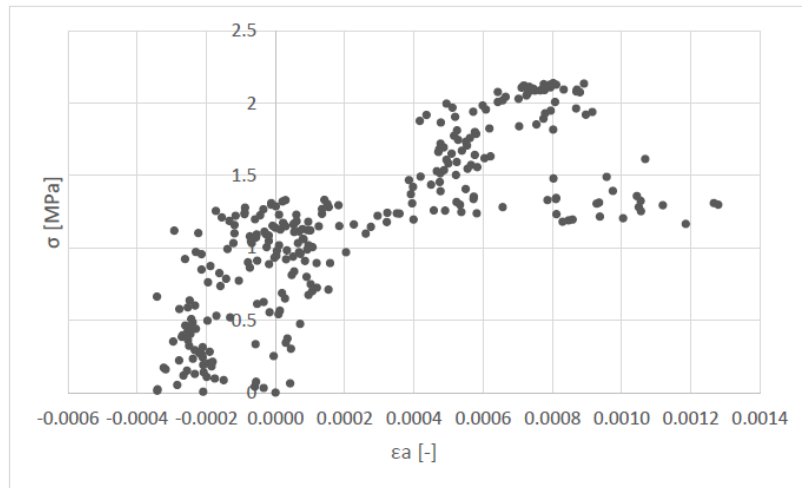


Figure 6.45: Results obtained from the DIC analysis on the specimen n.8 taking the axial deformation of a single point into account.

Moreover, since the deformability of the melange would have been defined according to the behavior of single points, this was considered as a major limitation due to the heterogeneity of the specimens. Hence, it was decided to take into account the deformations of the three vertical lines joining points 1-7, 2-8 and 3-9 of Figure 6.44. From the analysis of the axial displacements of these lines, intersecting both blocks and matrix, their deformations could easily be obtained from Eq. 6.13:

$$\varepsilon_{yP_0P_1,i} = \left(\delta_{yP_1,i} - \delta_{yP_0,i}\right)/l_{P_0P_1,in} \tag{6.13}$$

being:
$\varepsilon_{yP_0P_1,i}$ the axial deformation at time i between two points, say $P_0$ and $P_1$;
$\delta_{yP_1,i}$ and $\delta_{yP_0,i}$ vertical displacements of points $P_0$ and $P_1$ at time i;
$l_{P_0P_1,in}$ is the initial (vertical) distance between points $P_0$ and $P_1$.

The deformation values obtained were considered representative of the overall behavior of the melange. The results obtained (i.e., stress-strain curves) are shown in Figures 6.47, 6.48 and 6.49 for specimen n. 7, by way of example. The blue part of each curve indicates the data linearized and then used to determine the elastic modulus. This linearization interval was chosen so as to have an almost linear elastic stress-strain behavior.
The stress-strain curve constructed using the global axial deformations is also provided in Figure 6.46 for the same specimen.
Finally, Table 6.15 contains, for specimens 1, 2, 4, 5, 7 and 8, the elastic modulus obtained using the global deformations from the LVDT ($E_{glob}$), the three moduli obtained with the DIC technique with reference to the 3 lines (i.e., points 1-7, 2-8 and 3-9 of Figure 6.44) and their average value, $E_{averageDIC}$.
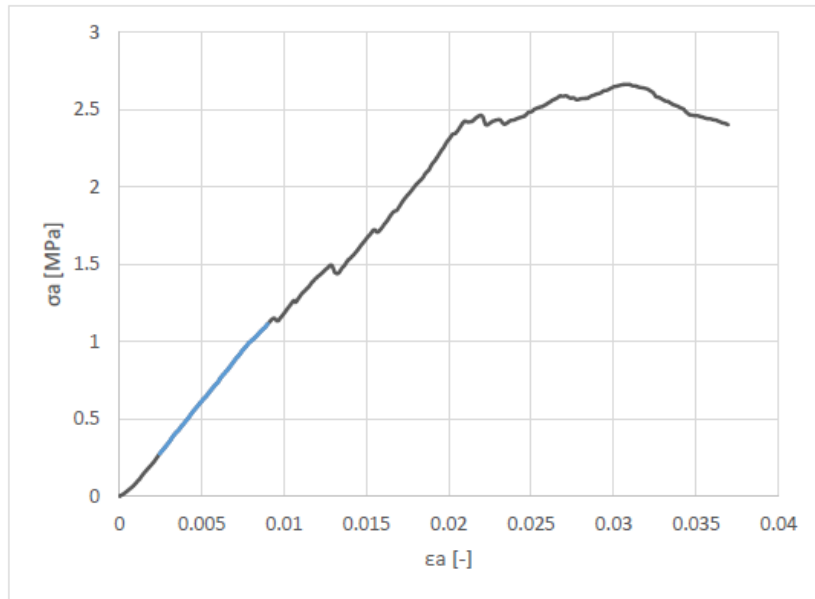
Figure 6.46: Axial stress vs. global axial strain curve. The blue segment corresponds to the data linearized and then used to determine the elastic modulus.
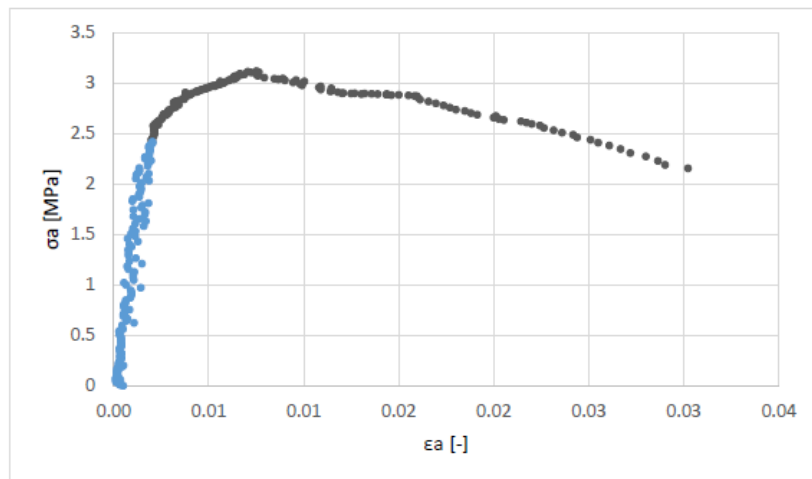


Figure 6.47: Axial stress vs. local axial strain curve of specimen n. 7, obtained for the first line with the DIC technique.
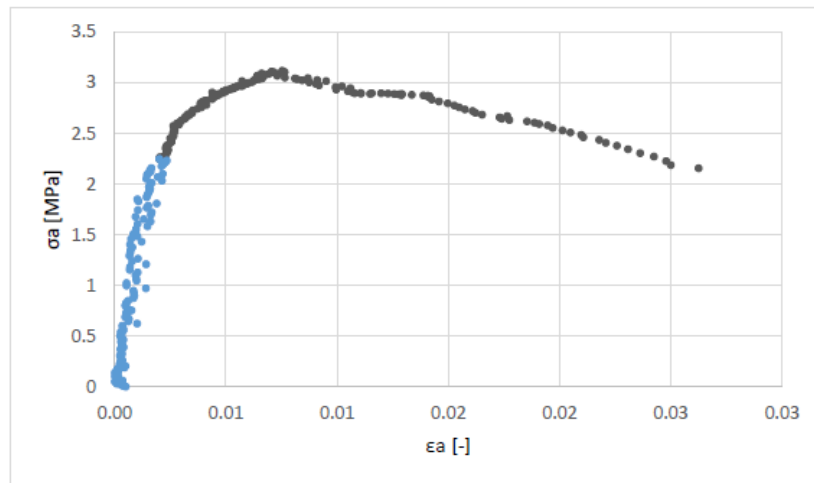
Figure 6.48: Axial stress vs. local axial strain curve of specimen n. 7, obtained for the second line with the DIC technique.
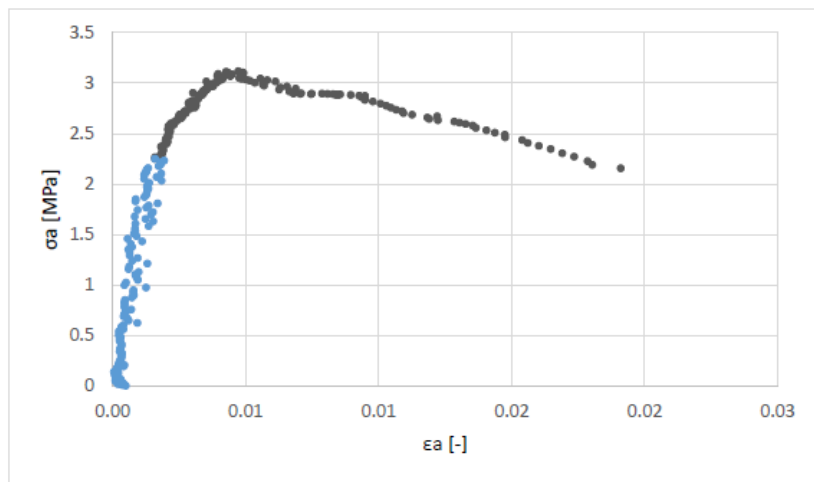


Figure 6.49: Axial stress vs. local axial strain curve of specimen n. 7, obtained for the third line with the DIC technique.

| Specimen | VBP [%] | UCS [MPa] | $E_{glob}$ [GPa] | $E_{1-7DIC}$ [GPa] | $E_{2-8DIC}$ [GPa] | $E_{3-9DIC}$ [GPa] | $E_{averageDIC}$ [GPa] |
|----------|---------|-----------|------------------|--------------------|--------------------|--------------------|------------------------|
| 1 | 0 | 2.20 | 0.30 | 0.32 | 0.29 | 0.40 | 0.39 |
| 2 | 0 | 0.98 | 0.30 | 1.47 | 2.10 | 0.76 | 1.44 |
| 4 | 5.13 | 2.03 | 0.13 | 0.22 | 0.16 | 0.23 | 0.20 |
| 5 | 6.88 | 2.40 | 0.17 | 0.38 | 0.39 | 0.38 | 0.38 |
| 7 | 4.93 | 3.12 | 0.45 | 1.27 | 1.10 | 1.32 | 1.23 |
| 8 | 2.56 | 2.15 | 0.18 | 1.15 | 1.09 | 0.99 | 1.08 |

Table 6.15: Elastic modulus obtained using the global deformations from the LVDT ($E_{glob}$), elastic moduli obtained with the DIC technique with reference to the 3 lines (i.e., points 1-7, 2-8 and 3-9 of Figure 6.44) and their average value, $E_{averageDIC}$.

As can be seen from Table 6.15, the three deformation moduli obtained by means of the DIC technique for the three lines of each specimen were definitely comparable. Although a slight difference can be observed in the results obtained for the specimen n. 2, the other specimens analyzed showed only a small variability, almost certainly caused by the heterogeneity of the geomaterial. This outcome seems to confirm the consistency and reliability of the results found with the DIC technique. Moreover, the average deformation modulus obtained for each specimen with the DIC analysis, $E_{averageDIC}$, is significantly higher (up to 5 times) than that found using the global deformations, $E_{glob}$.

This result indicates that the estimation of the deformability modulus should not be performed using global deformations, which are affected by the many uncertainties described above and can lead to a significant underestimation of the E values. Finally, the results shown in Table 6.15 also highlight that important differences in the deformability of this geomaterial do exist. Specifically, the deformability moduli of specimens 1, 4 and 5 seem to be much lower than those of specimens 2, 7 and 8, although not relevant differences in their UCS were generally found. Moreover, specimens 4 and 5 had the highest VBPs (which generally leads to higher elastic moduli) while specimen 2 had no blocks but the highest elastic modulus.

This discrepancy in the results is difficult to explain. However, it could be argued that factors such as the presence of overconsolidated clay inclusions in specimens 7 and 8, undulated (i.e., non-parallel) bedding planes, or innate micro-fractures within specimens 1, 4 and 5 may have affected the deformability of the melange differently. Likewise, microfractures or other defects on the surface of specimens analyzed with the DIC technique may also have influenced the result of this analyses, leading to lower elastic moduli than expected. This could be the case of specimen 7, whose elastic modulus $E_{averageDIC}$ is only 0.39 GPa. In fact, from the stress-strain curves of Figure 6.36, the highest elastic moduli were expected to be obtained for specimens 1 and 7.

To conclude, the specimens tested and analyzed with the DIC technique provided an overall average elastic modulus of 0.79 GPa, with a minimum of 0.2 GPa and a

maximum value equal to 1.44 GPa.

## 6.8 Ring shear tests

The residual shear strength represents the lowest shear stress that a soil reaches after very large displacements. This parameter is particularly important when assessing slope stability.

The test is carried out in drained conditions under controlled displacement rates, deforming an anular specimen of remolded cohesive soil of 5 mm thickness. The shear device keeps the cross-sectional area of the shear surface constant during the test. The specimen is subjected to a constant vertical stress and to a continuous rotational shear. In such a way, clay particles become oriented parallel to the direction of shear until a residual strength condition is achieved on a single shear plane.
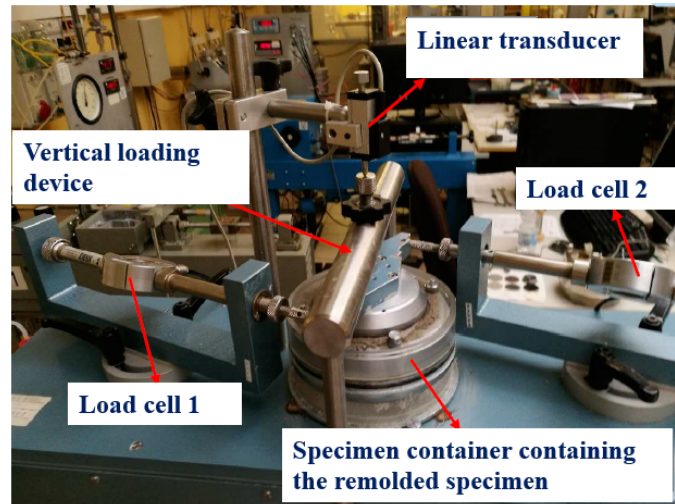


Figure 6.50: Shear apparatus of the Geotechnical Laboratory of Politecnico di Torino.

The ring shear test is very useful since it allows to test one specimen under variable normal stresses and to obtain a shear strength envelope for the material under study. This result is applicable to assign the shear strength in slopes with preexisting shear surfaces (i.e., sheared bedding planes, joints, faults, old landslides) (ASTM-D-6467 1999).

In order to determine the residual shear strength of the melange under study, it was decided to perform two ring shear tests (Figure 6.50). The choice of working with more than a single sample resulted from the heterogeneity of the geomaterial under study: in order to verify the reliability of the result, at least two tests were considered necessary.

## 6.8.1   Preparation of the remolded melange specimen

The melange was first properly sieved so that the maximum grain size did not exceed 10 per cent of the initial height of the specimen, equal to 5 mm. As suggested by the ASTM Standards, the material tested cannot contain grains greater than 0.425 mm (sieve 40 ASTM). The specimen was prepared using distilled water until a humidity approximately between the liquid limit and the plastic limit was obtained. In order to allow a complete rehydration, the soil paste obtained was film-protected and left for about 24 hours in a humidity controlled room. The material was then carefully placed in the anular cavity of the specimen container (on porous stones previously boiled) by means of a spatula, trying not to incorporate air bubbles (Figure 6.51). Finally, the specimen was submerged in distilled water.
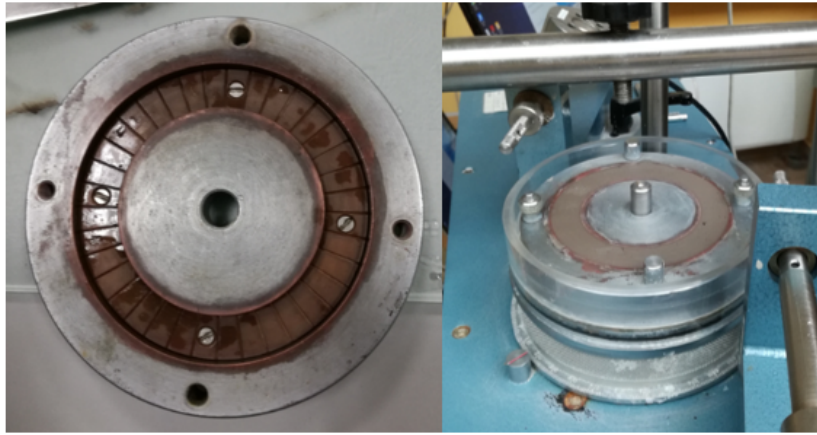


Figure 6.51: On the left: the porous stone; On the right: the anular cavity of the specimen container filled with the soil paste.

## 6.8.2   Procedure

After the specimen is placed in the anular specimen container, a vertical load has to be applied on it to induce a normal stress, $\sigma'_n$. The specimen is consolidated under this normal stress. This phase can be considered concluded when the curve of vertical displacements versus square root of time tends to an asymptote (i.e., when the volume changes due to dissipation of $\Delta$u are considered terminated). For the material under examination, primary consolidation lasted 24 hours. Once the consolidation phase is finished, a pre-shearing phase (i.e., rapid shear) starts. In this phase, fast rotations are applied to the ring shear base until the device makes two complete revolutions with a constant speed of 6°/min, in order to quickly create a well-defined shear surface. The deformations during the consolidation and cutting phases can be monitored using a linear transducer. The torsion transmitted to the specimen is measured by two load cells. Linear transducer and load cells must be

connected to a computer for data acquisition and processing. Before proceeding with the next phase, dissipation of excess pore pressure must be guaranteed by waiting for an adequate time. Then, the shearing phase starts. In order for the test to be considered drained, the rotation speed of the specimen must be slow enough to prevent the formation of interstitial overpressures. According to the BS regulations (BS 1377-7 British Standard 1990) a very slow speed of 0.048°/min, considered suitable for a wide variety of soils, was applied.

Once the shearing process (consolidation, pre-shearing and shearing phases) is completed, the procedure is repeated with higher normal stresses until the entire test sequence ends. The loads applied to the melange samples were 20 N, 40 N, 80 N and 160 N.

### 6.8.3 Results

The shear strength envelope was determined plotting the normal stresses applied versus shear stresses. The normal stress acting on the failure plane is given by the following Eq. 6.14:

$$\sigma'_n = \frac{P10g10^{-3}}{A} + \sigma_{tc} \tag{6.14}$$

where:
$\sigma'_n$ = normal stress [kPa]
P = normal vertical force acting on the specimen [N]
10 = lever ratio of the ring shear apparatus used
g = acceleration due to Earth's gravity, equal to 9.81 $m/s^2$
A = specimen cross section, equal to 40.055 $cm^2$
$\sigma_{tc}$ = stress induced by the top cap, equal to 4.4 kPa,
while the shear stress resisting slippage between the surfaces of the failure plane is given by Eq. 6.15:

$$\tau = \frac{3(F_1 + F_2)L}{4\pi(R_2^3 - R_1^3)} \tag{6.15}$$

where:
$\tau$ = shear stress [MPa]
$F_1$ and $F_2$ = load on the load cells [N]
$R_1$ and $R_2$ = inner and outer radii of the specimen, equal to 50 and 35 mm, respectively
L = torque arm length, equal to 152.5 [mm].

Since the two samples tested showed almost the same behavior, for the sake of brevity only the results of the first ring shear test are given in Table 6.52 and Figure 6.53. The residual friction angle found is $\phi_r = 6°$.

| Test | Load, P [N] | $\sigma'_n$ [kPa] | $\tau$ [kPa] |
|------|-------------|-------------------|--------------|
| 1 | 20 | 53.4 | 3.1 |
| 2 | 40 | 102.4 | 10.5 |
| 3 | 80 | 200.3 | 19.1 |
| 4 | 160 | 396.2 | 42.4 |

Figure 6.52: Ring shear test results.
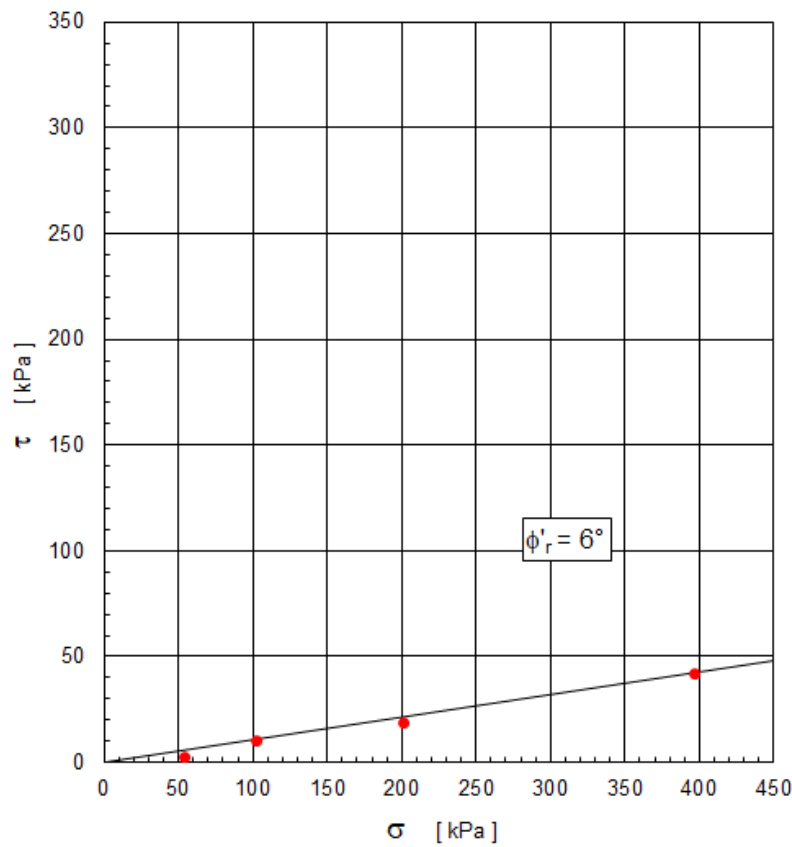


Figure 6.53: Shear strength envelope.

Since the clay fraction of the melange is very high, and greater than 50%, the residual strength is primarily dependent on the constituent minerals of the soil (Skempton 1964, Skempton 1985, Suzuki et al. 2005). According to previous findings from the literature, the angle of residual shearing resistance can reach very low values, for example around 15° for kaolinite, 10° for illite or clay mica and 5° for montmorillonite. Hence, a residual friction angle of about 6° for the melange can be explained by the presence of the montmorillonite clay mineral. However,

according to previous research related to similar geomaterials (D'Elia et al. 1986, Leroueil et al. 1997, D'Elia et al. 1998), this can be considered as a conservative result. In fact, the complex fabric of the undisturbed melange is characterized by the presence of angular and bonded coarse particles. This positively influences the behavior of the material that conversely, in remolded conditions, presents a lower shear strength.

# Chapter 7

# Triaxial tests

With the aim of investigating how the presence of blocks may affect the strength and deformability of a *soft bimrock*, a series of isotropically consolidated undrained (CIU) triaxial tests were carried out.

Since the collection and preparation of intact soft bimrock specimens is an extraordinarily difficult task, as discussed in detail in Chapter 5, and particularly because of the inherent variability of these heterogeneous formations, the use of reconstituted samples was necessary (Xu et al. 2011). In fact, natural specimens with different matrix properties and block dimensions, contents and positions do not allow tests to be carried out under controlled conditions and the results to be reliably compared. However, natural geomaterials were used to create both the matrix and blocks in order to simulate a real soft bimrock as closely as possible.

The consolidometer of the Geotechnical laboratory operating in the Department of Structural, Geotechnical and Building Engineering of Politecnico di Torino was used to consolidate the samples and obtain an overconsolidated clayey matrix, like that of the melange of the Oltrepò Pavese.

Three homogeneous specimens were tested to define the geomechanical characteristics of the consolidated soil, representing the matrix of the remolded soft bimrock. Then, two heterogeneous (remolded) specimens with different VBPs were tested at the same confining pressure to compare the results.

Another purpose of this laboratory investigation was to obtain all the necessary information to be able to set up and calibrate a 3D numerical model reproducing the experimental results. The model, which is beyond the scope of this work, could be an important tool to contribute to a deeper understanding of the mechanical behavior of soft bimrocks. In fact, by means of an appropriately set up numerical model based on laboratory test results obtained from natural geomaterials, it would be possible to analyze the behavior of similar soft bimrocks with other characteristics in terms of VBPs, mechanical parameters and geometrical configurations, as well as other stress history scenarios.

In order to allow accurate 3D specimen models to be created, the geometrical

properties of the specimens as well as the dimension and initial position of the rock inclusions were detected (before the tests) by means of X-ray Computed Tomographies (CT), which were carried out at Microservice S.r.l., Alpignano, Torino (see Section 7.1.4).

## 7.1 CIU triaxial tests

Consolidated undrained triaxial tests are used to determine the strength and stress-strain relationships of a cylindrical specimen of either an intact, reconstituted, or remolded saturated cohesive soil (ASTM 2020). The cylindrical specimen should have a minimum diameter of 33 mm and an average H/D ratio between 2 and 2.5. It must be enclosed in a thin rubber sleeve sealed to the top platen and to the base pedestal by rubber O-rings. The rubber sleeve is intended to (i) transmit a uniform cell pressure onto the soil specimen and (ii) provide reliable protection against leakage. Two rigid porous disks positioned at the ends of the specimen are used to allow the drainage. To avoid their clogging, filter-paper disks can be placed between the porous disks and specimen. Filter-paper strips for radial drainage are also generally used to decrease the time required for testing. They can be located on no more than 50% of the periphery of the specimen.
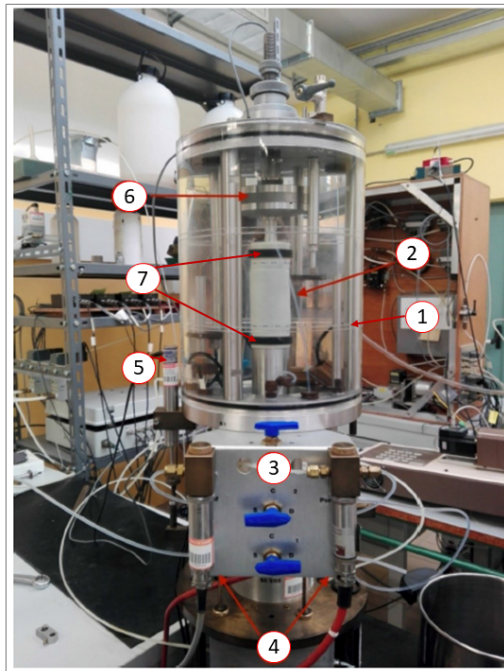


Figure 7.1: Triaxial apparatus of the DISEG Geotechnical laboratory - Politecnico di Torino. 1) Cell; 2) Rubber sleeve containing the specimen; 3) drainage valves; 4) differential pressure transducers; 5) LVDT; 6) Axial load cell; 7) O-rings.

Once the specimen is mounted in the triaxial chamber (Figure 7.1), this is filled with the chamber liquid and the first saturation phase can start.

Saturation is usually accomplished by applying a back pressure to the specimen pore water, in order to cause air in the pore space to compress and to drive it into solution after saturating the system. The chamber and back pressure must be incrementally and simultaneously increased in steps, with specimen drainage valves opened so that de-aired water from the burette connected to the top and bottom of the specimen may flow into it. Adequate time between pressure increments permits the equalization of pore-water pressure throughout the specimen, avoiding undesirable pre-stressing. The size of each increment may range from 35 kPa up to 140 kPa. Moreover, the difference between the chamber pressure and the back pressure (i.e. the effective stress) should not exceed 35 kPa (ASTM 2020). To determine if saturation is completed, the pore pressure Parameter B should be calculated with the specimen drainage valves closed. This parameter is defined by the following Eq. 7.1:

$$B = \frac{\Delta u}{\Delta \sigma_3} \tag{7.1}$$

where:

$\Delta u$ = change in the specimen pore pressure that occurs as a result of a change in the chamber pressure when the specimen drainage valves are closed

$\Delta \sigma_3$ = change in the chamber pressure.

Specimens can be considered to be saturated if the value of B is $\geq 0.95$.

After saturation, the specimen consolidation phase can start. The specimen is isotropically consolidated by maintaining the maximum back pressure constant and increasing the chamber pressure, until the difference between these two pressures equals the desired effective consolidation pressure. This phase allows the specimen to reach equilibrium in a drained state at a given effective consolidation stress level. Consolidation ends when the complete dissipation of the pore pressures occurs.

When consolidation is completed, the shear phase can start. The chamber pressure must be kept constant while advancing the axial load piston downward against the specimen cap at a constant rate of axial strain. During this phase, specimen drainage is not permitted.

The measurement of the axial load, axial deformation and pore-water pressure allows the total and effective stresses to be calculated.

Finally, a strength envelope can be obtained by performing three tests at different effective consolidation stresses.

## 7.1.1 Procedure

CIU triaxial tests were performed on 3 matrix-only and 2 heterogeneous reconstituted specimens at the Geotechnical laboratory operating in the Department of

Structural, Geotechnical and Building Engineering of Politecnico di Torino. Details on the preparation of the specimens are given in the next Section 7.1.2. The cylindrical specimens used had a diameter of 38.1 mm and a height of 76.2 mm, so that the H/D ratio was equal to 2. Filter-paper disks of a diameter equal to that of the specimens were placed between the two porous disks and specimens. Moreover, filter strips on the periphery of the specimens were also used to decrease the duration of the tests.

During the saturation phase, pressure increments of 50 kPa were applied and the difference between the chamber pressure and the back pressure was kept at 20 kPa. The results of the tests are illustrated in the Section 7.1.3.1.

## 7.1.2 Preparation of the specimens

As stated above, triaxial tests could not be carried out on the Oltrepò Pavese melange (Chapter 5), since cylindrical specimens could not be created. Moreover, the variability of the matrix and block characteristics would not have allowed controlled laboratory conditions to be achieved. Hence, reconstituted samples were fabricated in the laboratory, in order to simulate the Oltrepò Pavese melange as closely as possible.

Two consolidations were made using the consolidometer of the Geotechnical laboratory of Politecnico di Torino shown in Figure 7.3. The first was performed on a homogeneous matrix-only material while the second regarded a heterogeneous material.

### 7.1.2.1 Homogeneous specimens

The homogeneous specimens were obtained from a total of more than 2.5 kg of intact melange lumps. They were first submerged in distilled water and then sieved at 0.075 mm to remove (medium and coarse) sand and larger particles. Then, the sieved material was mixed at a relatively large water content (equal to about $1.2w_L$). This water content was considered sufficient to avoid the formation of air bubbles within the material during the consolidation phase.

The material finer than 0.075 mm obtained during the process for grading the melange (Section 6.4) was also used. Its dry weight was about 5 kg. Since it was dried in a oven (i.e. it was in a solid state), it was appropriately crumbled and remoistened to a water content of about $1.2w_L$.

Then, the soil-water mixture was thoroughly kneaded and stirred inside a plastic container to make it fluid and homogeneous (Figure 7.2). From the plastic container, the material was then transferred into the steel consolidometer cylinder (shown in Figure 7.5a) to fill it completely, a little at a time. The filling of the cylinder was done gradually to prevent the formation of air bubbles.

196

Figure 7.2: Sieved soil mixture inside the plastic container.

After assembling the apparatus, the soil was recompressed at the maximum surcharge load of the consolidometer (Figure 7.3), 500 kPa, to simulate the real Oltrepò Pavese melange conditions as closely as possible. In fact, since the sedimentary melange is heavily overconsolidated, a higher surcharge load allows triaxial tests to be performed on highly overconsolidated specimens.
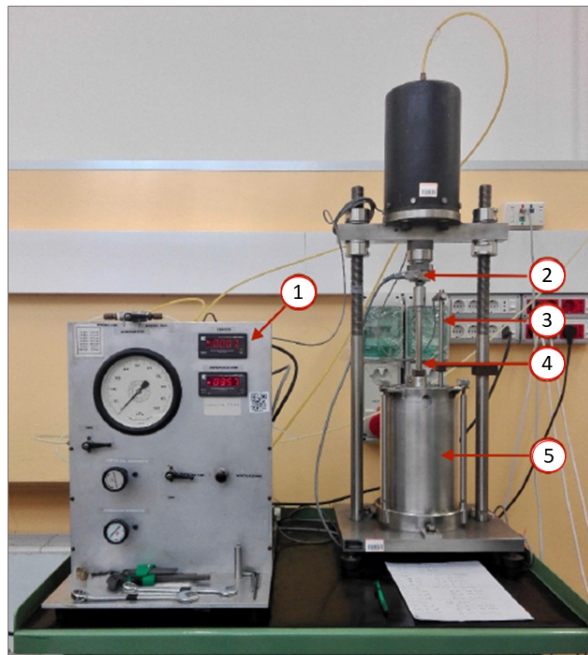


Figure 7.3: The Consolidometer of the DISEG Geotechnical laboratory - Politecnico di Torino. 1) Load cell display; 2) load cell; 3) LVDT; 4) loading piston; 5) consolidometer cylinder.

197

### 7.1.2.2 Heterogeneous specimens

The heterogeneous specimens were obtained in a similar way, with the difference that rock blocks in the range 2-4.75 mm (sieve ASTM E11) were added to the soil mixture. A mechanical mixer was used to distribute them homogeneously within the plastic container.

1.4 kg of gravel was used, which was estimated to produce a material with about 25% VBP. In fact, a settlement, d, of around 11 cm was expected to occur at the end of the consolidation phase. Such a settlement would provide a final volume of the material contained in the consolidometer equal to:

$V_{f_{cons}} = \pi R^2(\text{H-d}) = \pi\ 7.75^2(23\text{-}11) = 2148\ cm^3$.

Therefore, the corresponding 25% of the $V_{f_{cons}}$ was equal to 537 $cm^3$. Considering the average unit weight of the blocks to be about 26 kN/$m^3$ their volume was estimated to be equal to about 538 $cm^3$, which indeed corresponded to 25%$V_{f_{cons}}$.

Moreover, in order to have specimens with different VBPs, half of the consolidometer cylinder was filled with additional blocks, weighing in total 0.6 kg and with an expected volume of 231 $cm^3$ (i.e. 0.6 kg divided by 0.0026 kg/$cm^3$ = 231 $cm^3$), to achieve a total volume of the blocks of about 50% $V_{f_{cons}}$. These further blocks were added in subsequent stages, during the filling of the cylinder (Figure 7.4).

The real VBPs of the heterogeneous specimens were estimated after the tests, by means of sieve analyses, as described in the following Section 7.1.3.3.



Figure 7.4: Blocks added in half of the consolidometer cylinder to obtain 50%VBP specimens.

During the consolidation, the settlements were monitored to reach the asymptote. Each consolidation lasted about 6 weeks and the final settlements were about 95 mm for the homogeneous mixture and 113 mm for the heterogeneous mixture. This difference in the settlements was attributed to the higher water content used to mix

the material with the blocks, which was about $1.4w_L$ instead of the $1.2w_L$ used for the homogeneous material.

After each consolidation, the material was removed from the steel cylinder (Figure 7.5b) and cut into six slices (Figure 7.5c). Then a sampler was used to extrude the specimens (H=76.2 mm and D=38.1 mm), as shown in Figure 7.5d. Six specimens could be extracted from each consolidation, since the consolidometer cylinder was sufficiently large (230 mm high with an internal diameter of 155 mm).
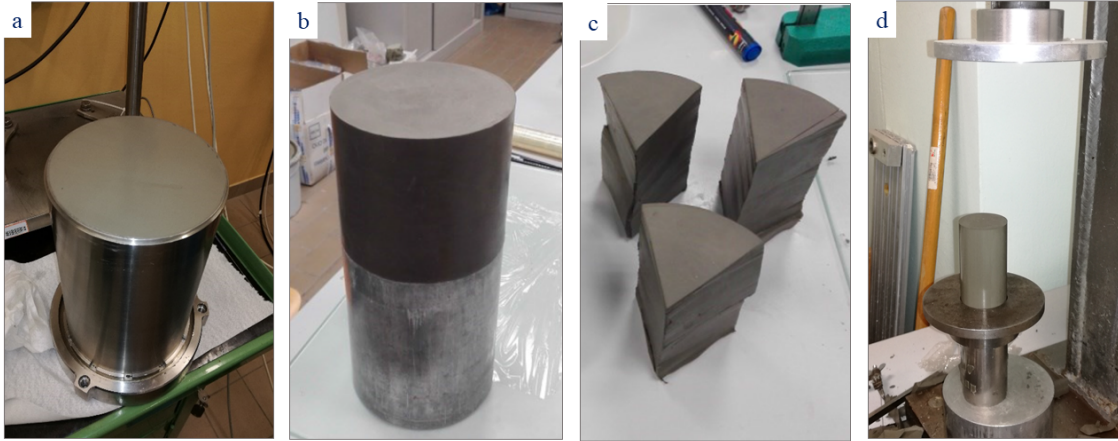


Figure 7.5: Homogeneous mixture. a) Bottom plate and cylinder (containing the remolded soil) of the consolidometer; b) extrusion of the consolidated soil; c) three of the six slices of consolidated soil for the specimen extrusion; d) a matrix-only specimen extruded.

However, when extruding the heterogeneous material from the sampler (Figure 7.6a), the presence of the blocks heavily damaged the boundary of the specimens. In fact, when the sampler encountered a block, this was dragged down, creating a furrow along the edge of the specimen, as clearly visible in Figure 7.6b.

In order to avoid potential breakages of the triaxial rubber membrane during the tests, the geometry of the heterogeneous specimens was regularized. The voids created by the blocks during the extrusion phase were filled manually with the consolidated matrix material, obtaining the result shown in Figure 7.6c. Moreover, in order to avoid membrane perforation during the triaxial tests, two membranes were used instead of one.
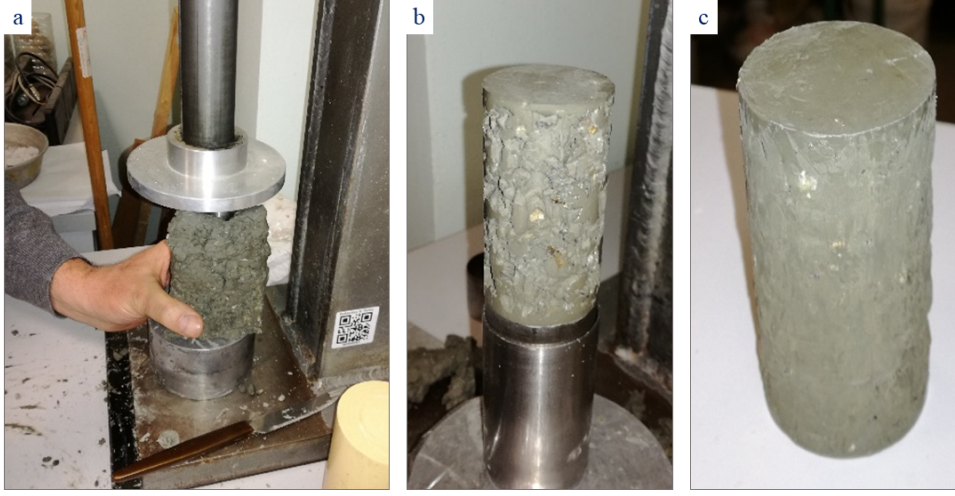
Figure 7.6: Extrusion phase of the heterogeneous material with 50%VBP. a) a slice of heterogeneous material before the extrusion; b) the extruded 50%VBP specimen; c) regularized heterogeneous specimen with 50%VBP.

After the regularization, the specimens were wrapped in thin plastic film and coated with wax, before being transported to the Microservice S.r.l. laboratory for the X-ray CT.

### 7.1.3   CIU test results

The characteristics of the 5 specimens tested are listed in Table 7.1. All the specimens had the same initial geometric dimensions (D=38.1 mm and H=76.2 mm) and were loaded at 0.016 mm/min.

| Specimen | VBP | $\sigma_{3f}$ | w | e | $\gamma_{dry}$ | $\sigma_c$ | BP | $q_{failure}$ | $\varepsilon_{failure}$ |
|---|---|---|---|---|---|---|---|---|---|
| | [%] | [kPa] | [%] | [-] | [kN/$m^3$] | [kPa] | [kPa] | [kPa] | [%] |
| 1 | 0 | 50 | 36.0 | 0.948 | 13.25 | 180 | 130 | 61.62 | 8.43 |
| 2 | 0 | 100 | 34.1 | 0.908 | 13.71 | 220 | 120 | 83.14 | 9.85 |
| 3 | 0 | 200 | 31.2 | 0.842 | 14.39 | 320 | 120 | 126.51 | 9.12 |
| 4 | 25 | 50 | - | - | - | 260 | 210 | 60.70 | 9.18 |
| 5 | 50 | 50 | - | - | - | 230 | 180 | 90.91 | 20.83 |

Table 7.1: VBPs, effective consolidation stress levels applied ($\sigma_{3f}$), water content (w), void ratio (e), dry unit weight ($\gamma_{dry}$), cell pressure ($\sigma_c$), back pressure (BP), deviator stress at failure ($q_{failure}$) and axial strain at failure of the specimens tested ($\varepsilon_{failure}$).

As shown in Table 7.1, the homogeneous specimens were tested at three different effective consolidation stress levels (i.e. $\sigma_{3f}$ = 50, 100 and 200 kPa) to define the strength envelope of the bimrock matrix. It is worth noticing that these $\sigma_{3f}$ values are lower than the 500 kPa applied by the consolidometer to the reconstituted material. Hence, overconsolidated specimens with an OCR ranging from 10 (for $\sigma_{3f}$ = 50 kPa) to 2.5 (for $\sigma_{3f}$ = 200 kPa) could be tested. In this regard, the minimum $\sigma_{3f}$ (i.e. 50 kPa) was used to consolidate the heterogeneous specimens in order to simulate the real Oltrepò Pavese melange as closely as possible, as well as to compare the results with those of the 0% VBP specimen (i.e. specimen 1).

### 7.1.3.1   Homogeneous specimen results

The effective (ESP) and total stress (TSP) paths obtained from the CIU triaxial compression tests on the remolded homogeneous specimens are shown on the p'-q diagram in Figure 7.7, being p' = $(\sigma'_1 + \sigma'_3)/2$ and q = $(\sigma_1 - \sigma_3)/2$.
For a clearer representation, the BP values were not considered (i.e. the TSP were shifted of a quantity BP on the left).
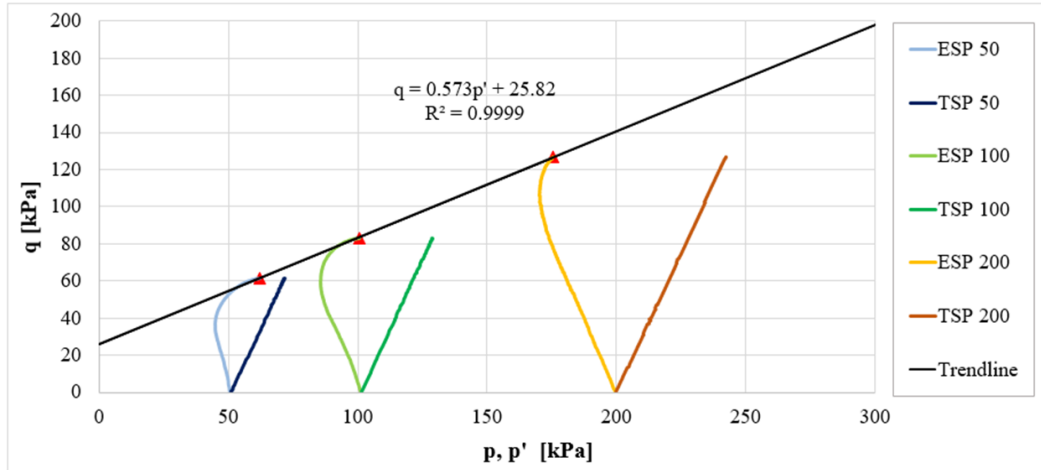


Figure 7.7: Effective and total stress paths obtained from CIU triaxial compression tests on remolded homogeneous specimens. The strength envelope is also shown.

The most striking result to emerge from the stress paths shown in Figure 7.7 is that the deviator stresses at failure ($q_{failure}$), highlighted with the red triangles, are almost perfectly aligned on a straight line. The coefficient of determination, $R^2$, of the black linear trendline in the same Figure is indeed 0.999. The equation of the trendline is:

$$q = m \cdot p' + q' \tag{7.2}$$

where: m = q/p' = 0.573 and q' = 25.82.

The strength parameters of the Mohr-Coulomb failure criterion (i.e. friction angle, $\varphi'$, and cohesion, c') were obtained from Eq. 7.3:

$$\frac{q}{p' + c'cotg(\phi')} = \frac{6 \cdot sen(\phi')}{3 - sen(\phi')} \tag{7.3}$$

as follows (Eqs. 7.4 and 7.5):

$$\varphi' = arcsen\left(\frac{m}{2 \cdot (1 + \frac{m}{2})}\right) = 15° \tag{7.4}$$

$$c' = q' \cdot \frac{3 - sen(\phi)}{6 \cdot cos(\phi)} = 12.2 \quad kPa \tag{7.5}$$

Since the tests were carried out under undrained conditions, the TSP and ESP are different because the pore pressures, $u$, changed during the tests. The horizontal distances between the TSP and ESP correspond to the excess pore pressures, $\Delta u$, generated during the tests (Lancellotta 2012). If the $\Delta u$ increases the soil compresses while if $\Delta u$ decreases the soil shows a dilatant behavior.

The ESP of specimens 1 and 2, represented in Figure 7.7, show an initial increase and subsequently a decrease in the pore pressures before reaching the peak. This is consistent with the behavior of oveconsolidated clays, which are contractant at the beginning of loading and then dilatant up to failure (Hicher et al. 2000).

The decrease of the $\Delta u$ is common when testing heavily overconsolidated soils because, when large strains occurr, strong discontinuities (i.e. slip planes) can start to form inside the specimen. Once a slip plane appears, water (which cannot enter or leave the sample) can move into it from nearby soil, creating a local drainage and increasing the water content of the soil in this shear band. The soil weakens and the slip plane continues growing till the failure occurs. As a consequence, lower $u$ and a dilatant behavior are registered.

Conversely, when testing a normalconsolidated or slightly overconsolidated soil, if a slip plane starts to form the soil generally strengthens and the slip plane cannot grow further (Atkinson 2007).

As a consequence, the mechanism of deformation and failure of normalconsolidated and slightly overconsolidated soils is generally remarkably different from that of heavily overconsolidated soils.

In this regard, a careful examination of the specimens after the tests showed an evident localization of the deformations in a shear band, inclined at an angle of about 52°, for the specimens 1 and 2 (Figure 7.8). On the other hand, as expected, a more diffuse failure was detected for the specimen 3, with the lowest OCR and highest confining pressure.

Figure 7.8: Failure modes of the three homogeneous specimens tested. From the left: specimens 1 (localized failure), 2 (localized failure) and 3 (diffuse failure), after the tests.

The relationship between the axial strain ($\varepsilon_a$) and deviator stress (q) is shown in Figure 7.9, where it can be seen that deformability decreases from specimen 1 to 3. Moreover, the stress-strain curves of all the specimens are characterized by a non linear pre-peak branch, the same strain at failure, equal to about 9%, and a post-peak slight strength reduction (i.e. softening branch), which is more marked for specimen 1.
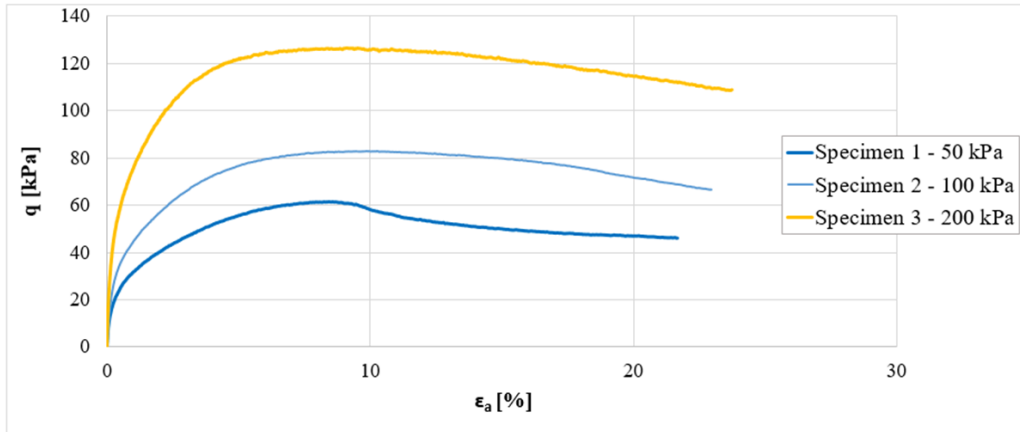


Figure 7.9: Deviator stress, q, versus axial deformation, $\varepsilon_a$.

The axial stress levels on the specimens are evaluated by the data acquisition system (as a function of time), as the ratio between the force recorded by the load cell and the current cross-sectional area of the specimen. This area is evaluated by

assuming that the specimen shape remains perfectly cylindrical during the test and that no volume change can occur. In this way, an equivalent radius is computed on the basis of the current axial strain of the specimen. However, this assumption can produce significant errors after localized or diffuse deformations appear in the specimen. Moreover, the stress state inside the specimen cannot be assumed to be uniform.

For these reasons, it was deemed appropriate to determine the deviator forces recorded by the load cell and plot them against the axial strains.

The results obtained are shown in Figure 7.10. It is apparent from this Figure that only specimen 1 presents a softening branch. Conversely, specimens 2 and 3 show a plastic-perfectly plastic post-peak behavior.
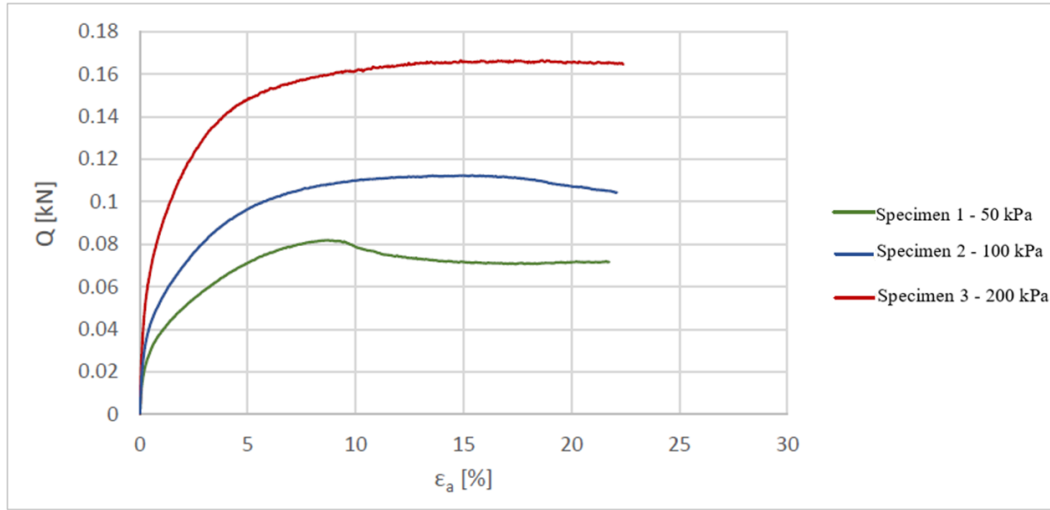


Figure 7.10: Axial deformation, $\varepsilon_a$, versus deviator force, Q, obtained from the load cell.

The lack of an evident post-peak strength reduction, at least for specimen 1, may seem anomalous since this specimen was strongly overconsolidated (i.e. OCR = 10). However, its stress-strain and force-strain relationships are more similar to those of a theoretical normalconsolidated soil.
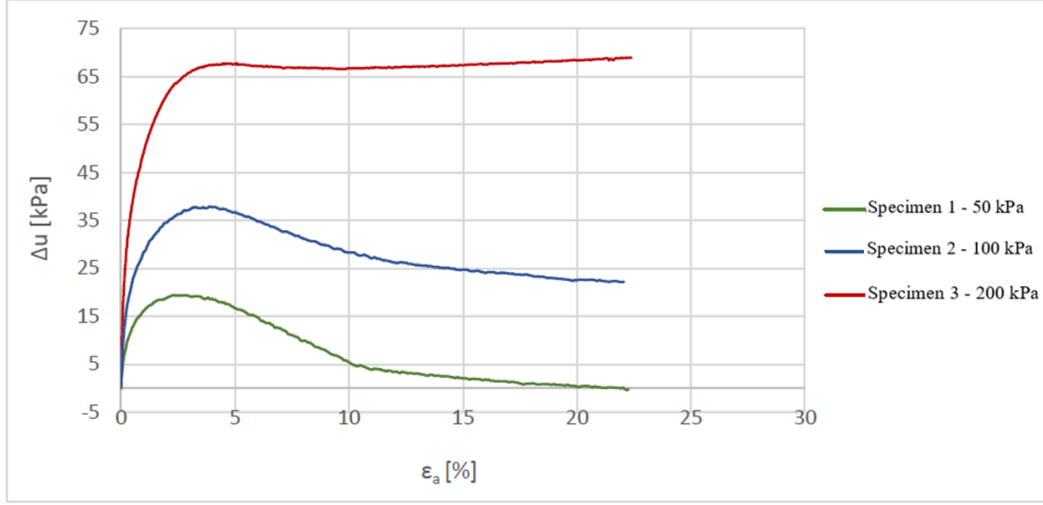
Figure 7.11: Axial deformation, $\varepsilon_a$, versus excess pore pressure, $\Delta u$. A clear decrease in the $\Delta u$ values characterizes specimens 1 and 2, confirming the dilatant behavior of the overconsolidated material. However, negative $\Delta u$, generally registered in heavily overconsolidated soils, were never achieved.

Likewise, the excess pore pressures, $\Delta u$, illustrated in Figure 7.11 against the axial deformations ($\varepsilon_a$), do not fully reflect the standard behavior of heavily overconsolidated soils. In fact, the dilatant behaviour of overconsolidated soils leads to a continuously decreasing pore pressure after failure, which generally results in both negative $\Delta u$ values and Skempton's pore pressure parameter A, which for saturated soils id defined as $\Delta u/\Delta \sigma_1$ (Burghignoli 1991). Typical values of Skempton's parameter A are listed in Table 7.2.

| Type of clay | Skempton's A parameter at failure |
|---|---|
| Normally consolidated clays | 0.5-1.0 |
| Lightly overconsolidated clays | 0.0-0.5 |
| Heavily overconsolidated clays | -0.5-0.0 |

Table 7.2: Typical parameter A values (Burghignoli 1991).

This parameter was found to be equal to only 0.147, 0.335 and 0.527 for specimens 1, 2 and 3, respectively. Hence, despite the rather high overconsolidation ratios of specimens 1 and 2, according to Table 7.2 the geomaterial should be classified as lightly overconsolidated soil, which is not the case.
A possible explanation of this result could be the low friction angle value, equal to 15° only, which could have limited the dilatancy. However, the one-dimensional

($K_0$) consolidation could also have induced microstructural changes in the re-moulded soil mixture. As proved by many authors, a reorientation of the clay particles perpendicular to the direction of loading can be registered after a one-dimensional consolidation (Martin and Ladd 1975, Sachan and Penumadu 2007, Gao 2020). Hence, this induced-anisotropic microstructure could strongly have affected the mechanical behaviour of the geomaterial tested.

Finally, the secant and tangent undrained Young's moduli ($E_{u-sec}$ and $E_{u-tan}$) of the specimens were determined from the q-$\varepsilon_a$ curves of Figure 7.9, by using the following Eqs. 7.6 and 7.7:

$$E_{u-sec} = \frac{\Delta q}{\Delta \varepsilon_a} \tag{7.6}$$

$$E_{u-tan} = \frac{\delta q}{\delta \varepsilon_a} \tag{7.7}$$

where $\Delta$ represents the change of stress and strain from the start of the test.
Specifically, the tangent moduli of the three specimens were measured at very small strains, in the range 0-0.1% $\varepsilon_a$. Since the stiffness of the specimens were highly non-linear, two secant moduli were calculated. The former at 50% of the deviator stress at failure, $q_{failure}$, and the second at $100\% q_{failure}$, corresponding to $\varepsilon_a$ equal to about 4.5% and 9%, respectively.
Then, by using the theory of elasticity the drained moduli could be found. In fact, the basic relationship between the elastic shear modulus, G, and the elastic Young's modulus, E, is given by Eq. 7.8:

$$G = \frac{E}{2 \cdot (1 + \nu)} \tag{7.8}$$

For an elastic material G'=$G_u$, hence the following Eq. 7.9 can be written:

$$\frac{E'}{2 \cdot (1 + \nu')} = \frac{E_u}{2 \cdot (1 + \nu_u)} \tag{7.9}$$

Since $\nu_u$ =0.5, the drained elastic modulus, E', can be determined from Eq. 7.10:

$$E' = \frac{2 \cdot E_u \cdot (1 + \nu')}{3} \tag{7.10}$$

by assuming a drained Poisson coefficient, $\nu'$, equal to 0.25.

The results obtained, listed in Table 7.3, confirm the strong non-linearity of the soil deformability and indicate that when higher confinements are applied (e.g. specimen 3) a significant gain in stiffness is exhibited.

| Specimen | $E'_{tan-0.1\%}$ [MPa] | $E'_{sec-4.5\%}$ [MPa] | $E'_{sec-9\%}$ [MPa] |
|----------|----------|----------|----------|
| 1 | 9.8 | 2.8 | 0.6 |
| 2 | 14.5 | 4.4 | 0.7 |
| 3 | 22.4 | 8.8 | 1.2 |

Table 7.3: Drained elastic tangent and secant moduli, E', for the three homogeneous specimens tested, assuming a drained Poisson's coefficient $\nu' = 0.25$.

### 7.1.3.2 Heterogeneous specimen results and comparison with specimen 1 results

The effective (ESP) and total stress (TSP) paths obtained from the CIU triaxial compression tests on the remolded heterogeneous specimens are shown on the p'-q diagram in Figure 7.12. The stress paths of specimen 1, subjected to the same consolidation stress, $\sigma_{3f} = 50$ kPa, are also shown, by way of comparison.
For a clearer representation, the BP values were not considered (i.e. the TSP were shifted of a quantity BP on the left).
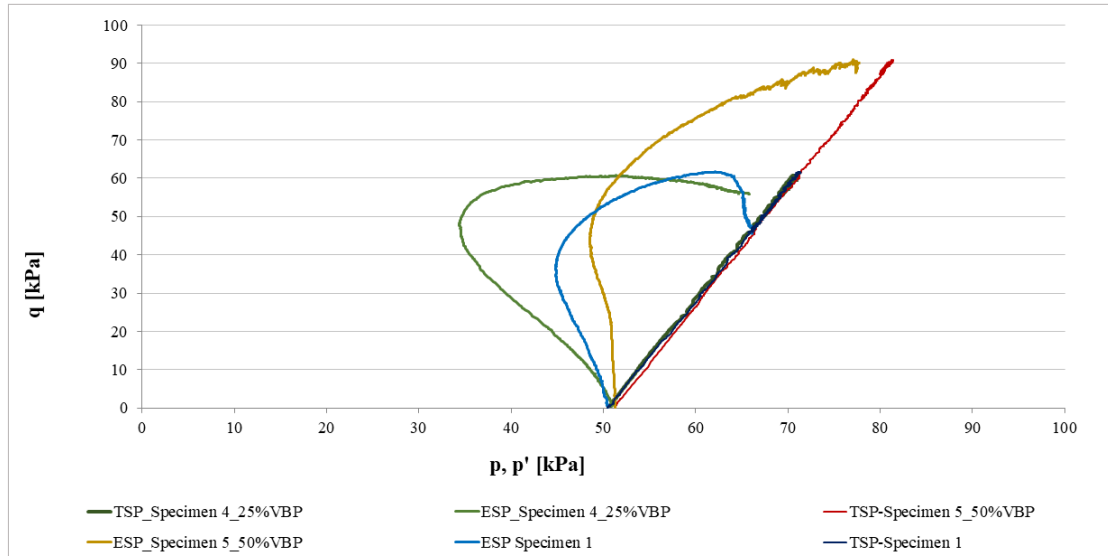


Figure 7.12: Effective and total stress paths obtained from CIU triaxial compression tests on remolded heterogeneous specimens with 25% and 50% VBPs. The ESP and TSP of specimen 1 is also shown, by way of comparison.
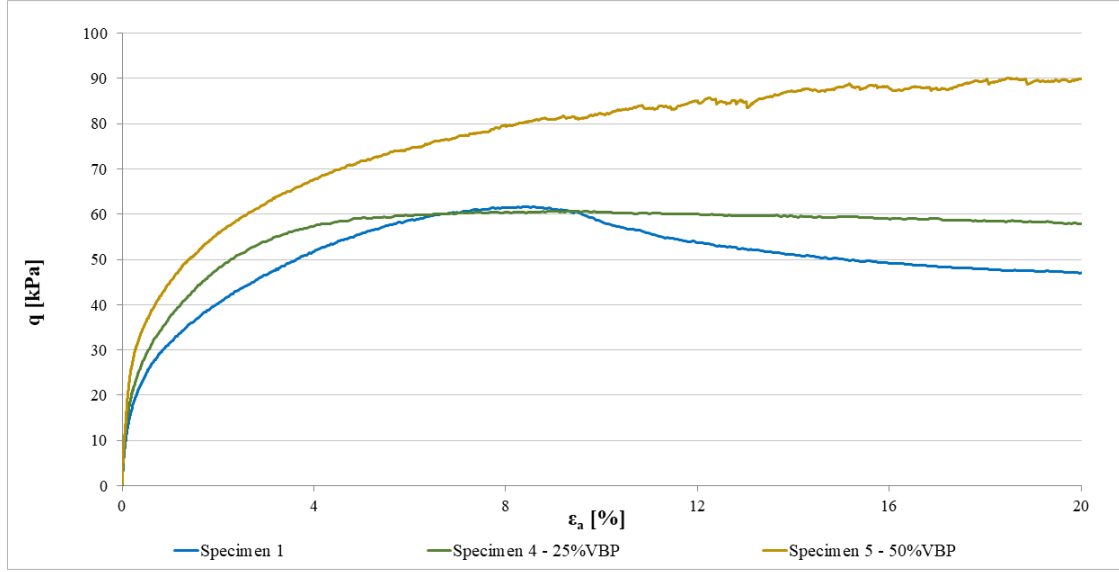
Figure 7.13: Deviator stress, q, versus axial deformation, $\varepsilon_a$. The q-$\varepsilon_a$ curve of specimen 1 is also shown, by way of comparison.

The results obtained (Figure 7.12 and 7.13) clearly indicate that when the block content is equal to 25% only (i.e. specimen 4), a rather significant stiffness increase is registered while no strength increase is observed, with respect to the homogeneous specimen 1. Moreover, the deviator stress and axial strain at failure are definitely comparable to those of specimen 1. In fact, $q_{failure}$ of specimen 4 is equal to 60.7 kPa and $\varepsilon_a$ is 9.18%. From the inspection of Figures 7.12 and 7.13, it seems that the presence of a moderate quantity of rock blocks (i.e. 25%) also led to a rather significant reduction in the matrix dilation and softening behavior. As a result, the mechanical behavior of specimen 4 resembles that of normalconsolidated (or lightly overconsolidated) clays and can be considered to be plastic-perfectly plastic. This finding is consistent with the different failure mechanism of this specimen with respect to that of the homogeneous specimen 1. As shown in Figure 7.14, the presence of the rock blocks did not allow the formation of the classic shear band to develop and the failure was not characterized by the rigid motion of the upper and lower portions of the specimen, as was observed in the case of the homogeneous material (Figure 7.8).

A much higher stiffness increase is shown when the block content is equal to 50% (i.e. specimen 5). Moreover, as can be seen from Figure 7.13, the deviator stress, q, of specimen 5 increases throughout the test and its $q_{failure}$ reaches 90.9 kPa at very large $\varepsilon_a$, greater than 20.8%.

Figure 7.14: Failure modes of the heterogeneous specimen with 25% VBP.

Unlike the homogeneous and 25%VBP specimens 1 and 4, a strain hardening behavior is exhibited by the heterogeneous specimen 5, due to the presence of a higher VBP, which limited the dilatancy. This outcome, which is in accordance with previous findings from the literature (Afifipour and Moarefvand 2014c, Xu et al. 2007, Guerra et al. 2016), can be ascribed to the interlocking of the rock blocks.

Similarly to the heterogeneous specimen 4, the presence of the rock blocks did not allow the formation of the classic localized shear band to develop within the specimen 5. The diffuse failure of this specimen is shown in Figure 7.15.



Figure 7.15: Failure modes of the heterogeneous specimen with 50% VBP.

From the inspection of Figure 7.12, it is also interesting to note that pore pressures of specimen 4 are much higher than those registered in specimen 1 and 5. This is

clearly shown in Figure 7.16, where it can be seen that the excess pore pressures, $\Delta u$, of specimen 5 are comparable to those of specimen 1, while a $\Delta u$ increase of about 60% is achieved by the specimen 4.
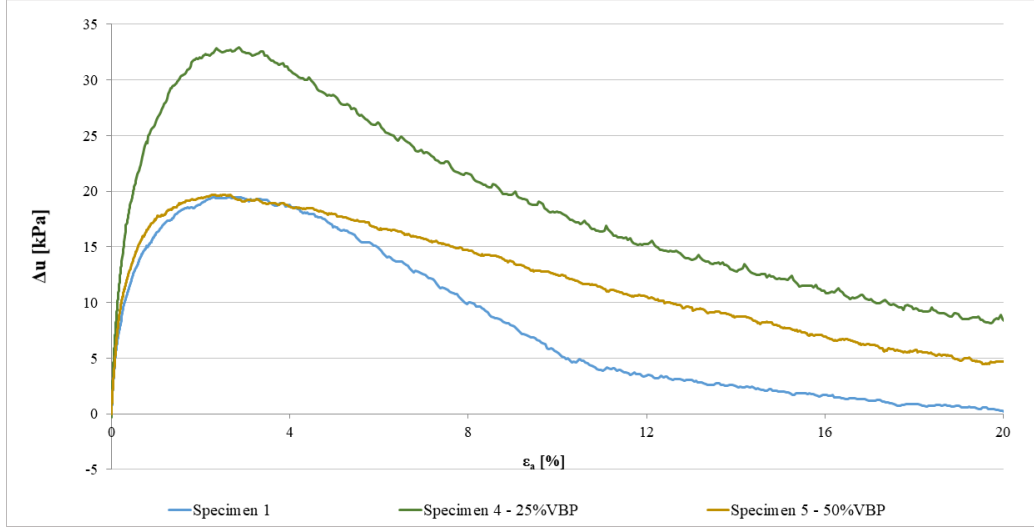


Figure 7.16: Axial deformation, $\varepsilon_a$, versus excess pore pressure, $\Delta u$ of the specimens 1, 4 and 5.

It is difficult to explain why this occurred. A possible reason could be that a difference in the overconsolidation ratio of the clayey matrix of the two heterogeneous specimens was provided by the consolidometer. In fact, although a consolidation pressure of 500 kPa was applied to both the heterogeneous specimens, the half of the cylinder with the highest VBP (i.e. equal to 50%) may have been loaded more than the other (i.e. with 25%VBP) because of its greater stiffness. This could have caused a greater consolidation of the 50%VBP specimen with respect to the 25%VBP specimen. This hypothesis, although difficult to demonstrate, seems to be consistent with the results obtained. In fact, the specimen with 25%VBP yielded results closer to those of slightly overconsolidated soils, since it was characterized by higher positive $\Delta u$ values.

Finally, Table 7.4 provides the secant and tangent drained Young's moduli ($E_{u-sec}$ and $E_{u-tan}$) of the heterogeneous specimens. Similarly to the homogeneous specimens, these moduli were determined from the q-$\varepsilon_a$ curves of Figure 7.13, by using the Eqs. 7.6 and 7.7 described in the previous Section 7.1.3.1.

| Specimen | $E'_{tan-0.1\%}$ [MPa] | $E'_{sec-4.5\%}$ [MPa] | $E'_{sec-9\%}$ [MPa] |
|:---:|:---:|:---:|:---:|
| 1 | 9.8 | 2.8 | 0.6 |
| 4 | 11.6 | 4.4 | 0.6 |
| 5 | 14.3 | 3.7 | 0.8 |

Table 7.4: Drained elastic tangent and secant moduli, E', for the heterogeneous specimens 4 and 5. The drained Poisson's coefficient $\nu'$ was assumed to be equal to 0.25. The results of the homogeneous specimen 1, with the same consolidation pressure of 50 kPa, was also listed by way of comparison.

The results confirm the strong non-linearity in the deformability of the heterogeneous specimens and indicate that a significant gain in stiffness is exhibited by specimen 5, because of the higher VBP.

### 7.1.3.3   Estimation of the exact VBP of the heterogeneous specimens

In order to check the consistency of the VBP predicted with the real block content of the two heterogeneous specimens 4 and 5, they were dissolved in water and sieved after the tests, in order to recover the gravel particles (i.e. rock blocks). The blocks were dried and subsequently put into a measuring cylinder (burette) completely filled with distilled water to the brim. The water overflowed from the burette, as a result of the insertion of the gravel inside it, was measured and then converted into volume. From these measurements, the VBP of the specimen 4 was found to be 24.5%, while that of the specimen 5 was found to be 47.2%.
The slight difference between these block contents and the VBPs assumed (i.e. 25% and 50%) is due to the random position of the blocks within the consolidometer cylinder as well as to the extrusion of the small specimens from the two half-cylinder heterogeneous materials. Since the VBP differences are absolutely neglegible, for consistency with the above, the VBPs of the specimens 4 and 5 will continue to be defined equal to 25% and 50% in the following Section 7.1.4.

## 7.1.4   Computed tomography

X-ray CT imaging is a non-destructive technique for visualizing high quality images of a solid object and its interior components, obtaining digital information on their 3D geometries and properties.
This technique was applied at Microservice S.r.l. (Alpignano, Torino) using the Computed Tomography NIKON XTEK XTH320 machine. The CT data processing

was performed by an expert laboratory technician of Microservice S.r.l.. 3D gray-scale images with 256 shades of gray per voxel were obtained. A low gray level corresponds to a material with low density. Conversely, higher gray levels indicate materials with higher density.

The CT output of a 25%VBP specimen is shown in Figure 7.17.
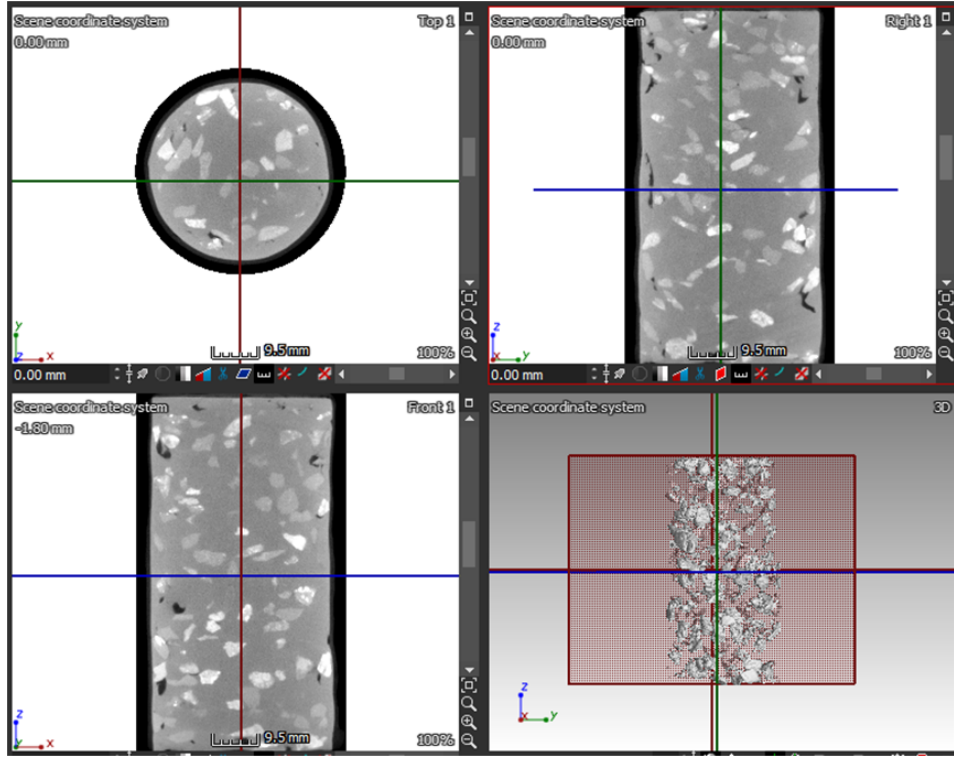


Figure 7.17: CT output for a 25%VBP specimen, visualized with *myVGL* software. The bottom right "3D" image contains the rock inclusions only.

From Figure 7.17 the gravel can easily be distinguished from the soil matrix, since the brighter elements correspond to higher density materials (i.e. rock inclusions). However, several black areas can also be identified near the periphery of the specimen. These areas correspond to macro-voids, which were almost certainly created during the extrusion phase (see Figure 7.6).

From the histogram of the distribution of gray levels, two threshold values were identified to exclude the wax layer and separate the blocks from the matrix. The result of this operation is illustrated in Figure 7.18 and Figure 7.19 for a 25%VBP and 50%VBP specimen, respectively.

External wax layer      Soil      Blocks
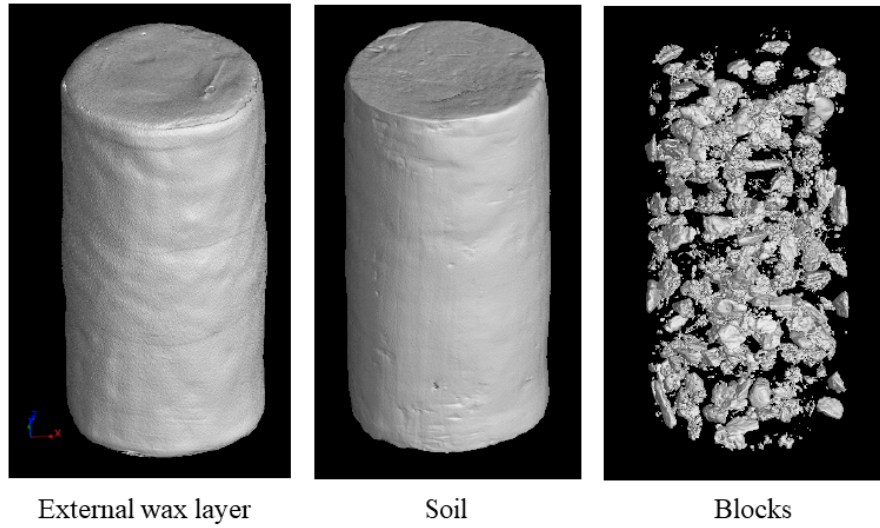
Figure 7.18: CT results for the 25%VBP specimen.



External wax layer      Soil      Blocks
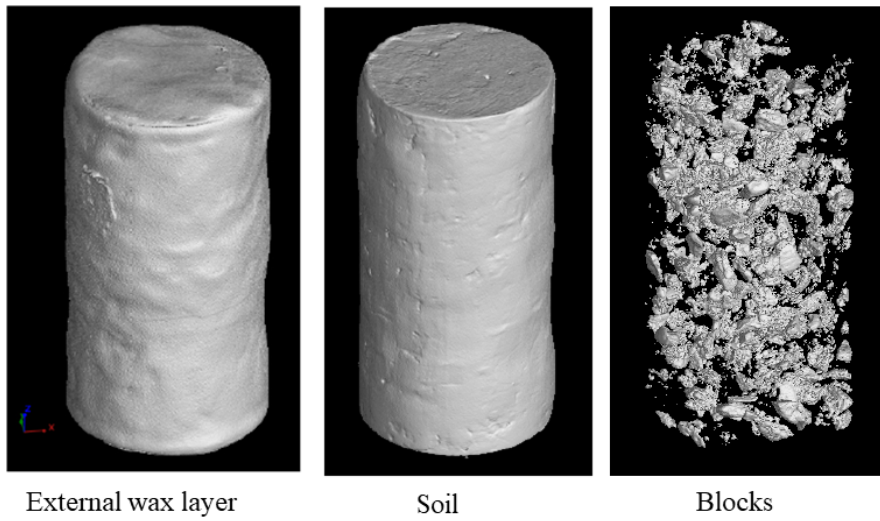
Figure 7.19: CT results for the 50%VBP specimen.

All the images were visualized and carefully manipulated by the laboratory technician of Microservice S.r.l. to provide an STL file for each specimen. These files can easily be imported into a software such as *Rhino* 3D for noise removal (i.e. elimination of thin protrusions, smoothing of block contours, etc.) and for the mesh generation.

The result of these operations will allow the original 3D geometry of the specimens to be accurately reconstructed and the experimental results to be numerically reproduced by means of an appropriately calibrated 3D numerical model. This model can

then be used to investigate the mechanical behavior of similar soft bimrocks, subjected to different stress histories and with different characteristics such as VBPs, block-size distributions, blocks shapes and mechanical parameters.

# Chapter 8

# Conclusions and suggestions for further research

This Ph.D. research was concerned with geotechnically complex formations, particularly focusing on those with a block-in-matrix internal arrangement (bimrocks and bimsoils).

A detailed geologic overview was provided and special attention was paid to melanges, which are the most abundant block-in-matrix formations. A correct identification of the geomaterial under study is indeed essential in order to make correct predictions about its properties (geometrical, hydraulic, etc.) and mechanical behavior.

Since there is great confusion in the terminology used to denote these heterogeneous geomaterials in the literature, a new classification of geotechnically complex formations was proposed. Of particular importance for this new classification is the degree of lithification-consolidation of the matrix, since it greatly influences the collection and preparation of regular specimens, the laboratory testing equipment to be used, testing procedures and test results. In this regard, bimrocks were subdivided into "soft" and "hard" bimrocks, according to their matrix characteristics and water sensitivity.

The first studies concerning melanges and similar bimrocks were carried out in the '90s, when serious technical problems occurred during many engineering works in and on these heterogeneous geomaterials. Experimental investigations and numerical analyses were carried out with the aim of investigating the major factors which influence the mechanical behavior of such complex formations. The results of these first studies, subsequently confirmed by more recent works, demonstrated that the presence and the characteristics of the rock inclusions play a key role in the mechanical response of these materials. Therefore, it was concluded that most of the technical problems and risks that occurred during construction works were caused by geologic and geotechnical mischaracterizations. In fact, for the sake of

simplicity, a common practice followed by geopractitioners was, and still is, to ignore the presence of rock inclusions, instead planning engineering works in and on block-in-matrix formations according to the strength and deformation properties of the weaker matrix only, or considering bimrocks and bimsoils to be equivalent and homogeneous materials whose mechanical properties depend on the block quantities.

In this research, in order to investigate and quantify the potential errors that these simplified approaches can produce when analyzing stability problems of slopes and tunnels in bimrocks, a great number of 2D and 3D numerical simulations were performed. To capture the inherent spatial and dimensional variability of bimrocks, a novel stochastic approach was developed and applied to generate slope and tunnel models with different block contents and characteristics (dimensions, positions, shapes and orientations). For each volumetric block proportion (VBP) and combination of block characteristics, many bimrock configurations were created by means of Matlab codes and analyzed with the RS2 FEM or FLAC3D FDM codes.

The results of the 2D FEM analyses on bimrock slopes and tunnels confirmed previous findings from the literature. They indicated that up to about 25% VBPs the presence of the blocks provides relatively little geomechanical advantage. In fact, on inspecting the results provided by the various 25% VBP simulations, no relevant differences were observed either in the average safety factors and failure surfaces of the slopes or in the average radial displacements and yielded zones of the tunnel models. On the contrary, the bimrock models with higher block contents (40%, 55% and 70%) showed a significant strength increase (higher average safety factors for the slopes and lower average radial displacements for the tunnels) and more tortuous failure surfaces, which were far different from those of the matrix-only slope and tunnel models. Hence, this outcome clearly indicates that if blocks are neglected in the analyses, extremely over conservative results and wrong positions and shapes of failure surfaces can be obtained. Similarly to the matrix-only model, if equivalent homogeneous approaches are used, the results are rather conservative and do not fully reflect the actual failure modes of these complex formations. Hence, these last approaches can conveniently be used in predesign stages only.

As expected, the 2D slope stability analyses revealed that both the inclination and shape of the blocks affected the stability of the slopes. In particular, the highest SFs were provided by elliptical shaped blocks when their major axes were inclined 0° to the horizontal. This inclination, which deviates greatly from that of the slopes, could have produced more tortuous failure surfaces and, consequently, a higher strength. Rounded blocks and randomly orientated elliptical blocks also yielded rather high safety factors, especially for VBPs above 55%.

Unlike the results of the 2D simulations, the 3D slope stability analyses already showed an evident increase in the safety factors for 15%VBP models. Higher safety factors than those provided by the 2D analyses were also registered for all the other

VBPs considered. This variability was attributed to the different geometric modeling of the rounded blocks, which actually corresponded to infinite-length cylinders in the 2D plane-strain conditions, and consequently to the different stress distribution around the spherical 3D blocks with respect to the circular 2D blocks.

Due to the high computational time required by the 3D analyses, and since potential mistakes resulting from 2D rather than 3D analyses appear to err on the side of safety, the use of a 2D stochastic approach seems adequate to analyze these heterogeneous formations.

Moreover, important differences were observed in the results of the many configurations analyzed for each VBP considered (safety factors and failure surface positions for the 2D and 3D slopes and radial displacements for the 2D tunnel models), whatever the type of stability analyses. This outcome was ascribed to the different block sizes and locations, assigned randomly by the Matlab codes, within the bimrock models with the same VBP, which affected the overall behavior of both the slopes and tunnels. This finding highlighted the benefit of adopting a statistically-based rather than a deterministic approach, since it allows both favorable and unfavorable conditions to be taken into account.

The findings of the numerical simulations carried out could be more firmly established by analyzing real case studies, through the generation of additional bimrock models with different block shapes (e.g. tabular or irregular blocks) and the inclusion of the block-matrix interfaces.

The results of the numerical analyses performed in this research confirmed that the strength, deformability and failure mode of bimrocks depend on the VBP and block characteristics. These parameters have also been found to strongly affect the construction phases of any engineering work. For example, when excavating in these complex formations, the presence of large rock blocks can induce, among other problems, face instabilities, significant settlements, obstructions and damage to cutters, with consequent safety risks, delays and cost increments. However, the evaluation of the VBP and block-size distribution of a bimrock or bimsoil is not a simple matter and represents one of the most critical issues in this field.

In an attempt to address these research gaps, two statistically-based tools were developed in this Ph.D. research. The first statistically investigates the degree of error that can be introduced by inferring the 3D block content of a heterogeneous geomaterial using 2D outcrop measurements (i.e. ABP). The potential of the proposed approach lies in the fact that working with 2D, rather than the widely used 1D measurements, can often be more convenient. In fact, outcrops, geologic maps and photographs are generally easy to analyze and, above all, cheaper than borehole drillings. A Matlab code was written to generate bimrock models, representing heterogeneous complex formations, with known VBPs and block-size distributions. For each VBP, an increasing size of the area investigated was considered, which was related to the dimension of the engineering problem at hand. The error in assuming the stereological equivalence between the ABP and VBP was then calculated,

217

providing a chart to adjust the initial 2D estimates by means of an uncertainty factor, selected on the basis of the outcrop size and ABP measured. As expected, the results indicated that inferring the 3D block content from 2D measurements on outcrops that are not large enough, with respect to the dimension of the engineering work under study, yields significantly incorrect estimates. However, a significant decreasing trend of the uncertainty factor for increasing outcrop sizes was obtained for all the VBPs analyzed. Interestingly, much lower uncertainty factors were obtained for bimrocks with VBPs above 30%, for which an almost negligible adjustment has to be made if an outcrop at least 5 times larger than the dimension of the engineering work under study is investigated.

The second statistically-based tool, implemented in a Matlab routine performing Monte Carlo simulations, estimates the probability of encountering blocks of variable sizes when their area of intersection with the tunnel face is greater than given critical values. The blocks considered in the analysis can be partially or totally contained within both the whole excavation face and the perimeter of the tunnel. The Matlab script, converted into the executable free application "PBE code", performs a great number of simulations and provides results that can be extremely useful for reducing risks when tunneling in heterogeneous ground by choosing the most appropriate TBM type, including face access, cutterhead design (i.e. shape, opening size, etc.), cutter types and machine power (i.e. torque, thrust and speed). A limitation of both these statistically-based tools is that only circular blocks can currently be simulated. Hence, further research could usefully be conducted to modify the codes in order to allow different block shapes (e.g. elliptical blocks) to be generated.

In order to explore the challenges of working with complex formations with a block-in-matrix internal arrangement, laboratory investigations were carried out.

To this end, a widespread chaotic Italian melange from the Oltrepò Pavese area was chosen and studied in detail. The melange was originated by a series of submarine debris flows producing a repetitive stratigraphy. Each stratigraphic layer is characterized by an inverse grading of the larger blocks. According to the new classification proposed, this material can be classified as a soft bimrock. In fact, in dry conditions it can be assimilated to a rock, but, since the matrix is actually an overconsolidated soil, it transforms into a bimsoil when it comes into contact with water. This peculiarity, as well as the presence of stronger rock blocks of different lithologies and dimensions, made the collection and preparation of intact specimens extremely complex and time consuming tasks. Since standard drilling techniques could not be used without damaging the material, a manual coring was necessary and irregular samples were extracted with hammers, picks and chisels. Given the inverse grading of the blocks within each stratigraphic layer, the samples were taken at different depths of the outcrop in order to have both heterogeneous and matrix-only specimens. In any case, sufficiently small rock blocks had to be contained within the samples to be able to perform representative laboratory tests

with standard equipment.

The weak nature of the marly matrix did not allow standard techniques to be used to produce regular specimens for laboratory tests without irreversibly damaging them. The solution used to overcome this problem was to (i) construct a diamond band saw to work in dry conditions, (ii) design and print in 3D a plastic element to be connected to a vacuum cleaner to contain the dust produced during the sample cut and (iii) stabilize the irregular melange samples by incorporating them in the mortar. However, the irregular shapes of the samples and the presence of innate micro and macro fractures, bedding planes and rock inclusions, which often detached, producing holes in the material, required a great number of cuts before a sufficiently regular specimen could be obtained. Due to these difficulties, some defects were in any case accepted in the specimens used for some of the subsequent laboratory tests.

The experimental investigation was carried out with the aim of characterizing separately the two components of the melange (blocks and matrix) and the heterogeneous geomaterial.

To investigate the basic behavior of the clay, composing the matrix, and the mineralogy of its grains the Atterberg limits and mineralogical analyses were carried out on the loose material. From these tests it was found that the matrix is an inorganic clay of high plasticity, with clay in the range 55-77%, that it is dominated by quartz and calcite and that its average natural water content, liquid limit, plastic limit and plasticity index are equal to 4.2%, 64.4%, 24.2% and 40.2%, respectively.

A uniaxial compressive strength (UCS) for three blocks with different lithologies in the range 33-62 MPa was obtained by using the Schmidt hammer test. In line with previous findings from the literature, the UCS of the matrix-only material was much lower than that of the blocks. Specifically, 37 point load tests and 8 uniaxial compressive tests were carried out on specimens with natural water content. The former, assuming a conversion factor C equal to 14 to correct the point load strength index, provided a matrix UCS equal to about 2.1 MPa. Interestingly, a similar result was obtained from the UC tests, which yielded a matrix UCS equal to 2.14 MPa. This finding confirmed that a conversion factor C equal to 14 can be applied to reliably predict the UCS of soft rocks, like the Oltrepò Pavese melange. It is worth highlighting that the specimens of both these tests were cut with the diamond band saw. Hence, it was only possible to obtain prismatic (not cylindrical) specimens. Due to the difficulties encountered during the cutting operations, the final geometry of the prismatic specimens was never completely free of irregularities. Moreover, variable slenderness ratios, ranging from 1.38 to 2.10, were obtained, which were always lower than that of 2.5 suggested by the ISRM Standards. Nevertheless, from reviewing the literature, it can be asserted that both the non-standard slenderness ratios and the non-conventional cross-sectional shapes of the specimens will only have produced modest effects on the UCS results obtained. Consequently, they can be considered only slightly overestimated and in any case

quite representative of the real strength of the geomaterial.

Contrary to expectations, significant differences in the failure modes of the heterogeneous and homogeneous specimens could be observed. The former, in fact, showed tortuous failure surfaces, which developed within the matrix and around the blocks, although the low specimen VBPs, always less than 7%, would not have justified this outcome. This behavior was ascribed to the presence of an often relevant number of non-rocky inclusions, composed of highly overconsolidated clay, within the heterogeneous melange samples. They were found after the tests, when the specimens were disaggregated, but they could not be quantified due to their sensitivity to water. Since they often showed cracks during the tests, it can be assumed that their strength is lower than that of the rock blocks but greater than that of the matrix. Consequently, the presence of these inclusions could have enhanced the development of tortuous failure surfaces, probably affecting the strength of the material to some degree, as well.

From the UC tests, and by means of Digital Image Correlation (DIC) analyses, an overall average elastic modulus of 0.79 GPa was found. This technique was used since, due to the fragility of the geomaterial, neither strain gauges nor direct contact extensometers could be used to measure local strains and the results provided by the LVDT (global strains) could not be considered reliable.

The peak shear strength of the matrix melange was estimated by performing 15 non-conventional direct shear tests. A non-conventional approach was used since, due to the peculiarity of this geomaterial, cylindrical specimens could not be produced to be placed in the circular Casagrande shear box. Therefore, prismatic specimens with as horizontal as possible bedding planes were obtained by means of the diamond band saw and, in order to place and hold them firmly within the shear box, a special formwork was designed and printed in 3D to incorporate the samples within two cylindrical layers of mortar. The results of these tests showed a significant data dispersion, which was almost certainly caused by the presence of non-horizontal bedding planes in the specimens, which affected their strength.

Two ring shear tests were carried out on the remolded sieved matrix to estimate the residual shear strength of the melange under study. The tests provided an average residual friction angle equal to about 6°. In line with previous findings from the literature on geomaterials like that under study, this value can be considered as a conservative result. In fact, the presence of angular and bonded coarse particles positively influences the mechanical behavior of the material that conversely, in remolded conditions, presents a lower shear strength.

The different matrix properties and block characteristics of the natural samples, as well as their innate micro-fractures, water sensitivity and variably oriented bedding planes, did not allow laboratory tests to be performed under controlled and repeatable conditions. Hence, in order to explore how the presence of blocks may affect the strength and deformability of a soft bimrock, a series of triaxial tests were carried out on reconstituted specimens, composed by the sieved matrix of the

Oltrepò Pavese melange and gravel of 2.75-4 mm. Specifically, isotropically consolidated undrained (CIU) tests were performed on 3 homogeneous specimens (to determine the mechanical properties of the matrix) and 2 heterogeneous specimens with VBPs equal to 25% and 50% (to compare the results). In order to obtain an overconsolidated clayey matrix, similar to that of the Italian melange, the specimens were consolidated using the consolidometer of the Geotechnical Laboratory of Politecnico di Torino, by recompressing the soil at the maximum surcharge load of the consolidometer, equal to 500 kPa. The homogeneous specimens were tested at three different effective consolidation stress levels (from 50 to 200 kPa) to define the strength envelope of the bimrock matrix. The minimum confinement of 50 kPa was applied to the heterogeneous specimens to obtain the maximum overconsolidation ratio (OCR), equal to 10, in order to simulate the real Oltrepò Pavese melange as closely as possible. In fact, although the OCR of the melange could not be determined, it can without any doubt be considered heavily overconsolidated.

The results of the homogeneous specimens, estimated using a linear failure criterion, yielded a friction angle equal to 15° and a cohesion equal to about 12 kPa. Moreover, a dilatant behavior and a localization of deformations in a shear band were observed for the specimen with the highest OCR. On the contrary, a more diffuse failure surface and a rather contractant behavior were registered for the other two specimens. Surprisingly, a lack of an evident post-peak strength reduction was observed in all the specimen stress-strain curves. In fact, this behavior was more similar to those of normalconsolidated soils and was probably caused by a reorientation of the clay particles perpendicular to the direction of loading after the one-dimensional consolidation, which could strongly have affected the mechanical behavior of the geomaterial tested.

The results obtained from the heterogeneous specimens indicated that when the block content is equal to 25% only, a rather significant stiffness increase is registered while no relevant strength variation is observed, with respect to the homogeneous specimen tested at the same confinement stress. A much higher stiffness increase and a strain hardening behavior was exhibited by the specimen with 50% VBP, although a comparable strength with the homogeneous specimen was shown. Moreover, the presence of the rock blocks did not allow the formation of the classic shear band to develop in the heterogeneous specimens. As a consequence, the failure was not characterized by a clear shear band, as was observed in the case of the homogeneous material.

In order to overcome the many difficulties inherent in the characterization of soft bimrocks, the findings of these tests can be used to set up and calibrate a 3D numerical model reproducing the experimental results. The model, which is beyond the scope of this work but could certainly be the subject of further research, could be an important tool to contribute to a deeper understanding of the mechanical behavior of soft bimrocks like that produced in the laboratory, but with other VBPs, OCR ratios, mechanical parameters, stress histories and geometrical characteristics. In

this regard, and in order to allow accurate 3D specimen models to be created, the geometrical properties of the rock inclusions contained in the heterogeneous specimens were detected (before the tests) by means of X-ray Computed Tomographies (CT), which were carried out at Microservice S.r.l. (Torino).

# Bibliography

Adam, D., R. Markiewicz, and M. Brunner (2014). "Block-in-Matrix Structure and Creeping Slope: Tunneling in Hard Soil and/or Weak Rock". In: *Geotechnical and Geological Engineering* 32.6, pp. 1467–1476. ISSN: 09603182. DOI: `10.1007/s10706-012-9591-5`.

Afifipour, M. and P. Moarefvand (2014a). "Experimental study of post-peak behavior of bimrocks with high rock block proportions". In: *Journal of Central South University* 21.2, pp. 761–767. ISSN: 21622388. DOI: `10.1007/s11771-014-1999-z`.

Afifipour, M. and P. Moarefvand (2014b). "Failure patterns of geomaterials with block-in-matrix texture: Experimental and numerical evaluation". In: *Arabian Journal of Geosciences* 7.7, pp. 2781–2792. ISSN: 18667538. DOI: `10.1007/s12517-013-0907-4`.

Afifipour, M. and P. Moarefvand (2014c). "Mechanical behavior of bimrocks having high rock block proportion". In: *International Journal of Rock Mechanics and Mining Sciences* 65, pp. 40–48. ISSN: 13651609. DOI: `10.1016/j.ijrmms.2013.11.008`.

Agustawijaya, D. S. (2007). "The uniaxial compressive strength of soft rock". In: *Civil Engineering Dimension* 9.1, pp. 9–14.

Akram, M. S. (2010). "Physical and numerical investigation of conglomeratic rocks. Ph.D. Thesis". PhD thesis. The University of new South Wales - Sydney, Australia, p. 346.

Alitalesh, M., M. Mollaali, and M. Yazdani (2016). "Correlation between uniaxial strength and point load index of rocks". In: *Japanese Geotechnical Society Special Publication The 15th Asian Regional Conference on Soil Mechanics and Geotechnical Engineering*, pp. 504–507.

Anagnostou, G., R. Schuerch, and M. Ramoni (2014). "TBM tunnelling in complex rock formations". In: *Chapter 15, In: XV MIR Conference "Interventi e opere nelle formazioni complesse", 19-20 November, Torino*, pp. 307–330.

ASTM (2020). *ASTM D4767-11 Standard Test Method for Consolidated Undrained Triaxial Compression Test for Cohesive Soils*. DOI: `10.1520/D4767-11.2`. URL: `http://www.astm.org/cgi-bin/resolver.cgi?D4767`.

ASTM-D-6467 (1999). *Torsional ring shear test to determine drained residual shear strength of cohesive soils*.

ASTM D5731 (1995). *Standard Test Method for Determination of the Point Load Strength Index of Rock*.

Atkinson, J. (2007). *The mechanics of soils and foundations*. Second Ed. CRC Press-Taylor & Francis Group, p. 2007.

Aydin, A. (2009). "ISRM Suggested Method for Determination of the Schmidt Hammer Rebound Hardness : Revised Version". In: *International Journal of Rock Mechanics and Mining Sciences* 46.3, pp. 627–634. DOI: 10.1016/j.ijrmms.2008.01.020.

Aydin, A and A Basu (2005). "The Schmidt Hammer in rock material characterization". In: *Engineering Geology* 81, pp. 1–14. DOI: 10.1016/j.enggeo.2005.06.006.

Bailey, E. B. and W. J. McCallien (1950). "The Ankara Melange and the The Ankara Mélange and the Anatolian Thrust". In: *Nature* 166, pp. 938–940. DOI: 10.1038/166938a0.

Barbero, M., M. Bonini, and M. Borri-Brunetto (2006). "Analisi numeriche della stabilità di un versante in bimrock". In: *Incontro Annuale dei Ricercatori di Geotecnica 2006 - IARG*. 1. Pisa, 26-28 Giugno 2006, pp. 26–28.

Barbero, M., M. Bonini, and M. Borri-Brunetto (2007). "Numerical modelling of the mechanical behaviour of bimrock". In: *11th Congress of the international Society for Rock Mechanics (ISRM 2007)*. Lisbon, Portugal, 9-13 July.

Barbero, M., M. Bonini, and M. Borri-Brunetto (2012). "Numerical simulations of compressive tests on bimrock". In: *Electronic Journal of Geotechnical Engineering* 17 X, pp. 3397–3414. ISSN: 10893032.

Barla, G. and P. Perello (2014). "Introduzione alla caratterizzazione geologica e geotecnica delle formazioni complesse". In: *MIR 2014 - XV ciclo di conferenze di meccanica e ingegneria delle rocce*. Torino, 19-20 novembre 2014., pp. 11–38.

Basu, A., T. B. Celestino, and A.A. Bortolucci (2007). "Predicting weathering grades by Schmidt hammer test : an investigation on granitic rock materials from southeastern Brazil". In: *11th Congress of the International Society for Rock Mechanic*. July. Lisbon, Portugal, pp. 385–390.

Blaber, J., B. Adair, and A. Antoniou (2015). "Ncorr: Open-source 2D Digital Image Correlation Matlab software". In: *Experimental Mechanics*. DOI: 10.1007/s11340-015-0009-1.

BS 1377-7 British Standard (1990). *Shear strength tests (total stress)*.

Burghignoli, A. (1991). *Lezioni di meccanica delle terre*. Ed. by ESA. Second edi, p. 256.

Button, E. et al. (2004). "Tunnelling in tectonic melanges accommodating the impacts of geomechanical complexities and anisotropic rock mass fabrics". In: *Bulletin of Engineering Geology and the Environment* 63.2, pp. 109–117. ISSN: 1435-9529. DOI: 10.1007/s10064-003-0220-7.

Cancelli, A. (1986). "The determination of shear strength parameters for sheared clay shales". In: *Proceedings of the International Symposium on Engineering in complex rock formations*. Beijing, China, pp. 297–304.

Caselle, C. et al. (2019). "Evolution of local strains under uniaxial compression in an anisotropic gypsum sample". In: *Geotechnical Research for Land Protection and Development, CNRIG*, pp. 454–461.

Cen, D., D. Huang, and F. Ren (2017). "Shear deformation and strength of the interphase between the soil-rock mixture and the benched bedrock slope surface". In: *Acta Geotechnica* 12.2, pp. 391–413. ISSN: 1861-1133. DOI: 10.1007/s11440-016-0468-2.

Clark, C. M. and L. Dutrow B (2012). "Single-crystal X-ray Diffraction." In: *Integration Research and Education: Geochemical Instrumentation and Analysis*, p. 2012.

Cloos, M. (1984). "Flow mélanges and the structural evolution of accretionary wedges." In: *Mélanges: Their Nature, Origin, and Significance. Special Paper*. Ed. by L. A. Raymond. 198. The Geological Society of America, pp. 71–79.

Coli, N. (2010). "Metodi avanzati di indagine di ammassi rocciosi a blocchi in matrice (bimrock)". PhD thesis. Bologna University, p. 245.

Coli, N., P. Berry, and D. Boldini (2011). "In situ non-conventional shear tests for the mechanical characterisation of a bimrock". In: *International Journal of Rock Mechanics and Mining Sciences* 48.1, pp. 95–102. ISSN: 13651609. DOI: 10.1016/j.ijrmms.2010.09.012. URL: http://dx.doi.org/10.1016/j.ijrmms.2010.09.012.

Coli, N. et al. (2009). "In situ large size non conventional shear tests for the mechanical characterization of a bimrock in The Santa Barbara open pit mine (Italy)". In: *43rd US Rock Mechanics Symposium and 4th U.S.-Canada Rock Mechanics Symposium*. Asheville, NC June 28th-July 1, 2009: American Rock Mechanics Association.

Coli, N. et al. (2012). "The contribution of geostatistics to the characterisation of some bimrock properties". In: *Engineering Geology* 137-138.SEPTEMBER, pp. 53–63. ISSN: 00137952. DOI: 10.1016/j.enggeo.2012.03.015.

Cowan, D. S. (1974). "Deformation and Metamorphism of the Franciscan Subduction Zone Complex Northwest of Pacheco Pass, California". In: *Geological Society of America Bulletin* 85.October, pp. 1623–1634.

Cowan, D.S. (1978). "Origin of blueschist-bearing chaotic rocks in the Franciscan Complex, San Simeon, California". In: *Geological Society of America Bulletin* 89, pp. 1415–1423.

Cowan, D.S. (1985). "Structural styles in Mesozoic and Cenozoic mélanges in the western Cordillera of North America". In: *Geological Society of America Bulletin* 96.November 2016, pp. 451–462. ISSN: 0016-7606. DOI: 10.1130/0016-7606(1985)96<451.

Crosta, G. B., P. Frattini, and N. Fusi (2007). "Fragmentation in the Val Pola rock avalanche, Italian Alps". In: *Journal of Geophysical Research: Earth Surface* 112.1, pp. 1–23. ISSN: 21699011. DOI: `10.1029/2005JF000455`.

De Biagi, Valerio et al. (2017). "Estimation of the return period of rockfall blocks according to their size". In: *Natural Hazards and Earth System Sciences* 17.1, pp. 103–113. ISSN: 16849981. DOI: `10.5194/nhess-17-103-2017`.

D'Elia, B. et al. (1986). "Slope movements in structurally complex formations". In: *Proceedings of the International Symposium on Engineering in complex rock formations, 3-7 November, 1986, Beijing, China*, pp. 430–436.

D'Elia, B. et al. (1998). "Geotechnical characterisation of slope movements in structurally complex clay soil and stiff jointed clays." In: *Rivista italiana di geotecnica* 3, pp. 5–32.

Della Valle, G. et al. (2015). "The Gondola Slide: a mass trans - port complex controlled by margin topography (South-western Adriatic Margin, Mediterranean Sea)". In: *Marine Geology* 366, pp. 97 –113.

DiPonio, M. A., D. Chapman, and C. Bournes (2007). "EPB tunnel boring machine design for boulder conditions". In: *Rapid Excavation and Tunneling Conference*, pp. 215–228.

Dong, W., E. Pimentel, and G. Anagnostou (2013a). "Experimental Investigations into the Mechanical Behaviour of the Breccias Around the Proposed Gibraltar Strait Tunnel". In: *Rock Mech Rock Eng* 46, pp. 923–944. DOI: `10.1007/s00603-012-0350-y`.

Dong, W, E Pimentel, and G Anagnostou (2013b). "On the Mechanical Behaviour of the Gibraltar Strait Breccias". In: *Constitutive Modeling of Geomaterials, SSGG*, pp. 409–416.

Elter, P. and G. Raggi (1965). "Contributo alla conoscenza dell'Apennino ligure: 1. Osservazioni preliminari sulla posizione delle ofioliti nella zona di Zignago (La Spezia); 2. Considerazioni sul problema degli olistostromi". In: *Bollettino della Società Geologica Italiana* 84, pp. 303–322.

Erguler, Z. A. and R. Ulusay (2009). "Water-induced variations in mechanical properties of clay-bearing rocks". In: *International Journal of Rock Mechanics & Mining Sciences* 46, pp. 355–370. DOI: `10.1016/j.ijrmms.2008.07.002`.

Esu, F. (1977). "Behaviour of Slopes in Structurally Complex Formations". In: *General report, Session IV. Proc. Int. Symp. The Geotechnics of Structurally Complex Formations, Capri, Italy*, pp. 292–304.

Fagereng, Å. (2011). "Frequency-size distribution of competent lenses in a block-in-matrix mélange: Imposed length scales of brittle deformation?" In: *Journal of Geophysical Research* 116.B05302, pp. 1–12. DOI: `10.1029/2010JB007775`.

Festa, A. (2011). "Tectonic, sedimentary, and diapiric formation of the Messinian mélange: Tertiary Piedmont Basin (northwestern Italy)". In: *Mèlanges - Processes of formation and societal significance. In: The Geological Society of America - Special Paper 480*. Chap. 10, pp. 215–232.

Festa, A., K. Ogata, and G. A. Pini (2019a). "Mélanges: 100th anniversary of the inception of the term and concept". In: *Gondwana Research* 74, pp. 1–6. ISSN: 1342937X. DOI: `10.1016/j.gr.2019.07.002`.

Festa, A., K. Ogata, and G. A. Pini (2020). "Polygenetic mélanges: a glimpse on tectonic, sedimentary and diapiric recycling in convergent margins". In: *Journal of the Geological Society*, jgs2019–212. ISSN: 0016-7649. DOI: `10.1144/jgs2019-212`.

Festa, A. et al. (2010). "Mélanges and mélange-forming processes : a historical overview and new concepts Mélanges and mélange-forming processes : a historical overview and new concepts". In: *International Geology Review* 52, pp. 1040–1105. DOI: `10.1080/00206810903557704`.

Festa, A. et al. (2012). "Mechanisms and processes of stratal disruption and mixing in the development of mélanges and broken formations : Redefining and classifying mélanges". In: *Tectonophysics* 568-569, pp. 7–24. DOI: `10.1016/j.tecto.2012.05.021`.

Festa, A. et al. (2014). "Geology of the Aventino River Valley (eastern Majella, central Italy)". In: *Journal of Maps* 10.4, pp. 584–599. ISSN: 17445647. DOI: `10.1080/17445647.2014.899524`. URL: `http://dx.doi.org/10.1080/17445647.2014.899524`.

Festa, A. et al. (2015). "Late Oligocene - early Miocene olistostromes (sedimentary mélanges) as tectono-stratigraphic constraints to the geodynamic evolution of the exhumed Ligurian accretionary complex (Northern Apennines, NW Italy)". In: *International Geology Review* April, pp. 37–41. DOI: `10.1080/00206814.2014.931260`.

Festa, A. et al. (2016). "Origin and significance of olistostromes in the evolution of orogenic belts: A global synthesis". In: *Gondwana Research* 39, pp. 180–203. ISSN: 1342-937X. DOI: `10.1016/j.gr.2016.08.002`. URL: `http://dx.doi.org/10.1016/j.gr.2016.08.002`.

Festa, A. et al. (2019b). "Diagnostic features and field-criteria in recognition of tectonic, sedimentary and diapiric mélanges in orogenic belts and exhumed subduction-accretion complexes". In: *Gondwana Research* 74.February, pp. 7–30. ISSN: 1342937X. DOI: `10.1016/j.gr.2019.01.003`.

Flores, G. (1955). "Les résultats des études pour les recherches pétroliféres en Sicile". In: *4th World Petroleum Congress: Rome, Casa Editrice Carlo Colombo, Section 1/A/2*, pp. 121–122.

Flores, G. (1956). *The results of the studies on petroleum exploration in Sicily. Discussion: Bollettino del Servizio Geologico d'Italia, (English translation of the 1955 paper).*

Frank, G. and D. R. Chapman (2005). "A new model for characterizing the cobble and boulder fraction for soft ground tunneling". In: *Rapid Excavation and Tunneling Conference.* Seattle, pp. 780–791.

Frankovská, J. and T. Durmekova (2011). "Specific features of weak rock laboratory testing". In: *15th European Conference on Soil Mechanics and Geotechnical Engineering*, pp. 337–342.

Gansser, A. (1955). "New aspects of the geology in Central Iran". In: *Proc.4th World Petrol, eongr. Rome sect. I/A/5*, pp. 280–300.

Gao, Q.F. (2020). "Micro-macro approach of dilatancy phenomenon in remoulded clays. Study of the behaviour under saturated and unsaturated conditions". PhD thesis. Université de Lorraine, p. 227.

Gao, W. et al. (2014). "Geomechanical Characterization of Zhangmu Soil-Rock Mixture Deposit". In: *Geotech Geol Eng* 32, pp. 1329–1338. DOI: `10.1007/s10706-014-9808-x`.

Gokceoglu, C. and K. Zorlu (2004). "A fuzzy model to predict the uniaxial compressive strength and the modulus of elasticity of a problematic rock". In: *Engineering Applications of Artificial Intelligence* 17.1, pp. 61–72. ISSN: 09521976. DOI: `10.1016/j.engappai.2003.11.006`.

Goodman, R. E. and C. S. Ahlgren (2000). "Evaluating Safety of Concrete Gravity Dam on Weak Rock: Scott Dam". In: *Journal of Geotechnical and Geoenvironmental Engineering* 126.5, pp. 429–442. DOI: `10.1061/(ASCE)1090-0241(2000)126:5(429)`.

Guerra, C. I. et al. (2016). "Multiscale Modelling of the Slope Stability of Block-in-Matrix Materials". In: *Geo-Chicago 2016 GSP 270 644*, pp. 658–667.

Gwildis, U., J. Aguilar, and K. Mosavat (2018). "TBM Tool Wear Analysis for Cutterhead Configuration and Resource Planning in Glacial Geology". In: *North American Tunneling Conference*. Washington, DC, USA 24-27 June 2018.

Haneberg, W. C. (2004). "Simulation of 3D block populations to charaterize outcrop sampling bias in bimrocks". In: *Felsbau* 22.5, pp. 19–26. ISSN: 01746979. URL: `http://www.scopus.com/inward/record.url?eid=2-s2.0-5444265918{\&}partnerID=tZOtx3y1`.

Harrison, J.P. (2014). "What do we mean about complexity?" In: *Chapter 2, In:XV MIR Conference "Interventi e opere nelle formazioni complesse", Torino*, pp. 39–48.

Hawkins, A. B. (1998). "Aspects of rock strength". In: *Bulletin of Engineering Geology and the Environment* 57.1, pp. 17–30. ISSN: 14359529. DOI: `10.1007/s100640050017`.

Head, K H and R J Epps (2011). *Manual of Soil Laboratory Testing, Vol. II: Permeability, Shear Strength and Compressibility Tests*. Ed. by Scotland Whittles Publishing, Caithness. 3rd. Vol. II.

Hicher, P. Y., H. Wahyudi, and D. Tessier (2000). "Microstructural analysis of inherent and induced anisotropy in clay". In: *Mechanics of Cohesive-Frictional Materials* 5.5, pp. 341–371. ISSN: 10825010. DOI: `10.1002/1099-1484(200007)5:5<341::AID-CFM99>3.0.CO;2-C`.

Hoek, E. (1994). "Strength of rock and rock masses". In: *ISRM News Journal* 2.2, pp. 4–16.

Hsu, K. J. (1968). "Principles of Melanges and Their Bearing on the Franciscan-Knoxville Paradox". In: *Geological Society of America Bulletin* 79.August, pp. 1063–1074.

Hsu, K. J. (1974). "Melanges and Their Distinction from Olistostromes". In: *The Society of Economic Paleontologists and Mineralogists (SEPM) Modern and Ancient Geosynclinal Sedimentation (SP19) - Special Publication N.19*, pp. 321–333.

Hunt, S. W. (2014). "Managing Risk of Tunneling in Cobbly , Bouldery Ground". In: *TAC 2014: Tunnelling in a Resource Driven World!* Vancouver.

Hunt, S.W. (2017). *Tunneling in Cobbles and Boulders - Breakthroughs in Tunneling Short Course, Chicago IL, August 14-16*. Chicago.

Hunt, S.W. and D.E. Del Nero (2010). "Two Decades of Advances Investigating, Baselining and Tunneling in Bouldery Ground". In: *World Tunneling Congress*. Vancouver, pp. 1–8.

INGV (2014). *Il laboratorio di Diffrattometria a raggi X (Istituto Nazionale di Geofisica e Vulcanologia, Napoli): identificazione e stima quantitativa delle fasi in campioni polverizzati*. Tech. rep., pp. 1–24. DOI: ISSN:2039-7941.

Irfan, T.Y. and K.Y. Tang (1993). *Effect of the coarse fractions on the shear strength of colluvium. Geo Report 23*. Tech. rep. Hong Kong Government, p. 224.

ISRM (2007). *The complete ISRM suggested methods for rock characterization, testing & monitoring: 1974-2006*. Ed. by R. Ulusay and J.A. Hudson. ISBN: 978-975-93675-4-1.

Itasca Consulting Group, Inc (2017). *FLAC3D Modeling - Sixth Edition*.

Jiang, J. et al. (2016). "Research on mechanical parameters of coarse-grained sliding soil based on CT scanning and numerical tests". In: *Landslides* 13, pp. 1261–1272. ISSN: 1612-510X. DOI: 10.1007/s10346-015-0635-9. URL: http://dx.doi.org/10.1007/s10346-015-0635-9.

Jiméneze Ugalde, D. A. and S. A. B. da Fontoura (2016). "Numerical modeling of a conglomeratic rock from Costa Rica, Central America". In: *VII Brazilian Symposium on Rock Mechanics-SBMR 2016 Rock Mechanics and Rock Engineering for Innovation and Development ISRM Specialized Conference*. February 2017. Belo Horizonte, Minas Gerais, Brazil, 9-22 October 2016. DOI: 10.20906/CPS/SBMR-05-0004.

John, M. (1972). *The influence of length to diameter ratio on rock properties in uniaxial compression: a contribution to standardisation in rock mechanics testing*.

Kahraman, S. and M. Alber (2006). "Estimating unconfined compressive strength and elastic modulus of a fault breccia mixture of weak blocks and strong matrix". In: *International Journal of Rock Mechanics and Mining Sciences* 43.8, pp. 1277–1287. ISSN: 13651609. DOI: 10.1016/j.ijrmms.2006.03.017.

Kahraman, S. et al. (2015). "An assessment on the indirect determination of the volumetric block proportion of Misis fault breccia (Adana, Turkey)". In: *Bulletin of Engineering Geology and the Environment* 74.3, pp. 899–907. ISSN: 1435-9529. DOI: 10.1007/s10064-014-0666-9. URL: http://link.springer.com/10.1007/s10064-014-0666-9.

Kalender, A. et al. (2014). "An approach to predicting the overall strengths of unwelded bimrocks and bimsoils". In: *Engineering Geology* 183, pp. 65–79. ISSN: 00137952. DOI: 10.1016/j.enggeo.2014.10.007. URL: http://dx.doi.org/10.1016/j.enggeo.2014.10.007.

Kanjii, M.A. (2014). "Critical issues in soft rocks". In: *Journal of Rock Mechanics and Geotechnical Engineering* 6.3, pp. 186–195. ISSN: 1674-7755. DOI: 10.1016/j.jrmge.2014.04.002. URL: http://dx.doi.org/10.1016/j.jrmge.2014.04.002.

Karaman, K. and A. Kesimal (2015). "A comparative study of Schmidt hammer test methods for estimating the uniaxial compressive strength of rocks". In: *Bulletin of Engineering Geology and the Environment* 74, pp. 507–520. ISSN: 1435-9529. DOI: 10.1007/s10064-014-0617-5. URL: http://dx.doi.org/10.1007/s10064-014-0617-5.

Kaufmann, F.J. (1886). "Emmenund Schlierengegenden nebst Umgebungen bis zur Brünigstrasse und Linie Lungern-Grafenort." In: *Geologische Karte der Schweiz* 24.1, p. 608.

Khorasani, E. et al. (2019). "Statistical analysis of bimslope stability using physical and numerical models". In: *Engineering Geology* 254.March, pp. 13–24. ISSN: 00137952. DOI: 10.1016/j.enggeo.2019.03.023.

Kim, C., C. Smell, and E.W. Medley (2004). "Shear strength of franciscan complex melange as calculated from back analysis of a landslide". In: *Proceedings of the fifth International Conference on Case Histories in Geotechnical Engineering.* New York, pp. 13–17.

Lancellotta, R. (2012). *Geotecnica.* Ed. by Zanichelli. IV edition.

Lebourg, T., J. Riss, and E. Pirard (2004). "Influence of morphological characteristics of heterogeneous moraine formations on their mechanical behaviour using image and statistical analysis". In: *Engineering Geology* 73, pp. 37–50. DOI: 10.1016/j.enggeo.2003.11.004.

Lenoir, N. et al. (2007). "Volumetric digital image correlation applied to x-ray microtomography images from triaxial compression tests on argillaceous rock". In: *Strain* 43.3, pp. 193–205. ISSN: 00392103. DOI: 10.1111/j.1475-1305.2007.00348.x.

Leroueil, S. et al. (1997). "large deformation shear strength of two types of structured soils". In: *Symposium on deformation and progressive failure in geomechanics*, pp. 217–222.

Li, C.s. et al. (2016). "Computed tomography based numerical simulation for triaxial test of soil-rock mixture". In: *Computers and Geotechnics* 73, pp. 179–

188. ISSN: 0266-352X. DOI: 10.1016/j.compgeo.2015.12.005. URL: http://dx.doi.org/10.1016/j.compgeo.2015.12.005.

Li, X., Q. L. Liao, and J. M. He (2004). "In situ tests and a stochastic structural model of rock and soil aggregate in the Three Gorges reservoir area, China". In: *International Journal of Rock Mechanics and Mining Sciences* 41.3, p. 494. ISSN: 13651609. DOI: 10.1016/j.ijrmms.2003.12.030. URL: http://linkinghub.elsevier.com/retrieve/pii/S136516090300279X.

Lin, Q. and J. F. Labuz (2013). "Fracture of sandstone characterized by digital image correlation". In: *International Journal of Rock Mechanics and Mining Sciences* 60, pp. 235–245. ISSN: 13651609. DOI: 10.1016/j.ijrmms.2012.12.043.

Lindquist, E. S. (1994a). "The mechanical properties of a physical model melange." In: *7th International IAEG Congress*. Balkema, Rotterdam, pp. 819–826.

Lindquist, E. S. (1994b). "The Strength and Deformation Properties of Melange. Ph.D. Thesis". PhD thesis. University of California, Berkeley, p. 288.

Lindquist, E. S. and Richard E. Goodman (1994). *Strength and deformation properties of a physical model melange*. Ed. by P.P. Nelson and S.E. Laubach. Austin: A.A. Balkema, pp. 843–850.

Lindquist, E.S. (1991). *Franciscan and Fractures, Term Paper for CE 280, Rock Mechanics. Instructor: Prof. R.E Goodman, Dept. Civil Engineering, University of California, Berkeley*.

Lucente, C.C. and G.A. Pini (2008). "Basin-wide mass-wasting complexes as markers of the Oligo-Miocene foredeep-accretionary wedge evolution in the Northern Apennines, Italy". In: *Basin Research* 20, pp. 49 –71.

Lunardi, P., F. Cassani, and F. Pennino (2014). "Lo scavo a piena sezione di gallerie in formazioni complesse". In: *Chapter 14, In:XV MIR Conference: Interventi e opere nelle formazioni complesse, Torino*, pp. 277–305.

Mahdevari, S. and P. Maarefvand (2016). "An investigation into the effects of block size distribution function on the strength of bimrocks based on large-scale laboratory tests". In: *Arabian Journal of Geosciences* 9.7, p. 509. ISSN: 1866-7511. DOI: 10.1007/s12517-016-2499-2. URL: http://link.springer.com/10.1007/s12517-016-2499-2.

Mahdevari, S. and P. Maarefvand (2017). "Applying ultrasonic waves to evaluate the volumetric block proportion of bimrocks". In: *Arab J Geosci (2017)* 10, p. 204. DOI: 10.1007/s12517-017-2999-8.

Mandelbrot, B. B. (1983). *The fractal geometry of nature*. New york: W.H. Freeman and Company. ISBN: 0716711869.

Marinos, P. and E. Hoek (2001). "Estimating the geotechnical properties of rock masses such as flysch". In: *Bulletin of Engineering Geology and Environment* 60, pp. 85–92.

Marinos, V. et al. (2019). "Selection of TBM and geotechnical assessment of a microtunnel in a difficult geological environment: a case of a natural gas pipeline

beneath an active landslide ( Albania )". In: *Bulletin of Engineering Geology and the Environment (2019)* 78, pp. 1795–1813. DOI: https://doi.org/10.1007/s10064-018-1241-6.

Martin, R. Torrence and Charles C. Ladd (1975). "Fabric of consolidated kaolinite". In: *Clays and Clay Minerals* 23.1, pp. 17–25. ISSN: 00098604. DOI: 10.1346/CCMN.1975.0230103.

Medley, E. W. (1997). "Uncertainty in estimates of block volumetric proportions in melange bimrocks". In: *International symposium on Engineering Geology and The Environment.* January 1997, pp. 267–272.

Medley, E. W. (2001). "Orderly Characterization of Chaotic Franciscan Melanges". In: *Felsbau* 19.4. ISSN: 01746979.

Medley, E. W. (2002). "Estimating Block Size Distributions of Melanges and Similar Block-in-Matrix Rocks (Bimrocks)". In: *Proceedings of 5th North American Rock Mechanics Symposium (NARMS)*, pp. 509–606.

Medley, E. W. (2004). "Observations on Tortuous Failure Surfaces in Bimrocks". In: *Felsbau* 22, pp. 35–43. ISSN: 01746979.

Medley, E. W. (2007a). "Bimrocks - Part 1: Introduction." In: *Newsletter of the Hellenic Society of Soil Mechanics and Geotechnical Engineering, Athens, Greece* 7, pp. 17–21.

Medley, E. W. (2007b). "Bimrocks - Part 2: Case histories and Practical Guidelines". In: *Newsletter of the Hellenic Society of Soil Mechanics and Geotechnical Engineering, Athens, Greece* 8, pp. 26–31.

Medley, E. W. (2008). "Engineering the Geological Chaos of Franciscan and Other Bimrocks Engineering the Geological Chaos of Franciscan and Other Bimrocks". In: *42nd U.S. Rock Mechanics Symposium and 2nd U.S.-Canada Rock Mechanics Symposium.* San Francisco, California.

Medley, E. W. and R. E. Goodman (1994). "Estimating the Block Volumetric Proportions of Melanges and Similar Block-in-Matrix Rocks (Bimrocks)". In: *Proceedings of the 1st North American rock mechanics symposium.* Austin, Texas, pp. 851–858.

Medley, E. W. and P. F. Sanz Rehermann (2004). "Characterization of Bimrocks (Rock/Soil Mixtures) With Application to Slope Stability Problems". In: *Eurock 2004 & 53rd geomechanics colloquium.* October.

Medley, E. W. and D. Zekkos (2011). "Geopractitioner approaches to working with antisocial mélanges". In: *Mélanges: Processes of Formation and Societal Significance - Geological Society of America Special Paper 480.* Ed. by John Wakabayashi and Yildirim Dilek. Vol. 42. Chap. 13, pp. 261–277. ISBN: 9780123742919. DOI: 10.1016/S0065-2156(09)70001-8. arXiv: arXiv:1011.1669v3.

Medley, E.W. (1994). "The engineering characterization of melanges and similar Block-in-matrix rocks (Bimrocks)." PhD thesis. University of California at Berkeley, p. 338.

Medley, E.W. (2012). "Simple Concepts Useful for Characterizing Complex Bim-rocks Underlying Slopes." In: *Landslide and slope stability short course AEG-IE/ASCE-IE, UC Riverside Extension Center, CA* May, pp. 1–96.

Medley, E.W. and E. S. Lindquist (1995). "The engineering significance of the scale-independence of some Franciscan melanges in California, USA". In: *Rock Mechanics Proceedings of the 35th U.S. Symposium.* Ed. by R. A. Daemen, J. J. K. and Schultz. Rotterdam, pp. 907–914.

Minuto, D. and L. Morandi (2015). "Geotechnical Characterization and Slope Stability of a Relict Landslide in Bimsoils (Blocks in Matrix Soils) in Dowtown Genoa, Italy." In: *Engineering geology for society and territory, Landslide processes* 2.January, pp. 1083–1088. DOI: 10.1007/978-3-319-09057-3.

Montoya-Araque, E. A. and L. O. Suarez-Burgoa (2018). "pyBIMstab: Application software for 2D slope stability analysis of block-in-matrix and homogeneous materials". In: *SoftwareX* 7, pp. 383–387. ISSN: 23527110. DOI: 10.1016/j.softx.2018.11.003. URL: https://doi.org/10.1016/j.softx.2018.11.003.

Montoya-Araque, E. A., L. O. Suarez-Burgoa, and E. W. Medley (2020). "Application of the tortuous surface method to stochastic analysis of bimslope stability". In: *Bulletin of Engineering Geology and the Environment.* ISSN: 14359537. DOI: 10.1007/s10064-020-01909-5.

Montoya-Araque, Exneyder A. and Ludger O. Suarez-Burgoa (2019). "Automatic generation of tortuous failure surfaces in block-in-matrix materials for 2D slope stability assessments". In: *Computers and Geotechnics* 112.April, pp. 17–22. ISSN: 18737633. DOI: 10.1016/j.compgeo.2019.04.002. URL: https://doi.org/10.1016/j.compgeo.2019.04.002.

Mutti, E. et al. (2009). "Turbidites and turbidity currents from Alpine "flysch" to the exploration of continental margins". In: *Sedimentology* 56, pp. 267–318. DOI: 10.1111/j.1365-3091.2008.01019.x.

Napoli, M. L., M. Barbero, and C. Scavia (2019a). "Slope stability in heterogeneous rock masses with a block-in-matrix fabric". In: *ISRM.* Foz do Iguassu, Brazil, pp. 3482–3489.

Napoli, M.L. (2020). "3D slope stability analyses of a complex formation with a block-in-matrix fabric". In: *16th International Conference of IACMAG.* Turin, In printing.

Napoli, M.L., M. Barbero, and R. Fontana (2020a). "Probability of boulder encounters when tunneling in heterogeneous ground". In: *International Journal of Geomechanics (Submitted GMENG-6158).*

Napoli, M.L., M. Barbero, and C. Scavia (2017). "Uso di un approccio stocastico per l'analisi di stabilità di versanti in bimrock". In: *Incontro Annuale dei Ricercatori di Geotecnica 2017- IARG 2017.* 5-7 July, Matera, Italy.

Napoli, M.L., M. Barbero, and C. Scavia (2018a). "Analyzing slope stability in bimrocks by means of a stochastic approach". In: *European Rock Mechanics Symposium, EUROCK 2018.* 22-26 May 2018, Saint Petersburg.

Napoli, M.L., M. Barbero, and C. Scavia (2019b). "Tunneling in heterogeneous rock masses with a block-in-matrix fabric." In: *International Journal of Rock Mechaics and Mining Science*, Submitted (IJRMMS_2019_885).

Napoli, M.L. et al. (2018b). "A stochastic approach to slope stability analysis in bimrocks". In: *International Journal of Rock Mechanics and Mining Sciences* 101, pp. 41–49. ISSN: 1365-1609. DOI: 10.1016/j.ijrmms.2017.11.009. URL: https://doi.org/10.1016/j.ijrmms.2017.11.009.

Napoli, M.L. et al. (2020b). "Identifying uncertainty in estimates of bimrocks volumetric proportions from 2D measurements". In: *Engineering Geology*, In press. DOI: https://doi.org/10.1016/j.enggeo.2020.105831.

Ogata, K. et al. (2014). "The carbonate mass transport deposits of the Paleogene Julian-Slovenian Basin (Italy/ Slovenia): internal anatomy and inferred genetic processes." In: *Marine Geology* 356, pp. 88 –110.

Ogata, K. et al. (2020). "No Submarine landslide deposits in orogenic belts: olistostromes and sedimentary mélanges". In: *Submarine Landslides: Subaqueous Mass Transport Deposits from Outcrop to Seismic Profiles*. Ed. by K. Ogata, A. Festa, and G.A. Pini. Geophysical Monograph Series. American Geophysical Union, pp. 3–26. ISBN: 9781119500513. DOI: https://doi.org/10.1002/9781119500513.ch1.

Ortner, H. (2001). "Growing folds and sedimentation of the Gosau Group, Muttekopf, Northern Calcareous Alps, Austria". In: *International Journal of Earth Sciences* 90, pp. 727–739. DOI: 10.1007/s005310000182.

Pan, Y.W., M.H. Hsieh, and J.J. Liao (2008). "Mechanical Properties of Virtual Block-in-matrix Colluvium". In: *American Rock Mechanics Association* 08-051.Jun- Jul, pp. 1–8.

Pellegrino, A., J. Sulem, and G. Barla (1997). "The effects of slenderness and lubrication on the uniaxial behavior of a soft limestone". In: *International Journal of Rock Mechanics and Mining Sciences* 34.2, pp. 333–340.

Peng, J., L. N.Y. Wong, and C. I. Teh (2018). "A re-examination of slenderness ratio effect on rock strength: Insights from DEM grain-based modelling". In: *Engineering Geology* 246.October, pp. 245–254. ISSN: 00137952. DOI: 10.1016/j.enggeo.2018.10.003.

Perfect, E. (1997). "Fractal models for the fragmentation of rocks and soils: a review". In: *Engineering Geology* 48.3-4, pp. 185–198. ISSN: 00137952. DOI: 10.1016/S0013-7952(97)00040-9. URL: http://linkinghub.elsevier.com/retrieve/pii/S0013795297000409.

Pilgerstorfer, T. and W. Schubert (2014). "Results of laboratory tests on artificial block-in-matrix rocks". In: *Rock Mechanics and Rock Engineering: Structures on and in rock masses - Proceedings of EUROCK 2014, ISRM European Regional Symposium*. Chap. 2, pp. 381–386. ISBN: 978-0-12-227410-7. DOI: http://dx.doi.org/10.1016/B0-12-227410-5/00669-4. URL: http://www.sciencedirect.com/science/article/pii/B0122274105006694.

Pini, G.A. (1999). "Tectonosomes and olistostromes in the Argille Scagliose of the Northern Apennines, Italy". In: *Geological Society of America Special Papers* 335, p. 73. DOI: `https://doi.org/10.1016/j.gr.2019.04.005`.

Poppe, L.J. et al. (2002). *A Laboratory Manual for X-Ray Powder Diffraction. U. S. Geological Survey Open-File Report 01-041*. Tech. rep., p. 88. URL: `http://pubs.usgs.gov/of/2001/of01-041/index.htm`.

Prokešová, R., D. Plašienka, and R. Milovský (2012). "Structural pattern and emplacement mechanisms of the Krížna cover nappe (Central Western Carpathians)". In: *Geologica Carpathica* 63.1, pp. 13–32. DOI: `10.2478/v10096-012-0001-y`.

Püstow, C.G.H. (2001). "Tunnelling in a tectonic melange of high structural complexity". PhD thesis. Aachen University of Technology.

Raymond, L. A. (1975). "Tectonite and Melange - A Distinction". In: *Geology* 3, pp. 7–9.

Raymond, L. A. (1984). "Classification of melanges. In: Raymond, L.A., Boulder, L.A. (Eds.), Melanges: Their Nature, Origin and Significance". In: *Geological Society of America Special Paper 198*, pp. 7–20.

Raymond, L. A. (2017). "What is Franciscan ?: revisited". In: *International Geology Review* 00.00, pp. 1–63. ISSN: 0020-6814. DOI: `10.1080/00206814.2017.1396933`. URL: `https://doi.org/10.1080/00206814.2017.1396933`.

Remitti, F., G. Bettelli, and P. Vannucchi (2007). "Internal structure and tectonic evolution of an underthrusted tectonic mélange: the Sestola-Vidiciatico tectonic unit of the Northern Apennines, Italy". In: *Geodinamica Acta* 20, pp. 37–51. DOI: `https://doi.org/10.3166/ga.20.37-51`.

Riedmüller, G. et al. (2001). "Engineering Geological Characterization of Brittle Faults and". In: *Felsbau* 19, pp. 13–19.

RIG (1994). *Raccomandazioni per la misura della resistenza al punzonamento*.

Roberts, R.C., S.W. Crossen, and L.J. Strachan (2014). "Underground Construction Challenges Associated with the Albany Conglomerate in Auckland". In: *Proceedings of the 15th Australasian Tunnelling Conferenc*. Sydney, pp. 1–13.

Sachan, A. and D. Penumadu (2007). "Effect of Microfabric on Shear Behavior of Kaolin Clay". In: *Journal of Geotechnical and Geoenvironmental Engineering*. DOI: `10.1061/(ASCE)1090-0241(2007)133:3(306)`.

Skempton, A.W. (1964). "Long-term stability of clay slopes". In: *Géotechnique* 14.2, pp. 77–102. DOI: `https://doi.org/10.1680/geot.1964.14.2.77`.

Skempton, A.W. (1985). "Residual strength of clays in landslides, folded strata and the laboratory". In: *Géotechnique* 35.1, pp. 3–18. DOI: `https://doi.org/10.1680/geot.1985.35.1.3`.

Song, C., P. Wang, and H. A. Makse (2008). "A phase diagram for jammed matter". In: *Nature* 453.29, pp. 629–632.

Sonmez, H., E. Tuncay, and C. Gokceoglu (2004a). "Models to predict the uniaxial compressive strength and the modulus of elasticity for Ankara Agglomerate".

In: *International Journal of Rock Mechanics and Mining Sciences* 41.5, pp. 717–729. ISSN: 13651609. DOI: `10.1016/j.ijrmms.2004.01.011`.

Sonmez, H. et al. (2004b). "Relationships between Volumetric Block Proportions and Overall UCS of a Volcanic Bimrock". In: *Felsbau Rock and Soil Engineering Journal for Engineering Geology, Geomechanics and Tunneling* 22.5, pp. 27–34.

Sonmez, H. et al. (2006). "Considerations in developing an empirical strength criterion for bimrocks". In: *4th Asian Rock Mechanics Symposium (ARMS 2006)*. Singapore, 6-10 Nov. 2006, p. 7.

Sonmez, H. et al. (2009). "A conceptual empirical approach for the overall strength of unwelded bimrocks". In: *ISRM Regional Symposium, Rock Engineering in Difficult Ground Condition, Soft Rock and Karst,* Dubrovnik, Croatia, 29-31 Oct. 2009. ISBN: 9780415804813. URL: `http://bimrocks.com/bimsite/wp-content/uploads/2010/07/Sonmez{\_}et{\_}al2009{\_}B050.pdf`.

Sonmez, H. et al. (2014). "Artificial neural network (ANN) based model for predicting of overall strength of volcanic bimrock". In: *Eurock 2014*. Vol. 22, pp. 83–87.

Sonmez, H. et al. (2016). "Predicting uniaxial compressive strength and deformation modulus of volcanic bimrock considering engineering dimension". In: *International Journal of Rock Mechanics and Mining Sciences* 86, pp. 91–103. ISSN: 13651609. DOI: `10.1016/j.ijrmms.2016.03.022`. URL: `http://dx.doi.org/10.1016/j.ijrmms.2016.03.022`.

Studer, B. (1872). "Index Der Petrographie Und Stratigraphie Der Schweiz Und Ihrer Umgebungen. Dalp, Bern". In: *Bern, Verlag der J. Dalp'schen Buch- und Kunsthandlung (K. Schmid)*, p. 272.

Suzuki, M., S. Tsuzuki, and T. Yamamoto (2005). "Physical and Chemical Index Properties of Residual Strength of Various Soils". In: *Mem Fac Eng.*

Tarkoy, P. J. (2008). "The boulder facts of life". In: *World Tunneling Congress.* December, pp. 25–28.

Tien, Y. M. et al. (2010). "Uncertainty in Estimation of Volumetric Block Proportion of Bimrocks by Using Scanline Method". In: *American Rock Mechanics Association (ARMA)*.

Tsiambaos, G. (2010). "Engineering Geological behaviour of heterogeneous and chaotic rock masses". In: *12th International Congress - Bulletin of the Geological Society of Greece.* November. Patras.

Tuncay, E. and N. Hasancebi (2009). "The effect of length to diameter ratio of test specimens on the uniaxial compressive strength of rock". In: *Bulletin of Engineering Geology and the Environment* 68.4, pp. 491–497. ISSN: 14359529. DOI: `10.1007/s10064-009-0227-9`.

Turcotte, L. (1986). "Fractals and fragmentation". In: *New York* 91.5, pp. 1921–1926.

Vezzani, L., A. Festa, and F. Ghisetti (2010). "Geology and Tectonic evolution of the Central-Southern Apennines, Italy". In: *Geological Society of America Special Papar* 469, p. 58. DOI: http://dx.doi.org/10.1130/2010.2469.

Wakabayashi, J. (2015). "Anatomy of a subduction complex: architecture of the Franciscan Complex, California, at multiple length and time scales". In: *International Geology Review* 57.5-8, pp. 669–746. ISSN: 0020-6814. DOI: 10.1080/00206814.2014.998728. URL: http://dx.doi.org/10.1080/00206814.2014.998728.

Wakabayashi, J. (2019). "Sedimentary compared to tectonically-deformed serpentinites and tectonic serpentinite mélanges at outcrop to petrographic scales: Unambiguous and disputed examples from California". In: *Gondwana Research* 74, pp. 55–71. DOI: https://doi.org/10.1016/j.gr.2019.04.005.

Wakabayashi, J. and E. W Medley (2004). "Geological Characterization of Melanges for Practitioners". In: *Felsbau* 22.5, pp. 10–18. ISSN: 01746979.

Wakabayashi, J. et al. (2002). *Tunnels through fault rocks and tectonic melanges: a short course for engineering geologists and geotechnical engineers*. Ed. by E. Lincoln Mathieson. San Francisco, p. 76.

Wu, J. et al. (2018). "A digital image analysis of gravel aggregate using CT scanning technique". In: *International Journal of Pavement Research and Technology* 11.2, pp. 160–167. ISSN: 1996-6814. DOI: 10.1016/j.ijprt.2017.08.002. URL: https://doi.org/10.1016/j.ijprt.2017.08.002.

Xu, W., R. Hu, and R. Tan (2007). "Some geomechanical properties of soil-rock mixtures in the Hutiao Gorge area, China". In: *Géotechnique* 3, pp. 255–264.

Xu, Wen-jie, Qiang Xu, and Rui-lin Hu (2011). "Study on the shear strength of soil-rock mixture by large scale direct shear test". In: *International Journal of Rock Mechanics and Mining Sciences* 48.8, pp. 1235–1247. ISSN: 1365-1609. DOI: 10.1016/j.ijrmms.2011.09.018. URL: http://dx.doi.org/10.1016/j.ijrmms.2011.09.018.

Xu, W.J., Z.Q. Yue, and R.L. Hu (2008). "Study on the mesostructure and mesomechanical characteristics of the soil-rock mixture using digital image processing based finite element method". In: *International Journal of Rock Mechanics and Mining Sciences* 45.June, pp. 749–762. ISSN: 13651609. DOI: 10.1016/j.ijrmms.2007.09.003. URL: http://linkinghub.elsevier.com/retrieve/pii/S1365160907001438.

Xu, Y. and M. Cai (2017). "Numerical study on the influence of cross-sectional shape on strength and deformation behaviors of rocks under uniaxial compression". In: *Computers and Geotechnics* 84, pp. 129–137. ISSN: 18737633. DOI: 10.1016/j.compgeo.2016.11.017.

Zhang, S. et al. (2015). "Investigation of scale effect of numerical unconfined compression strengths of virtual colluvial-deluvial soil-rock mixture". In: *International Journal of Rock Mechanics and Mining Sciences* 77, pp. 208–219. ISSN:

13651609. DOI: `10.1016/j.ijrmms.2015.04.012`. URL: `http://dx.doi.org/10.1016/j.ijrmms.2015.04.012`.